



12-2002

Using neutron scattering to study the structure and flexibility of hexadecyltrimethylammonium dichlorobenzoate and related micelles

Zhibin Li
University of Tennessee

Follow this and additional works at: https://trace.tennessee.edu/utk_graddiss

Recommended Citation

Li, Zhibin, "Using neutron scattering to study the structure and flexibility of hexadecyltrimethylammonium dichlorobenzoate and related micelles. " PhD diss., University of Tennessee, 2002.
https://trace.tennessee.edu/utk_graddiss/6262

This Dissertation is brought to you for free and open access by the Graduate School at TRACE: Tennessee Research and Creative Exchange. It has been accepted for inclusion in Doctoral Dissertations by an authorized administrator of TRACE: Tennessee Research and Creative Exchange. For more information, please contact trace@utk.edu.

To the Graduate Council:

I am submitting herewith a dissertation written by Zhibin Li entitled "Using neutron scattering to study the structure and flexibility of hexadecyltrimethylammonium dichlorobenzoate and related micelles." I have examined the final electronic copy of this dissertation for form and content and recommend that it be accepted in partial fulfillment of the requirements for the degree of Doctor of Philosophy, with a major in Chemistry.

Linda J. Lee Magid, Major Professor

We have read this dissertation and recommend its acceptance:

Accepted for the Council:

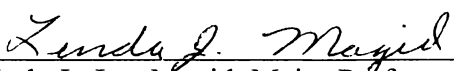
Carolyn R. Hodges

Vice Provost and Dean of the Graduate School

(Original signatures are on file with official student records.)

To the Graduate Council:

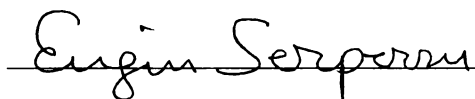
I am submitting herewith a dissertation written by Zhibin Li entitled "Using Neutron Scattering to Study the Structure and Flexibility of Hexadecyltrimethylammonium Dichlorobenzoate and Related Micelles". I have examined the final paper copy of this dissertation for form and content and recommend that it be accepted in partial fulfillment of the requirements for the degree of Doctor of Philosophy, with a major in Chemistry.


Linda J. Lee Magid, Major Professor

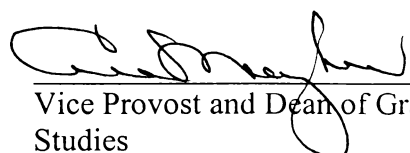
We have read this dissertation
and recommend its acceptance:







Accepted for the Council:


Vice Provost and Dean of Graduate
Studies

USING NEUTRON SCATTERING TO STUDY THE STRUCTURE AND
FLEXIBILITY OF HEXADECYLTRIMETHYLAMMONIUM
DICHLOROBENZOATE AND RELATED MICELLES

A Dissertation
Presented for the
Doctor of Philosophy
Degree
The University of Tennessee, Knoxville

Zhibin Li
December 2002

Thesis
2002b
.L525

To Yue

ACKNOWLEDGMENTS

I wish to express my heartfelt gratitude and appreciation to Dr. Lee Magid, for her guidance, encouragement and patience as a research advisor. She showed me the world of micellar systems, neutron science, and American life.

Appreciation is extended to Dr. Paul Butler for his help and contributions to the scattering work and illuminating discussions, and to Dr. Mark Dadmun for his help on understanding scattering and polymer science.

I thank all the faculty members who helped me in the last few years both inside and outside the classroom.

I also want to thank the following neutron facilities: NIST Center for Neutron Research, IPNS at Argonne National Laboratory and SINQ in Switzerland. I thank the University of Tennessee and the National Science Foundation for financial support.

I thank Dr. Jan Skov Pedersen and Dr. Peter Schurtenberger for providing some of the Fortran code used for data analysis.

Finally, I thank my wife Yue for her love, patience and help. I thank my parents, brothers and sister for their support and encouragement.

ABSTRACT

Certain ionic surfactants can self-assemble in aqueous solutions into giant flexible wormlike micelles that behave similarly to semi-flexible polymers. Small angle neutron scattering (SANS) has been used to study the sizes and flexibilities of these micelles. By allowing the probing of shorter length scales than light scattering, SANS is clearly preferable for determining micellar persistence lengths directly. SANS curves were fit to a series of micellar models to get information on persistence lengths, contour lengths and cross-sectional radii. The impact of different tail lengths, head groups, counterions, and varying ionic strengths were studied.

Counterions have major effects on micellar size and flexibility. For nonpenetrating counterions, such as chloride and bromide, the micellar size and flexibility increase as the concentrations of the counterion increase (by adding the common-ion salt), with bromide having the larger effect compared to chloride. For penetrating counterions, such as salicylate, 2,6-dichlorobenzoate, and tosylate, the micellar size and flexibility highly depend on the structure of the counterions. Mixed counterions (penetrating and non penetrating) have also been studied, and the micellar size found to increase dramatically in mixed counterions systems.

Unlike chloride and bromide, the penetrating counterion can also make the micellar size decrease, reverting back to globular at higher salt concentrations. By taking advantage of H/D substitution, SANS experiments have been used to determine rod-like and spherical micellar internal structures by the methods of external and internal contrast variation for the CTA26ClBz micellar system. By using deuterated sodium 2,6-dichlorobenzoate, deuterated surfactant and changing the D₂O/H₂O content in the solution, we got detailed information on counterion binding to study the micellar size reversion for a penetrating counterion.

TABLE OF CONTENTS

	page
CHAPTER I	
INTRODUCTION.....	1
1.1 GENERAL BACKGROUND.....	1
1.2 WORMLIKE MICELLES.....	8
1.2.1 Role of counterion: electrostatics and specific binding....	10
1.2.2 Micellar persistence lengths.....	12
1.3 STATEMENT OF PROBLEM	13
CHAPTER II	
SMALL-ANGLE NEUTRON SCATTERING.....	14
2.1 INTRODUCTION.....	14
2.2 FUNDAMENTALS OF NEUTRON SCATTERING AND STRUCTURE.....	16
2.3 SOLUTIONS OF PARTICLES.....	22
2.3.1 Radius of gyration.....	24
2.3.2 Radii of gyration for various geometrical shapes.....	25
2.3.3 Form factors.....	27
2.3.4 The effect of polydispersity.....	31
2.3.5 Structure factor for solution of interacting particles.....	34
2.3.6 Plots used for wormlike micelles.....	36
2.4 CONTRAST VARIATION EXPERIMENTS.....	38
CHAPTER III	
USING SANS TO STUDY MICELLE GROWTH AND FLEXIBILITY.....	41
3.1 INTRODUCTION.....	41
3.2 FLEXIBILITY OF ELONGATED SDS MICELLES IN SODIUM CHLORIDE SOLUTIONS.....	42
3.2.1 Local micellar structure.....	43
3.2.2 Overall micellar size and flexibility.....	51

3.3	TUNING SIZE AND FLEXIBILITY OF THE CATIONIC WORMLIKE MICELLES: THE ROLE OF SURFACTANT HEAD GROUP AND TAIL LENGTH.....	60
3.3.1	Detailed CTAB micellar structure.....	72
3.3.2	Detailed TTAB micellar structure.....	85
3.3.3	Detailed CPyBr micellar structure.....	96
3.3.4	Comparison between TTAB and CTAB – Tail length influence on micellar size and flexibility.....	107
3.3.5	Comparison between CPyBr and CTAB – Head group influence on micellar size and flexibility.....	113
3.4	THE INFLUENCE OF MIXED COUNTERIONS ON MICELLAR STRUCTURE AND FLEXIBILITY: NaTos/Cl, NaSal/Cl, AND Na ₂₆ CIBz/Cl.....	114
3.4.1	The CTATos/Cl micellar system in aqueous NaTos/Cl...116	
3.4.2	The CTASal/Cl micellar system in aqueous NaSal/Cl....143	
3.4.3	The CTA ₂₆ CIBz/Cl micellar system in aqueous Na ₂₆ CIBz/Cl.....	154
3.5	CONCLUSIONS	163
3.5.1	Micellar flexibility.....	163
3.5.2	Micellar size	170
CHAPTER IV	USING INTERNAL AND EXTERNAL CONTRAST VARIATION TO STUDY THE DETAILED STRUCTURE OF THE MICELLAR SURFACE.....	173
4.1	INTRODUCTION.....	173
4.1.1	External and internal contrast variation.....	174
4.1.2	Effect of salt on ρ_s	177
4.1.3	Core plus shell model for the micelles.....	178
4.1.4	Radius of gyration.....	179
4.2	EXTERNAL CONTRAST VARIATION FOR PROTIATED CTA USING DEUTERATED Na ₂₆ CIBz AS THE SALT.....	180
4.2.1	Radius of gyration.....	181
4.2.2	Match point and percentage of counterion binding	185

4.2.3	Details of the micellar structure.....	190
4.3	EXTERNAL CONTRAST VARIATION FOR CTA-d ₃₃	197
4.3.1	Local structure and match point	197
4.3.2	Shell structure and overall micellar structure	203
4.4	INTERNAL CONTRAST VARIATION USING CTA-d ₃₃ /CTA-d ₀ MIXTURES	208
4.5	DISCUSSION AND CONCLUSIONS.....	211
CHAPTER V	EXPERIMENTAL SECTION.....	225
5.1	MATERIALS.....	225
5.2	MAKING SOLUTIONS.....	225
5.3	SYNTHESIS OF DEUTERIATED 2,6-DICHLORO- BENZOIC ACID	226
5.4	PREPARATION OF CETYLTRIMETHYLAMMONIUM 2,6-DICHLOROBENZOATE.....	232
5.5	USING NMR TO DETERMINE THE DEUTERATION OF Na ²⁶ ClBz-d ₃	233
5.6	NEUTRON PRODUCTION AND DETECTION.....	234
5.7	DATA COLLECTION, CORRECTION AND NORMALIZATION.....	235
5.8	LEAST SQUARES FITTING FOR DATA REDUCTION	238
	LIST OF REFERENCES	240
	VITA	248

LIST OF TABLES

TABLE	PAGE
2.1 Scattering lengths and cross section for some common isotopes	22
3.1 Local micellar structure for SDS micelles.....	50
3.2 Fitted parameters for SDS micelles in aqueous NaCl without/with intermicellar interactions.....	52
3.3 Local micellar structure for CTAB micelles.....	74
3.4 Fitted parameters for CTAB micelles in aqueous NaBr without/with intermicellar interaction.....	76
3.5 Local micellar structure for TTAB micelles.....	86
3.6 Fitted parameters for TTAB micelles in aqueous NaBr without/with intermicellar interaction	89
3.7 Local micellar structures for CPyBr micelles.....	98
3.8 Fitted parameters for CPyBr micelles in aqueous NaBr without/with intermicellar interaction.....	100
3.9 Persistence length and a for CTAB, TTAB and CPyBr in aqueous NaBr.....	112
3.10 Fitted parameters for CTATos micelles in aqueous NaTos/NaCl mixed salt solutions, without taking intermicellar interactions into account.....	127
3.11 Results of c^* calculation for CTATos micelles in mixed salt.....	129
3.12 Fitted parameters for CTASal micelles in aqueous NaSal/NaCl mixed salt solutions without taking intermicellar interactions into account	148
3.13 Fitted parameters for CTA26ClBz/Cl micelles in aqueous Na26ClBz/Cl mixed salt solutions, without taking intermicellar interactions into account.....	157
4.1 Volume, scattering length and densities used in contrast variation experiments...	176
4.2 ρ_s for external contrast variation and ρ_c for internal contrast variation	177
4.3 R_g and $I(0)$ from Guinier plots for 1M salt and $R_{g,cs}$ and $I(0)$ together with N/L from Guinier-like plots for 0.4M salt.....	188
4.4 Results of fitting the full scattering curves in the Q range $0.1-1.2\text{\AA}^{-1}$ for CTA micelles in 1M Na26-d ₃ -ClBz. External contrast variation studies	194
4.5 Results of external contrast variation for CTA-d ₃₃ micelles: R_g and $I(0)$ from Guinier plots for 1M salt and $R_{g,cs}$ and $I(0)$ together with N/L from Guinier-like plot for 0.2M salt.....	204

4.6	Results of fitting the full scattering curves in the Q range 0.02~0.38 Å for CTA-d ₃₃ micelles and CTA-d ₀ micelles in 1M Na ₂ 6ClBz. External and internal contrast variation respectively.....	209
4.7	R _g and I(0) from Guinier-plots for 1M Na ₂ 6ClBz and R _{g,cs} and I(0) together with N/L from Guinier-like plots for 0.4M, 0.2M Na ₂ 6ClBz by using CTA-d ₃₃ /CTA-d ₀ in internal contrast variation experiments.....	219
4.8	Comparison of three different series of the counterion binding(<i>f</i>) on the micellar surface and the radius of gyration.....	223

LIST OF FIGURES

FIGURE	PAGE
1.1 Common example of each type of surfactant.....	2
1.2 Schematic diagram: surfactant volume fraction F vs. molar ratio C_s/C of salt over surfactant concentration. Represent from ref 1.....	4
2.2 The geometry of neutron scattering. From reference [8].....	18
2.3 Example of Guinier plot $\ln(I(Q))$ vs. Q^2	27
2.4 An example of Guinier-like plot: $\ln(I(Q)*Q)$ vs. Q^2	38
3.1 SANS curves for SDS micelles in 1M NaCl solutions at 45°C.....	44
3.2 SANS curves for SDS micelles in 1.2M NaCl at 45°C.....	45
3.3 SANS curves for SDS micelles in 1.5M NaCl at 45°C.....	46
3.4 SANS curves for SDS micelles in 2.0M NaCl at 45°C.....	47
3.5 Bending rod plot for 4.8mM SDS in NaCl solutions at 45°C.....	48
3.6 Guinier-like plot for SDS micelles in 1.5M NaCl solutions.....	49
3.7 Bending rod plots of SANS data for SDS with fits in 1M NaCl without taking intermicellar interactions into account.....	53
3.8 Bending rod plots of SANS data for SDS with fits in 2M NaCl without taking intermicellar interactions into account.....	54
3.9 Dependence of micellar contour lengths on SDS concentration in different NaCl solutions	55
3.10 Dependence of micellar Kuhn lengths on SDS concentration in different NaCl solutions	57
3.11 Bending rod plots of SANS data for SDS with fits in 1.2M NaCl, with including the effect of intermicellar interactions	58
3.12 Bending rod plots of SANS data for SDS with fits in 1.5M NaCl, with including the effect of intermicellar interactions.....	59
3.13 SANS curves for CTAB micelles in 0.15M NaBr at 40°C.....	62
3.14 SANS curves for CTAB micelles in 0.25M NaBr at 40°C.....	63
3.15 SANS curves for CTAB micelles in 0.50M NaBr at 40°C.....	64
3.16 SANS curves for CTAB micelles in 1.0M NaBr at 40°C.....	65

3.17	SANS curves for TTAB micelles in 1.5M NaBr at 40°C.....	66
3.18	SANS curves for TTAB micelles in 3.0M NaBr at 40°C.....	67
3.19	SANS curves for CPyBr micelles in 0.25M NaBr at 30°C.....	68
3.20	SANS curves for CPyBr micelles in 0.5M NaBr at 30°C.....	69
3.21	SANS curves for CPyBr micelles in 0.8M NaBr at 30°C.....	70
3.22	Comparison of 3.8mM CTAB, TTAB, and CPyBr at NaBr concentrations of 0.5, 0.5, and 3.0M respectively	71
3.23	Guinier-like plots for CTAB in 0.5M NaBr.....	73
3.24	Bending rod plots of SANS data for CTAB with fits in 0.25M NaBr without taking intermicellar interactions into account.....	78
3.25	Dependence of micellar contour lengths on CTAB concentrations in different NaBr solutions	79
3.26	Dependence of micellar Kuhn lengths on CTAB concentrations in different NaBr solutions	80
3.27	Bending rod plots of SANS data for CTAB with fits in 0.25M NaBr taking intermicellar interactions into account	82
3.28	Bending rod plots of SANS data for CTAB with fits in 0.50M NaBr taking intermicellar interactions into account	83
3.29	Bending rod plots of SANS data for CTAB with fits in 1.0M NaBr taking intermicellar interactions into account	84
3.30	Guinier-like plots for TTAB in 1.5M NaBr aqueous solutions.....	88
3.31	Bending rod plots of SANS data for TTAB with fits in 1.5M NaBr without taking intermicellar interactions into account.....	90
3.32	Bending rod plots of SANS data for TTAB with fits in 3.0M NaBr without taking intermicellar interactions into account.....	91
3.33	Dependence of micellar contour lengths on TTAB concentrations in different NaBr solutions	92
3.34	Dependence of micellar Kuhn length on TTAB concentrations in different NaBr solutions	94
3.35	Bending rod plots of SANS data for TTAB with fits in 1.5M NaBr taking intermicellar interactions into account.....	95
3.36	Bending rod plots of SANS data for TTAB with fits in 3.0M NaBr taking intermicellar interactions into account.....	96
3.37	Guinier-like plots for CPyBr in 0.5M NaBr solutions	97

3.38	Bending rod plots of SANS data for CPyBr with fits in 0.25M NaBr without taking intermicellar interactions into account.....	102
3.39	Bending rod plots of SANS data for CPyBr with fits in 0.50M NaBr without taking intermicellar interactions into account.....	103
3.40	Bending rod plots of SANS data for CPyBr with fits in 0.80M NaBr without taking intermicellar interactions into account.....	104
3.41	Dependence of micellar contour lengths on CPyBr concentration in different NaBr solutions.....	105
3.42	Dependence of micellar Kuhn lengths on CPyBr concentration in different NaBr solutions.....	106
3.43	Bending rod plots of SANS data for CPyBr with fits in 0.25M NaBr, including the effects of intermicellar interaction	108
3.44	Bending rod plots of SANS data for CPyBr with fits in 0.50M NaBr, including the effects of intermicellar interaction	109
3.45	Bending rod plots of SANS data for CPyBr with fits in 0.80M NaBr, including the effects of intermicellar interaction	110
3.46	Evolution of micellar size as a function of c_s and mole fraction of 26ClBz, taking the $1/Q_{max}$ value derived from bending rod plots as proportional to the micellar R_g values. From reference [27].....	115
3.47	SANS curves for 7.5mM CTATos micelles in NaTos solutions at 40°C.....	117
3.48	SANS curves for CTATos in 2 mole % NaTos/Cl in 0.15M total salt at 40°C....	117
3.49	SANS curves for CTATos in 12 mole % NaTos/Cl in 0.15M salt at 40°C.....	119
3.50	SANS curves for CTATos in 2 mole % NaTos/Cl in 0.25M salt.....	120
3.51	SANS curves for CTATos in 5% mole NaTos/Cl in 0.25M salt at 40°C.....	121
3.52	SNAS curves for CTATos in 12 mole % NaTos/Cl in 0.25M salt at 40°C.....	122
3.53	SANS curves for CTATos in 2 mole % NaTos/Cl in 1M salt at 40°C.....	123
3.54	SANS curves for CTATos in 5 mole % NaTos/Cl in 1M salt at 40°C.....	124
3.55	SANS curves for CTATos in 12 mole % NaTos/Cl in 1M salt 40°C.....	125
3.56	Bending rod plots of SANS data for CTATos in NaTos solutions (fits are shown for wormlike chain)	130
3.57	Bending rod plots of SANS data for CTATos in 2 mole % NaTos in 0.15M NaTos/NaCl. Fit without taking intermicellar interactions into account.....	131
3.58	Bending rod plots of SANS data for CTATos in 12 mole % NaTos in 0.15M NaTos/NaCl. Fit without taking intermicellar interactions into account.....	132

3.59	Bending rod plots of SANS data for CTATos in 2 mole % NaTos in 0.25M NaTos/NaCl. Fit without taking intermicellar interactions into account.....	133
3.60	Bending rod plots of SANS data for CTATos in 5 mole % NaTos in 0.25M NaTos/NaCl. Fit without taking intermicellar interactions into account.....	134
3.61	Bending rod plots of SANS data for CTATos in 12 mole % NaTos in 0.25M NaTos/NaCl. Fit without taking intermicellar interactions into account.....	135
3.62	Bending rod plots of SANS data for CTATos in 2 mole % NaTos in 1.0M NaTos/NaCl. Fit without taking intermicellar interactions into account.....	136
3.63	Bending rod plots of SANS data for CTATos in 5 mole % NaTos in 1.0M NaTos/NaCl. Fit without taking intermicellar interactions into account.....	137
3.64	Bending rod plots of SANS data for CTATos in 12 mole % NaTos in 1.0M NaTos/NaCl. Fit without taking intermicellar interactions into account.....	138
3.65	Dependence of micellar contour lengths on CTATos concentration in NaTos/Cl systems.....	140
3.66	Dependence of micellar Kuhn lengths on CTATos concentration in NaTos/Cl systems.....	141
3.67	SANS curves for CTA micelles in 2 mole % NaSal/Cl in 0.15M salt at 40°C.....	144
3.68	SANS curves for CTA micelles in 2 mole % NaSal/Cl in 0.25M salt at 40°C.....	145
3.69	10mM CTACl in NaSal/Cl at 0.25M total salt, with the mole % of NaSal changing from 0% to 100%.....	146
3.70	Bending rod plots of SANS data for CTASal with fits in 2 mole percent NaSal in 0.15M NaSal/NaCl. Fit without taking intermicellar interactions into account.....	149
3.71	Bending rod plots of SANS data for CTASal with fits in 2 mole percent NaSal in 0.25M NaSal/NaCl. Fit without taking intermicellar interactions into account.....	150
3.72	Bending rod plots of SANS data for CTASal with fits in 0.25M total salt with mole percent of NaSal changing from 0% to 100%. Fit without taking intermicellar interactions into account.....	151
3.73	Contour lengths for CTASal micelles in 2mole% NaSal/Cl solutions.....	152
3.74	Dependence of micellar Kuhn lengths on CTASal concentration in 2 mole% NaSal/Cl in 0.15M salt	153
3.75	SANS curves for CTA26ClBz in 4M Na26ClBz/Cl at various mole percents of Na26ClBz at 25°C.....	155
3.76	SANS curves for CTA26ClBz in 2M Na26ClBz/Cl at various mole percents of Na26ClBz at 25°C	156

3.77	Bending rod plots of SANS data with fits for CTA26ClBz in 2M Na26ClBz/Cl at various mole percents of Na26ClBz at 25°C.....	158
3.78	Bending rod plots of SANS data with fits for CTA26ClBz in 4M Na26ClBz/Cl at various mole percents of Na26ClBz at 25°C.....	159
3.79	Contour lengths for CTA26ClBz in 2M and 4M total salt, as a function of the mole % of Na26ClBz	160
3.80	Dependence of micellar Kuhn lengths for CTA26ClBz, in 2M and 4M total salt, on the mole % of Na26ClBz.....	162
3.81	$\ln(I_p)$ vs. $\ln(c_s)$ for SDS micellar systems at 45°C	166
3.82	$\ln(I_p)$ vs. $\ln(c_s)$ for CTAB micellar systems at 40°C.....	167
3.83	$\ln(I_p)$ vs. $\ln(c_s)$ for TTAB micellar systems at 40°C.....	168
3.84	$\ln(I_p)$ vs. $\ln(c_s)$ for CPyBr micellar systems at 30°C.....	169
4.1	Scattering length density profiles for CTA/26-d ₃ -ClBz micelles in H ₂ O/D ₂ O mixture containng 1M Na26-d ₃ -ClBz. Percents of D ₂ O are by volume.....	182
4.2	External contrast variation for CTA micelles in 1M salt, using deuterated Na26ClBz to increase the shell contrast with the core at different volume percents of D ₂ O in the solvent.....	183
4.3	External contrast variation for CTA micelles in 0.4M salt, using deuterated Na26ClBz to increase the shell contrast with the core at different volume percents of D ₂ O in the solvent.....	184
4.4	Guinier plot of 20mM CTA26ClBz in 1M Na26-d ₃ -ClBz solutions at 70% D ₂ O in the solvent	186
4.5	Guinier plot of 20mM CTA26ClBz in 0.4M Na26-d ₃ -ClBz solutions at 70% D ₂ O in the solvent	187
4.6	Guinier-like plot of 20mM CTA26ClBz in 0.4M Na26-d ₃ -ClBz solutions at 70% D ₂ O in the solvent	189
4.7	$I(0)^{1/2}$ vs. fraction of D ₂ O in the solvent for CTA micelles in 1M Na26-d ₃ -ClBz. From external contrast variation.....	191
4.8	$I(0)^{1/2}$ vs. fraction of D ₂ O in the solvent for CTA micelles in 0.4M Na26-d ₃ -ClBz. From external contrast variation.....	192
4.9	Scattering curve and related fits for 20mM CTA in 1M salt at 70% D ₂ O.....	196
4.10	Scattering length density profiles for CTA-d ₃₃ /26ClBz micelles in H ₂ O/D ₂ O mixture containng 1M Na26ClBz. Percents of D ₂ O are by volume.....	198
4.11	External contrast variation for CTA micelles in 1M salt, using CTA-d ₃₃ to increase the shell contrast with the micellar core at different volume % of D ₂ O in the solvent.....	199

4.12	External contrast variation for CTA micelles in 0.2M salt, using CTA-d ₃₃ to increase the shell contrast with the micellar core at different volume % of D ₂ O in the solvent	200
4.13	Guinier plot for external contrast variation in 1M salt by using CTA-d ₃₃ at 20% of D ₂ O in the solvent.....	201
4.14	Guinier-like plot for external contrast variation in 0.2M salt by using CTA-d ₃₃ at 20% of D ₂ O in the solvent	202
4.15	I(0) ^{1/2} vs. volume fraction of D ₂ O in the solvent for CTA-d ₃₃ micelles in 1M Na ₂₆ ClBz, from external contrast variation.....	205
4.16	I(0) ^{1/2} vs. volume fraction of D ₂ O in the solvent for CTA-d ₃₃ micelles in 0.2M Na ₂₆ ClBz, from external contrast variation.....	206
4.17	External contrast variation for CTA micelles in 1M Na ₂₆ ClBz using CTA-d ₃₃ to increase the shell contrast with the core at different volume % of D ₂ O in the solvent. Fits to the experimental data are also shown.....	207
4.18	Scattering length density profiles for micelles of CTA-d ₃₃ /h ₃₃ -26ClBz mixture in D ₂ O containing 1M Na ₂₆ ClBz. Percents of D ₂ O are by volume.....	210
4.19	Internal contrast variation for CTA micelles in 1M Na ₂₆ ClBz (D ₂ O) by varying CTA-d ₃₃ mole percents.....	212
4.20	Internal contrast variation for CTA micelles in 0.4M Na ₂₆ ClBz (D ₂ O) by varying CTA-d ₃₃ mole percents.....	213
4.21	Internal contrast variation for CTA micelles in 0.4M Na ₂₆ ClBz (D ₂ O) by varying CTA-d ₃₃ mole percents.....	214
4.22	I(0) ^{1/2} vs.mole fraction of CTA-d ₃₃ for CTA micelles in 1.0M Na ₂₆ ClBz, D ₂ O solvent.....	215
4.23	I(0) ^{1/2} vs. mole fraction of CTA-d ₃₃ for CTA micelles in 0.4M Na ₂₆ ClBz, D ₂ O solvent.....	216
4.24	I(0) ^{1/2} vs. mole fraction of CTA-d ₃₃ for CTA micelles in 0.2M Na ₂₆ ClBz, D ₂ O solvent	217
4.25	Internal contrast variation for CTA micelles in 1M Na ₂₆ ClBz using CTA-d ₃₃ to increase the shell contrast with the core at different mole % of CTA-d ₃₃ in the core. Fits to the experimental data are also shown.....	218

CHAPTER I

INTRODUCTION

1.1 GENERAL BACKGROUND

Amphiphilic molecules such as surfactants – surface active agents – have a water-seeking (hydrophilic) polar or charged head group at one end and a water-avoiding (hydrophobic) aliphatic tail or tails connected to the head group. Due to this dual character, amphiphilic molecules can spontaneously self-assemble into a variety of structures. The tail is usually some long chain alkyl group. The tails can vary in both number and length. A minimum length is required in order for the molecules to exhibit the characteristic properties of surfactants. When a small amount of surfactant is introduced into water or into an oil/water two phase system, it adsorbs at the air/water or oil/water interface and forms a thin monolayer with the head group in the water and the tail in contact with the other phase.

Surfactants are usually divided into four classes according to the type of head group: anionic, cationic, nonionic or zwitterionic. Figure 1.1 gives the structure of a common surfactant from each class: SDS, sodium dodecylsulfate, also known as sodium lauryl sulfate, an anionic surfactant and common ingredient in many detergents; CTAB, cetyltrimethylammonium bromide also called hexadecyltrimethylammonium bromide, a well studied cationic surfactant having good germicidal properties; $C_{12}E_n$, a polyoxyethene monododecylether, the most commonly studied family of nonionic surfactants, in which the head group may larger than the tail; and 3-dimethyldodecylaminopropanesulfonate (DDPS), a simple example of a zwitterionic.

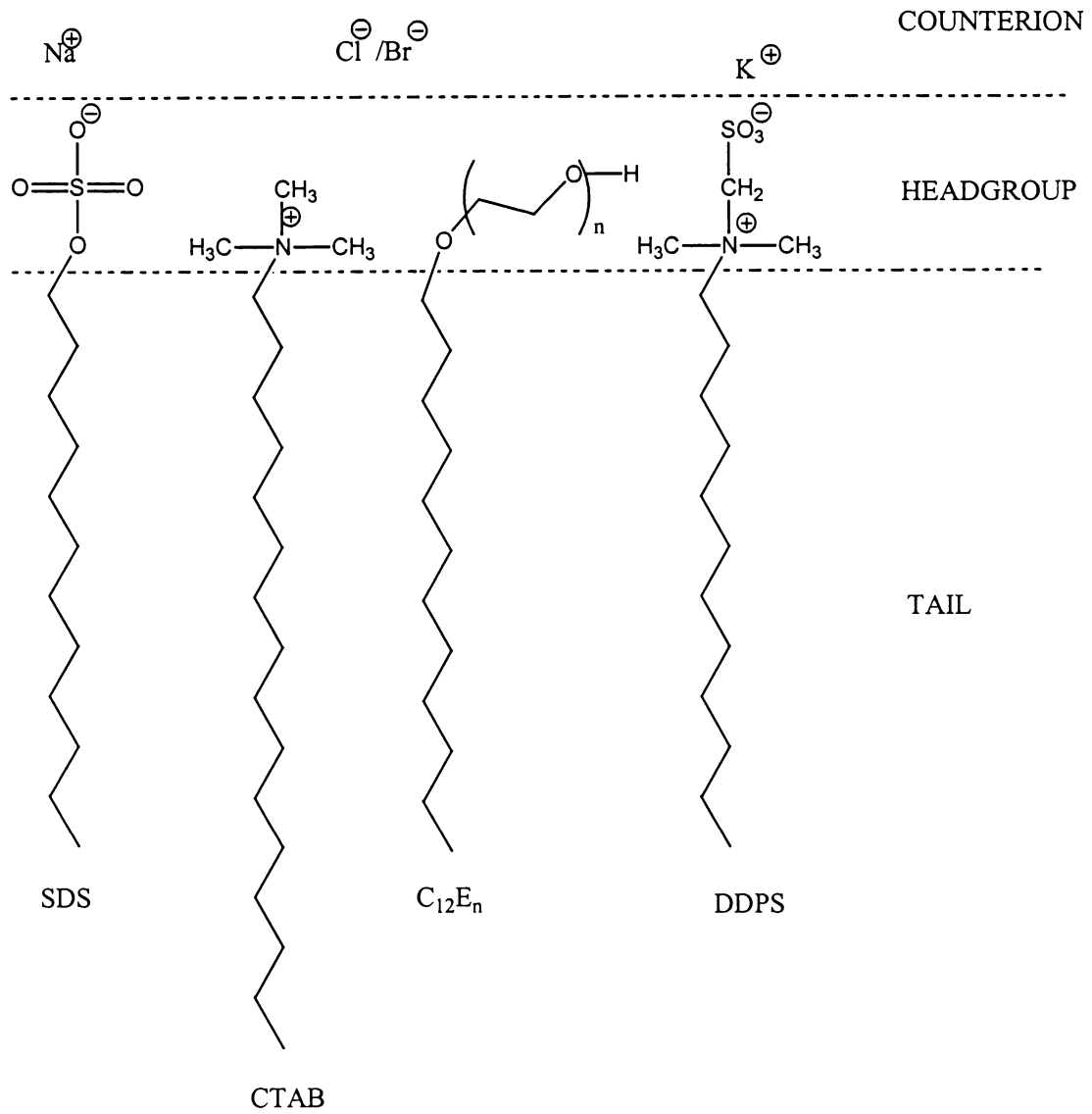


Figure 1.1 Common example of each type of surfactant.

Physico-chemical properties of surfactant solutions may show a peculiar concentration dependence. The concept of a critical micelle concentration (cmc) has been found useful. It is the midpoint of a small concentration range over which micelles form. At low concentrations many physico-chemical properties such as self-diffusion coefficients, activities, turbidity, conductance, surface tension and NMR spectral features indicate that there is no appreciable aggregation of the surfactant.^{1,2} Above the cmc, these properties change in a way indicating that an extensive association to large aggregates, called micelles, occurs.

The formation of micelles and the capability of the micelles to solubilize materials that are otherwise insoluble in the solvent are the most prominent features of the amphiphilic molecules. The usefulness of soap, shampoo and other detergents is based on this feature. Other examples includes: microencapsulation for drug delivery; the use of emulsions in photography; microemulsions for oil recovery in the petroleum industry; the absorption of corrosive products by motor oil. Studying micelles can also provide fundamental information of use in studying other self-assembled systems and their applications, such as block copolymers in nanomaterials; lipids in biochemistry; macrosurfactants in drug delivery; and polymeric surfactants as emulsion stabilizers.

Above the cmc, surfactant molecules can reversibly assemble into a variety of structures, including spherical micelles at low concentration, that may then undergo unidimensional (uniaxial) growth to make rodlike micelles as the volume fraction, Φ , of surfactant is increased. At some length scale, these rods become flexible and behave like wormlike chains, e.g. like polymers. There are also cases of bidimensional growth with the spheres transforming to disclike micelles. The wormlike linear micelles may become

very long and entangled with each other, at relatively low total volume fractions of surfactant. As Φ keeps increasing the micellar structure can form ordered phases such as nematic and hexagonal mesophases. Figure 1.2 presents a schematic diagram of micellar growth.¹ This dissertation will mainly focus on the structure and flexibility of wormlike micelles and the impact that the surfactant tail length, head group structure, counterion identity, and ionic strength have on these properties.

One cannot understand micellar formation and growth without understanding the thermodynamics. There are good books^{3,4} and articles^{5,6} that provide more detail than this brief introduction. The thermodynamic properties of an ionic micellar solution are usually described by partitioning the Gibbs free energy into hydrophobic energy, surface energy, and electrostatic energy terms:⁷

$$G_{\text{total}} = G_1 + G_2 + G_3 \quad (1.1)$$

where G_1 is the hydrophobic free energy, G_2 is the micellar surface free energy, and G_3 is the electrostatic free energy. The formation and growth of micelles are due to a balance among these three energies.

The formation of amphiphilic aggregates can be seen as a compromise between the tendency of alkyl-alkyl and water-water contacts to be preferred over alkyl-water contacts, and the strong affinity of the polar group for water. For straight-chain aliphatic hydrocarbons, the hydrophobic free energy will be seen to be a strictly linear function of the number of the CH_2 groups in the chain. A detailed description can be found in reference [4].

Surface energy is the free energy change when the surface area of a medium is increased by unit area. It is always associated with the solvation energy of the solvent

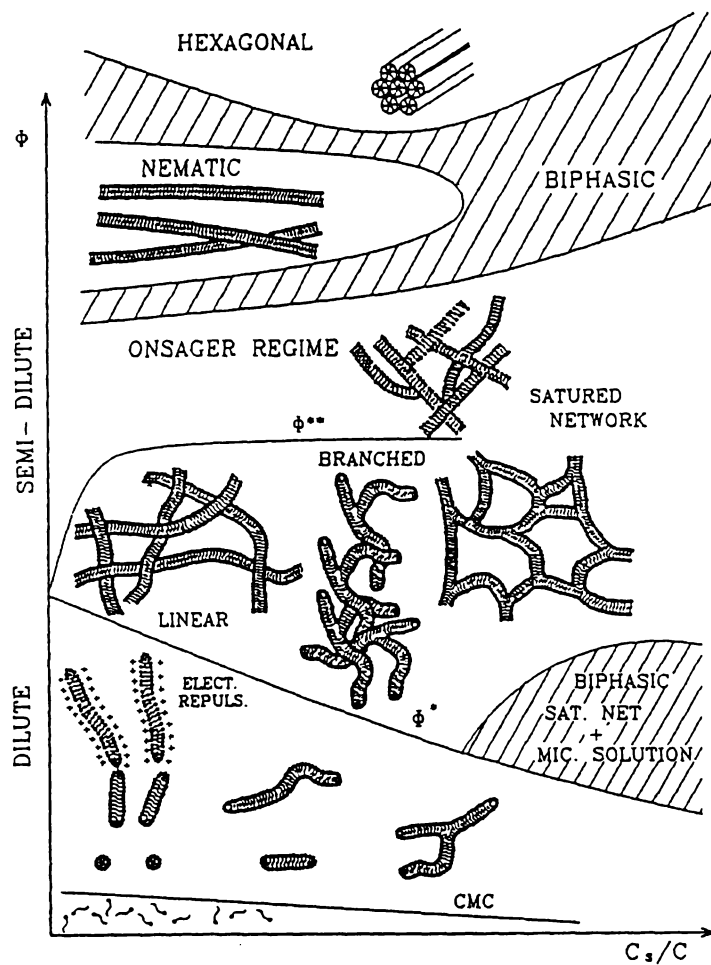


Figure 1.2 Schematic diagram: surfactant volume fraction Φ vs. molar ratio C_s/C of salt over surfactant concentration. Represent from ref 1.

molecules at the hydrophobic and hydrophilic interface and the surface area. The solvation energy is influenced by the physical properties of the solvent and the micellar head groups. The area per head group at the micellar surface is mainly based on the shape of the micelle, the hydrocarbon tail structure and length, the geometry and packing of the head groups and also the volume of the micelle. For a specific surfactant, we know that the radius of a spherical micelle or the radius of the cross section of a rodlike micelle cannot exceed the length of the extended surfactant molecule.

The third term is the electrostatic energy G_3 . The electrostatic interaction is the sum of Coulombic attractions and repulsions among all the ionic species in micellar solutions, including the counterions. For example, if we have CTAB forming spherical micelles in aqueous solutions of low ionic strength, the cationic head groups prefer to be far away from each other because of electrostatic repulsions. The micellar surface has a high charge density and the stability of the aggregate is heavily dependent on the binding of counterions to the surface. In a classic model⁸ an electrical double layer is formed by the ionic head groups and their counterions. The counterions are partly bound to the hydrophilic surface of the micelle and partly constitute a diffuse ion cloud surrounding the micelle.

The micellar aggregates formed at the cmc normally have aggregation numbers that one would expect for spherical micelles. The aggregation number increases with increasing alkyl chain length in all surfactants. For some ionic surfactants, such as CTAB, when the concentration of the surfactant is raised above the cmc, to a first approximation all added molecules go into new aggregates, increasing the number of the aggregates without changing the size. There are also some examples, e.g. CTASal (Sal is

salicylate counterion), for which the micellar size starts increasing right away above the cmc. For ionic surfactants, the increase in aggregate size is related in general to increases in salt concentration and surfactant concentration. For all systems, there is a decrease in micellar size with increasing temperature.

Because of geometrical constraints, each surfactant has a preferred method of packing into the aggregates. Israelachvili and coworkers have discussed aggregate shapes in detail.⁹ They have described a preferred packing arrangement that depends on three parameters: the area occupied by the surfactant head group (a), the effective volume of surfactant tail (v), and the effective length of the surfactant tail (l). The quantity v/al is known as the surfactant packing parameter, and its value determines the preferred shape for a given surfactant's aggregates, e.g. $1/3$ for spherical micelles; $1/2$ for infinite cylinders; and 1 for planar bilayers. For ionic surfactants, the area per head group is largely determined by the electrostatic interactions between head groups, which are affected by counterion binding and ionic strength.³

Since the energetics of micellization is driven by the tendency for water to avoid contact with the alkyl chains, in combination with the affinity of water for the polar head group, the shape of the micelle depends on the relative size of the alkyl chain, head group and counterions. From the above, we can see that micellar size, shape and flexibility vary with various factors in a manner that is complex and difficult to predict. Using experiments to study micellar size, shape, and flexibility are important to quantifying the impact of these factors and to designing surfactants for application. Detailed experimental results will be discussed in following chapters.

The concept of hydration numbers for head groups and counterions can also be important for understanding interactions between micelles and water. Because the micelle-water interactions are highly dynamic and stoichiometrically undefined, hydration numbers depend on the experimental approach used to measure them. If the hydration number is defined as the number of water molecules moving with the micelle as a kinetic entity, it can be deduced from transport properties, e.g., viscosity and diffusion. We can state that the polar head groups are certainly hydrated and that hydrophilic counterions may at least in certain cases become dehydrated.^{10,11} There is no water penetration into the interior of the micelles.² Hydration numbers will be used in our data fitting in the following chapters.

1.2 WORMLIKE MICELLES

Wormlike micelles have been studied since the 1980s^{12,13} because of the analogies between their solutions and those of polymers. Unlike the monomer units of polymers, surfactant molecules can reversibly self-assemble to form polymerlike micelles, also called equilibrium polymers. As a result, the micelles' molecular weight depends on surfactant concentration.

Above the cmc, micellar growth occurs as the surfactant concentration increases; some surfactants, see the material on packing parameters, undergo more rapid growth than others. A unidimensional growth can lead the micelles to undergo transitions from spheres to ellipsoids, rods, to elongated wormlike micelles. This dissertation focuses on several important parameters, or length scales, for these wormlike micelles: contour length (micellar end-to-end distance), $\langle L_n \rangle$, which is related to the micellar aggregation

number, cross-sectional radius, $R_{g,cs}$, which is related to the surfactant tail length, and the persistence length (memory of chain's direction is retained on length scale shorter than persistence length, but lost once exceeded), l_p , which is related to the bending modulus w for these 1D objects through:

$$l_p = w/k_B T \quad (1.2)$$

where k_B is Boltzmann's constant. In 1980s, Appell and Porte¹⁴ found that the larger the cross-sectional diameter, the more rigid the micelles. More recently, Ben-Shaul and coworkers¹⁵ provided a microscopic model for estimating bending modulus and presented a numerical estimate for the free energy change associated with the formation of an intermicellar junction. These calculations were limited to the single-component surfactant solutions and the theory employed is approximate, as both head group and the hydrocarbon chain contributions to the packing free energies were treated at a mean field level.

As the micelles grow, $\langle L_n \rangle$ increases, the cross sectional micellar structure remains constant, although changes in the packing of surfactant tails may lead to a smaller radius for the rods or worms than for the spheres.⁶ In 1990s, Candau and others^{16,17} have used the idea of end-cap energies, E_c , to explain the micellar growth. A end-cap energy defined as the energy required to create two (hemispherical) end caps as a result of scission of a rodlike micelles. At high salt concentration, the micelles are highly screened in solution with short Debye lengths (smaller than the mean micellar size), and the $\langle L_n \rangle$ can be expressed as:

$$\langle L_n \rangle \cong 2c^{1/2} \exp\left(\left(\frac{1}{2}\right)\left(E_c/2k_B T - l_B a \delta^2 / c^{1/2}\right)\right) \quad (1.3)$$

10

where c is surfactant concentration, T the temperature, a the cross-sectional radius of micelles, δ is the effective charge per unit length, and l_B is the Bjerrum length and is constant for a given solvent and temperature: (about 7\AA in water at room temperature)

$$l_B = \frac{e^2}{4\pi\epsilon_0\epsilon k_B T} \quad (1.4)$$

where e is the elementary charge, ϵ_0 is the dielectric constant in vacuum, and ϵ is the solvent dielectric constant. The growth rate depends both on E_c and the micelle ionization fraction δ that is related to Debye length κ^{-1} by:

$$\kappa^2 = 4\pi l_B \rho \delta \quad (1.5)$$

where ρ is the number density of polar heads and Debye length κ^{-1} is

$$\kappa^{-1} = \left(\frac{\epsilon_0 \epsilon k_B T}{2e^2 I} \right)^{1/2} \quad (1.6)$$

where I is the ionic strength of the solution. The end-cap energy is related to G_1 , G_2 , and G_3 in equation 1.1. As E_c increases, the micellar size increases. When E_c very large, there are predicted to be no end caps and the micelles start to branch.

As the surfactant concentration keeps increasing, a certain concentration c^* may be reached,

$$c^* = \frac{3M_w}{4\pi N_0 \langle R_g^2 \rangle^{3/2}} \quad (1.7)$$

above which the elongated micelles start contacting and entangling. This marks the transition from a dilute to a semidilute solution, just as in polymer solutions.^{12,13} R_g is the radius of gyration of the overall micelle and can be derived from $\langle L_n \rangle$ and l_p . M_w is the

weight-average molecular weight of the micelle and can be derived from $\langle L_n \rangle$. In this dissertation, we focus on the wormlike micelles in the dilute regime.

1.2.1 Role of counterion: electrostatics and specific binding

The nature of the counterion can have spectacular effects for ionic surfactants on the evolution of micellar morphology, with spheres persisting to very high surfactant concentration, c , and salt concentration, c_s , in some cases or disappearing in other cases at very low c and c_s dependent on the extent of the counterion binding and the orientation of the bound counterions at the micellar surface.¹⁸ For cationic surfactants such as CTA⁺, certain aromatic counterions such as salicylate (Sal), tosylate (Tos), 2,6-dichlorobenzoate (26ClBz), and 3,5-dichlorobenzoate (35ClBz) are known to insert between the surfactant head groups into the micelles at a depth that depends strongly on the counterion's structure. NMR and surface potential measurements have been used to study the counterions' penetration.¹⁹ Those causing significant micellar growth produce dramatic lowering of micellar surface potentials and increase the surfactant packing parameter by affecting both the volume and area per head group of the micelles, while the nonpenetrating counterions like chloride and bromide can only affect the area per head group of the micelles. In both cases, the counterion with or without hydration can influence the size and fraction of the counterion binding. Different micellar models, both with and without hydration will be used for the micelles studied in this dissertation.

In salt-free aqueous micellar solutions, CTACl micelles start elongating at 0.6M,²⁰ while CTAB micelles start elongating to ellipsoids at 0.12 – 0.15M, and then rods, displaying a c^* at 0.3M.²¹ The micelles with penetrating counterions are large at lower

concentration: for CTASal, CTATos, and CTA35ClBz the micelles are rods, presumably flexible, from the cmc on, while CTA26ClBz micelles start elongating at 0.04M and reach overlap at 0.14M.²² Values of δ , the micellar ionization fraction, show similar behavior with Cl>Br>26ClBz>35ClBz, Sal, Tos.

When the common ion salts are added to a CTAX micellar solution, the micellar size is highly dependent on salt concentration c_s .²³ The effect of c_s on the micellar size is also counterion-dependent, e.g., NaCl has less effect on the micellar size compared with NaBr. For nonpenetrating counterions, the increase in micellar size from sphere to rod to elongated wormlike micelles, continues as the salt concentration increases.²⁴ In contrast, for many penetrating counterions a reversion from giant wormlike micelles back to spherical micelles occurs at high salt^{25,26} including Sal, 26ClBz and Tos. The possible explanation for this phenomenon will be studied in chapter IV.

1.2.2 Micellar persistence lengths

In the early 1960s, Elworthy and McFarlane recognized that the rodlike micelles can be flexible.²⁷ After that, static light scattering (SLS) and dynamic light scattering (DLS) were used to measure a variety of ionic micellar systems at high ionic strength in an effort to determine persistence lengths, and hence micellar bending moduli. The total persistence length,²⁸ $l_{p,t}$, can be represented as the sum of an intrinsic and an electrostatic length, $l_{p,0}$ and $l_{p,e}$, respectively:

$$l_{p,t} = l_{p,0} + l_{p,e} \quad (1.8)$$

For vinylic polymers with charges, the $l_{p,0}$ of polyelectrolytes are 10-20 Å.^{29,30} Persistence length are larger for micelles because of their large cross-sections. Appell and Porte¹⁴ have estimated that the $l_{p,0}$ expected for C₁₆Py surfactant micelles is 90 Å.

In the length scale regime accessible in static light scattering, two important micellar length scales, l_p ($\equiv l_{p,l}$) and r_{cs} , are not directly detectable and are derived indirectly from R_g and molecular weight. Alternatively, the ratio of R_g to R_h , where R_h is the hydrodynamic radius, can be used to determine l_p . The early attempts of Appell and Porte gave the l_p of CPyBr/NaBr systems with a reasonable range 150-200 Å.^{31,32} But later on, the experiments on CTASal/NaSal, CTAB/NaBr etc. gave larger l_p 's around 700 Å,³³⁻³⁵ which are unreasonably large and were found to increase rather than decrease with increasing salt, as theory predicts.³⁶⁻³⁹

1.3 STATEMENT OF PROBLEM

Small-angle neutron scattering (SANS), by allowing the probing of shorter length scales, is clearly preferable for determining l_p 's directly. In chapter II, a detailed introduction on SANS and its application to micellar systems will be discussed. Experimental work on persistence lengths, contour lengths of different micellar systems with different tail lengths, head groups, counterions, at varying ionic strength will be discussed in chapter III. Contrast variation experiments, taking the advantage of the H/D substitution in neutron scattering, will be discussed in chapter IV, providing more detailed information on counterion binding. Reasons will also be discussed for reversions in micellar size at high concentrations of salts containing counterions that penetrate the micellar surface.

CHAPTER II

SMALL-ANGLE NEUTRON SCATTERING

2.1 INTRODUCTION

The interaction of electromagnetic radiation with matter has been used extensively to study the sizes, shapes, interactions and motions of molecules or particles: X-rays for crystal structure, IR for molecular vibrations, quasielastic light scattering and neutron scattering for diffusive motions of molecules and aggregates. These techniques have the advantage of being relatively non-intrusive and non-destructive. For example, in X-ray crystallography (wide angle X-ray scattering), one measures relative positions of all atoms, thus elucidating the structure of crystals while keeping the crystal structure untouched. With small-angle X-ray (SAXS) and small-angle neutron scattering (SANS), one can measure a variety of length scales on the order of 20 Å to 200 Å, including shape parameters, such as radius for a sphere, major and minor axes for ellipsoids, cross-sectional radius and persistence length for rod or wormlike micelles, etc. With classical or static light scattering (LS), one can measure a variety of length scales larger than with SAXS and SANS on the order of 200 Å to 1500 Å, weight averaged molecular weights, and shape parameters for much larger particles. Because these length scales overlap, one can also use a combination of LS and SAXS or SANS to study systems having multiple length scales on the order of 20 Å to 1500 Å.⁴⁰⁻⁴³ For our micellar systems, we are interested primarily in the length scales that fit into the range of SAXS and SANS experiments.

X-rays and light are scattered by atoms' electron clouds. Because the wavelength of visible light is so much larger than atomic sizes, the scattering is simply proportional to the polarizability. For SAXS and SANS, typical wavelengths are no more than a few times typical interatomic distances. For X-rays, the scattering power is proportional to the electron density around the atom, meaning heavy atoms are necessary to get good scattering contrast. Contrast is what allows the particle of interest to be distinguished from the solvent. This means the scattering properties of the particle and the solvent must be different. Since LS arises from the polarizabilities, which are related to the index of refraction, it follows that the refractive index difference between the solvent and the particle should be large in order for the particle to be distinguished. For dilute aqueous micellar systems, the surfactants used are mainly hydrocarbon, which has little electron density contrast with the solvent, H₂O or D₂O. Some SAXS experiments have also been done to study micellar solutions,^{44,45} but in both cases the counterions are heavy ions, cesium and bromide respectively. Since the counterions are localized at or near the micellar surfaces, the scattering patterns observed are from objects that appear as hollow shells.

We study micellar systems having different counterions. Some of them are organic counterions, which do not provide the same high contrast as Br or Cs in X-ray scattering, meaning we can not see the scattering or we need very long times for data acquisition in order to get adequate signal-to-noise ratios. Neutron scattering has a different origin than X-ray scattering: neutrons scattered off the nuclei. For neutron scattering the fluctuation is coming from the nuclear neutron scattering length, b . Isotopes will scatter differently, and in particular ¹H and ²H have vastly different scattering characteristics, allowing for

some very interesting experiments using deuterium labeling. For example, we can use deuteration of counterions or surfactant tails in order to study the micelles in both bulk and shell contrast. To do this, we must assume that isotopic substitution does not substantially alter the system. There are cases where this is a problem: high molecular weight deuterated and protiated polymers undergo phase separation.⁴⁶

In our micellar systems, we used D₂O as the solvent to increase the contrast between the solvent and the micellar structure to get strong scattering. We also used deuterated Na₂₆CIBz and deuterated CTAB to increase the contrast between the shell and the core to study the detailed structure on the micellar surface. The disadvantage of neutron scattering technique is the requirement of using high intensity neutron beams. Such beams are provided by large scale facilities where the demand for beam time exceeds time available. The details of neutron production, data collection and reduction will be discussed in the experimental section, chapter V.

2.2 FUNDAMENTALS OF NEUTRON SCATTERING AND STRUCTURE

Neutrons have particle as well as wave properties. The wavelength, λ , associated with a particle in terms of its mass m and velocity v is:

$$\lambda = h/mv \quad (h \text{ is Planck's constant}) \quad (2.1)$$

The wavelengths can be selected by selecting the neutron velocity. Neutrons have two main interactions with matter: a nuclear interaction with atomic nuclei and a magnetic interaction with atomic moments. In this section we shall only be concerned with the neutron-nuclear interaction, which produces static neutron scattering. The neutrons interact with the nuclei in the sample, and a small fraction of the incident beam

is scattered in the form of spherical waves originating from each scattering nucleus in the sample. The scattered waves interfere with one another to form the scattering curve.

One can define the probability that neutrons will be scattered. Let us consider a nucleus which is irradiated with a neutron flux I , whose unit is particles per second per unit area. Out of this number, n are scattered. We define a coefficient σ , the cross section, as $n = I\sigma$, where σ has the units cm^2 . Cross sections are usually expressed in special units, called barns, $1 \text{ barn} = 10^{-24} \text{cm}^2$

If we consider a small solid angle $\mathcal{A}\Omega$, Figure 2.1,⁴⁷ and the neutrons scattered per second into it, their number will depend on their energy, on the orientation of $\mathcal{A}\Omega$, and on

I_0 . The number $I_0 \frac{\partial^2 \sigma_s}{\mathcal{A}\Omega \partial E} \mathcal{A}\Omega \partial E$ will be called the partial differential cross section.

Integrating over all the final energies gives the differential cross section $\partial\sigma/\mathcal{A}\Omega$ which corresponds to the total number of neutrons scattered per second into $d\Omega$, regardless of their energies.

$$I_0 d\Omega \int \frac{\partial^2 \sigma_s}{\mathcal{A}\Omega \partial E} \partial E = I_0 \frac{\partial\sigma}{\mathcal{A}\Omega} d\Omega \quad (2.2)$$

Integrating over all directions gives the product of the total scattering cross section σ_s by the incident intensity.

The fundamental variable in a scattering experiment is the so-called momentum transfer vector, defined by

$$\vec{Q} = \vec{k}_f - \vec{k}_i \quad (2.3)$$

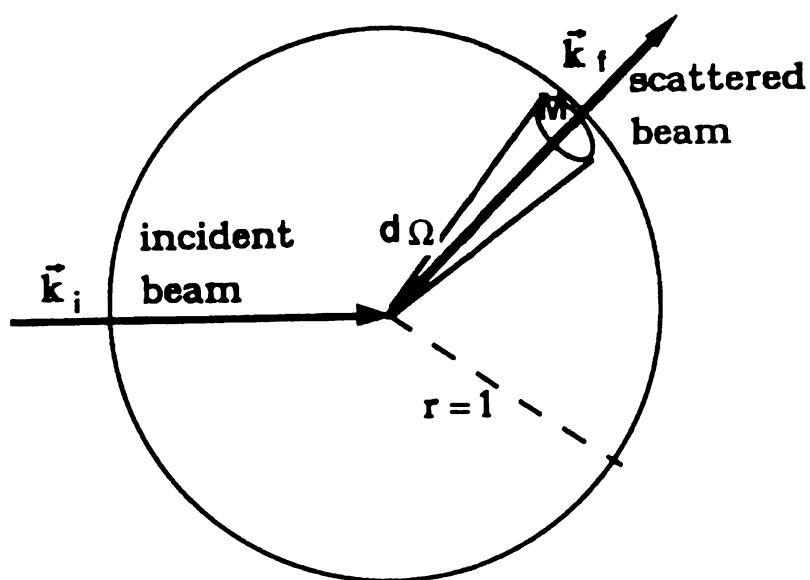


Figure 2.1 The geometry of neutron scattering. From reference [47].

where \vec{k}_i and \vec{k}_f are the initial and final wave vectors of the radiation in the medium. In a small-angle neutron scattering experiment from an isotropic medium, one measures predominantly the elastic and quasielastic scatterings for which $|k_i| = |k_f| = 2\pi n\lambda$, consequently, the Q vector has a magnitude:

$$Q = |Q| = \frac{4\pi \sin \theta}{\lambda} \quad (2.4)$$

An area detector allows detection of scattering through many angles, 2θ , simultaneously. Scattering data are presented as a function of the scattering vector Q or its magnitude. For SANS both the sample-to-detector distance (SDD) and the wavelength of the neutrons can be varied. Typical values are from 1.2m to 20m for the SDD with wavelengths between 5Å and 20Å in order to get a Q range from 0.0004 to 1Å⁻¹.

It should also be pointed out that any special distribution of the scattered neutrons result solely from the properties of atomic arrangements within the sample or from their motions. Nuclear scattering of cold and thermal neutrons is isotropic in space. The wave function of a scattered neutron of a wavevector k at the point r can be written as

$$\Psi_{sc} = -\frac{b}{r} \exp(ikr) \quad (2.5)$$

It is characterized by a single parameter b, independent of neutron energy and the scattering direction. Indeed, within the Born approximation, such scattering is described by the Fermi pseudopotential:⁴⁸

$$V(r) = \frac{2\pi\hbar}{m} b\delta(r) \quad (2.6)$$

where \hbar is $h/2\pi$, m is the neutron mass, r denotes the position of the neutron relative to the nucleus, and b is the same constant, known as scattering length, which, in general, can be a complex number:

$$b = b' - ib' \quad (2.7)$$

It depends on the spin state of the nucleus-neutron system and on the mass of the nuclide, and is thus different for different isotopes of a given element. Consequently, for each element in a real scattering system, we have a different scattering length. Making use of the Fermi pseudopotential, we can derive the following formula for the double differential cross section:⁴⁹

$$\frac{\partial^2 \sigma}{\partial \Omega \partial E_f} = \frac{k_f}{k_i} \frac{1}{2\pi\hbar} \sum_{j,j'} \overline{b_j b_{j'}} \int \left\langle \exp(-iQ \cdot R_{j'}(0)) \exp(-iQ \cdot R_j(t)) \right\rangle \exp(-i\omega t) dt \quad (2.8)$$

Each element of the above sum is weighted by the average product $\overline{b_j b_{j'}}$. This comes from the average over all possible initial and final states that can be encountered in the system. Since the b values of different nuclei are uncorrelated, we have

$$\begin{aligned} \overline{b_j b_{j'}} &= \overline{b_j} \cdot \overline{b_{j'}} = |\overline{b}|^2 \quad (j \neq j') \\ \overline{b_j b_{j'}} &= |\overline{b}|^2 \quad (j = j') \end{aligned}$$

Whit this in mind, we can express the double differential cross section as the sum of two terms, one for coherent and one for incoherent scattering:

$$\left(\frac{\partial^2 \sigma}{\partial \Omega \partial E_f} \right)_{coh} = \frac{\sigma_{coh}}{4\pi} \frac{k_f}{k_i} \frac{1}{2\pi\hbar} \sum_{j,j'} \int \left\langle \exp(-iQ \cdot R_{j'}(0)) \exp(-iQ \cdot R_j(t)) \right\rangle \exp(-i\omega t) dt \quad (2.9)$$

$$\left(\frac{\partial^2 \sigma}{\partial \Omega \partial E_f}\right)_{inc} = \frac{\sigma_{inc}}{4\pi} \frac{k_f}{k_i} \frac{1}{2\pi\hbar} \sum_{j,j'} \int \left\langle \exp(-iQ \cdot R_{j'}(0)) \exp(-iQ \cdot R_j(t)) \right\rangle \exp(-i\omega t) dt \quad (2.10)$$

The constants σ_{coh} and σ_{inc} are defined as

$$\begin{aligned} \sigma_{coh} &= 4\pi |\bar{b}^2| \\ \sigma_{inc} &= 4\pi (|b|^2 - |\bar{b}^2|) \end{aligned} \quad (2.11)$$

The incoherent term accounts for the correlation between the position of the same nucleus at different times and it is Q independent, so it is connected with the motion of the nucleus, no matter whether the latter is engaged in some kind of collective vibrations or is undergoing stochastic displacements. On the other hand, the coherent cross section involves correlations between nuclear positions at different times, and therefore includes collective phenomena and structural information.

In practice, it is the two operations applied to the scattering lengths, that makes the difference between the coherent and incoherent cross sections: the coherent one results from first taking an average scattering length, and then it is squared. The incoherent cross section involves averaging of squared scattering length. Table 2.1 gives nuclear scattering parameters for the most common isotopes.

In our research we concentrate on static scattering; the relative motions of molecules are ignored. We also restrict ourselves to coherent scattering, excluding incoherent scattering, which does not contain structural information. Incoherent neutron scattering is produced by both H and D nuclei, irrespective of whether they belong to the micelles or to the solvent.

Table 2.1 Scattering lengths and cross section for some common isotopes

Atomic nucleus	Natural abundance	b_{coh} 10^{-15}m	b_{inc} 10^{-15}m	σ_{coh} 10^{-28}m^2	σ_{inc} 10^{-28}m^2	σ_{scatt} 10^{-28}m^2	σ_{abs} 10^{-28}m^2
H	---	-3.7390	---	1.7568	80.26	82.02	0.3326
1H	99.985	-3.7406	25.274	1.7583	80.27	82.03	0.3326
2H	0.015	6.671	4.04	5.592	2.05	7.64	0.000519
3H	(12.32 a)	4.792	-1.04	2.89	0.14	3.03	0
C	---	6.6460	---	5.551	0.001	5.551	0.0035
12C	98.9	6.6511	0	5.559	0	5.559	0.00353
13C	1.1	6.19	-0.52	4.81	0.034	4.84	0.00137
N	---	9.36	---	11.01	0.5	11.51	1.9
14N	99.63	9.37	2.0	11.03	0.5	11.53	1.91
15N	0.37	6.44	-0.02	5.21	0.00005	5.21	0.000024
O	---	5.803	---	4.232	0.0008	4.232	0.00019
16O	99.762	5.803	0	4.232	0	4.232	0.0001
17O	0.038	5.78	0.18	4.2	0.004	4.2	0.236
18O	0.2	5.84	0	4.29	0	4.29	0.00016
Na	100	3.63	3.59	1.66	1.62	3.28	0.53
S	---	2.847	---	1.0186	0.007	1.026	0.53
32S	95.02	2.804	0	0.988	0	0.988	0.54
33S	0.75	4.74	1.5	2.8	0.3	3.1	0.54
34S	4.21	3.48	0	1.52	0	1.52	0.227
36S	0.02	3.(1.)	0	1.1	0	1.1	0.15
Cl	---	9.5770	---	11.5257	5.3	16.8	33.5
35Cl	75.77	11.65	6.1	17.06	4.7	21.8	44.1
37Cl	24.23	3.08	0.1	1.19	0.001	1.19	0.433
Br	---	6.795	---	5.8	0.1	5.9	6.9
79Br	50.69	6.80	-1.1	5.81	0.15	5.96	11
81Br	49.31	6.79	0.6	5.79	0.05	5.84	2.7

* More information please go to: <http://www.ncnr.nist.gov/resources/n-lengths/list.html>

For typical SANS experiments, the intensity $I(Q)$ is measured as a function of scattering angle and converted to an absolute differential cross-section using SANS data collected for a calibration standard. We assume that our micellar solutions are isotropic. Thus the coherent cross section we measure is

$$\partial\sigma/\partial\Omega = F(Q,0) = \left\langle \sum_{j,j'} b_j b_{j'} \exp[iQ \cdot (R_{j'} - R_j)] \right\rangle \quad (2.12)$$

2.3 SOLUTIONS OF PARTICLES

For normal scattering experiments, the intensity $I(Q)$ or the cross section of the scattering is related to the form factor $P(Q)$ and structure factor $S(Q)$, $I(Q) \sim P(Q)S(Q)$. Here the $S(Q)$ is determined by the range and strength of intermicellar interactions. For some of our dilute micellar solutions, interparticle interactions can be neglected.⁴⁹ We can divide the sample into N equal volumes V , each containing just one particle. We first consider monodisperse particles, in which case the coherent cross section becomes

$$\partial\sigma/\partial\Omega = N \left\langle \left| \sum_{j(V)} \bar{b}_j \exp[iQ \cdot R_j] \right|^2 \right\rangle_Q \quad (2.13)$$

where N is the number of particles, $\langle \rangle_Q$ denotes an average over all orientations of the particles relative to Q and the sum is over all atoms in the volume V .

SANS experiments are insensitive to detail on the atomic scale, so we can replace atomic scattering lengths by averages over, for example, functional chemical groups of several atoms, or even whole molecules (e.g. in the solvent). We define the scattering length density $\rho(r)$ in a small volume δV at a point r by

$$\rho(r) = \frac{1}{\delta V} \sum_{j(v)} b_j \quad (2.14)$$

where the sum is over those atoms lying in δV . Replacing the sum in Eqn.(2.13) by an integral then yields

$$\partial\sigma/\partial\Omega = N \left\langle \left| \int_V \rho(r) \exp[iQ \cdot r] dr \right|^2 \right\rangle_Q \quad (2.15)$$

where the integral is over the volume V . Since we are only interested in scattering from the particles, the solvent scattering must be measured separately and subtracted, giving finally

$$\partial\sigma/\partial\Omega = N \langle F^2(Q) \rangle_Q \quad (2.16)$$

where the single particle form factor is defined as

$$F(Q) = \int_{V_p} [\rho(r) - \rho_s] \exp[iQ \cdot r] dr \quad (2.17)$$

For the form factor of spheres we have:

$$P(Q) = F^2(Q) \quad (2.18)$$

The effect of particle shape on form factors will be discussed later in this section.

In static scattering, the excess scattered intensity due to the micelles in the absence of intermicellar interactions is then given by

$$I(Q, c) = KcM_w \langle P(Q, c) \rangle + BD \quad (2.19)$$

K is the usual collection of constants appropriate for neutrons, X-rays or light, proportional in the case of LS to the square of the refractive index increment and in SANS to the square of the contrast in scattering length density between micelles and

solvent, $\left[v(\rho_m - \rho_s) \right]^2 / N_A$. The specific micellar volume, v , is expressed in cm^3/g , and the scattering length densities for micelles and solvent, ρ_m and ρ_s , are expressed in cm^{-2} . The Q independent background term BD accounts for residual scattering from solvent and/or incoherent background and is typically $\leq 0.06 \text{ cm}^{-1}$ for D_2O solvent. $\langle P(Q,c) \rangle$ is the form factor averaged over the micellar molecular weight distribution.

2.3.1 Radius of gyration

The radius of gyration, R_g , may be the most frequently obtained quantity from scattering curves for colloidal particles, micelles and polymers. The quantity R_g^2 is defined as the mean square distance away from the center of gravity, $R_g^2 = (1/N) \sum_{i=1}^N r_i^2$, of N scattering points at distance r_i . This can be related to the contrast in the scattering curve. The correlations at large distances within a particle are measure by the second moment of the correlation function $P(r)$; this moment has the dimensions of a squared radius,

$$R_g^2 = \frac{\int r^2 P(r) 4\pi r^2 dr}{2 \int P(r) 4\pi r^2 dr} \quad (2.20)$$

For a centrosymmetric particle, this is also identical to the second moment of the distribution of excess scattering length within the particle,⁵⁰

$$R_g^2 = \frac{\int R^2 \left[\rho(\vec{R}) - \rho_s \right] d\vec{R}}{\int \left[\rho(\vec{R}) - \rho_s \right] d\vec{R}} \quad (2.21)$$

The radius of gyration can be obtained experimentally through the Guinier approximation,⁵¹ which is an expansion of the intensity at small Q,

$$\frac{I(Q)}{I(0)} \sim 1 - \frac{Q^2 R_g^2}{3} \quad (2.22)$$

If nothing is known about the shape of the particles, this expansion can be used only for $Q R_g \ll 1$. If the shape is known, other expansions are used, which minimize the higher-order terms and remain valid up to $Q R_g \sim 1$. For globular particles, Guinier's expression applies,

$$\ln \frac{I(Q)}{I(0)} \sim - \frac{Q^2 R_g^2}{3} \quad (2.23)$$

We can plot $\ln I(Q)$ vs. Q^2 to get the radius of gyration for globular micelles. Figure 2.2 presents a typical Guinier plot for a globular micelle. The radius of gyration is also the least credible of all the quantities that may be derived from the scattering curve of a surfactant solution. It is obtained from an expansion of $I(Q)$ at low Q, a range where interparticle interactions can have profound effects on the scattering curves.

2.3.2 Radii of gyration for various geometrical shapes

This section will only give the result of a purely geometrical calculation without the effect of the solvent

$$R_g^2 = \frac{3}{5} r^2 \quad (2.24)$$

for a sphere of radius r

$$R_{g,cs}^2 = \frac{1}{2} r^2 \quad (2.25)$$

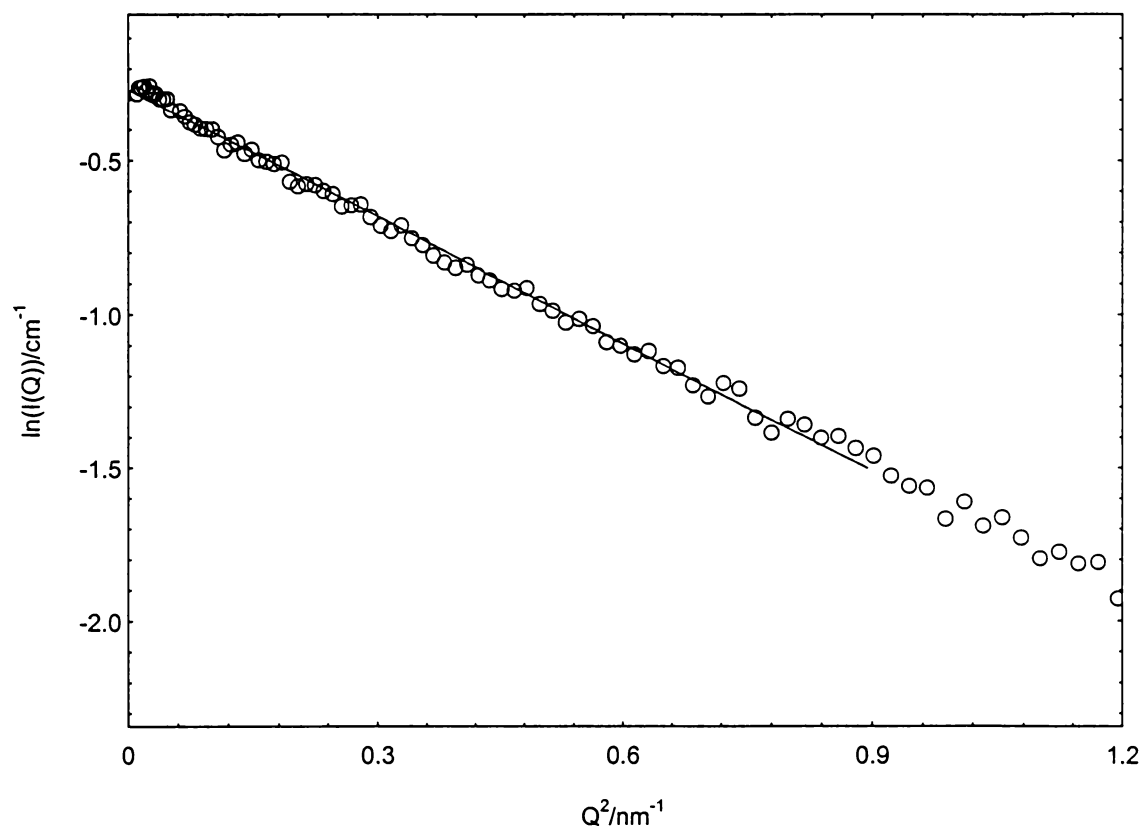


Figure 2.2 Example of Guinier plot $\ln(I(Q))$ vs. Q^2

for a cross-section of radius r in a cylinder or wormlike chain

$$R_g^2 = \frac{1}{5}(a^2 + b^2 + c^2) \quad (2.26)$$

for an ellipsoid of half axes a, b, c ; it reduces to a sphere if $a = b = c$

$$R_g^2 = \frac{L^2}{12} \quad (2.27)$$

for a rod or wormlike chain with negligible diameter

$$R_g^2 = \frac{3 r_{sh}^5 - r_c^5}{5 r_{sh}^3 - r_c^3} \quad (2.28)$$

for a spherical shell structure with outer radius r_{sh} and inner radius r_c

$$R_{g,cs}^2 = \frac{1}{2} \frac{r_{sh}^4 - r_c^4}{r_{sh}^2 - r_c^2} \quad (2.29)$$

for a shell structure of cross-section with outer radius r_{sh} and inner radius r_c in a cylinder or wormlike chain

$$R_g^2 = \frac{1}{5} \frac{\left[(a + t_a)^2 + 2(b + t_b)^2 \right] (a + t_a)(b + t_b)^2 - (a^2 + 2b^2)ab^2}{(a + t_a)(b + t_b)^2 - ab^2} \quad (2.30)$$

for an ellipsoidal shell of half axes a, b, b ; and thickness t_a and t_b

2.3.3 Form factors

In this section, we introduce complete analytical expressions valid for different micellar structures in solution.⁴⁷ Since the molecules are randomly oriented we can average over all orientations to obtain the form factor from Eqn. 2.17-18.

$$P(Q) = F^2(Q) = \left\{ \int_{V_p} [\rho(r) - \rho_s] \exp[iQ \cdot r] dr \right\}^2 \quad (2.31)$$

We can also count the number $n(r)$ of pairs at each distance r and write the equation as follows:

$$P(Q) = F^2(Q) = \left\{ \frac{1}{\int n(r) dr} \int_{V_p} n(r) [\rho(r) - \rho_s] \left(\frac{\text{Sin}qr}{qr} \right) dr \right\}^2 \quad (2.32)$$

This expression is used mainly for continuous bodies for which the sums are transformed into integrals. From this general equation, one can get form factors for monodisperse particles of various shapes.

The Sphere

Spheres are a simple case because the scattering does not depend on the orientation of the sphere. One can evaluate the amplitude scattered by the sphere, transformed from discrete to continuous notation and normalized to unity for $Q=0$, using:

$$F(Q) \approx \frac{1}{V} \iiint_V [\rho(r) - \rho_s] \exp(-iQ \cdot r) r^2 \sin \theta d\theta d\phi dr \quad (2.33)$$

The factor V comes from the fact that the normalization condition $P(0)=1$ has to be satisfied. The final expression depends only on R and the form factor is:

$$P(Q) = V \Delta \rho \frac{9}{(QR)^6} (\sin QR - QR \cos QR)^2 \quad (2.34)$$

Core + Shell Sphere

For spheres having an inhomogeneous scattering length density, the expression is more complicated. The final result is:

30

$$F(Q) = 3(\rho_c - \rho_s)V_c(\sin QR_c - QR_c \cos QR_c) + 3(\rho_{sh} - \rho_s)V_t[(\sin QR_t - QR_t \cos QR_t) - (\sin QR_c - QR_c \cos QR_c)] \quad (2.35)$$

or

$$F(Q) = (\rho_c - \rho_s)V_c \frac{3(\sin QR_c - QR_c \cos QR_c)}{QR_c^3} + (\rho_{sh} - \rho_s)V_t \frac{3(\sin QR_t - QR_t \cos QR_t)}{QR_t^3} \quad (2.36)$$

where $\rho_c, \rho_{sh}, \rho_s$ are the neutron scattering length densities of the particle core, shell and solvent respectively; V_c, V_t are the volumes of the core and the total volume of core plus shell; and R_c, R_t , are the radii of the core and of the overall particle, core plus shell. When the scattering length density of the core is close to that of the solvent, the shell structure becomes more visible and the intensity at low angles becomes smaller while a secondary maximum at high Q appears. When the shell scattering length density is close to the solvent, scattering from the core dominates. Between these two cases, we observe both contributions to the micellar structure.

Ellipsoid

For an ellipsoidal core with semiaxes (R, R, ϵR), the single chain form factor is given by⁵¹

$$P(Q) = \int_0^{\pi/2} \Phi^2[Qr(R, \epsilon, \theta)] \sin \theta d\theta \quad (2.37)$$

$$\text{where, } \Phi(X) = \frac{3[\sin(X) - X \cos(X)]}{X^3}, \quad (2.38)$$

and $r(R, \epsilon, \theta) = R(\sin^2 \theta + \epsilon \cos^2 \theta)^{1/2}$ is the orientation-dependent radius.

Rigid cylinder or rod

When we have rigid cylinders or rods, we assume that both the cross-section and the contour length of the rod contribute to the form factor. We use the same methods, taking the center of the rod as the origin for calculating the scattering amplitude. Using the classical coordinate system with the z axis in the direction of the vector Q ($Q \cdot r = QR \cos \theta$) and assuming homogeneous cylinder or rod systems, we immediately obtain

$$P(Q) = \frac{1}{2} \int_0^{\pi/2} \left[\frac{\sin(QL \cos \theta)}{QL \cos \theta} \cdot 3\Phi(QR \sin \theta) \right]^2 \sin \theta d\theta \quad (2.39)$$

where L the length of the rod and R the radius of the cross section.

From here, we can also get the form factor of a thin rod whose cross-sectional radius can be ignored. The final result after integration as:

$$P(Q) = \frac{2}{QL} Si(QL) - \frac{\sin^2 \frac{QL}{2}}{\left(\frac{QL}{2}\right)^2} \quad (2.40)$$

where Si(x) is the sine integral function

$$Si(x) = \int_0^x \frac{\sin u}{u} du \quad (2.41)$$

Semi-flexible or wormlike chain model

The wormlike chain model, also called the Kratky-Porod model, is based on the polymer chain approximation. The detailed model for scattering from polymer chains has been discussed elsewhere.⁵²⁻⁵⁶ In this section we will focus on application to wormlike micelles.

The three important length scales $\langle L(c), l_p, r_{cs} \rangle$ are reasonably well-separated for most wormlike micelles. $L(c)$ is the micellar contour length, l_p is the persistence length,

equal to one-half the Kuhn length, and r_{cs} is the cross sectional radius. Schurtenberger and Pedersen^{57,58} found that it is reasonable to decouple the form factor in Eqn.2.19 into the micellar cross-section, P_{cs} , and that of the wormlike chain, P_{wc} , so that the form factor becomes

$$\langle P(Q, c) \rangle = P_{cs}(Q, r_{cs}) \langle P_{wc}(Q, L(c), l_p) \rangle \quad (2.42)$$

The micelles can be considered to be solid cylinders, comprised of surfactant tails, so that P_{cs} is simply $[2J_1(Qr_{cs})/(Qr_{cs})]^2$. J_1 is the first order Bessel function. We treat the wormlike chain as a solid chain by ignoring its core plus shell cross-sectional structure because the thickness of the shell is small. The wormlike chain form factor P_{wc} for semiflexible chains with excluded-volume interactions was used: the parametrized expression for P_{wc} was derived by Pedersen and Schurtenberger^{57,58} on the basis of a series of Monte Carlo simulations. Polydispersity is also taken into account:

$$\langle P_{wc}(Q, L(c), l_p) \rangle = \int N(L) L^2 P_{wc}(Q, L(c), l_p) dL / \int N(L) L^2 dL \quad (2.43)$$

Micellar radii of gyration, R_g , are given by

$$R_g^2(L, l_p) = \alpha_s^2(L, l_p) \cdot l_p^2 \left\langle \left(\frac{L}{3l_p} \right) - 1 + \left(\frac{2l_p}{L} \right) - \left(\frac{2l_p^2}{L^2} \right) \left[1 - \exp\left(-L/l_p\right) \right] \right\rangle \quad (2.44)$$

$$R_g = \langle R_g^2 \rangle^{1/2} = \left[\int N(L) L^2 R_g^2(L, l_p) dL / \int N(L) L^2 dL \right]^{1/2} \quad (2.45)$$

where α_s is the expansion factor accounting for the effect of intrachain excluded volume.

2.3.4 The effect of polydispersity

Since it is rare to have a system made of rigorously identical molecules or particles, it is important to consider the effect of a distribution of dimensions. For quenched

polymer systems, the polydispersity is generally expressed by the polydispersity index $PDI = M_w/M_n$. In micellar systems, variations in surfactant aggregation number, which occur as surfactant concentration changes,^{59, 60} are analogous to variations in the number of monomer units per molecule of quenched polymer. In the case of spherical micelles, the distribution of \bar{n} 's is narrow (or in other words the $PDI \approx 1$), because the radius of the sphere is predetermined by the length of the surfactant, and thus the volume of the sphere is determined. This in turn determines \bar{n} . For cylindrical or wormlike micelles, cross sectional radii are determined by the length of the surfactant, while the lengths of the micelles are determined by the surfactant aggregation number. In this case, the aggregation number varies in the system and the system is polydispersed.⁶¹

For a polydisperse system, I_0 is proportional to the weight average aggregation number N_w . For a dilute system the scattering amplitude can be obtained by extrapolating the scattering intensity back to the $Q = 0$ point.

The ladder model is able to predict the distribution X_N of surfactant among the various sizes of micelles, and the mean aggregation number $\langle N_w \rangle$ for all the concentrations.^{59,60,62} One of the model's parameters is the free energy difference per surfactant ion in a spherical vs. a cylindrical micelle. The larger the advantage for the cylindrical environment the more rapidly $\langle N_w \rangle$ and polydispersity increase. For very large micelles, theory⁵⁹ predict $M_w/M_n=2$. For wormlike micelles, polydispersity in lengths was included by computing the average of $\left\langle P_{wc}(Q, L(c), l_p) \right\rangle$, using a Schulz-Zimm distribution for $N(L)$ with the polydispersity fixed at 2 ($z=1$).

2.3.5 Structure factor for solution of interacting particles

In 1980s, Hayter⁶² and coworkers developed analytical solutions for $S(Q)$ in the case of particles interacting with each other, either because the particle number density is large, or because the particles are numerically dilute but have a long-ranged interaction potential due for example to electrostatic repulsions. This second case makes the solutions behave as if they are concentrated. Here, we restrict discussion to spherical particles, which may be mono- or polydisperse. Isotropic solutions of slightly elliptical globular particles are also can also be treated by this description, but analytical expression for $S(Q)$'s for interacting particles with high degree of asphericity (especially rod or wormlike) are not available.

Our starting point is again Eqn. (2.12), which we now separate into interparticle ($m \neq n$) and intraparticle ($m = n$) terms:

$$\frac{d\sigma}{d\Omega} = \left\langle \sum_{j(n)} \sum_{k(n)} \bar{b}_j \bar{b}_k \exp[iQ(r_j - r_k)] \right\rangle + \left\langle \sum_{n \neq m=1}^N \exp[iQ \cdot R_{mn}] \sum_{j(n)} \sum_{k(m)} \bar{b}_j \bar{b}_k \exp[iQ(r_j - r_k)] \right\rangle \quad (2.46)$$

Here R_{mn} is the center-to-center distance between particles labelled m and n and there are N particles. Here, $j(n)$ refers to j -th atom in the n -th particle (at position r_j relative to the particle center), and the corresponding sum runs over all the scattering center atoms in the particle. The average in the second term of Eqn. 2.46 cannot be evaluated exactly at present for any type of interparticle interaction.

For the ellipsoid and spherical micelles with high salt, the intermicellar electrostatic interaction are completely screened, so that $S(Q)$ become just a Percus-Yevick⁶³ hard sphere solution structure factor. For macroion solutions, with electrostatic interactions

between particles, Hayter and Penfold⁶⁴ used the Ornstein-Zernike equation in the mean spherical approximation to obtain the closed analytical structure factor

For the wormlike chain, as already observed by Schurtenberger, Pedersen, and coworkers, neglecting intermicellar interactions leads to an apparent dependence on surfactant concentration of the fitted values of l_p – they increase with c .^{58,61} In previous work,⁶⁵ fits incorporating interactions succeeded only when l_p was constrained to its extrapolated value at $c = 0$. When interactions are included, Eqn. 2.19 is replaced by

$$I(Q, c) = KcM_w S_{RPA}(Q, c) + BD \quad (2.47)$$

Pedersen and Schurtenberger found that fits at finite Q to the results of their Monte Carlo simulations on chain conformations in many-chain systems suggest the following form for the full scattering function, $S_{RPA}(Q, c)$, sometimes also called the structure factor, in the random-phase approximation:

$$S_{RPA}(Q, c) = S_1(Q, c) / \left\{ 1 + [S(0, c)^{-1} - 1] f_D(Q^2 R_g^2) \right\} \quad (2.48)$$

$$f_D(x) = 2(e^{-x} - 1 + x) / x^2 \quad (2.49)$$

$S_1(Q, c)$ is the single chain scattering function, given by equation 2.42 for the wormlike micelles. An approximate expression for $S(0, c)$ comes from applying renormalization group theory (RGT)

$$S(0, c)^{-1} = 1 + \frac{1}{8} [9X - 2 + 2 \ln(1 + X) / X] \exp \left\{ \frac{1}{4} \left[\frac{1}{X} + \left(1 + \frac{1}{X^2} \right) \ln(1 + X) \right] \right\} \quad (2.50)$$

$$X = (cA_2 M_w) / (9/16 - \ln(M_w / M_n) / 8) \quad (2.51)$$

Where A_2 is the second virial coefficient given by $4\pi^{3/2} N_A \left[\langle R_g^2 \rangle^{3/2} / M_w^2 \right] \varphi$, and φ is the penetration factor, obtained from the work of Huber and Stockmayer.⁶⁶

2.3.6 Plots used for wormlike micelles

The most noticeable feature of scattering curves for wormlike chains is that the intensities increase very fast in the small Q region. Guinier plots ($\ln(I(Q))$ vs. Q^2) have already been discussed in Section 2.3.1. From Guinier plots of wormlike scattering curves, one can see two different regions with very different slopes. In the small Q region, $Q^2 \leq 0.001 \text{ \AA}^{-2}$, the plot can give an estimate of the radius of gyration of the whole micelle, but the result is not accurate for a very polydisperse system. For $Q^2 \geq 0.005 \text{ \AA}^{-2}$, the slope is less negative, suggesting a smaller length scale, namely the cross-sectional radius.

Bending rod (BR) plots, $I(Q) \cdot Q$ vs. Q , or Holtzer plots,⁶⁷⁻⁶⁹ remove the Q^{-1} dependence due to $L(c)$, see Eqn. 2.42. Some examples of a BR plot will be in chapter III. BR plot is useful for highlighting the Q ranges sensitive to the various micellar length scales of interest. Provided the average contour length, $\langle L(c) \rangle$, is greater than the Kuhn length, a maximum appears in the BR plot. The micellar radius of gyration, R_g , can be obtained approximately from the Q position of the plot's maximum, using the relationship $u = Q_{max} R_g$. The numerical value of u depends on polydispersity; it is 1.41 for monodisperse chains and 1.78 when $M_w/M_n = 2$. At higher Q , a plateau (or inflection) in the BR plot is observed, whose extent in Q depends on r_{cs} . The ratio of the height of the maximum to the height of the plateau is a measure of the number of l_p 's per chain.⁶⁹ Thus simple visual comparison of two scattering curves in BR format allows an

assessment of flexibility. Because $\langle P(Q,c) \rangle$ takes a different functional form for scattering from spherical or ellipsoidal micelles rather than wormlike chains, BR plots of their scattering curves lack this clear separation of length scales, but the position Q_{max} in a bending rod plot is still a useful indicator of micelle size.

The intermediate Q range in a BR plot can be used to get the cross-sectional radius of gyration, $R_{g,cs}$, of the wormlike micelles. By employing a Guinier approximation for the scattering form factor of the cross section, one gets:

$$Q \cdot I(Q) = K_{BR} \exp\left(-Q^2 R_{g,cs}^2 / 2\right) \quad (2.52)$$

For a circular cross section, the micellar radius is $r_{cs} = \sqrt{2} R_{g,cs}$. The value of K_{BR} is given by

$$K_{BR} = \pi c \left\langle \frac{N}{L} \right\rangle_w (b_m - V_m \rho_s)^2 \quad (2.53)$$

where b_m and V_m are the sum of the neutron scattering length and the volume per surfactant monomer in the micelles, respectively; ρ_s is the scattering length density of the solvent. The number of monomers (N_w or just N) per unit length, L , is expressed as N/L . The value N/L is derived from K_{BR} , given a value for the contrast term, $(b_m - V_m \rho_s)^2$, and the area per surfactant head group, A_{hg} , which equals $2\pi r_{cs} L/N$. A Guinier-like plot ($\ln(I(Q)*Q)$ vs. Q^2) is introduced to derive these quantities directly from the scattering and some example will be seen in Chapter III. From Guinier-like plots (Figure 2.3), the $R_{g,cs}$ can be obtained from fitting of the slope in the intermediate Q regime of the plot, and N/L can be derived from Eqn. 2.53.

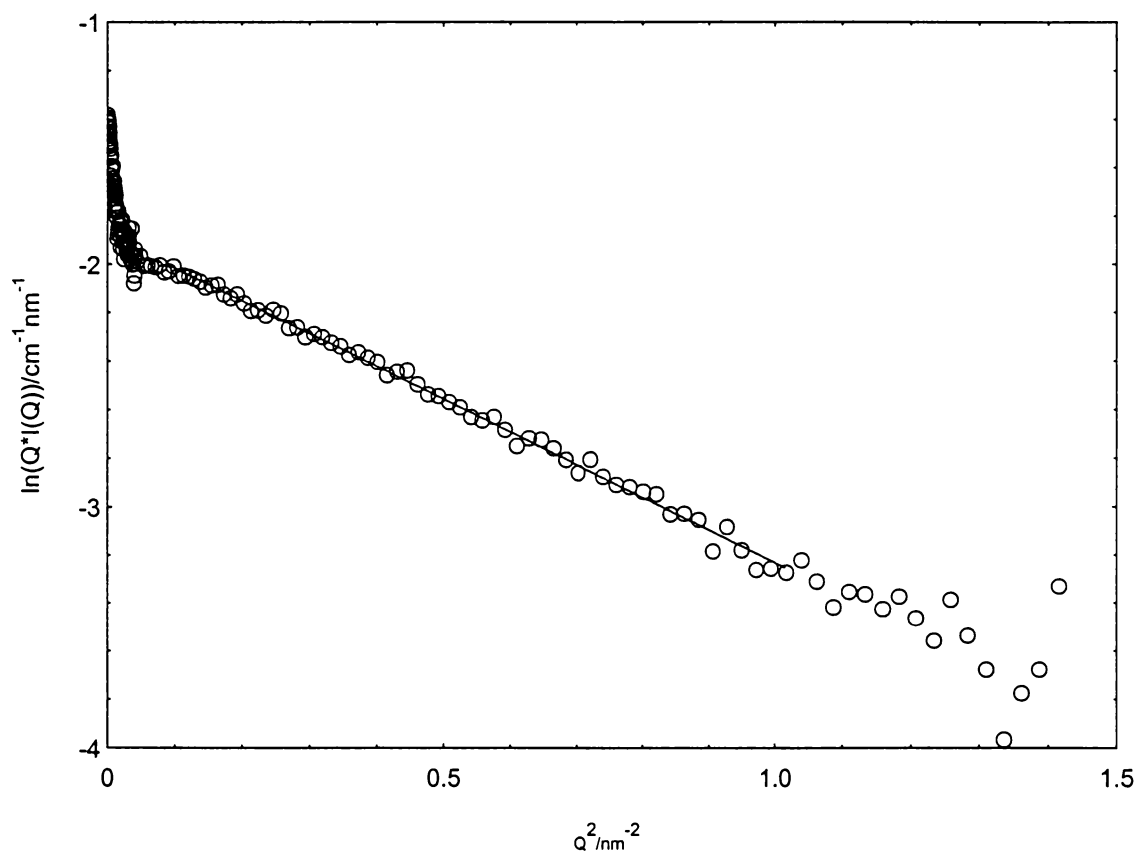


Figure 2.3 An example of Guinier-like plot: $\ln(I(Q) \cdot Q)$ vs. Q^2

2.4 CONTRAST VARIATION EXPERIMENTS

The contrast variation experiment in small-angle scattering was first introduced by Bragg and Perutz⁷⁰ in 1952. After that, this technique has been widely used to determine detailed structures of macromolecules, biomolecules and various multicomponent complexes. Neutron scattering with H/D substitution is now the dominant form of contrast variation used in scattering experiments.⁷¹ Contrast variation has been used to study details of micellar structures, including internal structure of rodlike micelles;⁷² cross sections of cylindrical micelles;⁷³ and mixed micellar systems.^{74,75} Any particle with a nonuniform distribution of scattering length density will have a contrast-dependent radius of gyration. The variation of contrast between the solvent and micelle contributes to the scattering intensity through the term K in Eqn. 2.52.

There are two kinds of contrast variation experiments, external and internal. These involve changing respectively the scattering length density of the solvent or the micelles. From Eqn. (2.17), one can see that the scattering form factor is directly related to the scattering length density contrast. We can either change the ρ_s by changing the percentage of the D₂O in the solvent for external contrast variation or change the ρ_m by changing the deuteration of surfactant tails, headgroup or counterion. There are different methods to extract information from contrast variation experiments.

From Eqn. 2.53, one gets a relationship between I(0) and contrast:

$$I_0^{1/2} = (C - C_{CMC})^{1/2} N^{1/2} V_m (\rho_m - \rho_s) \quad (2.54)$$

By plotting $I(0)^{1/2}$ vs. the percentage of the D₂O, or ρ_s , one obtains a straight line. From $I(0) = 0$, one gets the match point, at which $\rho_s = \langle \rho_m \rangle$. From $\langle \rho_m \rangle$, one can determine

the contents of the dry micelle and from that the amount of counterion visible in the objects responsible for the scattering. For internal contrast variation, ρ_m is changed while keeping ρ_s constant. $I(0)$'s variation with ρ_m gives the same information in this case.

The other advantage of the contrast variation is that you can find the scattering density of solvent to match some part of the micellar structure and make other(s) visible in the scattering. As a result, the micellar radius of gyration will change. The detailed function dependence, $R_g(\rho)$, depends on the R_g 's and ρ 's of the individual micellar sub regions. A more detailed discussion on contrast variation will be given in Chapter IV.

CHAPTER III

USING SANS TO STUDY MICELLE GROWTH AND FLEXIBILITY

3.1 INTRODUCTION

We have performed a systematic SANS study of the effects of surfactant concentration, ionic strength, surfactant structure (head group and tail length), and different counterion effects on micellar structure. In this chapter, we focus on spherical and wormlike micelles. The details of performing SANS experiments and reducing the data were discussed in chapter II.

The giant wormlike micelles have properties similar to semi-flexible polymers in a good solvent. In the mid-1980s, certain similarities between polymer solutions and solutions containing elongated micelles (the micelle-polymer analogy) were first recognized in the study of ionic surfactants.^{12,13} In this work, small-angle scattering has been used to obtain detailed information on micellar contour lengths and persistence lengths, a measure of micellar flexibility. By using the scattering function developed by Pedersen and Schurtenberger^{57,58} for semiflexible wormlike chains, micellar size and flexibility can be studied.

We have studied the wormlike micelles formed by the anionic surfactant salt, sodium dodecylsulfate (SDS), in aqueous solutions, focusing on the impact of salt and surfactant concentrations on micellar size and flexibility. We also studied different cationic surfactants, in order to gain information about the influence of surfactant structure on micellar structure and flexibility of wormlike micelles. The surfactants included cetyl(hexadecyl)trimethylammonium bromide (CTAB) and tetradecyl-

trimethylammonium bromide (TTAB), which have 16 and 14 carbon alkyl tails respectively, and CPyBr and CTAB, which have a pyridinium and trimethylammonium head group respectively. We also studied counterion effects on the micellar structure and flexibility by changing the type and concentration of the counterions. This work included a series of experiments on Cl, Br, which are not penetrating counterions, vs. salicylate, tosylate and 2,6-dichlorobenzoate, which penetrate the micellar surface, acting more like cosurfactants. The results are discussed in the following sections.

3.2 FLEXIBILITY OF ELONGATED SDS MICELLES IN SODIUM CHLORIDE SOLUTIONS

Numerous studies have been designed to study the anionic surfactant SDS forming micelles in water and in aqueous salt solutions. Micellar size (weight- or number-average aggregation numbers, $\langle n \rangle_w$ or $\langle n \rangle_n$), transitions in micellar shape from globular to elongated, and intermicellar interactions have been well studied. The major techniques used included static light scattering by Huisman and coworkers in the 1960s;⁷⁶ the use of fluorescence quenching techniques;⁷⁷ and the use of SANS,^{20,78,79} and SAXS.⁸⁰ For the globular SDS micelles in water, $\langle n \rangle_w$'s in the range of 70 to 90 are found using scattering techniques, and these correspond to a micellar radius of ~ 2.3 nm, somewhat larger than the extended surfactant tail length 1.67nm, of a C₁₂ chain. As NaCl is added, micellar growth is initially modest and then more rapid once the concentration of NaCl reaches 0.4M at 25°C and 0.5M at 40°C.⁸¹ We have used SANS to determine the detailed micellar structure and flexibilities at high salt concentrations, where the micelles are long

and wormlike. We found that the persistence lengths discussed in Chapter I for SDS larger than 700Å and increasing with salt are unreasonably large.³³⁻³⁵

SANS curves obtained for SDS micelles at 45°C in D₂O at NaCl concentrations of 1, 1.2, 1.5 and 2M are shown in Figure 3.1-3.4. Below 1M NaCl, the micelles are too small for the scattering curves to show clear evidence of flexibility. Surfactant concentrations ranged from 1.4mM to 30mM; the range at a given NaCl concentration was chosen so that most of the solutions were dilute rather than semidilute. From Figure 3.1-3.4, we can clearly see the micellar size increase as the surfactant concentration increases, especially in high salt solutions. The data for a single surfactant concentration, 4.8mM, at different salt concentrations are shown in a bending rod plot in Figure 3.5. Similar behavior is observed at other surfactant concentrations. The lower Q region makes obvious the significant micellar growth, while the coincidence of the scattering curves at higher Q illustrates that micelles all have a similar cross-sectional micellar structure. This agrees with unidimensional micellar growth..

3.2.1 Local micellar structure

A Guinier-like plot, $\ln(I(Q) \cdot Q)$ vs. Q^2 , for 1.5M NaCl shown in Figure 3.6 was fitted in the region $0.20\text{nm}^{-2} < Q^2 < 1\text{nm}^{-2}$ according to eqn. 2.52 after subtracting the flat background due to scattering from the salt solution. This value is 0.054cm^{-1} for 1M NaCl in D₂O. Table 3.1 reports the resulting micellar cross-sectional radii, r_{cs} , derived from the curves' slopes. For 1M NaCl, the mean value is 1.66 nm; values between 1.72 and 1.89 nm were found at other salt concentrations. However, fits of the full scattering curves give values for the micellar radii close to the length, 1.67 nm, of an extended C₁₂

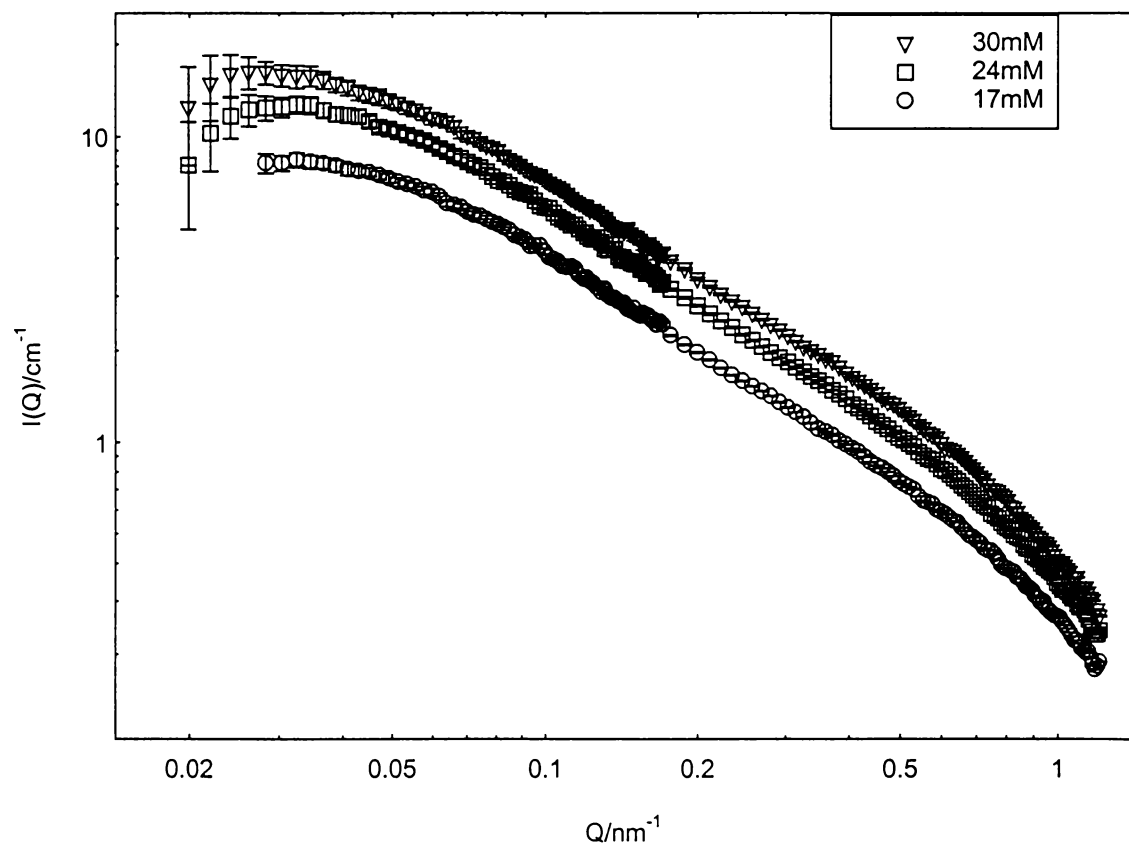


Figure 3.1 SANS curves for SDS micelles in 1M NaCl solutions at 45°C

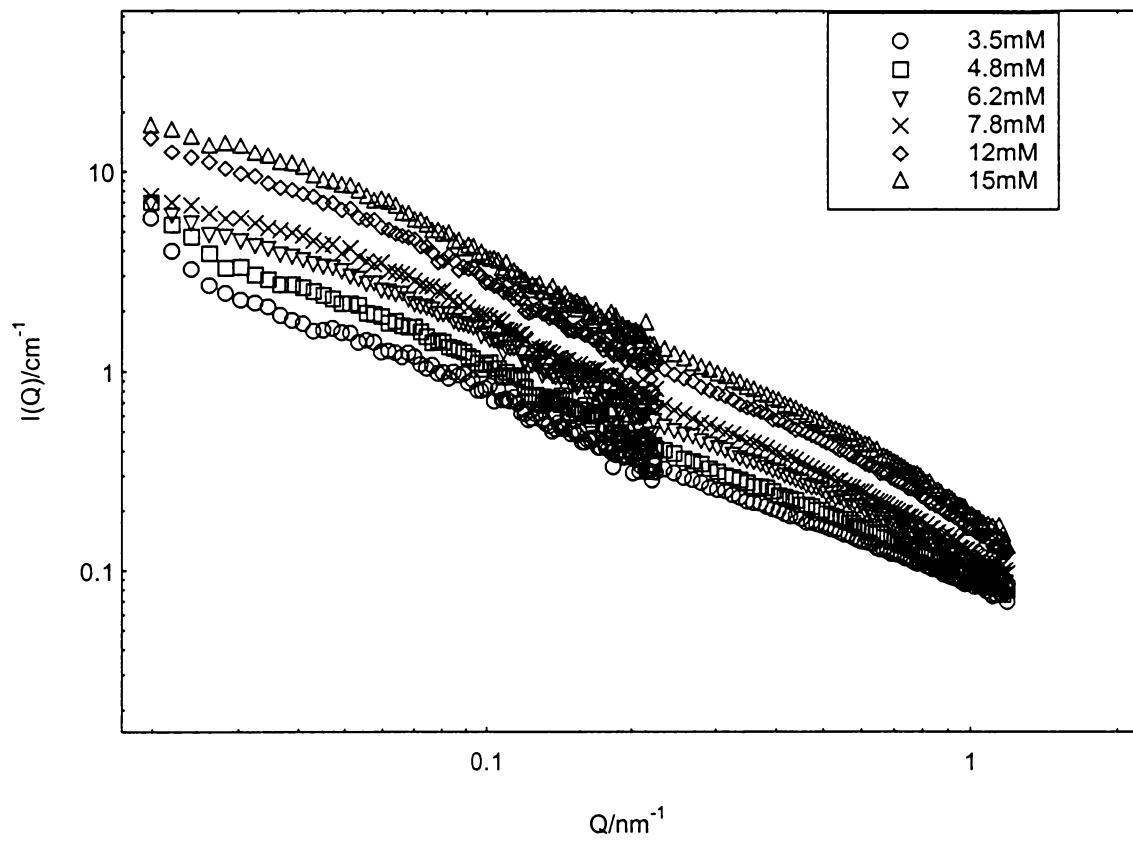


Figure 3.2 SANS curves for SDS micelles in 1.2M NaCl at 45°C

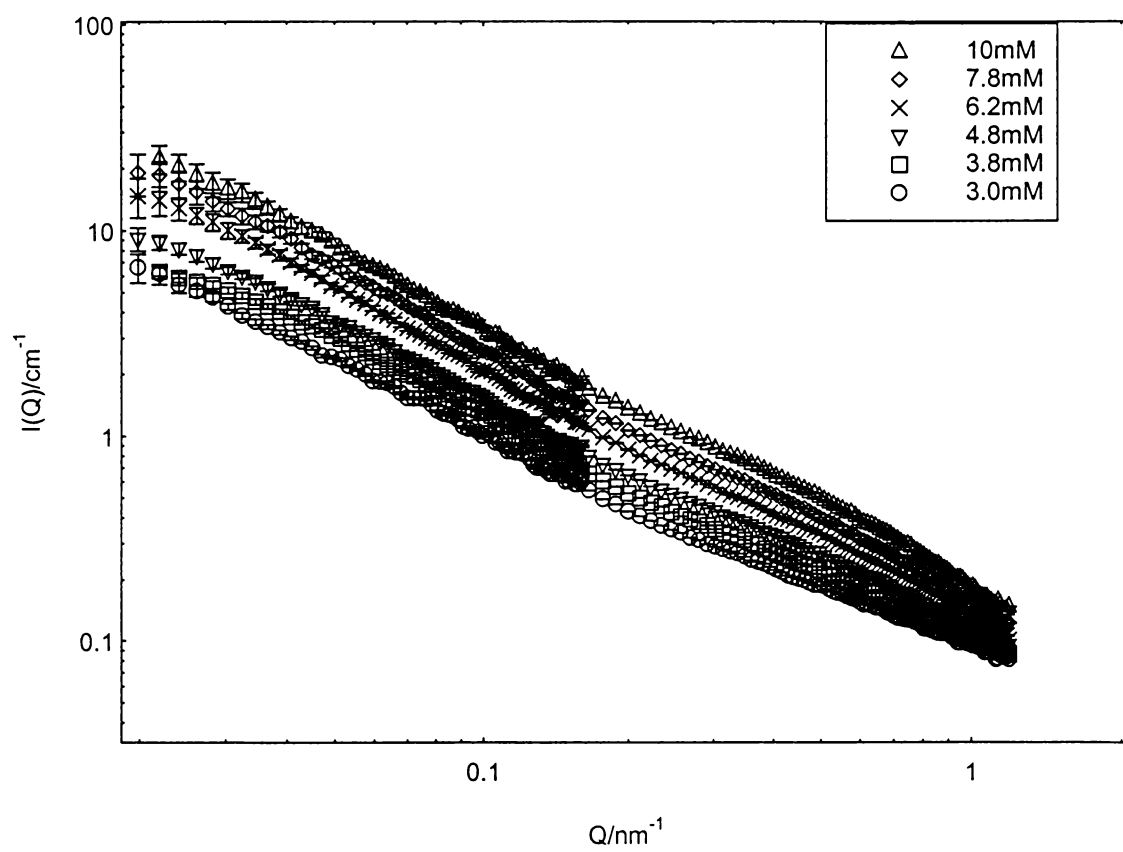


Figure 3.3 SANS curves for SDS micelles in 1.5M NaCl at 45°C

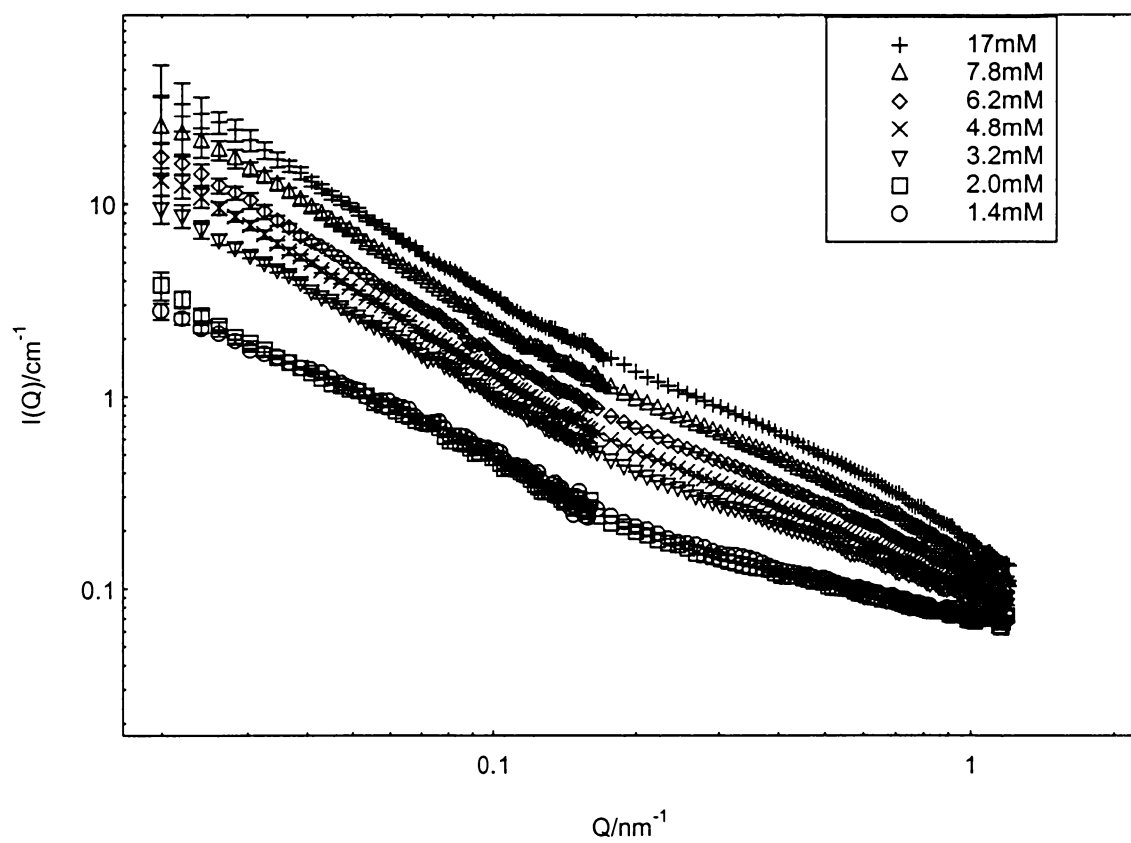


Figure 3.4 SANS curves for SDS micelles in 2M NaCl at 45°C

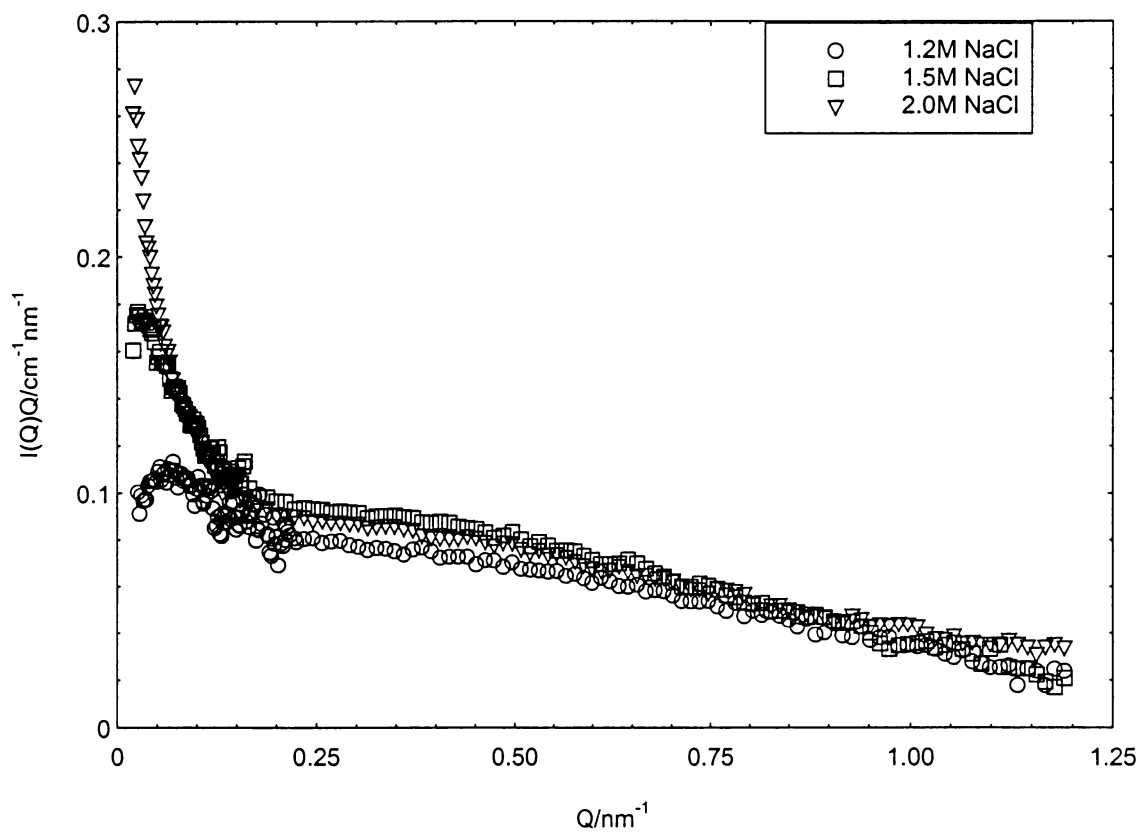


Figure 3.5 Bending rod plot for 4.8mM SDS in NaCl solutions at 45°C

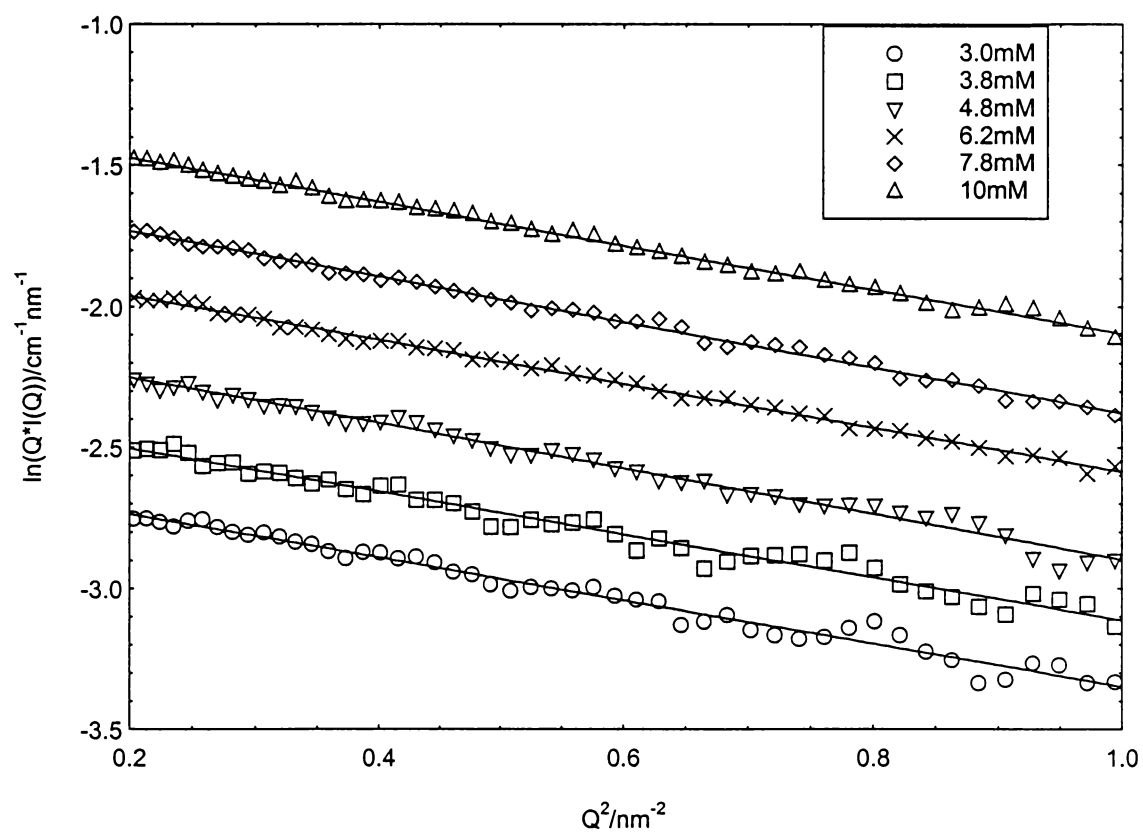


Figure 3.6 Guinier-like plot for SDS micelles in 1.5M NaCl solutions

Table 3.1 Local micellar structure for SDS micelles

SDS (mM)	[NaCl] (M)	N/L ($\times 10^8 \text{ cm}^{-1}$)	A_{hg} (\AA^2)	$R_{\text{g.cs}}$ (nm)	r_c (nm)
17	1.0	2.28 ± 0.02	45.2	1.16 ± 0.01	1.64
24	1.0	2.38 ± 0.02	45.1	1.18 ± 0.01	1.67
30	1.0	2.30 ± 0.02	45.7	1.18 ± 0.01	1.67
Mean:	1.0	2.30 ± 0.02			1.66
3.5	1.2	1.84 ± 0.02	59.4	1.23 ± 0.01	1.74
4.8	1.2	1.72 ± 0.02	62.6	1.21 ± 0.01	1.72
6.2	1.2	1.88 ± 0.02	58.3	1.23 ± 0.01	1.74
7.8	1.2	1.88 ± 0.02	58.9	1.24 ± 0.01	1.76
12.0	1.2	1.89 ± 0.02	58.1	1.24 ± 0.01	1.75
15.0	1.2	1.93 ± 0.02	57.6	1.25 ± 0.01	1.77
Mean:		1.87 ± 0.02			1.75
3.0	1.5	2.40 ± 0.02	46.3	1.25 ± 0.01	1.77
3.8	1.5	2.40 ± 0.02	46.1	1.25 ± 0.01	1.77
4.8	1.5	2.45 ± 0.02	46.2	1.27 ± 0.01	1.80
6.2	1.5	2.53 ± 0.02	44.0	1.25 ± 0.01	1.77
7.8	1.5	2.56 ± 0.02	44.6	1.29 ± 0.01	1.82
10.0	1.5	2.56 ± 0.02	43.3	1.25 ± 0.01	1.76
Mean:		2.54 ± 0.02			1.78
1.4mM	2.0	2.11 ± 0.02	56.2	1.33 ± 0.01	1.89
2.0mM	2.0	1.38 ± 0.02	94.4	1.46 ± 0.01	2.07
3.2mM	2.0	2.18 ± 0.02	54.5	1.34 ± 0.01	1.89
4.8mM	2.0	1.91 ± 0.02	62.1	1.33 ± 0.01	1.88
6.2mM	2.0	2.03 ± 0.02	56.7	1.30 ± 0.01	1.83
7.8mM	2.0	2.32 ± 0.02	48.4	1.26 ± 0.01	1.78
17.0mM	2.0	1.51 ± 0.02	75.6	1.28 ± 0.01	1.81
Mean		2.17 ± 0.02			1.85

* $(\rho_m - \rho_s)^2$: $3.53 \times 10^{-21} \text{ cm}^{-4}$

hydrocarbon chain. Using a micellar contrast term calculated only on the basis of the contrast between the hydrocarbon chain and the solvents, values of N/L were derived from the plots' intercepts, and the resulting N/L 's and the derived A_{hg} 's are also in Table 3.1. No dependence on salt concentration for the value of N/L indicates that the local packing of the surfactant, or the local micellar structure, is independent of NaCl concentration over the range from 1 to 2M NaCl.

3.2.2 Overall micellar size and flexibility

The full scattering curves were first fit using Eqn. 2.42-2.44 without taking intermicellar interactions into account.^{82,83} The fitting were performed by using weighted non-linear least square methods described in Chapter V. The value of the scattering from the solvent was fixed. The micellar polydispersity was also fixed, at $M_w/M_n = 2$ ($z = 1$), consistent with the description in Section 2.3.4. The parameters varied were the micellar contour length, $\langle L_n \rangle$, Kuhn length, $2\langle l_p \rangle$, and cross-sectional radii, r_{cs} . The overall micellar R_g was calculated from $\langle L_n \rangle$ and $\langle l_p \rangle$ from the fitted results. Table 3.2 tabulates the results, and Figure 3.7-3.8 shows the fits to the scattering curves in the bending rod plots for SDS in 1.0M and 2.0M salt. Figure 3.9 contains the plot of the observed concentration-dependent increases in micellar contour lengths at all four NaCl concentrations, c_s . With increasing salt concentration, the micellar size increases more rapidly as the surfactant concentration, c , increases. The exponent, α , in the scaling relationship, $\langle L_n \rangle \sim c^\alpha$, increases as follows: 0.15 ± 0.01 at 1M NaCl; 0.30 ± 0.01 at 1.2M NaCl; 0.43 ± 0.02 at 1.5M NaCl and 0.88 ± 0.02 at 2.0M NaCl. These values deviate strongly from the classical⁸⁴ (mean-field) value of 0.5. Other groups⁸⁵ also

Table 3.2 Fitted parameters for SDS micelles in aqueous NaCl without/with intermicellar interactions

SDSin 1.0M NaCl						
SDS mM	NaCl M	Background	r_{cs} (Å)	R_g (Å)	$\langle L_n \rangle$ (Å)	$\langle 2L_p \rangle$ (Å)
17.0	1.0	0.054	12.7±0.2	217	404±4	371±10
24.0	1.0	0.054	12.4±0.2	232	429±4	402±13
30.0	1.0	0.054	12.0±0.2	237	438±4	414±11
SDSin 1.2M NaCl						
3.5	1.2	0.054	14.3±0.4	307	683±20	359±15
4.8	1.2	0.054	14.6±0.4	341	851±21	321±10
6.2	1.2	0.054	14.7±0.3	336	852±16	309±8
7.8	1.2	0.054	15.5±0.2	345	865±13	325±6
12.0	1.2	0.054	15.4±0.2	346	1038±19	346±7
15.0	1.2	0.054	15.4±0.2	402	1097±20	325±7
SDSin 1.5M NaCl						
3.0	1.5	0.0608	16.3±0.3	474	1524±43	296±7
3.8	1.5	0.0608	16.4±0.2	459	1448±26	294±5
4.8	1.5	0.0608	16.0±0.2	518	1631±36	334±6
6.2	1.5	0.0608	16.3±0.2	607	2208±58	314±4
7.8	1.5	0.0608	16.8±0.1	644	2379±70	326±4
10.0	1.5	0.0608	16.4±0.1	621	2194±62	335±5
SDSin 2.0M NaCl						
1.4	2.0	0.0608	15.6±0.6	426	1557±51	218±8
2.0	2.0	0.0608	16.6±0.6	464	1892±74	203±7
3.2	2.0	0.0608	16.5±0.3	720	3367±16	258±5
4.8	2.0	0.0608	16.8±0.2	932	5100±258	268±3
6.2	2.0	0.0608	16.6±0.2	977	5162±70	295±4
7.8	2.0	0.0576	16.4±0.2	1147	6775±494	296±3
17.0	2.0	0.0576	16.7±0.2	1253	7539±483	316±3

With intermicellar interaction

	X	NaCl (M)	A	$\langle L_n \rangle$ (Å)	S(0)
3.5	0.127	1.2	3.97±0.09	752±18	0.871
4.8	0.231	1.2	7.05±0.18	1031±31	0.784
6.2	0.331	1.2	11.2±0.3	1162±31	0.713
7.8	0.490	1.2	17.1±0.3	1401±43	0.620
12.0	1.465	1.2	61.3±0.3	3213±142	0.325
3.0	0.201	1.5	8.03±0.21	1792±51	0.807
3.8	0.262	1.5	10.6±0.2	1861±31	0.760
4.8	0.355	1.5	14.5±0.4	2033±32	0.697
6.2	0.781	1.5	39.2±1.5	4044±160	0.495

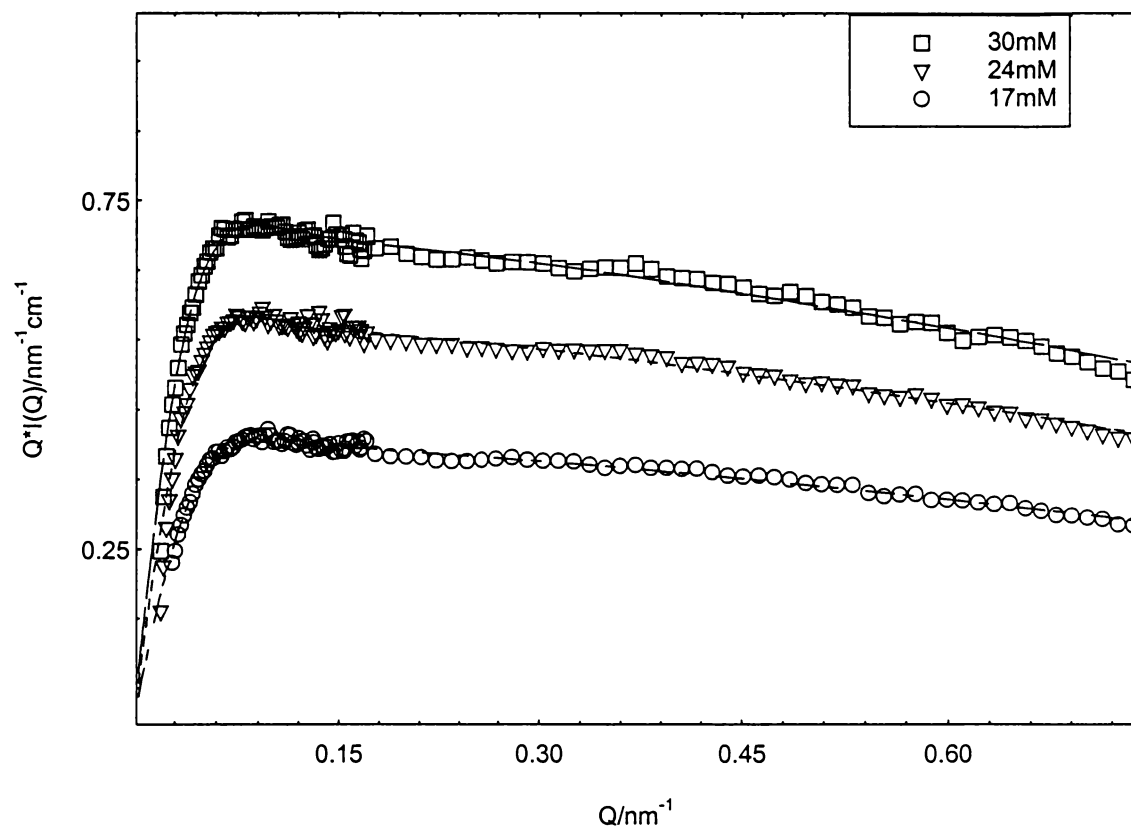


Figure 3.7 Bending rod plots of SANS data for SDS with fits in 1M NaCl without taking intermicellar interactions into account

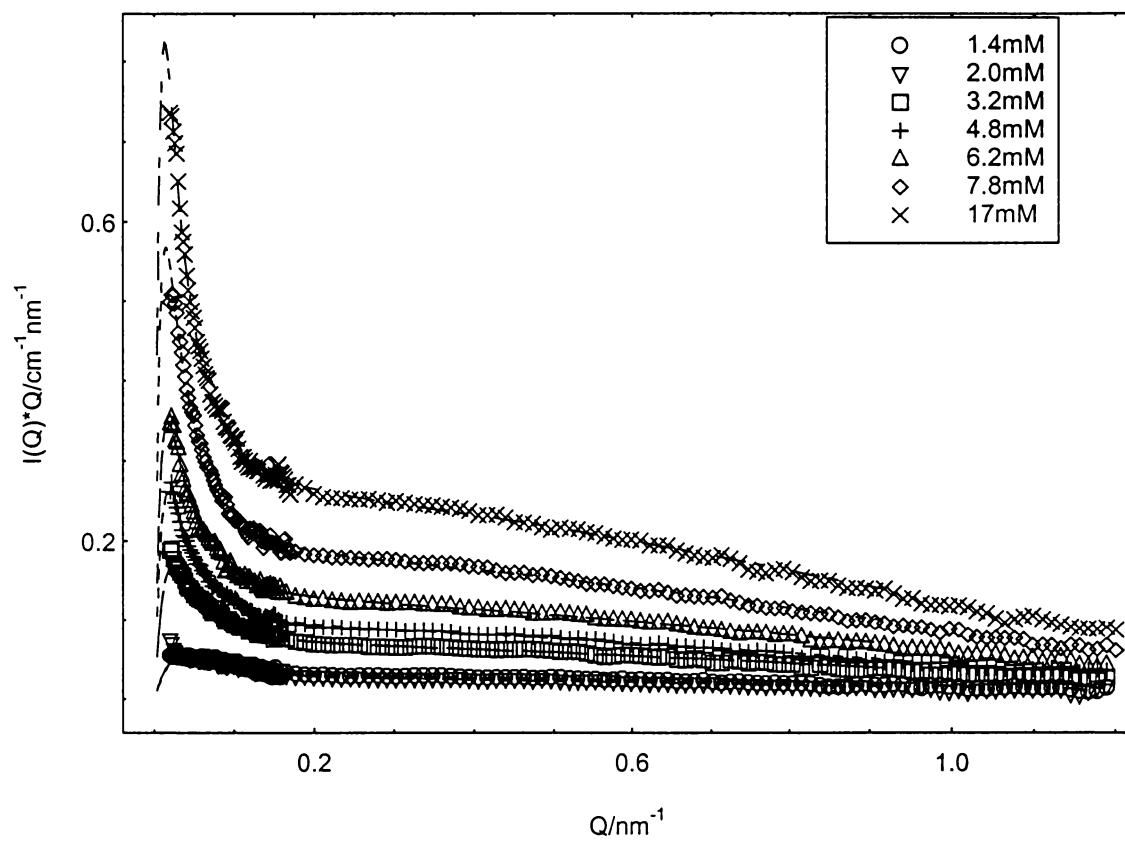


Figure 3.8 Bending rod plots of SANS data for SDS with fits in 2M NaCl without taking intermicellar interactions into account

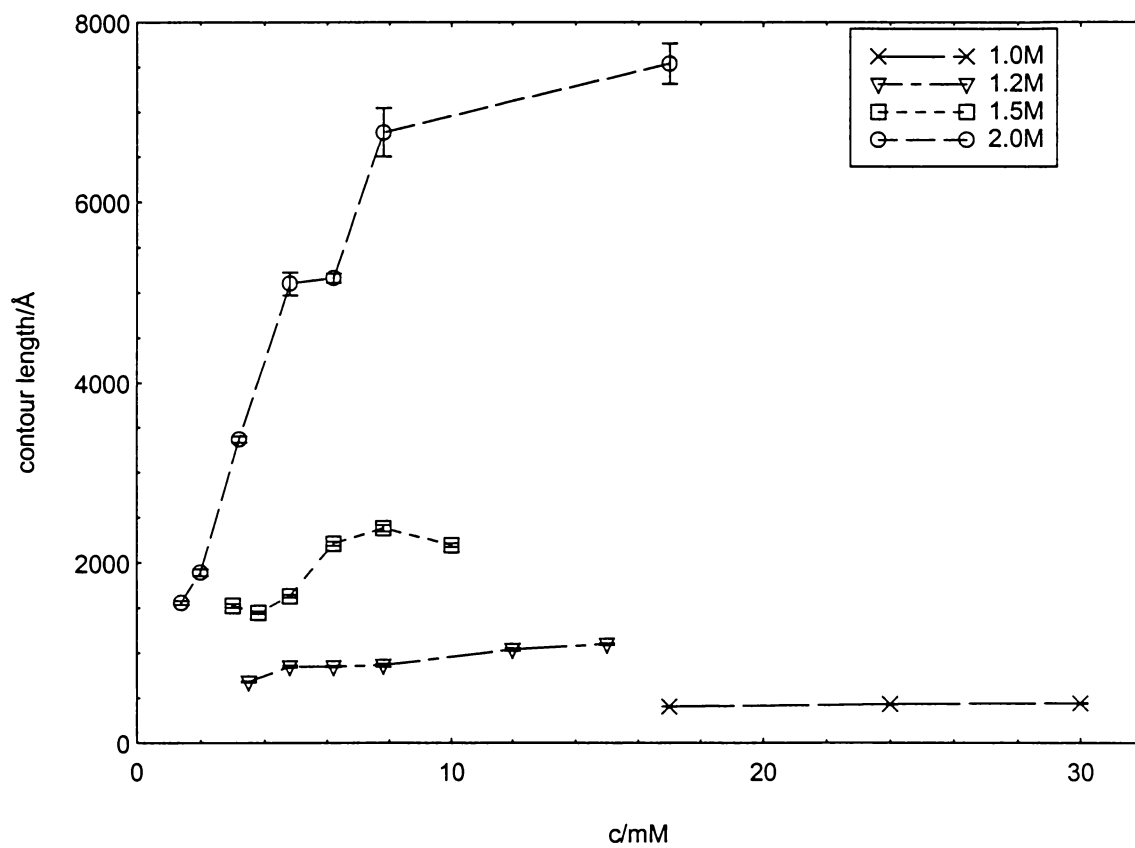


Figure 3.9. Dependence of micellar contour lengths on SDS concentration in different NaCl solutions

observed deviations from the value of 0.5. In Figure 3.9, a leveling off of contour length occurring in the range $7.8\text{mM} < c < 17\text{mM}$ in 2M salt is also observed, indicating a overlap concentration, c^* , is being approached as the surfactant concentration increases.

The fitted micellar Kuhn lengths, which are apparent values, are in Figure 3.10. The Kuhn length also increases as c increases, but with a relatively small change compared to the contour length. Since the increases in persistence length with c are apparent, and these come from the neglect of intermicellar interactions rather than from a real physical stiffening of the semiflexible wormlike chain, at each c_s , the real Kuhn length can be derived by extrapolating the fitted values to zero surfactant concentration. With increasing c_s , the persistence length, $l_{p,c=0}$, decreases as follows: $159 \pm 14 \text{Å}$ at 1M; $154 \pm 8 \text{Å}$ at 1.2M; $138 \pm 7 \text{Å}$ at 1.5M; and $98 \pm 7 \text{Å}$ at 2.0M.

To take the intermicellar interactions into account, we tried to fit the scattering data using Eqn. 2.48-2.51. Because the scattering curves are sensitive to intermicellar interactions as well as to contour length and persistence length at low Q ($Q < 0.2\text{nm}^{-1}$), some constraints are needed on the fitting parameters. At each surfactant concentration, l_p was set equal to the extrapolated value, $l_{p,c=0}$. The micellar cross sectional radii and background term are also fixed, with the values coming from the fits without intermicellar interactions. The only parameters varied are contour length and A , where A is equal to KcM_w .

Results of the fits for 1.2, and 1.5M NaCl are found in table 3.2 and Figures 3.11-12. As fitting proceeds, an updated value for the reduced value X (Eqn. 2.71), is derived from M_w , which is in turn derived from the fitting parameter contour length, $\langle L_n \rangle$, N/L , and molar mass of SDS: $M_w = (N/L) \cdot 2 \langle L_n \rangle \cdot 288\text{g/mol}$. Once X is ~ 0.5 , that is the

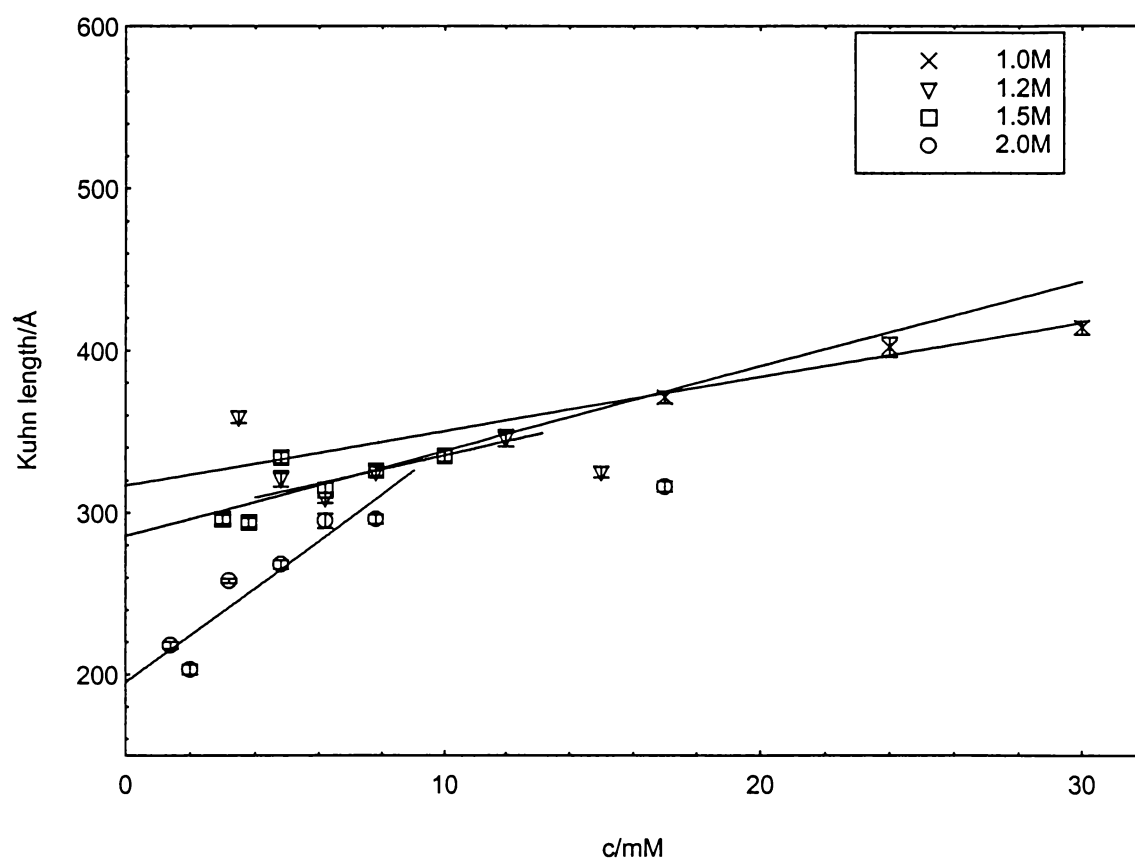


Figure 3.10 Dependence of micellar Kuhn lengths on SDS concentration in different NaCl solutions

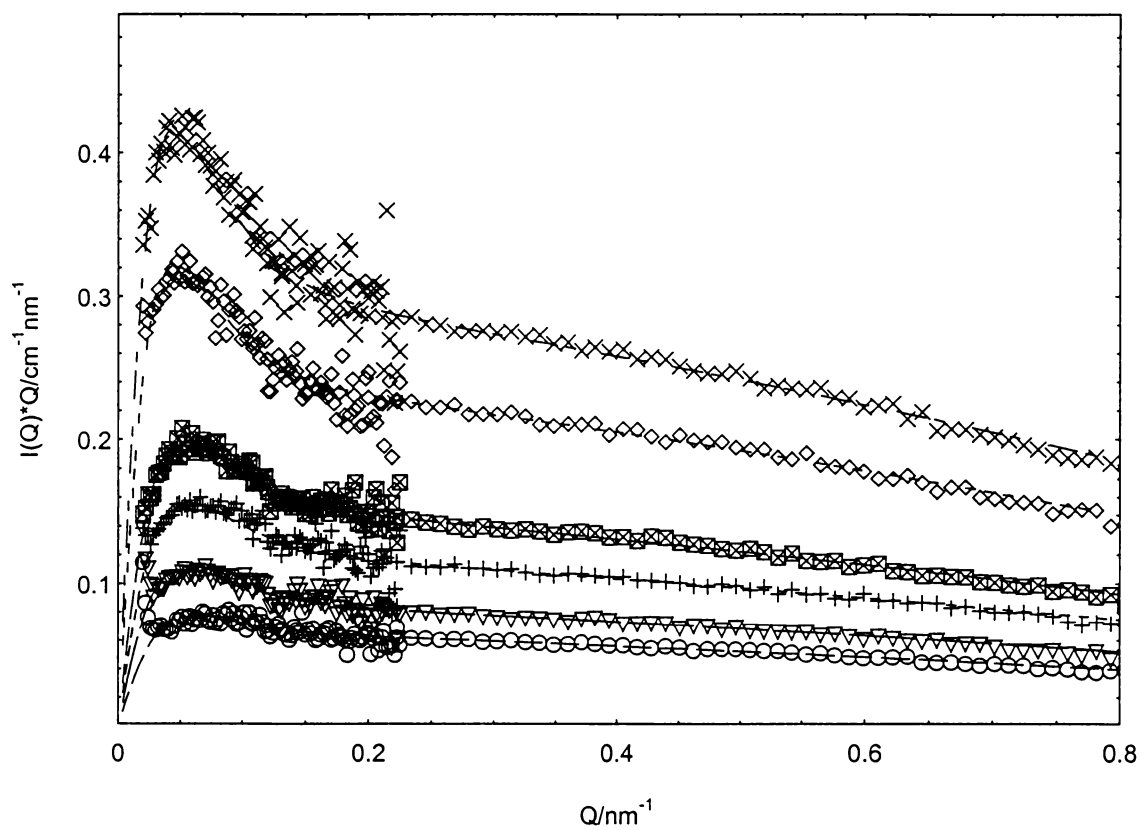


Figure 3.11 Bending rod plots of SANS data for SDS with fits in 1.2M NaCl, with including the effect of intermicellar interactions

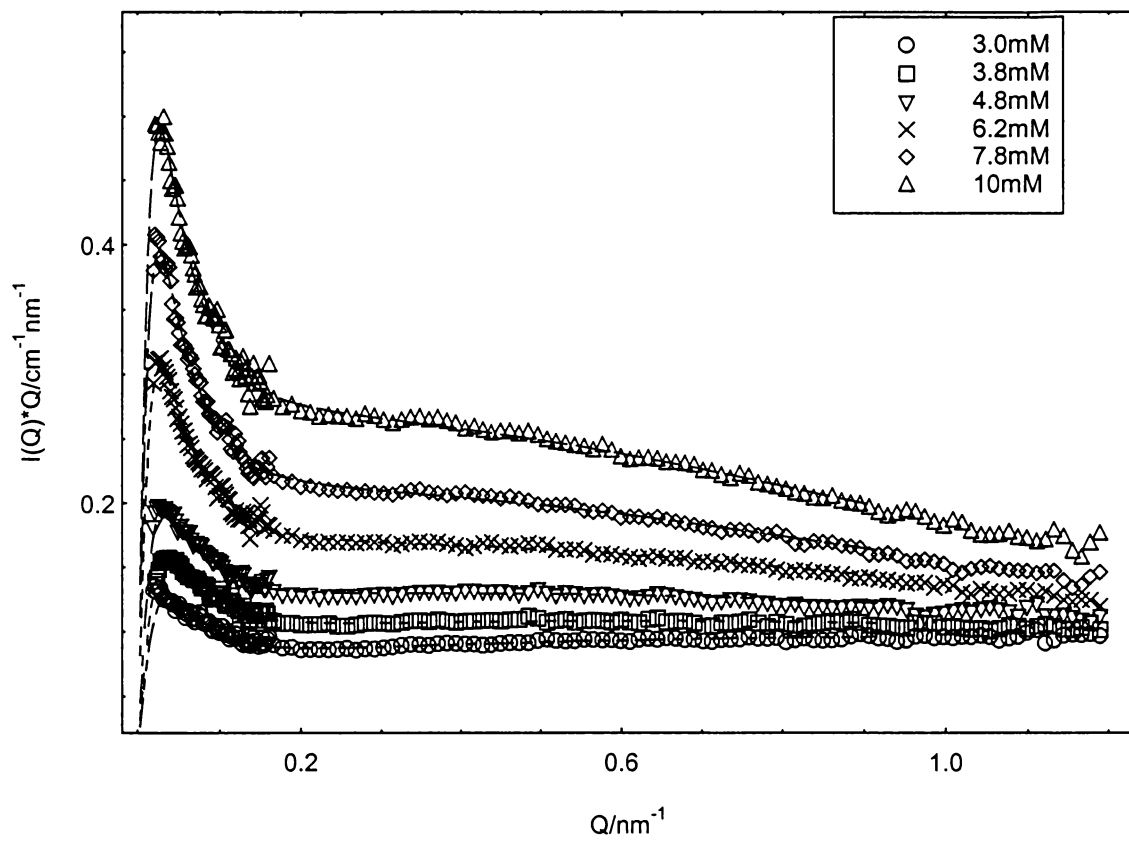


Figure 3.12 Bending rod plots of SANS data for SDS with fits in 1.5M NaCl, with including the effect of intermicellar interactions

surfactant concentration is about half of c^* and $S(0)$ is of order 0.3 – 0.5, the fitted micellar size undergoes a rapid increase. The value of A can be used to obtain values for K at each surfactant concentration. Provided that the scattering intensities have been converted properly to the absolute scale and that the scattering function used properly accounts for the intermicellar interactions, then K should be a true constant from which the square of the contrast factor, $(\rho_m - \rho_s)^2$, can be obtained. The fitted ρ_m agrees well with the calculated value, which indicates that the fitting process is very reliable in this case.

The availability of numerical expressions for the scattering functions of wormlike chains and for a structure factor describing interchain interactions between the chains at finite Q , both calculated by Pedersen and Schurtenberger from their Monte Carlo simulations, allows for a robust analysis of the SANS data. To our knowledge, the work described here is the first example of implementation of their protocol with adjustable parameters in a full least-squares fitting mode. Recently, Pedersen and Schurtenberger have also tried to fit some experimental data, but have not succeeded in full curve fits on noionic/ionic surfatant.^{86, 87} We will encounter similar difficulties in the following sections.

3.3 TUNING SIZE AND FLEXIBILITY OF THE CATIONIC WORMLIKE MICELLES: THE ROLE OF SURFACTANT HEAD GROUP AND TAIL LENGTH

Micelles of cationic surfactants such as cetyltrimethylammonium bromide (CTAB), tetradecyltrimethylammonium bromide (TTAB), and cetylpyridium bromide (CPyBr) have

been characterized using a variety of techniques. In the 1960s, light scattering was used to estimate the average molecular weight $M_w \sim L$ of the micelles, indicating a considerable increase of the aggregation number in some cases: up to 10^4 for instance for dilute CTAB in NaBr solutions.⁸⁵ Static scattering has been used by Imae and coworkers in the 1980s to give determinations of the sphere to rod transition for a series of cationic surfactants, C_n TAB with $n = 12, 14, 16$, as a function of salt concentration.³³ Dynamic light scattering (DLS) has been used to study the sphere to rod transition for CPyX and CTAX micelles in high ionic strength aqueous solutions. Persistence lengths can be derived by combined analysis of micellar hydrodynamic radii (R_H) from DLS and R_g 's from SLS.^{31,88} NMR and viscometry have also been used to study these systems.¹² In the last few years, several groups also used time-resolved fluorescence quenching methods to study the micellar aggregation number and micellar microviscosity.^{89,90} In this work, SANS measurements to determine micellar size and flexibilities will be discussed.

SANS curves were obtained for CTAB micelles at 40°C in D_2O at NaBr concentrations of 0.15, 0.25, 0.5 and 1.0M, TTAB micelles at 40°C in D_2O at NaBr concentrations of 1.5 and 3.0M, and CPyBr micelles at 40°C in D_2O at NaBr concentrations of 0.25, 0.5 and 0.8M. Short (rigid) rod or longer wormlike chains can be obtained at these salt concentrations for these micellar systems. The scattering curves for these systems, Figure 3.13 –3.21, show the micellar size increase in all the systems as the surfactant concentration increases, especially for the higher salt concentrations. A comparison at a single surfactant concentration, 3.8mM, for CTAB in 0.5M salt, CPyBr in 0.5M salt, and TTAB in 1.5M salt are shown in bending rod plot format in Figure 3.22. Significant differences in micellar size and flexibilities are apparent, caused by changes

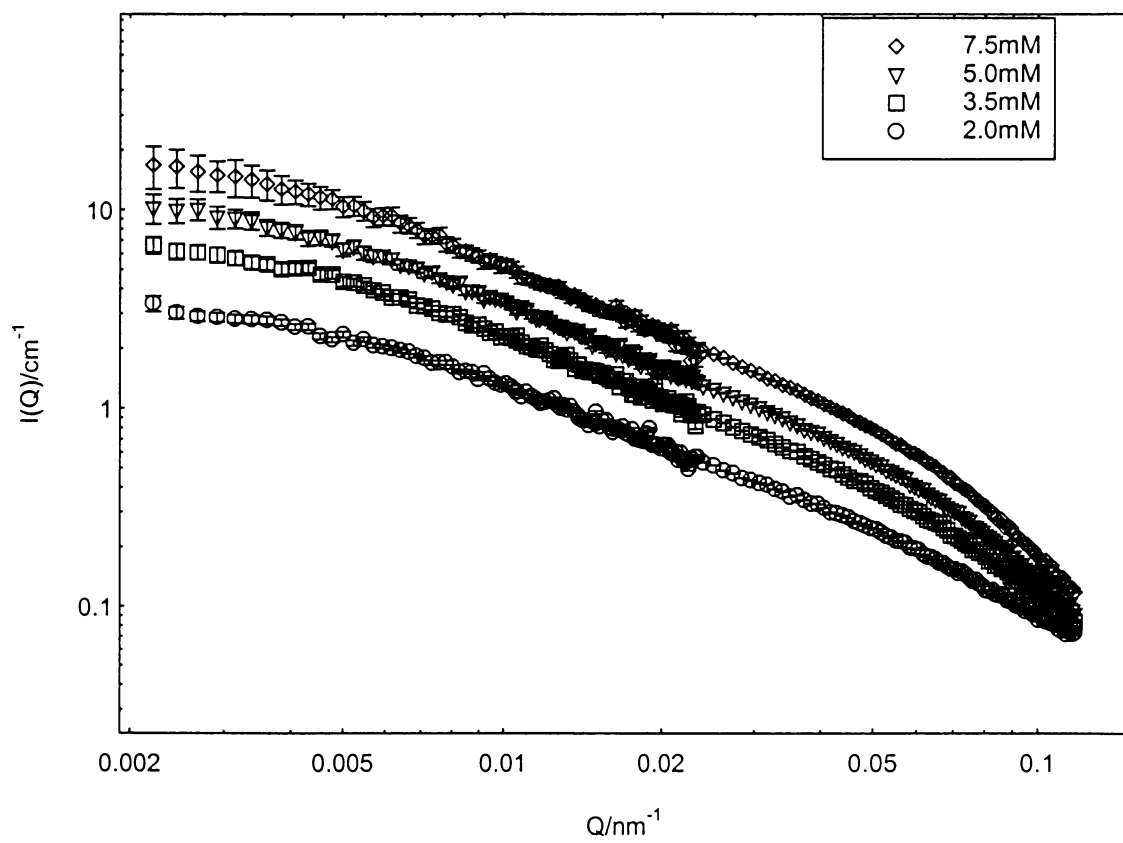


Figure 3.13 SANS curves for CTAB micelles in 0.15M NaBr at 40°C

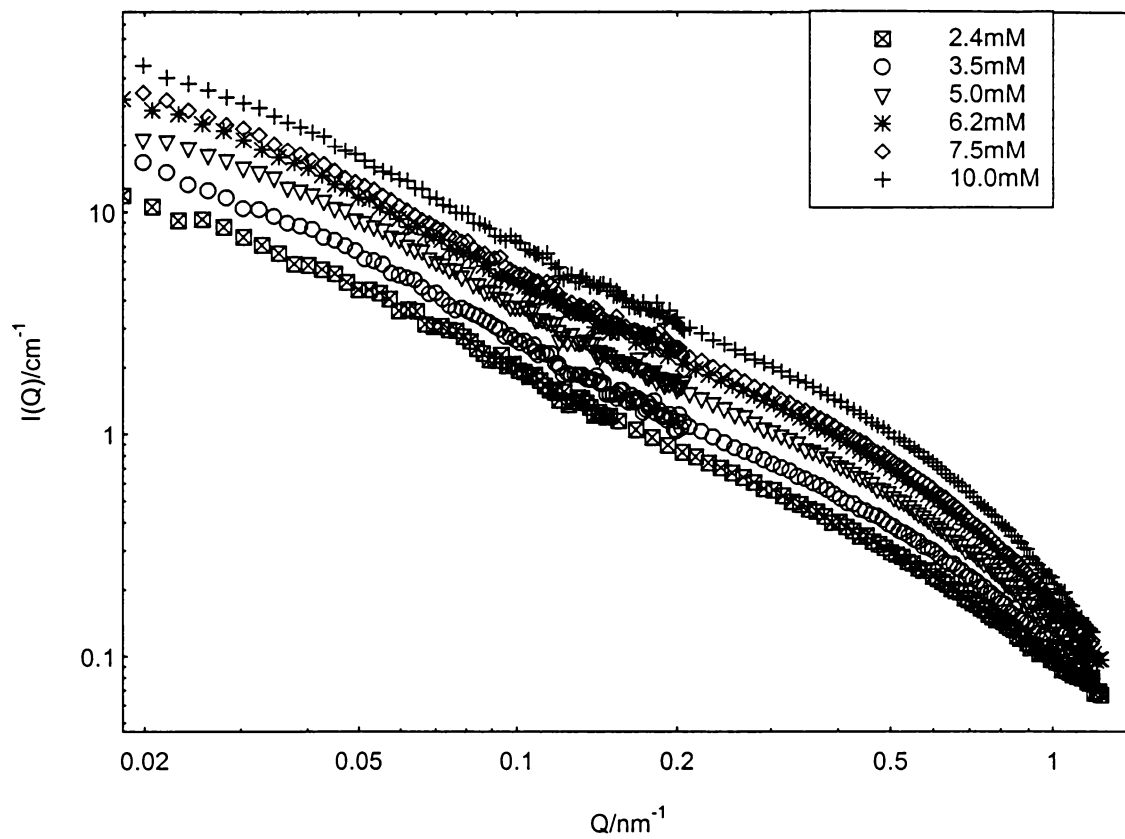


Figure 3.14 SANS curves for CTAB micelles in 0.25M NaBr at 40°C

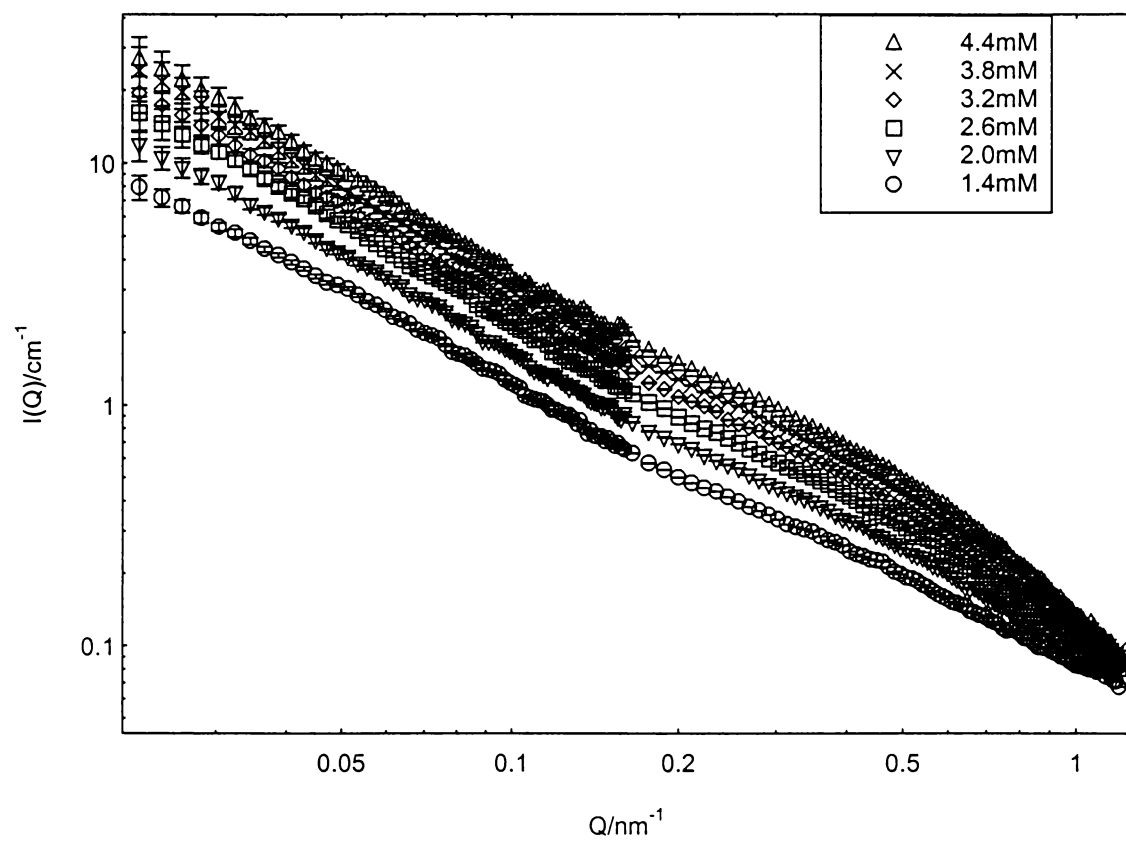


Figure 3.15 SANS curves for CTAB micelles in 0.50M NaBr at 40°C

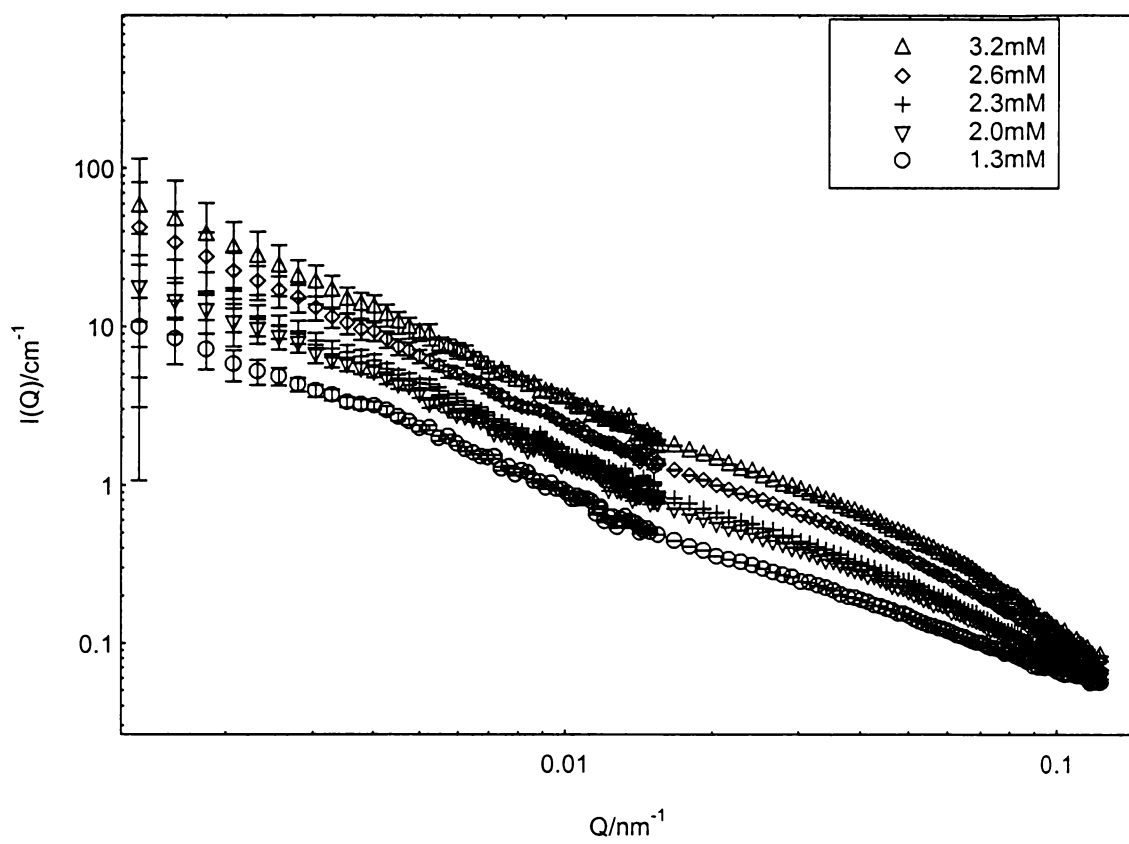


Figure 3.16 SANS curves for CTAB micelles in 1.0M NaBr at 40°C

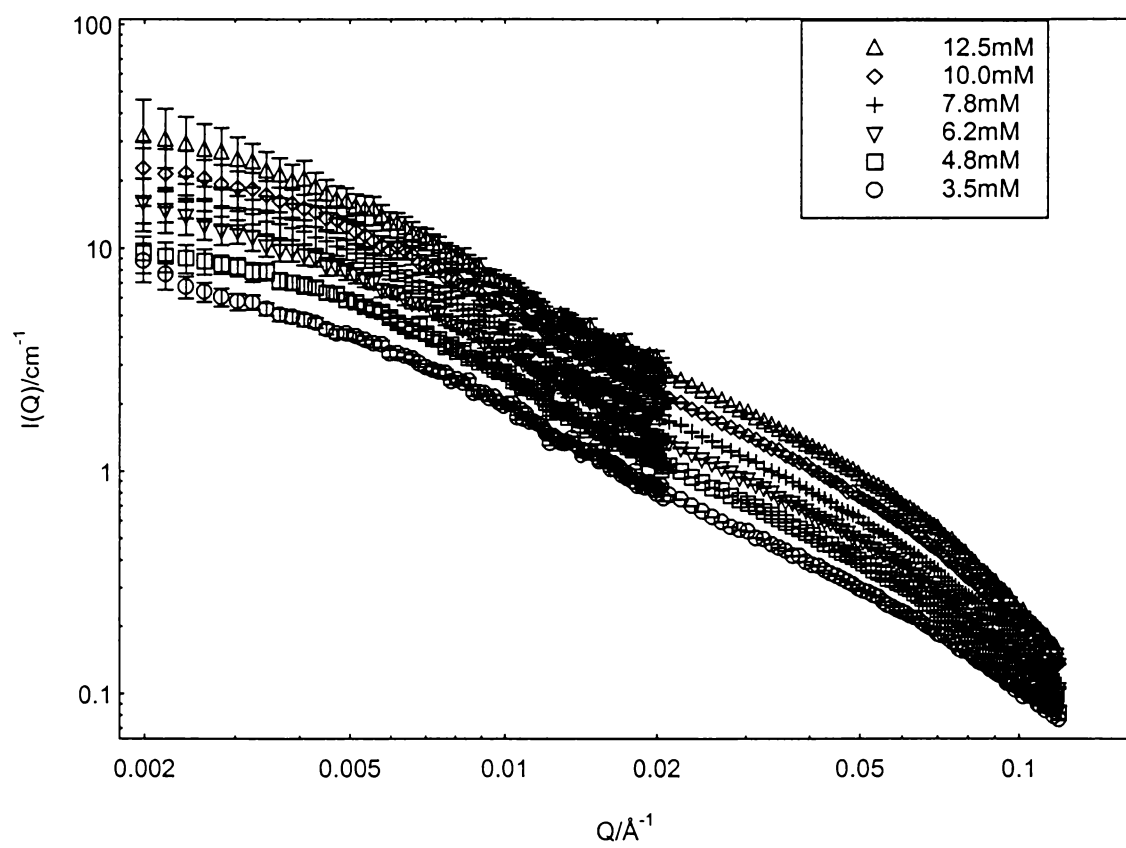


Figure 3.17 SANS curves for TTAB micelles in 1.5M NaBr at 40°C

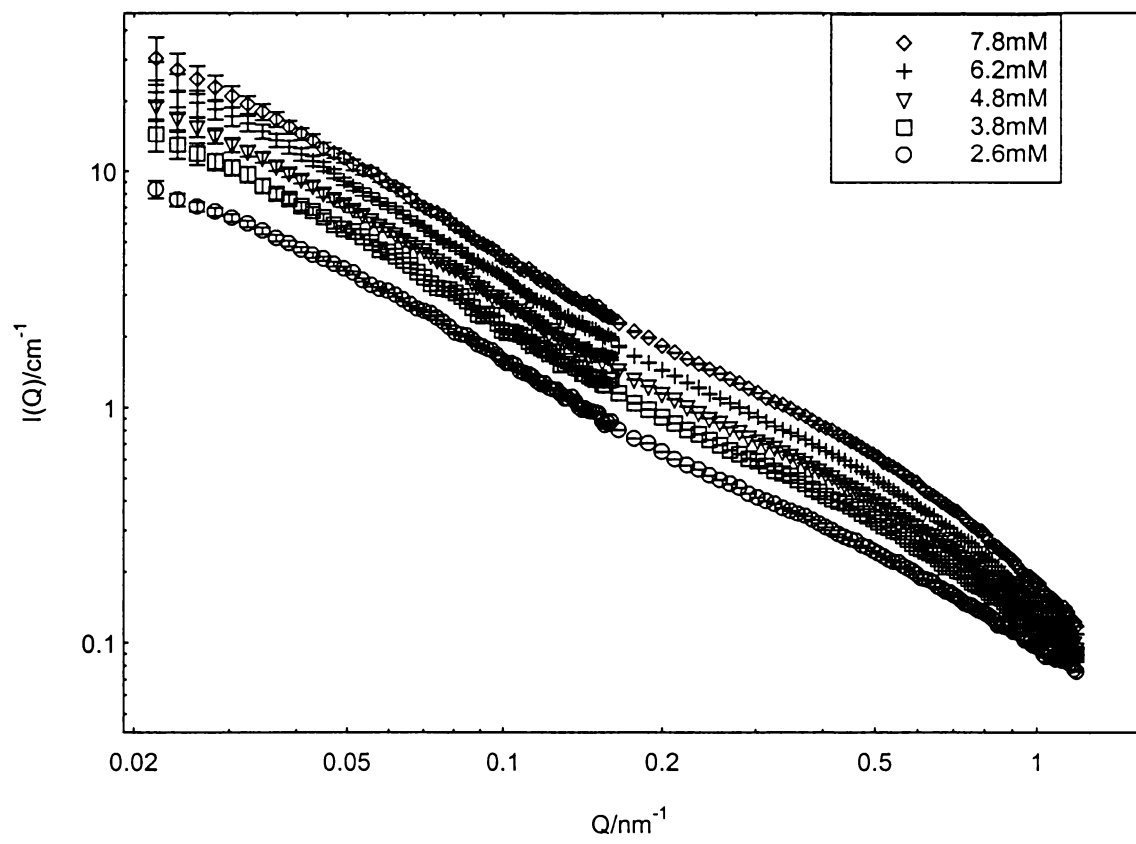


Figure 3.18 SANS curves for TTAB micelles in 3.0M NaBr at 40°C

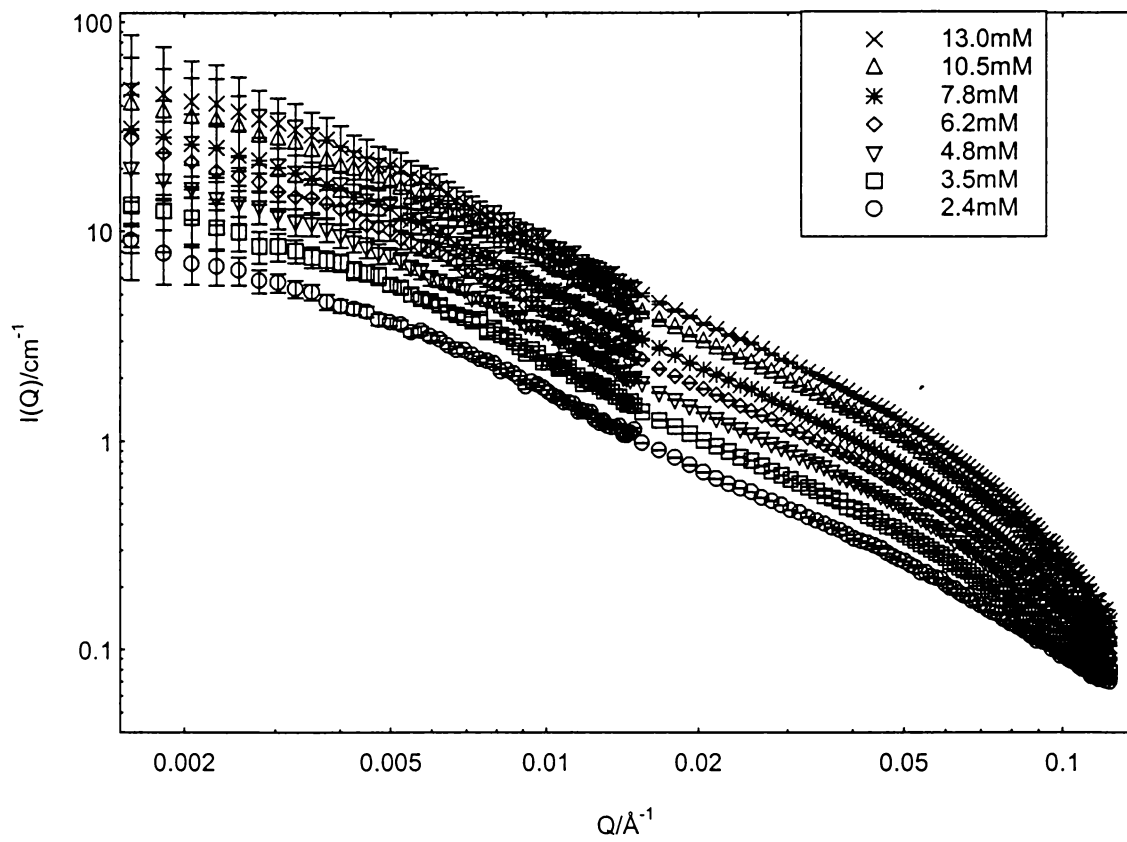


Figure 3.19 SANS curves for CPyBr micelles in 0.25M NaBr at 40°C

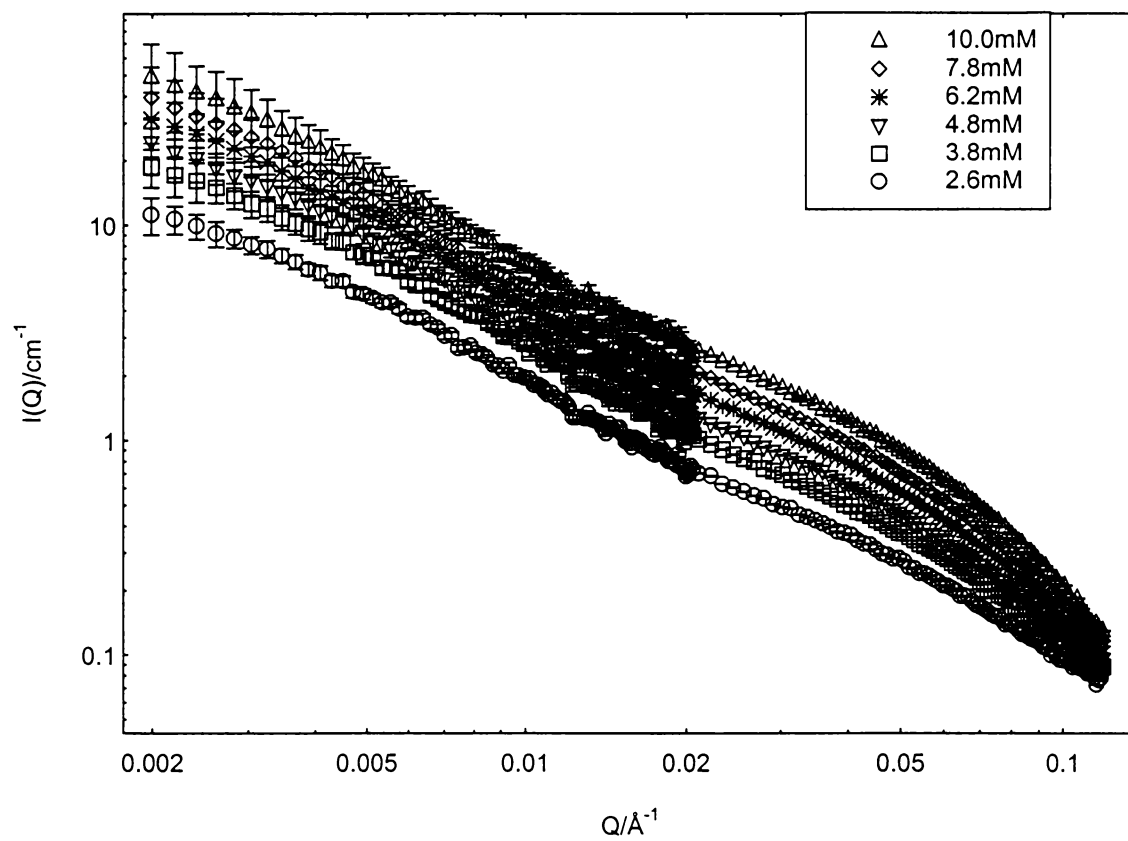


Figure 3.20 SANS curves for CPyBr micelles in 0.5M NaBr at 40°C

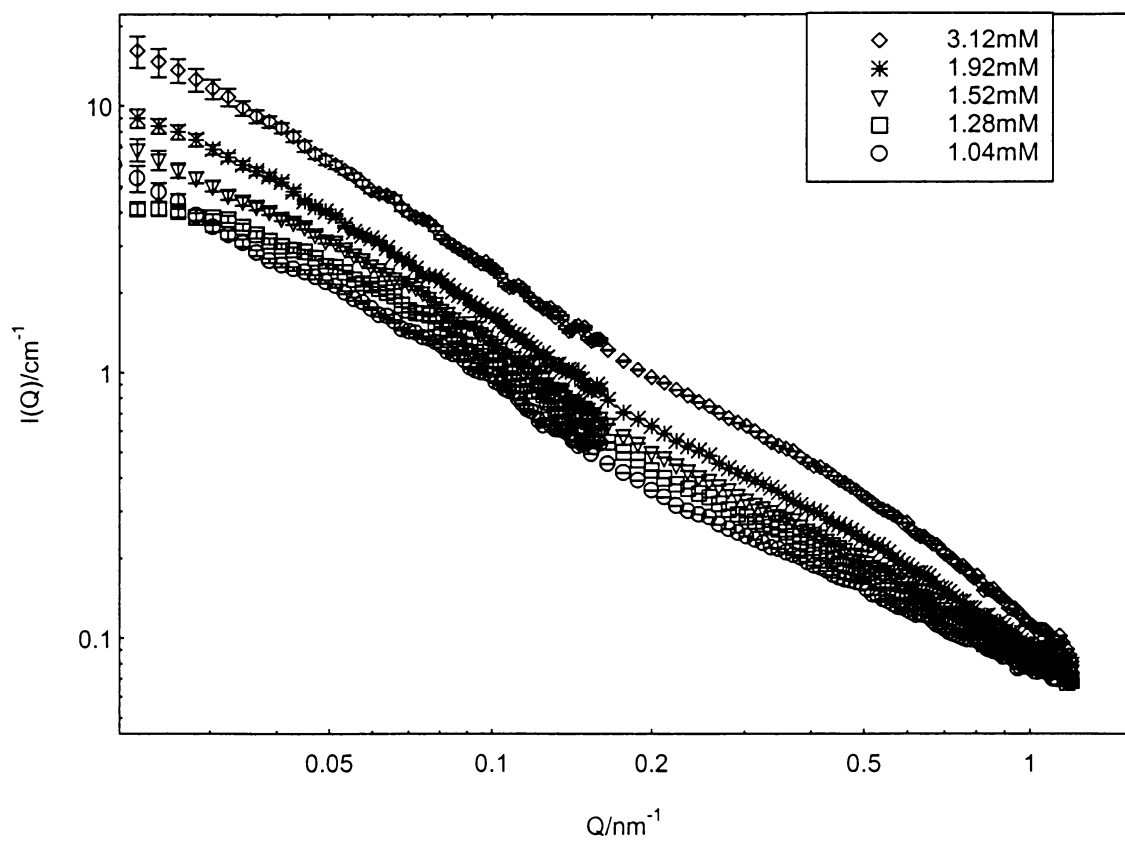


Figure 3.21 SANS curves for CPyBr micelles in 0.8M NaBr at 40°C

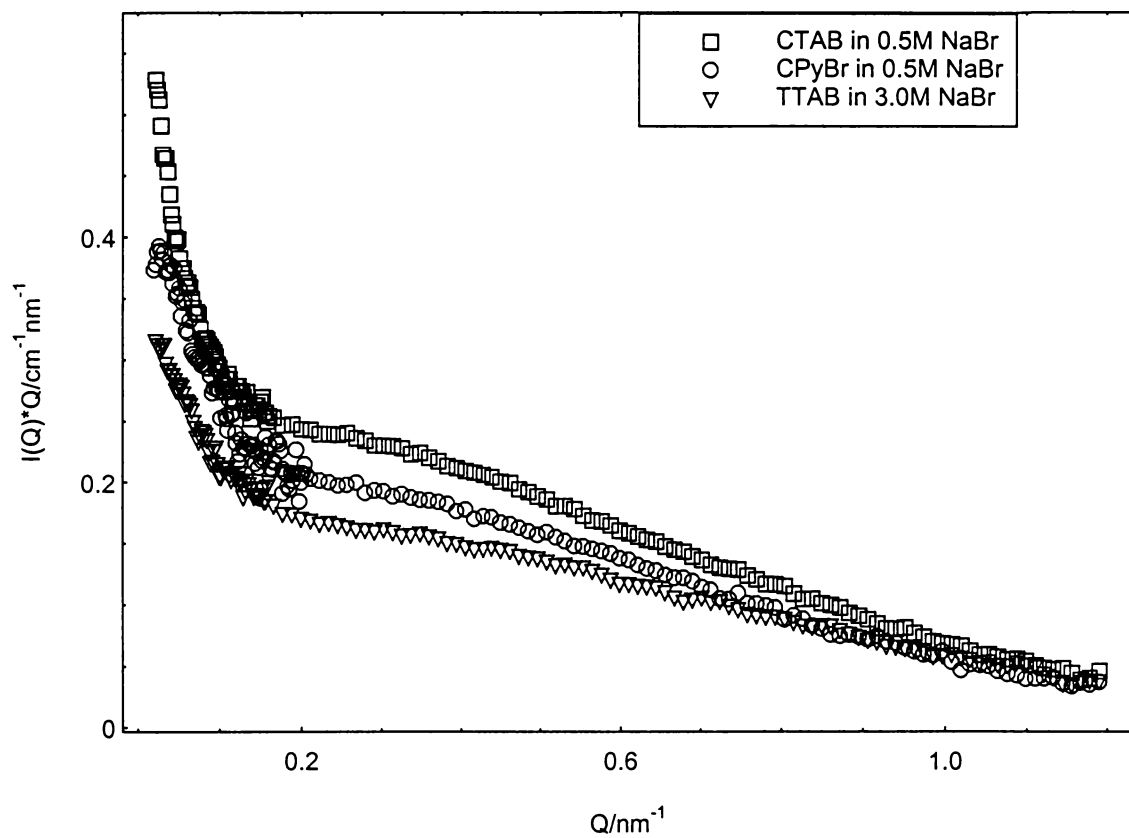


Figure 3.22 Comparison of 3.8mM CTAB, TTAB, and CPyBr at NaBr concentrations of 0.5, 0.5, and 3.0M respectively

in surfactant chain length and head group structure. The lower Q region makes obvious the significant micellar growth, while the coincidence of the scattering curves at higher Q illustrates a similar cross-sectional micellar structure. This agrees with the assumption that the micelles grow unidimensionally. Surfactant concentrations ranged from 1.3 to 7.5mM for CTAB; 2.6 to 12.5mM for TTAB and 1.04-13.0mM for CPyBr. The concentration range at a given NaBr concentration was chosen so that most of the solutions were dilute rather than semidilute and gave micellar sizes in the same range of $\langle L_n \rangle$'s if possible, in order to give the best comparison of l_p 's.

3.3.1 Detailed CTAB micellar structure

Local micellar structure

Guinier-like plots, $\ln(I(Q) \cdot Q)$ vs. Q^2 , for CTAB in 0.5M NaBr are shown in Figure 3.23, and the data are fitted in the region $0.20\text{nm}^{-2} < Q^2 < 1\text{nm}^{-2}$ according to Eqn. 2.52. Table 3.3 reports the resulting micellar cross-sectional radii, r_{cs} , at all the salt concentrations, derived from the slopes of the curves. For 0.5M NaBr, the mean value is 2.30 nm; values of 2.40 and 2.44 nm were found at 0.25M and 1M NaBr, respectively. However, fits to the full scattering curves give values for the radius close to the length, 2.23 nm, of an extended C_{16} hydrocarbon chain. Using a micellar contrast term calculated only on the basis of the contrast between the hydrocarbon chain and the solvents, values of N/L were derived from the intercepts of plots, and the resulting N/L's and the derived A_{hg} 's are also tabulated in Table 3.3. No dependence on salt concentration for the value of N/L indicates that the local packing of the surfactant, or the local micellar structure, is independent of NaBr concentration over the range from 0.15 to 1M NaBr.

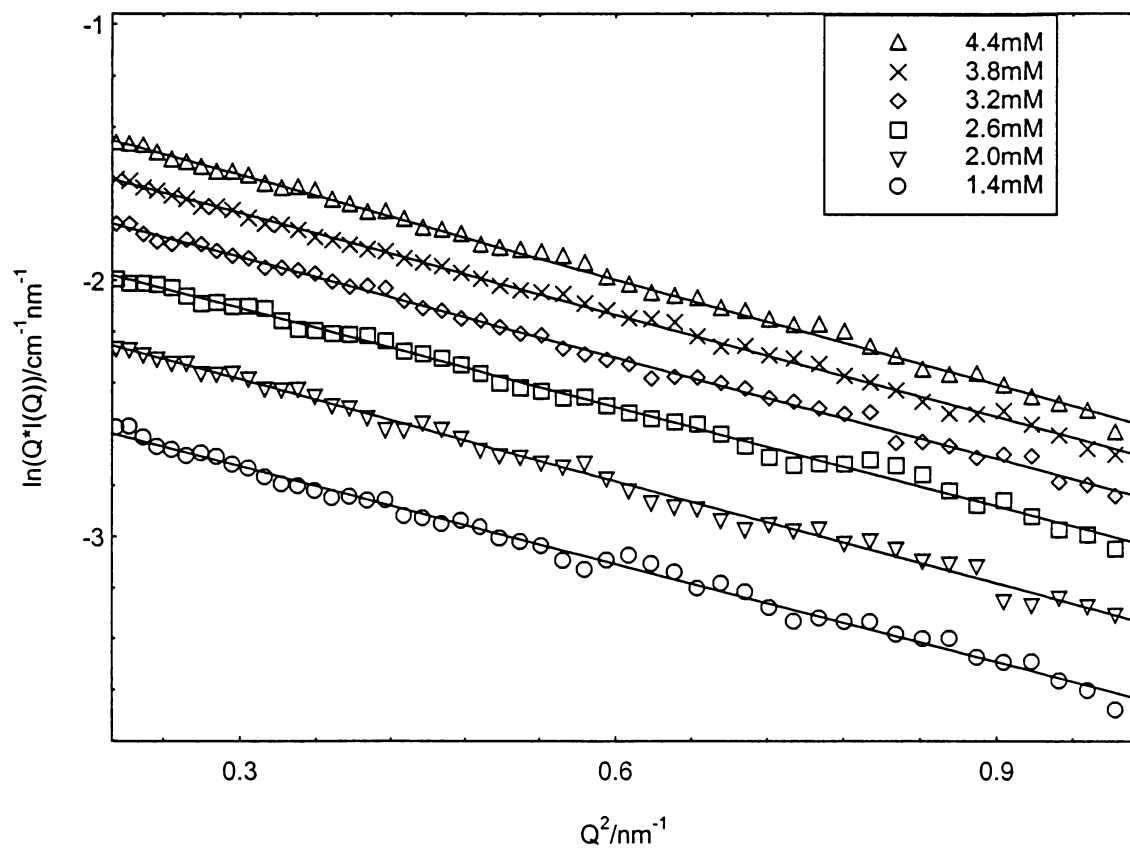


Figure 3.23 Guinier-like plots for CTAB in 0.5M NaBr

Table 3.3 Local micellar structure for CTAB micelles

CTAB in 0.25 M NaBr

CTAB/mM	$R_{g,cs}/nm$	r_{cs}/nm	$N/L \times 10^8/cm^{-1}$	$A_{hg}/\text{\AA}^2$
3.5	1.70 ± 0.01	2.41	2.48 ± 0.02	61.1
5.0	1.70 ± 0.01	2.40	2.46 ± 0.02	61.3
7.5	1.70 ± 0.01	2.41	2.46 ± 0.02	61.6
10.0	1.70 ± 0.01	2.40	2.47 ± 0.02	61.0
	Mean:	2.40	2.47 ± 0.02	61.2

CTAB in 0.25 M NaBr

CTAB/mM	$R_{g,cs}/nm$	r_{cs}/nm	$N/L \times 10^8/cm^{-1}$	$A_{hg}/\text{\AA}^2$
2.4	1.67 ± 0.01	2.358	2.62 ± 0.02	56.46
6.2	1.67 ± 0.01	2.358	2.66 ± 0.02	55.74
	Mean:	2.358	2.64 ± 0.02	56.10

CTAB in 0.50 M NaBr

CTAB/mM	$R_{g,cs}/nm$	r_{cs}/nm	$N/L \times 10^8/cm^{-1}$	$A_{hg}/\text{\AA}^2$
1.4	1.60 ± 0.01	2.263	2.49 ± 0.02	57.01
2.0	1.64 ± 0.01	2.324	2.50 ± 0.02	58.36
2.6	1.61 ± 0.01	2.280	2.50 ± 0.02	57.40
3.2	1.61 ± 0.01	2.280	2.48 ± 0.02	57.83
3.8	1.63 ± 0.01	2.307	2.50 ± 0.02	58.04
4.4	1.64 ± 0.01	2.324	2.51 ± 0.02	58.30
	Mean:	2.296	2.50 ± 0.02	57.82

CTAB in 0.50 M NaBr

CTAB/mM	$R_{g,cs}/nm$	r_{cs}/nm	$N/L \times 10^8/cm^{-1}$	$A_{hg}/\text{\AA}^2$
2.6	1.70 ± 0.01	2.408	2.31 ± 0.02	65.39

CTAB in 1.0 M NaBr, Dec.99

CTAB/mM	$R_{g,cs}/nm$	r_{cs}/nm	$N/L \times 10^8/cm^{-1}$	$A_{hg}/\text{\AA}^2$
2.0	1.81 ± 0.01	2.553	1.93 ± 0.02	83.17
3.2	1.74 ± 0.01	2.466	2.40 ± 0.02	64.45
4.8	1.74 ± 0.01	2.466	2.23 ± 0.02	69.51
	Mean:	2.495	2.19 ± 0.02	72.37

CTAB in 1.0 M NaBr

CTAB/mM	$R_{g,cs}/nm$	r_{cs}/nm	$N/L \times 10^8/cm^{-1}$	$A_{hg}/\text{\AA}^2$
1.3	1.78 ± 0.01	2.514	1.97 ± 0.02	80.20
1.7	1.73 ± 0.01	2.441	1.99 ± 0.02	76.97
2.0	1.70 ± 0.01	2.408	2.11 ± 0.02	71.68
2.3	1.73 ± 0.01	2.449	2.18 ± 0.02	70.73
2.6	1.72 ± 0.01	2.433	2.35 ± 0.02	65.02
3.2	1.71 ± 0.01	2.417	2.38 ± 0.02	63.81
3.8	1.72 ± 0.01	2.425	2.90 ± 0.02	52.52
	Mean:	2.441	2.27 ± 0.02	68.70

* $(\rho_m - \rho_s)^2: 3.71 \times 10^{-21} \text{ cm}^{-4}$

Overall micellar size and flexibility

The full scattering curves were first fit without taking intermicellar interactions into account using Eqn. 2.42-2.44. During the fitting, we vary the micellar r_{cs} , $2l_p$, $\langle L_n \rangle$, and the scaling factor, A , which is equivalent to KcM_w . As in the work on SDS micellar solution, we fixed polydispersity M_w/M_n at 2 ($z = 1$, in the Schulz-Zimm distribution) and the background, (~ 0.06 for NaBr solutions). Because the Q -dependent parameters (r_{cs} , $2l_p$, $\langle L_n \rangle$) can show significant correlation, a grid search method for weighted non-linear least squares fitting was used;⁸³ this involves optimizing the parameters one by one. The grid search cycles through the parameter by parameter optimization repeatedly, until the chi-square for successive cycles is essentially unchanged. Table 3.4 tabulates the results, and a bending rod plot in Figure 3.24 shows the fits to the scattering curves for CTAB in 0.25M NaBr. Figure 3.25 shows the dependence of micellar contour lengths on surfactant concentration at all four NaBr concentrations, c_s . With increasing salt concentration, the micellar size increase more rapidly as the surfactant concentration, c , increases so that the exponent, α , in the scaling relationship, $\langle L_n \rangle \sim c^\alpha$, increases as salt concentration increases. We obtained α values of 0.12 ± 0.01 at 0.25M NaBr; 0.40 ± 0.01 at 0.5M NaBr and 1.11 ± 0.02 at 1.0M NaBr.

The fitted micellar Kuhn lengths are shown in figure 3.26, the Kuhn length also increase as c increase. Since the increases in persistence length with c are apparent, we derived the real Kuhn length by extrapolating to zero surfactant concentration. With increasing c_s , the persistence length, $l_{p,c=0}$, decreases as follows: $174 \pm 9 \text{ \AA}$ at 0.25M; $144 \pm 12 \text{ \AA}$ at 0.5M; and $138 \pm 7 \text{ \AA}$ at 1.0M.

Table 3.4 Fitted parameters for CTAB micelles in aqueous NaBr without/with intermicellar interaction

CTAB in 0.5M NaBr						
[CTAB] /mM	[NaBr] /M	Background	r_{cs} /Å	R_g /Å	$\langle L_n \rangle$ /Å	$\langle 2L_p \rangle$ /Å
1.4	0.5	0.057	21.0±0.2	546	1844±55	317±6
2.0	0.5	0.057	21.3±0.1	656	2316±83	355±6
2.6	0.5	0.057	21.3±0.1	696	2591±87	348±5
3.2	0.5	0.057	21.8±0.1	737	2609±99	396±6
3.8	0.5	0.057	21.8±0.1	824	3107±132	404±5
4.4	0.5	0.057	21.8±0.1	773	2835±109	395±5
CTAB in 1.0M NaBr						
2.0	1.0	0.0552	22.1±0.2	646	2467±92	311±7
3.2	1.0	0.0552	22.6±0.1	1068	4757±337	411±7
4.8	1.0	0.0552	22.7±0.1	1048	4588±284	413±6
CTAB in 0.25M NaBr						
3.5	0.25	0.0552	21.6±0.1	514	1433±36	403±9
5.0	0.25	0.0552	22.0±0.1	531	1481±33	416±8
7.5	0.25	0.0552	22.1±0.1	598	1638±47	481±10
10.0	0.25	0.0552	22.1±0.1	593	1590±45	494±11
CTAB in 1.0M NaBr						
1.3	1.0	0.052	22.6±0.2	636	2358±145	319±9
1.7*	1.0	0.052	22.6±0.2	1230	6813±982	347±9
2.0	1.0	0.052	22.5±0.2	835	3299±226	382±11
2.3	1.0	0.052	22.5±0.4	777	2980±298	371±18
2.6	1.0	0.052	22.6±0.2	1092	4781±410	430±12
3.2	1.0	0.052	22.8±0.2	1404	7392±638	426±9
3.8	1.0	0.052	22.7±0.1	1316	6510±377	436±8
CTAB in 0.25M NaBr						
2.4	0.25	0.052	21.9±0.1	492	1307±41	418±11
6.2	0.25	0.052	22.1±0.1	619	1671±45	511±11
CTAB in 0.50M NaBr						
2.6	0.50	0.052	22.3±0.1	772	2792±92	402±7
CTAB in 0.15M NaBr						
2.0	0.15	0.0560	18.5±0.1	234	421±8	435±27
3.5	0.15	0.0560	19.2±0.1	267	493±9	469±24
5.0	0.15	0.0560	20.0±0.1	294	562±11	474±21
7.5	0.15	0.0560	20.4±0.1	327	654±13	478±18

Table 3.4 (continued)

With interactions

CTAB in 1.0M NaBr Use Kuhn length=272, N/L=2.50							
	X	Mw From Ln	A Scale Factor	Rg	Lc	S(0)	
	1.3	0.086	3.873*10 ⁶	8.8±0.5	576	2231±138	0.910
	1.7	0.196	7.978*10 ⁶	24.6±0.3	883	4595±523	0.812
	2.0	0.149	4.505*10 ⁶	17.3±1.4	631	2595±206	0.851
	2.3	0.170	4.453*10 ⁶	20.06±1.8	626	2565±239	0.833
	2.6	0.210	5.027*10 ⁶	27.9±2.7	673	2895±285	0.800
	3.2	0.377	8.228*10 ⁶	56.9±6.2	899	4738±521	0.684
	3.8	0.487	9.211*10 ⁶	92.0±11.5	960	5305±666	0.621
CTAB in 0.5M NaBr Use Kuhn length=280, N/L =2.49							
	X	Mw From Ln	A Scale Factor	Rg	Lc	S(0)	
	1.4	0.081	3.099*10 ⁶	10.0±0.3	512	1792±49	0.915
	2.0*	0.094	2.398*10 ⁶	11.9±1.1	439	1387±139	0.902
	2.6	0.187	4.086*10 ⁶	24.6±1.0	604	2363±104	0.819
	3.2	0.204	3.496*10 ⁶	25.9±1.4	550	2021±111	0.805
	3.8	0.256	3.759*10 ⁶	33.1±2.1	575	2174±142	0.765
	4.4	0.326	4.244*10 ⁶	43.1±2.7	618	2454±158	0.716
CTAB in 0.5M NaBr Use Kuhn length=280, N/L =2.49							
	2.6	0.191	4.209*10 ⁶	26.4±1.6	615	2434±148	0.815
CTAB in 0.25M NaBr Use Kuhn length=367, N/L =2.46							
	X	Mw From Ln	A Scale Factor	Rg	Lc	S(0)	
	3.5	0.294	3.099*10 ⁶	26.3±0.7	588	1886±55	0.738
	5.0	0.486	3.989*10 ⁶	45.2±1.3	654	2254±67	0.622
	7.5	0.991	5.677*10 ⁶	100±5.0	825	3322±170	0.429
	10.0	1.661	7.639*10 ⁶	181±11.0	983	4471±272	0.294
CTAB in 0.25M NaBr Use Kuhn length=367, N/L=2.46							
	2.4	0.162	2.486*10 ⁶	15.0±0.5	501	1455±45	0.840
	6.2	0.686	4.527*10 ⁶	71.3±3.6	721	2649±134	0.531

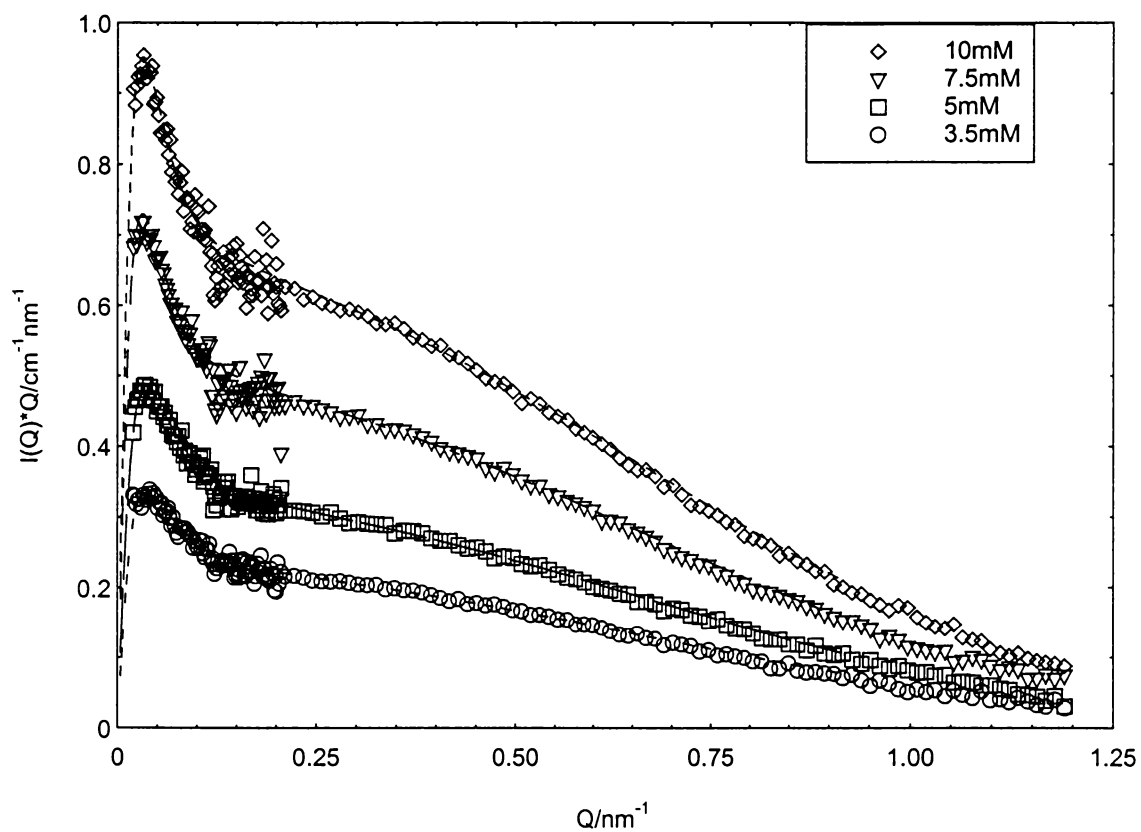


Figure 3.24. Bending rod plots of SANS data for CTAB with fits in 0.25M NaBr without taking intermicellar interactions into account

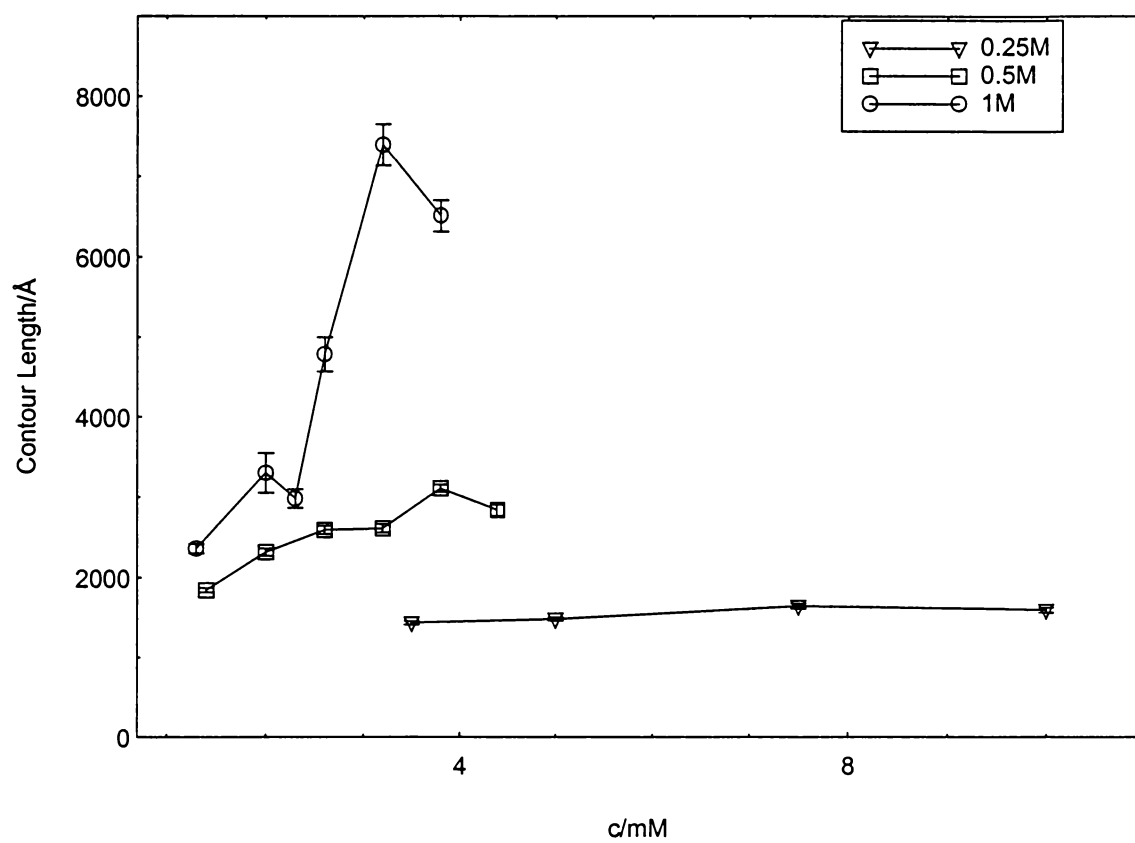


Figure 3.25 Dependence of micellar contour lengths on CTAB concentrations in different NaBr solutions

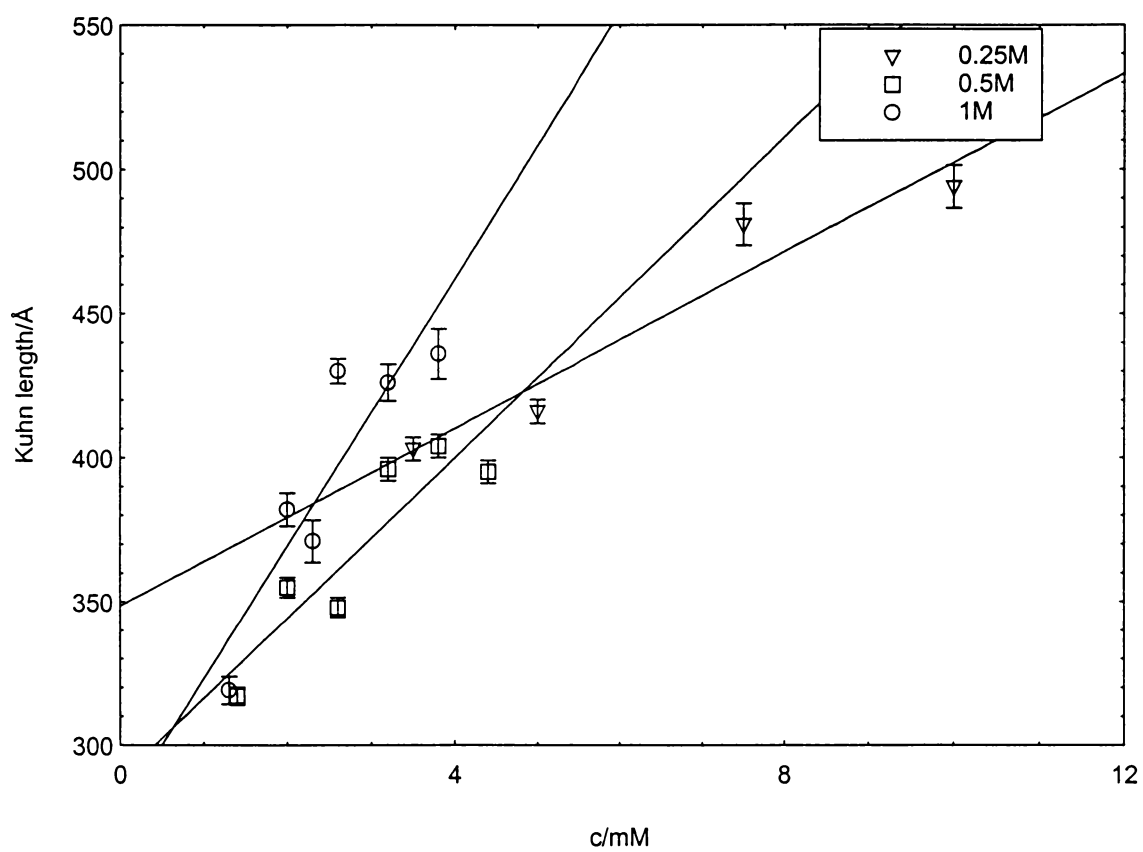


Figure 3.26 Dependence of micellar Kuhn lengths on CTAB concentrations in different NaBr solutions

To take the intermicellar interactions into account, we tried to fit the scattering data using Eqn. 2.48-2.51. As in the work on SDS, allowing the persistence length to vary gives physically unreasonable fits. Thus we fixed the persistence length to the extrapolated value, $l_{p,c=0}$. The micellar cross sectional radii was also fixed to the result from the fits without interaction. The only parameters varied are the contour length and A. Results of the fits are found in Table 3.4 and Figure 3.27-29. We observed that the results of the fits are poorer than in the SDS case, especially in the intermediate Q region at higher salt concentration.

In chapter I, we have introduced the overlap concentration c^* , above which the micelles start to overlap and entangle. Above c^* , the scattering curves should not be analyzed to obtain the dimensions of individual micelles. Instead, the scattering reports on the mesh size of the network. Using eqn 1.5, c^* can be calculated. We want to check whether any of our CTAB micellar solutions are at $c > c^*$ by using the result from the fits with and without intermicellar interactions. For the fits without inclusion of intermicellar interactions, M_w of the micelles can be obtained by calculation from N/L (the mean value of four concentrations was used, = 24.0 monomer/nm), $\langle L_n \rangle$ and the monomer molecular weight using $M_w = N/L \cdot \langle L_w \rangle \cdot 364.46 \text{ g/mol}$, where $\langle L_w \rangle = 2 \cdot \langle L_n \rangle$. At all three salt concentrations, we pick the micellar dimensions at the the highest surfactant concentration studied and estimate the c^* .

For 3.8mM CTAB in 1M NaBr, $M_w = 1.14 \times 10^7 \text{ g/mol}$ and $R_g = 131.6 \text{ nm}$, a c^* of 5.5mM is predicted; for 4.4mM CTAB in 0.5M NaBr, $M_w = 4.96 \times 10^6 \text{ g/mol}$ and $R_g = 77.3 \text{ nm}$, a c^* of 11.6mM is predicted; for 10.0mM CTAB in 0.25M NaBr, $M_w = 2.78 \times 10^6$

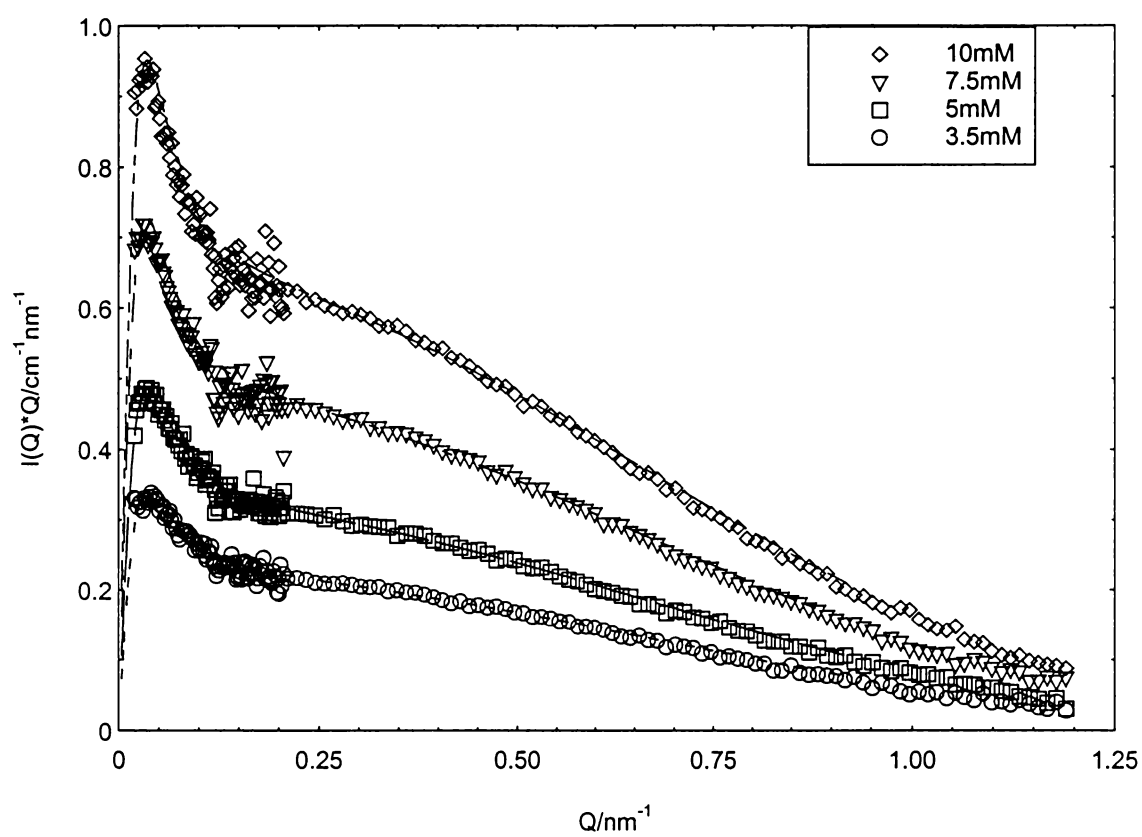


Figure 3.27 Bending rod plots of SANS data for CTAB with fits in 0.25M NaBr taking intermicellar interactions into account

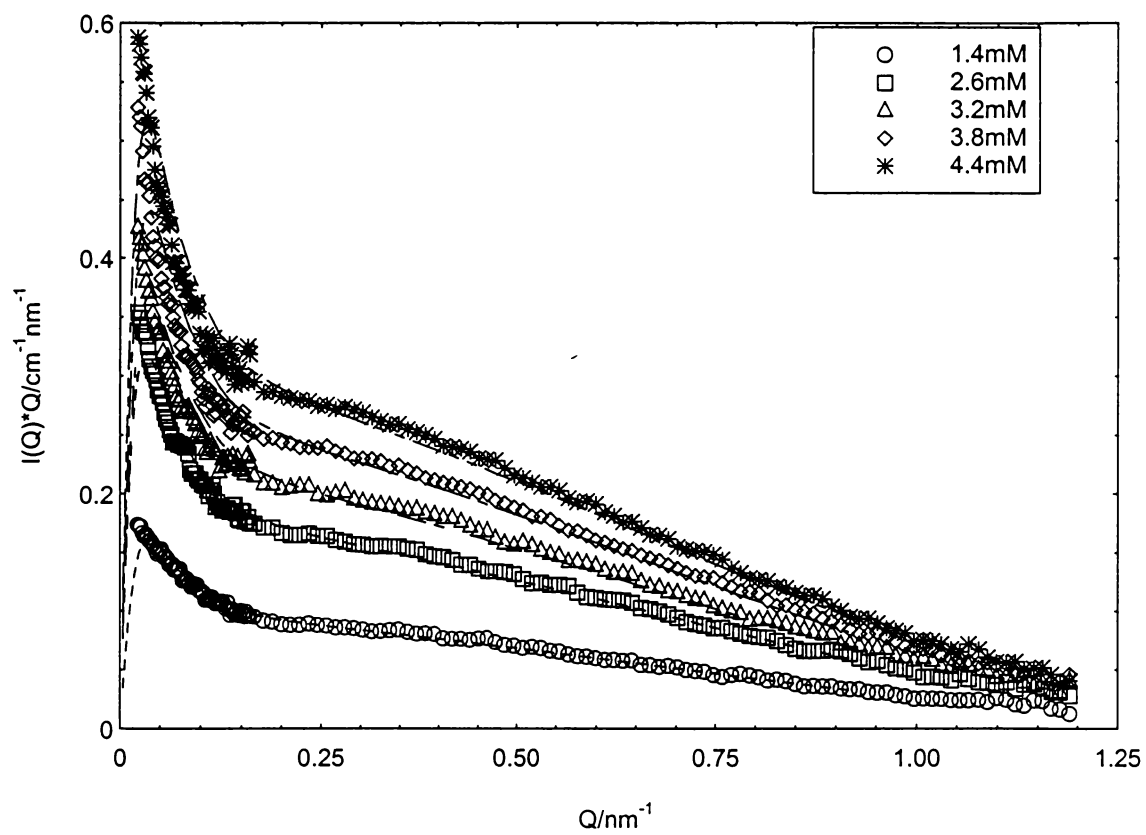


Figure 3.28. Bending rod plots of SANS data for CTAB with fits in 0.50M NaBr taking intermicellar interactions into account

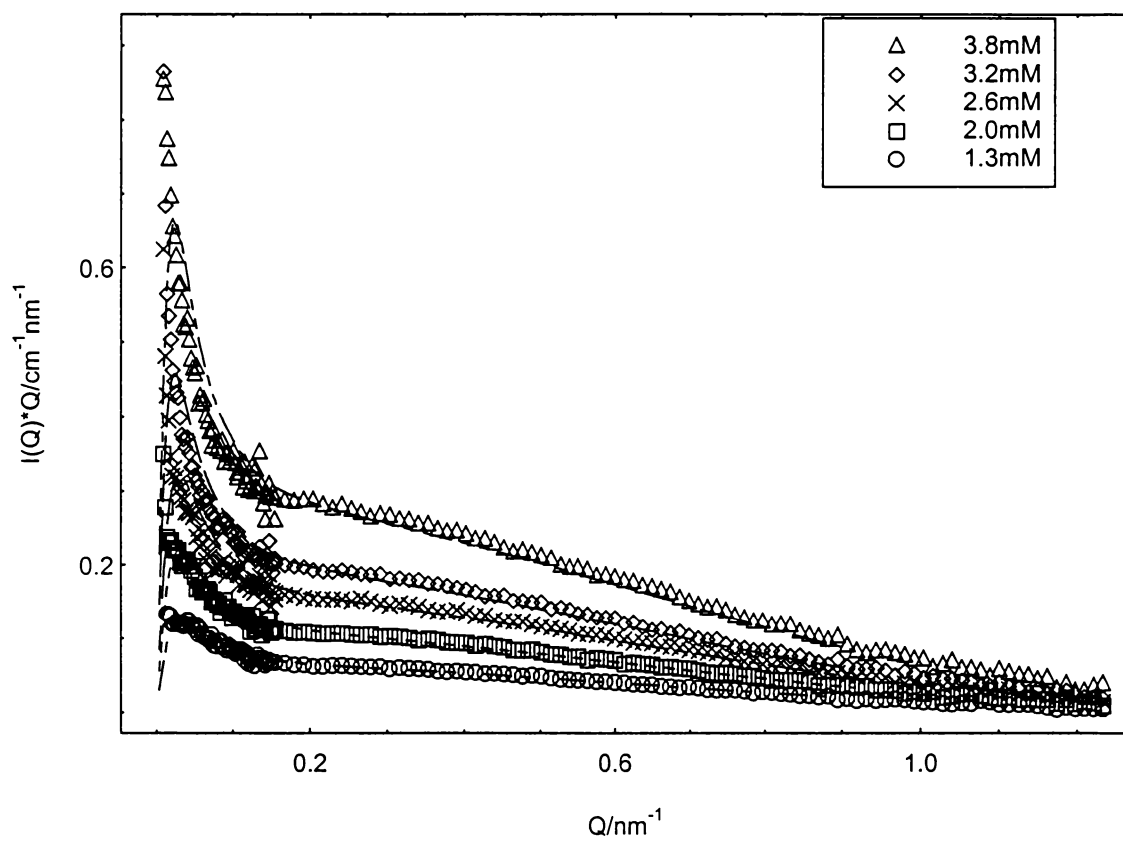


Figure 3.29 Bending rod plots of SANS data for CTAB with fits in 1.0M NaBr taking intermicellar interactions into account

g/mol and $R_g = 59.3\text{nm}$, a c^* of 15.0mM is predicted. A similar calculation directly using the results from the fits in which intermicellar interactions were taken into account was also performed. For 3.8mM CTAB in 1M NaBr, $M_w = 9.21 \times 10^6$ g/mol and $R_g = 96.0\text{nm}$, a c^* of 6.8mM is predicted; for 4.4mM CTAB in 0.5M NaBr, $M_w = 4.24 \times 10^6$ g/mol and $R_g = 61.8\text{nm}$, a c^* of 12mM is predicted; for 10.0mM CTAB in 0.25M NaBr, $M_w = 7.64 \times 10^6$ g/mol and $R_g = 98.3\text{nm}$, a c^* of 5mM is predicted. Comparing with these results with the experimental results for the contour lengths in Figure 3.25, the prediction using the result without taking intermicellar interactions into account seems more reasonable, and we did not observe a c^* crossover in the concentration studied.

3.3.2 Detailed TTAB micellar structure

Local micellar structure

TTAB micelles in 1.5M and 3.0M NaBr were studied using SANS. Information about the local micellar structure was obtained from Guinier-like plots, with fitting in the region $0.20\text{nm}^{-2} < Q < 1\text{nm}^{-2}$ according to eqn. 2.52. The results are tabulated in Table 3.5. Figure 3.30 gives the Guinier-like plots for TTAB in 1.5M NaBr. The mean value of the cross-sectional radii r_{cs} is 2.08nm for 1.5M NaBr and 2.01nm for 3.0M NaBr. Fits of the full scattering curves give values 1.93nm and 2.01nm for 1.5M and 3.0M , respectively. These numbers are very close to the extended length of the C_{14} hydrocarbon chain, 1.98nm . The resulting N/L's obtained from the plots' intercepts as previously described and the derived A_{hg} 's are also in Table 3.5. Similar values of N/L were obtained for the micelles in 1.5M NaBr and 3.0M NaBr, indicating that the local

Table 3.5 Local micellar structure for TTAB micelles

TTAB in 3.0 M NaBr

[TTAB]/mM	$R_{g,cs}/nm$	r_{cs}/nm	$N/L \times 10^8/cm^{-1}$	$A_{hg}/\text{\AA}^2$
2.6	1.58 ± 0.01	2.227	2.08 ± 0.02	67.28
3.8	1.54 ± 0.01	2.173	2.06 ± 0.02	66.26
4.8	1.56 ± 0.01	2.200	2.09 ± 0.02	66.01
6.2	1.56 ± 0.01	2.200	2.06 ± 0.02	67.07
7.8	1.53 ± 0.01	2.163	2.09 ± 0.02	65.19

TTAB in 1.5 M NaBr

[TTAB]/mM	$R_{g,cs}/nm$	r_{cs}/nm	$N/L \times 10^8/cm^{-1}$	$A_{hg}/\text{\AA}^2$
3.5	1.52 ± 0.01	2.145	1.98 ± 0.02	67.93
4.8	1.51 ± 0.01	2.135	2.01 ± 0.02	66.69
6.2	1.51 ± 0.01	2.135	2.02 ± 0.02	66.42
7.8	1.50 ± 0.01	2.126	2.00 ± 0.02	66.75
10.5	1.50 ± 0.01	2.126	2.02 ± 0.02	66.06
12.5	1.51 ± 0.01	2.135	2.04 ± 0.02	65.76

* $(\rho_m - \rho_s)^2: 3.63 \times 10^{-21} \text{ cm}^{-4}$

packing of the surfactant, or the local micellar structure, is at most slightly dependent on NaBr concentration.

Overall micellar size and flexibility

The full scattering curves were first fit without taking intermicellar interactions into account using eqn. 2.42-2.44. During the fitting, we vary the micellar r_{cs} , $2l_p$, $\langle L_n \rangle$, and the scaling factor, A. We fixed the polydispersity $M_w/M_n = 2$ ($z = 1$) and the background, (~ 0.06 for NaBr solutions). Table 3.6 tabulates the results, and bending rod plots in Figure 3.31 and 3.32 show fits to the scattering curves for TTAB in 1.5M and 3.0M NaBr respectively.

The contour lengths obtained from the fits are plotted in Figure 3.33. With increasing salt concentration, the micellar size increases more rapidly as the surfactant concentration, c , increases. The exponent, α , in the scaling relationship, $\langle L_n \rangle \sim c^\alpha$, is 0.22 ± 0.01 at 1.5M NaBr and 0.48 ± 0.01 at 3.0M NaBr.

The fitted micellar Kuhn lengths are shown in Figure 3.34. The apparent Kuhn lengths also increase as surfactant concentration (c) increases. At each c_s , the real Kuhn length, $l_{p,c=0}$, can be derived by extrapolating to $c = 0$. With increasing c_s , the persistence length, $l_{p,c=0}$, decreases as follows: $141 \pm 7 \text{ \AA}$ at 1.5M and $124 \pm 6 \text{ \AA}$ at 3.0M NaBr.

To take the intermicellar interactions into account, we tried to fit the scattering data using Eqn. 2.48-2.51. As before, we fixed the persistence length of the micelles at $l_{p,c=0}$. The micellar cross sectional radii were also fixed to the value obtained from Guinier-like plots. The only parameters varied are contour length and A. Results of the fits are found in Table 3.6 and Figure 3.35-36. We observed that the results of the fits are quite poor in all Q regions at these two salt concentrations. This indicates that further improvements in

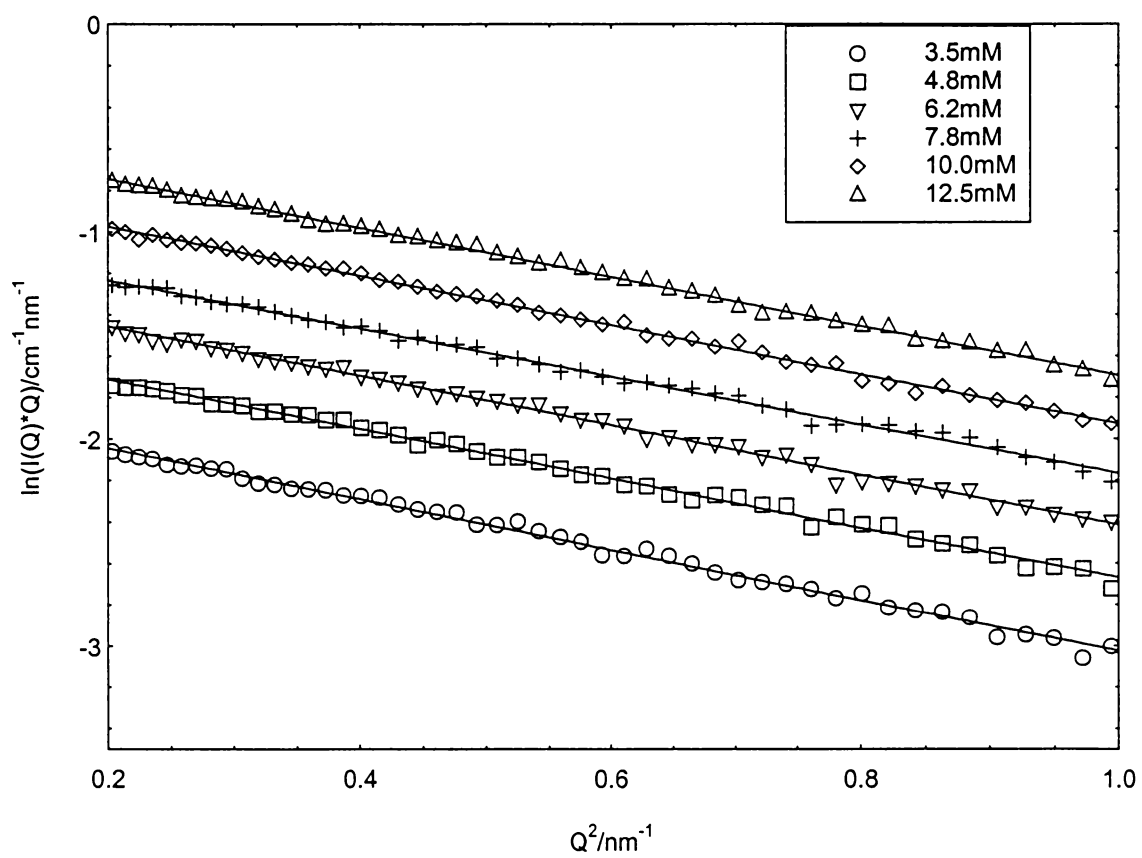


Figure 3.30 Guinier-like plots for TTAB in 1.5M NaBr aqueous solutions

Table 3.6 Fitted parameters for TTAB micelles in aqueous NaBr without/with intermicellar interaction

TTAB in 3.0M NaCl						
[TTAB] /mM	[NaBr] /M	Background	r_{cs} /Å	R_g /Å	$\langle L_n \rangle$ /Å	$\langle 2L_p \rangle$ /Å
2.6	3.0	0.061	19.9±0.2	435	1361±22	283±5
3.8	3.0	0.061	20.2±0.2	552	1833±51	327±6
4.8	3.0	0.061	20.0±0.2	564	1914±42	324±4
6.2	3.0	0.061	20.2±0.1	620	2134±53	348±4
7.8	3.0	0.061	20.2±0.1	636	2103±51	380±5
TTAB in 1.5M NaCl						
3.5	1.5	0.0566	19.3±0.2	324	814±13	303±7
4.8	1.5	0.0566	19.1±0.2	332	836±10	308±5
6.2	1.5	0.0566	19.3±0.2	375	985±14	323±6
7.8	1.5	0.0566	19.6±0.1	389	1001±14	348±6
10.0	1.5	0.0566	19.2±0.1	384	980±13	349±6
12.5	1.5	0.0566	19.4±0.2	411	1081±18	355±7

With intermicellar interaction

TTAB in 3.0M NaBr Use Kuhn length=247, N/L =2.054						
[TTAB] /mM	X	Mw	A	R_g /Å	$\langle L_n \rangle$ /Å	S(0)
2.6	0.110	1.523*10 ⁶	8.8±0.5	373	1156±68	0.887
3.8	0.178	1.726*10 ⁶	14.7±1.2	403	1311±115	0.826
4.8	0.245	1.915*10 ⁶	20.9±1.9	429	1454±138	0.774
6.2	0.319	1.941*10 ⁶	27.3±3.0	433	1473±168	0.721
7.8	0.393	1.887*10 ⁶	34.2±4.0	426	1433±176	0.674

With intermicellar interaction

TTAB in 1.5M NaCl Use Kuhn length=284, N/L =2.012						
[TTAB] /mM	X	Mw	A	R_g /Å	$\langle L_n \rangle$ /Å	S(0)
3.5	0.123	0.986*10 ⁶	7.7±0.4	304	765±40	0.874
4.8	0.183	1.076*10 ⁶	11.8±0.6	322	835±47	0.822
6.2	0.292	1.368*10 ⁶	19.5±1.9	374	1061±76	0.740
7.8	0.379	1.423*10 ⁶	25.8±2.2	383	1103±96	0.682
10.0	0.562	1.688*10 ⁶	39.0±3.6	425	1309±123	0.584
12.5	0.863	2.166*10 ⁶	63.3±9.8	495	1679±266	0.467

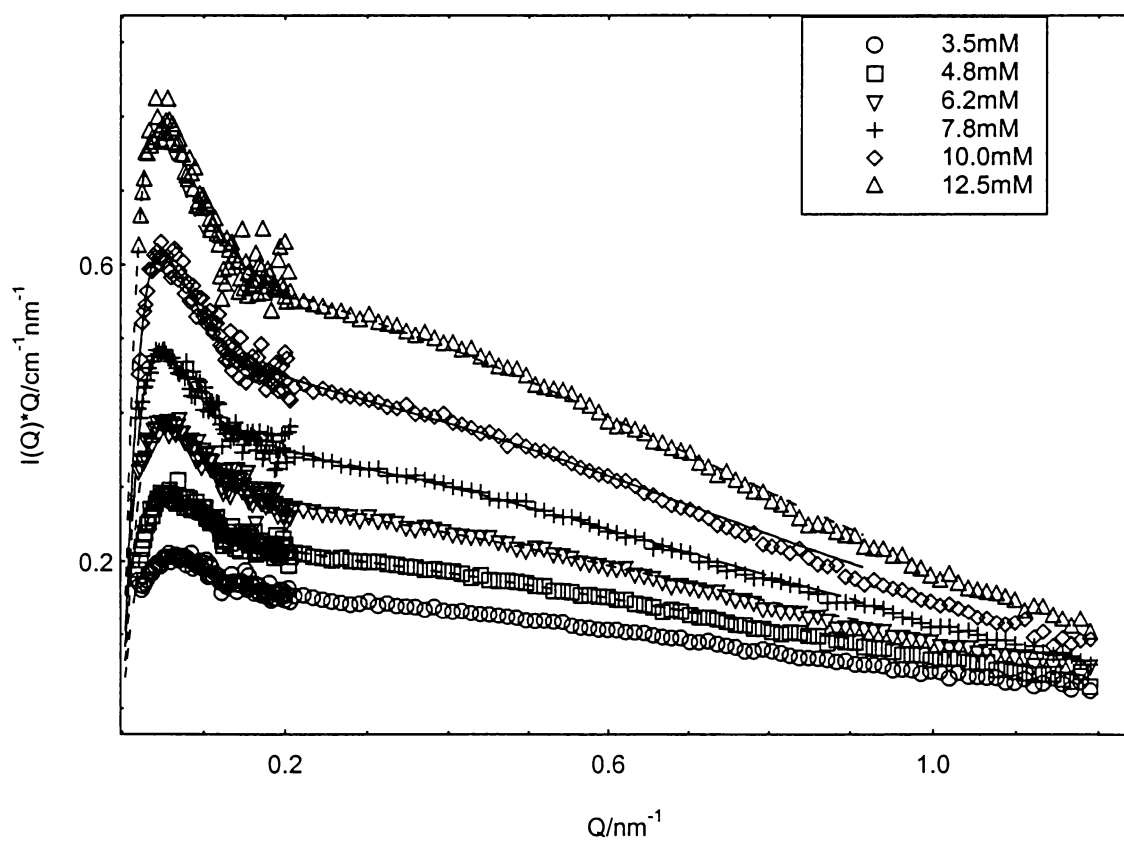


Figure 3.31 Bending rod plots of SANS data for TTAB with fits in 1.5M NaBr without taking intermicellar interactions into account

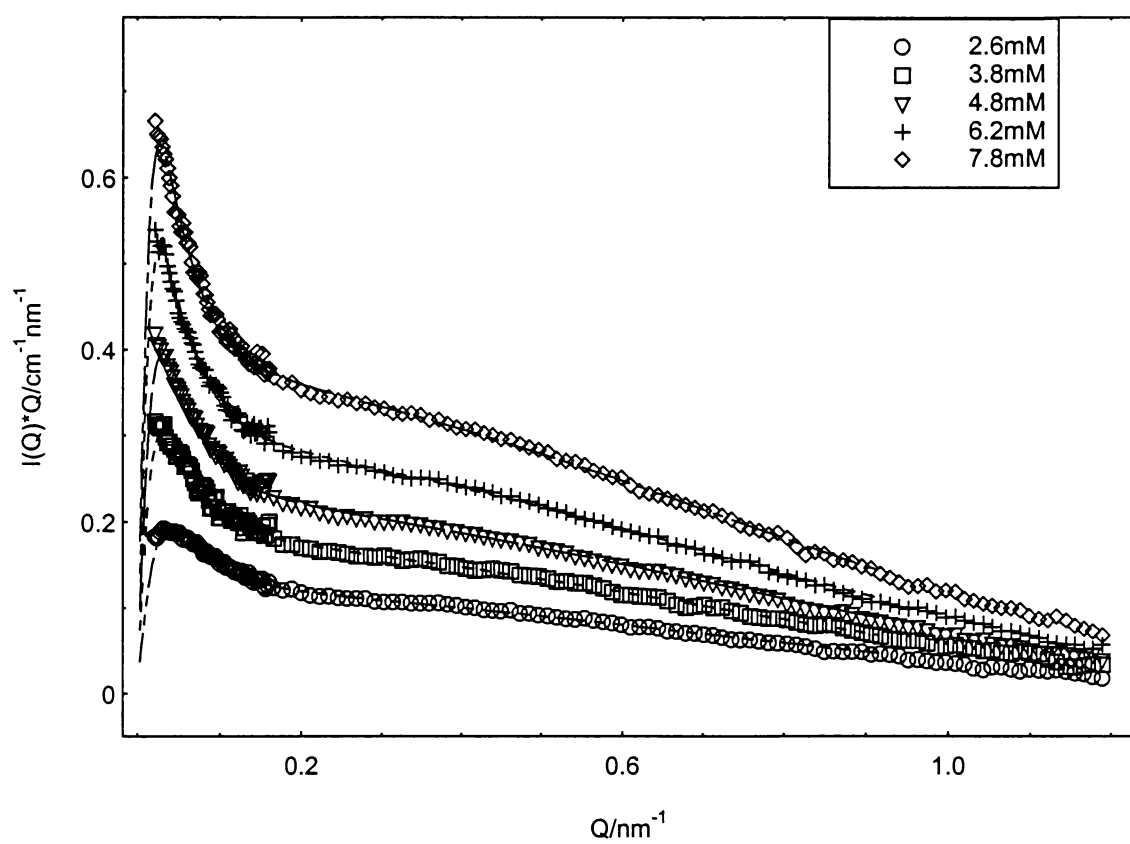


Figure 3.32 Bending rod plots of SANS data for TTAB with fits in 3.0M NaBr without taking intermicellar interactions into account

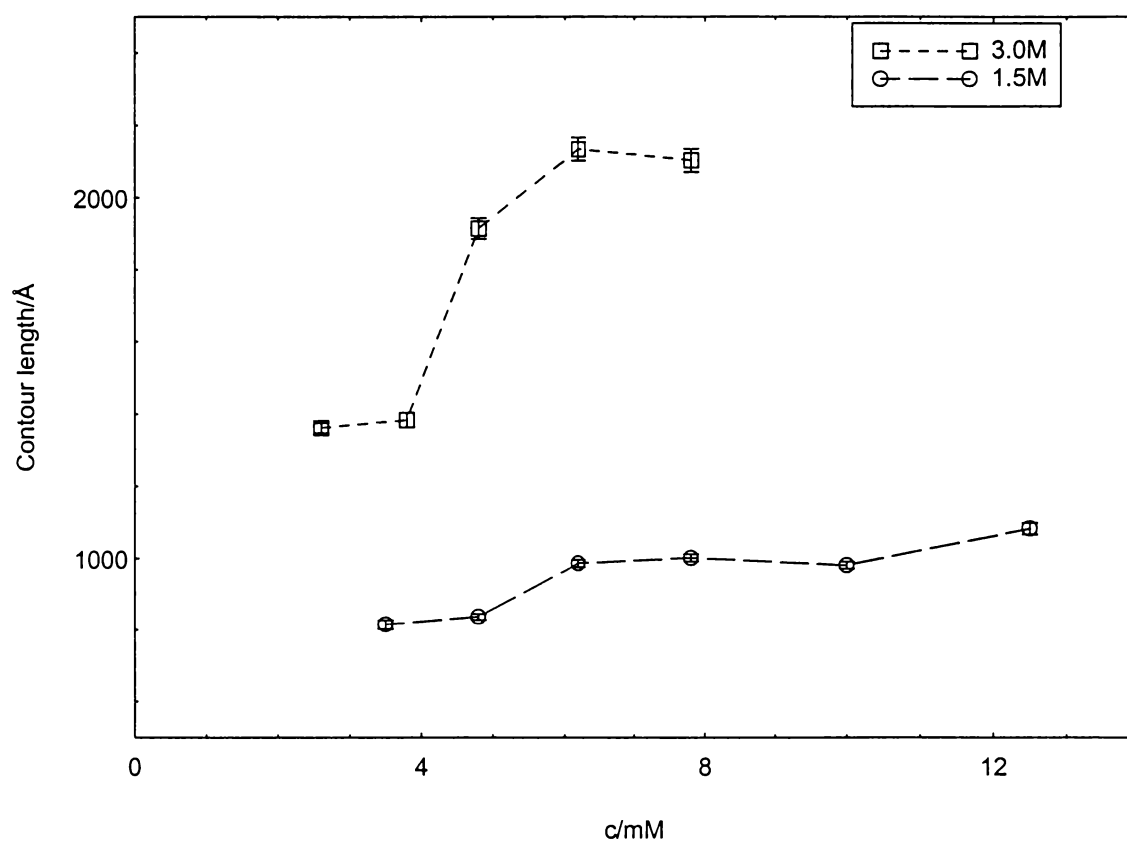


Figure 3.33 Dependence of micellar contour lengths on TTAB concentrations in different NaBr solutions

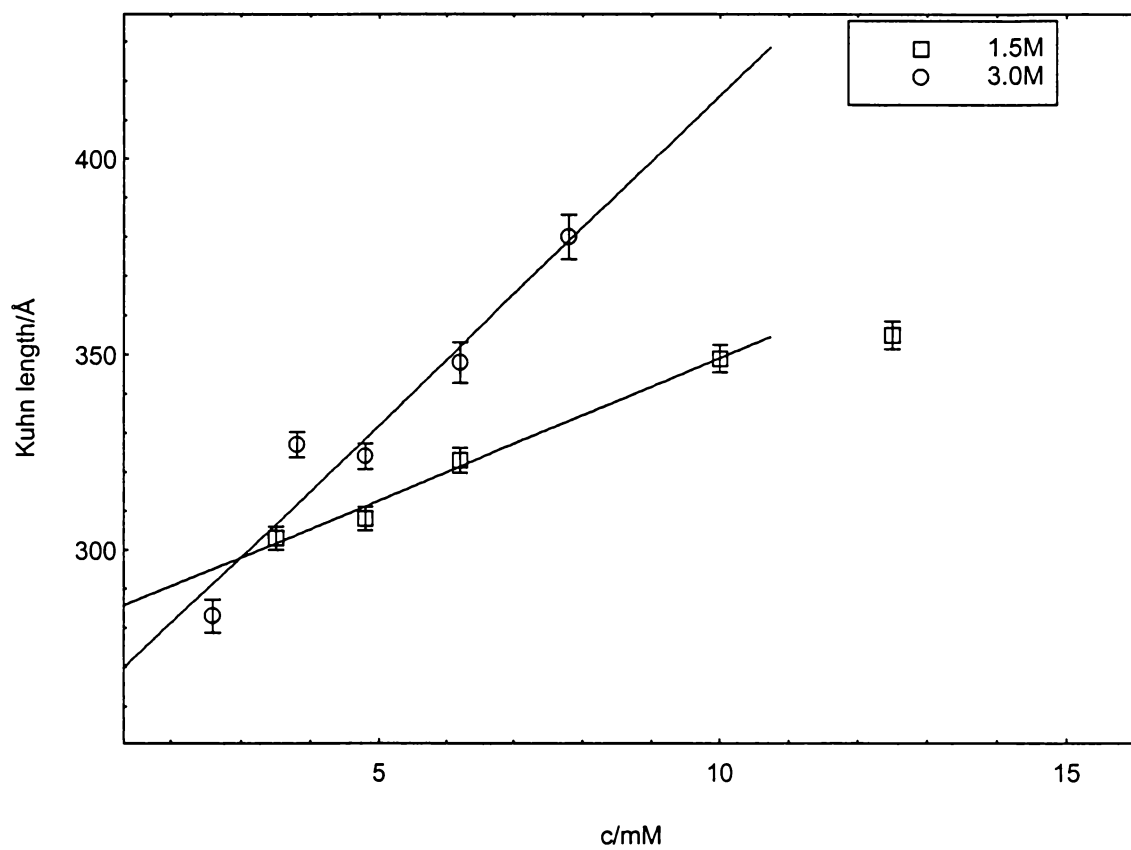


Figure 3.34 Dependence of micellar Kuhn length on TTAB concentrations in different NaBr solutions

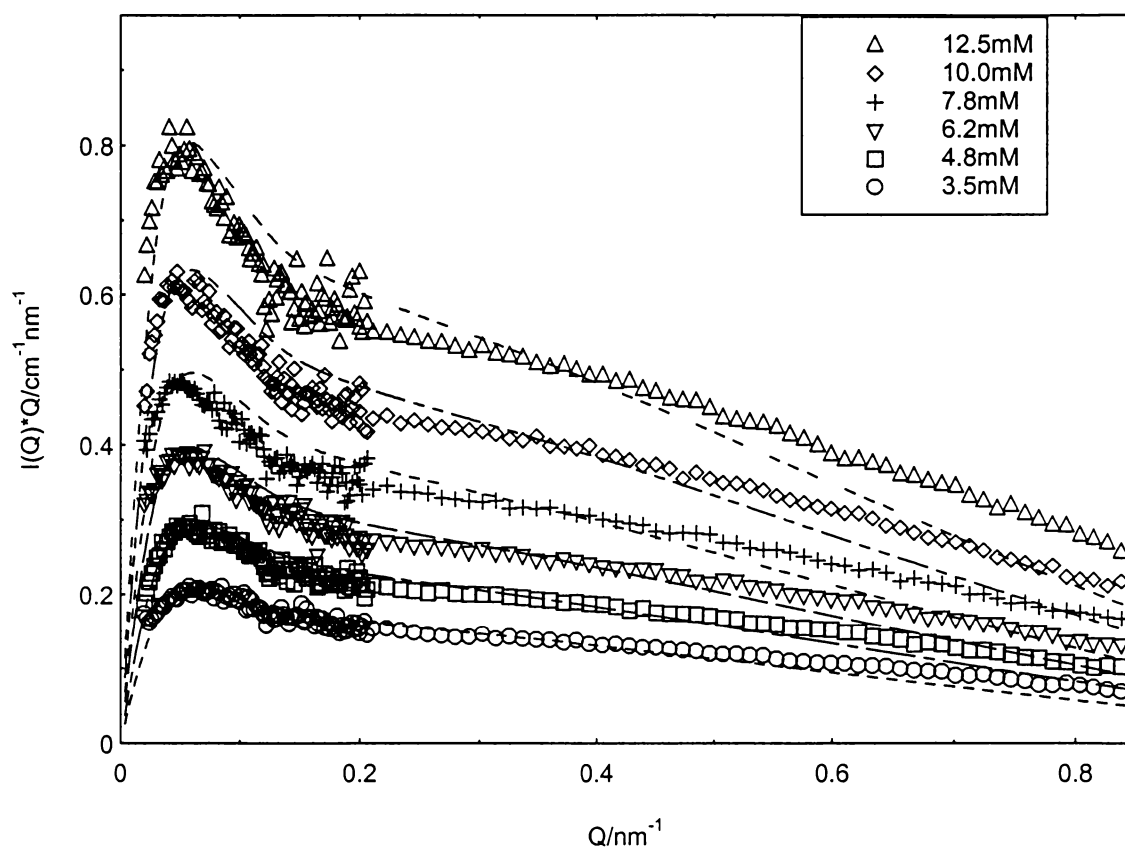


Figure 3.35 Bending rod plots of SANS data for TTAB with fits in 1.5M NaBr taking intermicellar interactions into account

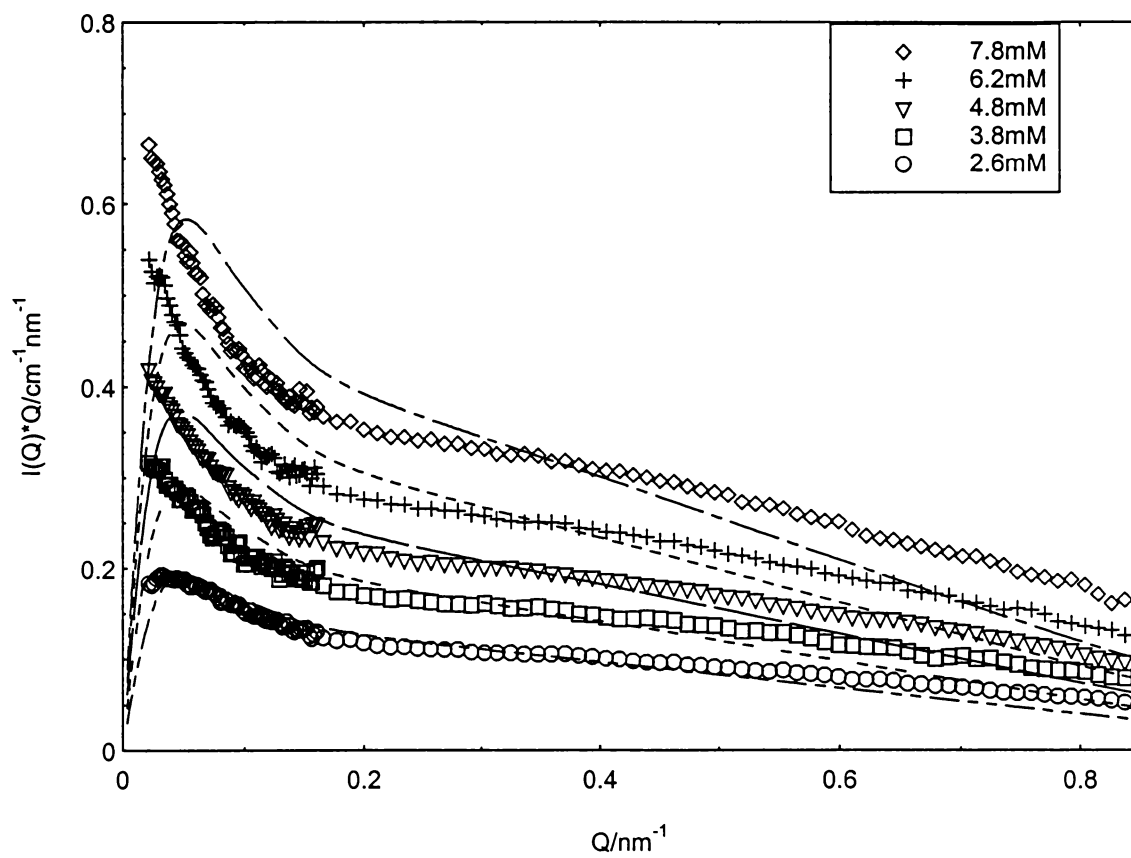


Figure 3.36 Bending rod plots of SANS data for TTAB with fits in 3.0M NaBr taking intermicellar interactions into account

the Pedersen/Schurtenberger model for interactions between wormlike micelles are needed.

Values of c^* for the TTAB micelles were determined in the same way as described for the CTAB micelles. We used the results of the fits without taking intermicellar interaction into account, the mean value of N/L from Guinier-like plots of $20.5 \text{ monomer} \cdot \text{nm}^{-1}$, the $\langle L_n \rangle$'s from the fits without intermicellar interaction, and the TTAB molecular weight of 336 g/mol . For 12.5 mM TTAB in 1.5 M NaBr, we obtain $M_w = 1.49 \times 10^6 \text{ g/mol}$ and $R_g = 41.1 \text{ nm}$. Thus c^* is 25 mM . For 7.8 mM TTAB in 3.0 M NaBr, $M_w = 2.90 \times 10^6 \text{ g/mol}$ and $R_g = 63.6 \text{ nm}$, giving a c^* value of 13.5 mM . In both cases, c^* s were not reached in our experiments.

3.3.3 Detailed CPyBr micellar structure

Micelles of CPyBr were studied by SANS in solutions containing 0.25 M , 0.5 M and 0.8 M NaBr. As before, we obtain micellar cross-sectional radii r_{cs} for all salt concentrations from the slopes of Guinier-like plots in the region $0.20 \text{ nm}^{-2} < Q < 1 \text{ nm}^{-2}$. Figure 3.37 show the plots of CPyBr micelles in 0.5 M salt, and the results are tabulated in Table 3.7. For 0.25 M NaBr, the mean value of the cross-sectional radius is 2.24 nm ; values of 2.30 nm and 2.22 nm were found at 0.5 M and 0.8 M NaBr, respectively. Fits of the full scattering curves give values for the cross-sectional radius close to the length, 2.23 nm , of an extended C_{16} hydrocarbon chain. Values of N/L were derived from the plots' intercepts by using the micellar contrast term calculated only on the basis of the contrast between the hydrocarbon chain and the solvents, and the resulting N/L 's and the derived A_{hg} 's are also tabulated in Table 3.7. No effect of salt concentration on the value

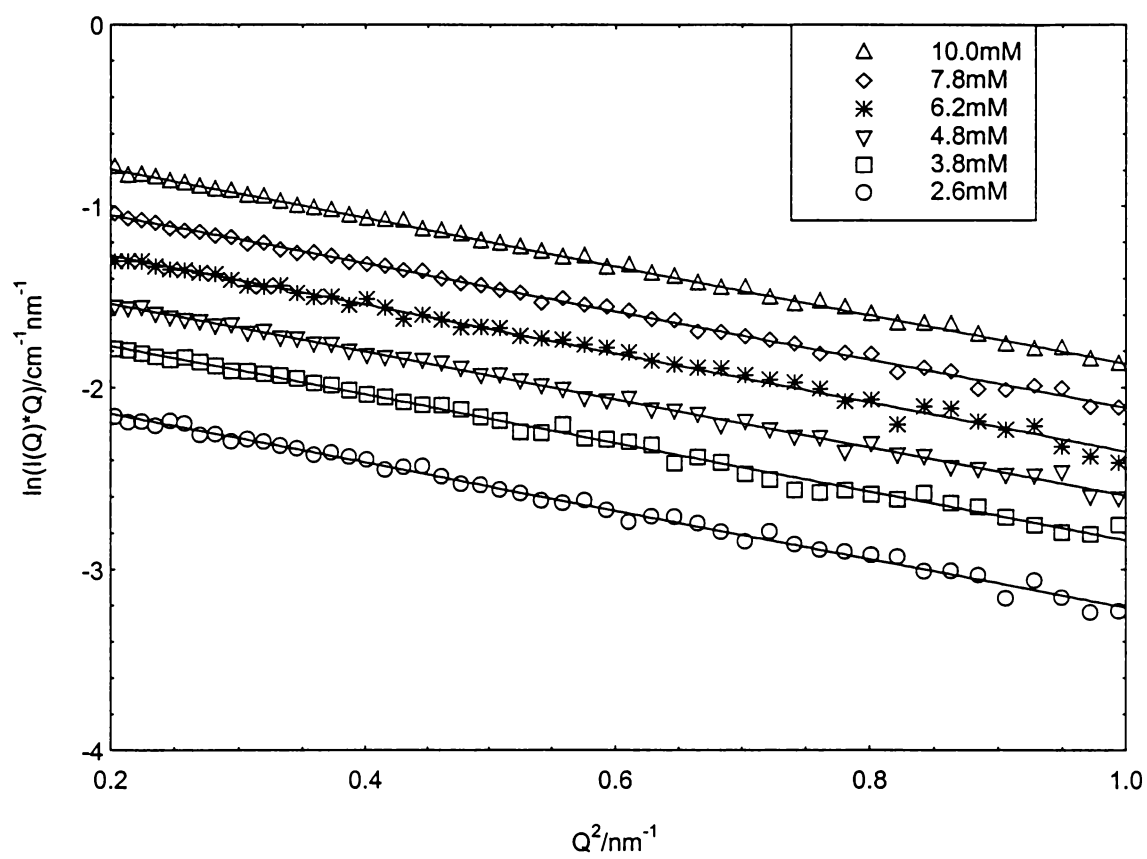


Figure 3.37 Guinier-like plots for CPyBr in 0.5M NaBr solutions

Table 3.7 Local micellar structures for CPyBr micelles

CPyBr in 0.80 M NaBr				
[CPyBr] mM	$R_{g,cs}/nm$	r_{cs}/nm	$N/L \times 10^8/cm^{-1}$	$A_{hg}/\text{\AA}^2$
1.04	1.49 ± 0.01	2.107	2.31 ± 0.02	57.34
1.28	1.49 ± 0.01	2.107	2.29 ± 0.02	57.79
1.52	1.50 ± 0.01	2.126	2.29 ± 0.02	58.41
1.92	1.52 ± 0.01	2.154	2.30 ± 0.02	58.79
3.12	1.56 ± 0.01	2.209	2.31 ± 0.02	60.03
CPyBr in 0.80 M NaBr				
[CPyBr] mM	$R_{g,cs}/nm$	r_{cs}/nm	$N/L \times 10^8/cm^{-1}$	$A_{hg}/\text{\AA}^2$
2.5	1.67 ± 0.01	2.358	2.20 ± 0.02	67.25
3.1	1.65 ± 0.01	2.332	2.21 ± 0.02	66.18
4.0	1.66 ± 0.01	2.341	2.18 ± 0.02	67.44
CPyBr in 0.50 M NaBr				
[CPyBr] mM	$R_{g,cs}/nm$	r_{cs}/nm	$N/L \times 10^8/cm^{-1}$	$A_{hg}/\text{\AA}^2$
2.6	1.64 ± 0.01	2.324	2.18 ± 0.02	66.89
3.8	1.64 ± 0.01	2.324	2.16 ± 0.02	67.54
4.8	1.63 ± 0.01	2.307	2.15 ± 0.02	67.28
6.2	1.65 ± 0.01	2.332	2.19 ± 0.02	67.07
7.8	1.63 ± 0.01	2.307	2.17 ± 0.02	66.80
10.0	1.64 ± 0.01	2.315	2.18 ± 0.02	66.85
CPyBr in 0.50 M NaBr				
[CPyBr] mM	$R_{g,cs}/nm$	r_{cs}/nm	$N/L \times 10^8/cm^{-1}$	$A_{hg}/\text{\AA}^2$
2.6	1.59 ± 0.02	2.245	2.30 ± 0.02	61.48
3.8	1.60 ± 0.01	2.263	2.32 ± 0.02	61.32
4.8	1.61 ± 0.01	2.280	2.33 ± 0.02	61.40
CPyBr in 0.25 M NaBr				
[CPyBr] mM	$R_{g,cs}/nm$	r_{cs}/nm	$N/L \times 10^8/cm^{-1}$	$A_{hg}/\text{\AA}^2$
2.4	1.58 ± 0.01	2.227	2.25 ± 0.02	62.22
3.5	1.60 ± 0.01	2.263	2.23 ± 0.02	63.68
4.8	1.59 ± 0.01	2.245	2.24 ± 0.02	62.91
6.2	1.61 ± 0.01	2.272	2.29 ± 0.02	62.40
7.8	1.59 ± 0.01	2.254	2.27 ± 0.02	62.38
10.5	1.60 ± 0.01	2.263	2.31 ± 0.02	61.65
13.0	1.59 ± 0.01	2.254	2.28 ± 0.02	62.00

* $(\rho_m - \rho_s)^2$: $3.75 \times 10^{-21} \text{ cm}^{-4}$

of N/L indicates that the local packing of the surfactant, or the local micellar structure, is independent of NaBr concentration over the range from 0.25 to 0.8M NaBr.

As before, the fits of the full scattering curves were first performed without taking intermicellar interactions into account using eqn. 2.42-2.44. The polydispersity of the micellar system are fixed ($z=1$) and the value of scattering from solvent was also fixed. A grid search method for weighted non-linear least squares fitting was also used here. Table 3.8 tabulates the results, and bending rod plots in Figure 3.38-3.40 for CPyBr micelles in 0.25M, 0.5M and 0.8M are shown together with fits.

The contour lengths from the fits are shown in Figure 3.41, and they increase with surfactant concentration all three NaBr concentrations, c_s . With increasing salt concentration, the micellar size increases more rapidly as the surfactant concentration, c , increases. The exponent, α , in the scaling relationship, $\langle L_n \rangle \sim c^\alpha$, has values of 0.33 ± 0.02 for 0.25M NaBr, 0.34 ± 0.02 for 0.5M NaBr and 0.45 ± 0.03 for 0.8M NaBr.

The fitted micellar Kuhn lengths are shown in Figure 3.42, and the apparent Kuhn length also increases as surfactant concentration (c) increase. At each c_s , the real Kuhn length, $l_{p,c=0}$, can be derived from the extrapolating to $c = 0$. With increasing c_s , the persistence length, $l_{p,c=0}$, decreases as follows: $144 \pm 8\text{\AA}$ at 0.25M NaBr; $126 \pm 6\text{\AA}$ at 0.5M NaBr and $96 \pm 5\text{\AA}$ at 0.8M NaBr.

To take the intermicellar interactions into account, we tried to fit the scattering data using eqn. 2.48-2.51. We fixed the persistence length of the micelles at $l_{p,c=0}$. The micellar cross sectional radii were also fixed to the value obtained from the Guinier-like plots. The only parameters varied are contour length and A . Results of the fits are

Table 3.8 Fitted parameters for CPyBr micelles in aqueous NaBr without/with intermicellar interaction

CPyBr in 0.8M NaBr						
[CPyBr] /mM	[NaBr] /M	Background	r_{cs} /Å	R_g /Å	$\langle L_n \rangle$ /Å	$\langle 2L_p \rangle$ /Å
1.04	0.8	0.056	18.5±0.4	413	1414±42	234±7
1.28	0.8	0.056	18.4±0.3	377	1210±26	237±6
1.52	0.8	0.056	19.3±0.2	433	1461±32	251±5
1.92	0.8	0.056	19.8±0.2	492	1713±35	271±5
3.12	0.8	0.056	20.3±0.2	588	2096±56	313±5
CPyBr in 0.8M NaBr						
2.5	0.8	0.0552	20.7±0.2	602	2261±71	296±6
3.1	0.8	0.0552	20.7±0.2	688	2789±98	303±5
4.0	0.8	0.0552	21.3±0.2	860	3768±199	339±5
CPyBr in 0.5M NaBr						
2.6	0.5	0.0552	20.3±0.5	519	1716±96	309±14
3.8	0.5	0.0552	20.6±0.2	578	2053±49	310±5
4.8	0.5	0.0552	20.8±0.2	603	2147±46	322±5
6.2	0.5	0.0552	21.3±0.5	666	2325±62	366±6
7.8	0.5	0.0552	21.2±0.1	687	2349±64	390±6
10.0	0.5	0.0552	21.2±0.1	670	2266±57	386±6
CPyBr in 0.5M NaBr						
2.6	0.5	0.0516	21.1±0.2	599	2147±76	317±7
3.8	0.5	0.0516	21.4±0.1	722	2694±107	359±8
4.8	0.5	0.0516	21.6±0.1	860	3344±130	402±8
CPyBr in 0.25M NaBr						
2.4	0.25	0.0516	20.7±0.1	363	904±21	344±8
3.5	0.25	0.0516	21.0±0.1	413	1066±28	369±8
4.8	0.25	0.0516	20.9±0.1	450	1148±28	409±9
6.2	0.25	0.0516	21.0±0.5	483	1246±33	432±11
7.8	0.25	0.0516	21.1±0.1	472	1210±28	426±9
10.5	0.25	0.0516	20.9±0.1	477	1213±30	436±10
13.0	0.25	0.0516	20.9±0.1	473	1164±28	459±11
CPyBr in 0.5M NaBr Delete the first 5 points for the reason of lenses						
2.6	0.5	0.0516	21.0±0.2	552	1915±64	306±6
3.8	0.5	0.0516	21.3±0.1	642	2273±86	346±6
4.8	0.5	0.0516	21.5±0.1	713	2541±98	379±6
CPyBr in 0.25M NaBr Delete the first 5 points for the reason of lenses						
2.4	0.25	0.0516	20.6±0.1	351	869±21	337±8
3.5	0.25	0.0516	21.0±0.1	395	1008±29	360±8
4.8	0.25	0.0516	20.9±0.1	426	1076±29	396±9
6.2	0.25	0.0516	21.0±0.1	456	1159±36	417±10
7.8	0.25	0.0516	21.1±0.1	464	1185±38	422±10
10.5	0.25	0.0516	20.9±0.1	469	1188±42	431±12
13.0	0.25	0.0516	20.9±0.1	467	1144±38	455±13

Table 3.8 (Continued)

CPyBr in 0.8M NaBr, Mar.99 + Dec.* 99 use Kuhn Length=197 N/L=2.199						
	X	Mw	A	R_g /Å	$\langle L_n \rangle$ /Å	S(0)
1.04	0.031	$1.846 \cdot 10^6$	4.26 ± 0.20	340	1146 ± 58	0.966
1.28	0.034	$1.603 \cdot 10^6$	4.62 ± 0.22	312	995 ± 52	0.962
1.52	0.044	$1.769 \cdot 10^6$	6.13 ± 0.35	331	1098 ± 67	0.952
1.92	0.061	$1.977 \cdot 10^6$	8.63 ± 0.53	354	1227 ± 82	0.935
2.5*	0.089	$2.301 \cdot 10^6$	12.1 ± 1.2	388	1428 ± 142	0.906
3.1*	0.121	$2.575 \cdot 10^6$	17.0 ± 1.7	415	1598 ± 167	0.876
3.12	0.093	$1.842 \cdot 10^6$	13.1 ± 1.1	339	1143 ± 104	0.902
4.0*	0.146	$2.363 \cdot 10^6$	20.3 ± 2.5	394	1467 ± 186	0.854

* Did in Dec. 99, others Mar. 99

CPyBr in 0.5M NaBr use Kuhn Length=262 N/L=2.172						
	X	Mw	A	R_g /Å	$\langle L_n \rangle$ /Å	S(0)
2.6	0.134	$2.301 \cdot 10^6$	13.4 ± 1.1	438	1446 ± 125	0.865
3.8	0.244	$3.031 \cdot 10^6$	26.0 ± 2.4	517	1905 ± 183	0.774
4.8	0.330	$3.301 \cdot 10^6$	35.9 ± 3.7	544	2074 ± 217	0.714
6.2	0.421	$3.254 \cdot 10^6$	46.3 ± 5.8	539	2045 ± 264	0.658
7.8	0.507	$3.080 \cdot 10^6$	54.9 ± 8.3	522	1936 ± 299	0.611
10.0	0.833	$4.232 \cdot 10^6$	98.3 ± 16.4	630	2659 ± 452	0.477

CPyBr in 0.5M NaBr use Kuhn Length=220 N/L=2.315						
	X	Mw	A	R_g /Å	$\langle L_n \rangle$ /Å	S(0)
2.6	0.087	$2.008 \cdot 10^6$	11.8 ± 1.5	362	1184 ± 152	0.909
3.8	0.112	$1.736 \cdot 10^6$	15.4 ± 2.4	331	1023 ± 171	0.884
4.8	0.137	$1.666 \cdot 10^6$	18.6 ± 2.9	323	982 ± 158	0.862

CPyBr in 0.8M NaBr use Kuhn Length=286 N/L=2.268						
	X	Mw	A	R_g /Å	$\langle L_n \rangle$ /Å	S(0)
2.4	0.063	$1.044 \cdot 10^6$	5.89 ± 0.55	269	628 ± 62	0.933
3.5	0.093	$1.062 \cdot 10^6$	8.84 ± 1.26	272	639 ± 95	0.903
4.8	0.133	$1.108 \cdot 10^6$	12.8 ± 1.8	279	667 ± 99	0.865
6.2	0.185	$1.199 \cdot 10^6$	17.9 ± 2.8	294	722 ± 115	0.821
7.8	0.242	$1.253 \cdot 10^6$	23.9 ± 4.1	302	754 ± 134	0.775
10.5	0.361	$1.400 \cdot 10^6$	36.2 ± 6.9	324	843 ± 167	0.694
13.0	0.471	$1.487 \cdot 10^6$	47.3 ± 9.1	337	895 ± 178	0.630

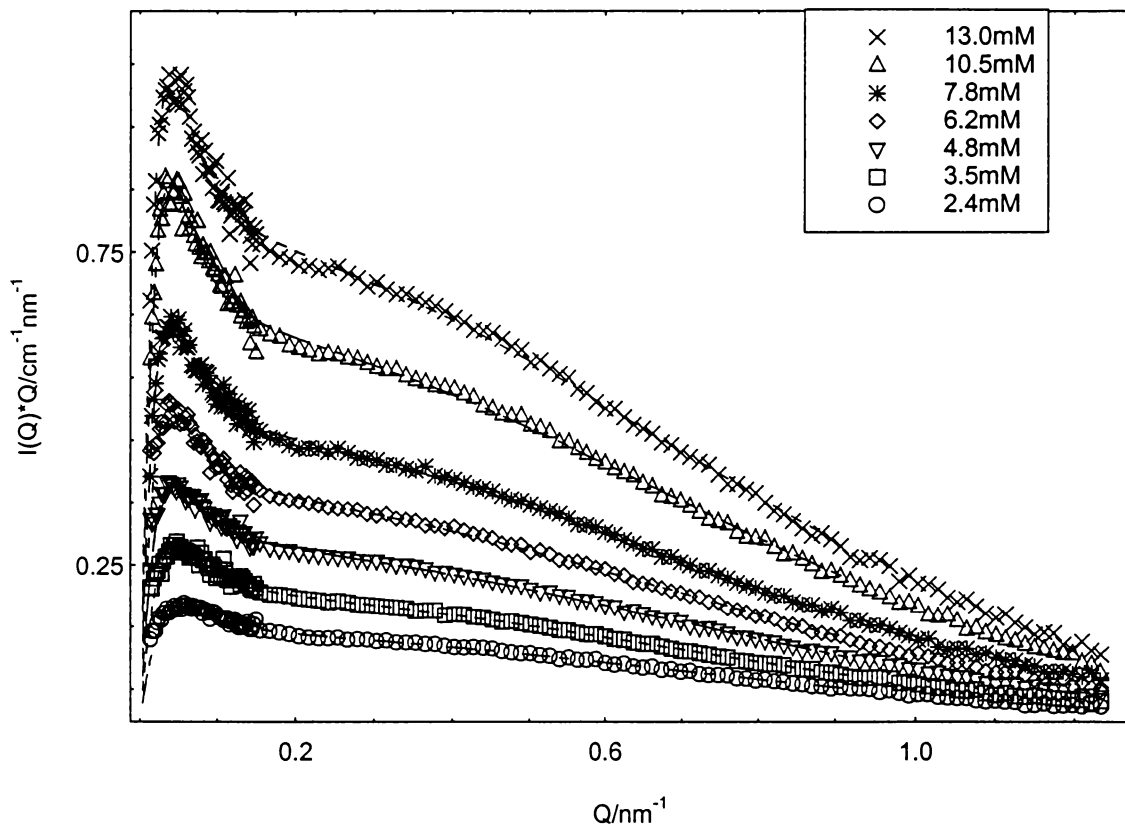


Figure 3.38 Bending rod plots of SANS data for CPyBr with fits in 0.25M NaBr without taking intermicellar interactions into account

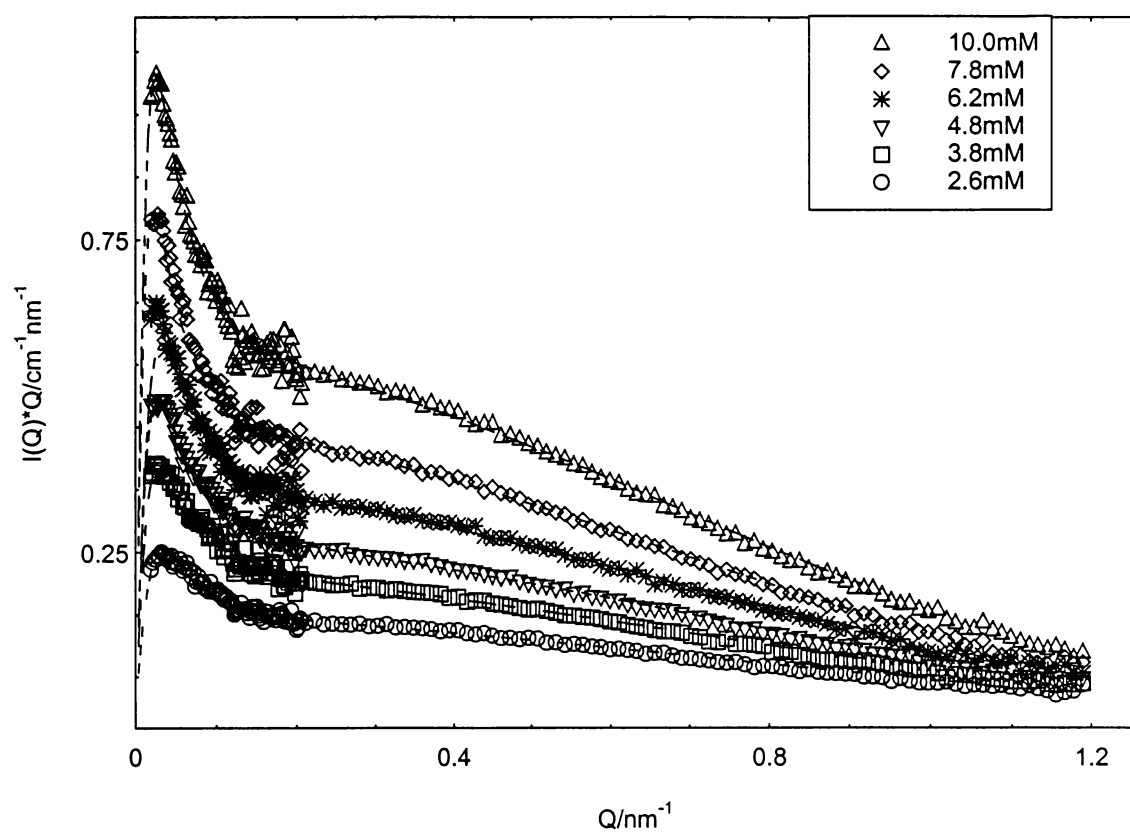


Figure 3.39 Bending rod plots of SANS data for CPyBr with fits in 0.50M NaBr without taking intermicellar interactions into account

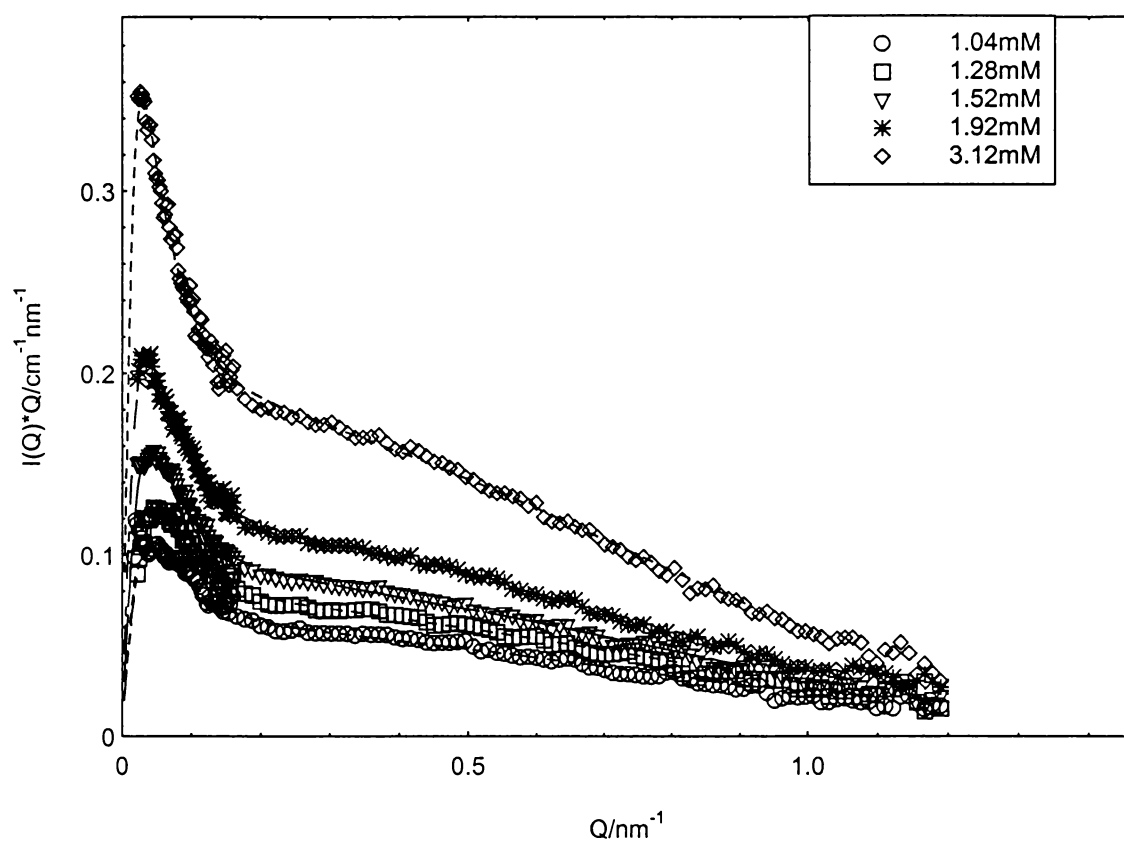


Figure 3.40 Bending rod plots of SANS data for CPyBr with fits in 0.80M NaBr without taking intermicellar interactions into account

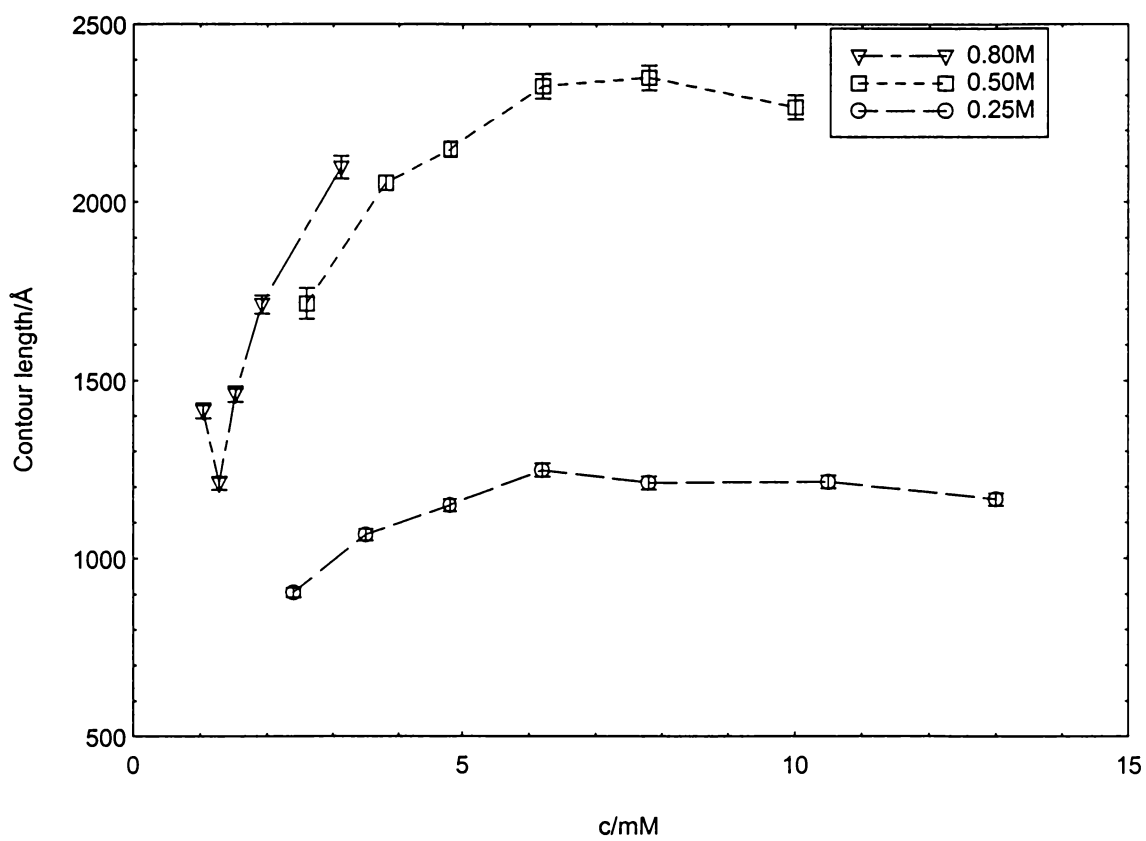


Figure 3.41 Dependence of micellar contour lengths on CPyBr concentration in different NaBr solutions

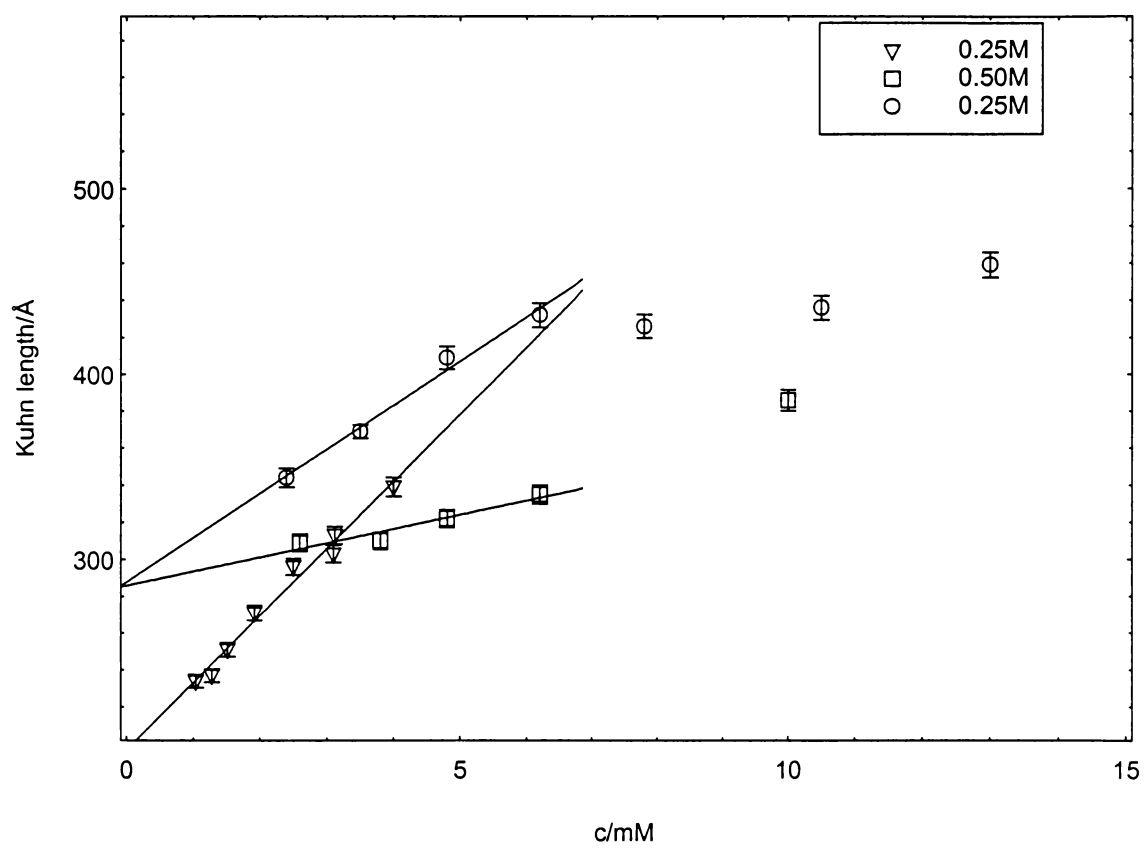


Figure 3.42 Dependence of micellar Kuhn lengths on CPyBr concentration in different NaBr solutions

found in Table 3.8. We observed that the results of the fits in Figures 3.43-45 are very poor in all Q regions, especially at high salt and surfactant concentrations.

Values of c^* for the CPyBr micelles were determined in the same way as described for the CTAB micelles. The mean value of N/L from Guinier-like plots is $22.5 \text{ monomer} \cdot \text{nm}^{-1}$, and the CPyBr molecular weight is 402 g/mol . Using the $\langle L_n \rangle$'s from the fits without intermicellar interactions, for 4.0 mM CPyBr in 0.8 M NaBr we obtain $M_w = 6.82 \times 10^6 \text{ g/mol}$ and $R_g = 86.0 \text{ nm}$. Thus c^* is 10 mM . For 10.0 mM CPyBr in 0.5 M NaBr with $M_w = 4.10 \times 10^6 \text{ g/mol}$ and $R_g = 67.0 \text{ nm}$, c^* is 13.3 mM ; for 13.0 mM CPyBr in 0.25 M NaBr with $M_w = 2.11 \times 10^6 \text{ g/mol}$ and $R_g = 47.3 \text{ nm}$, c^* is 20 mM . In these cases, c^* was not exceeded by our experiments at all three salt concentrations. Figure 3.41 supports this only in 0.25 M NaBr. We observed the contour length level off or decrease at the two higher salt concentrations, indicating that c^* predicted might be too large for these systems. The experimental results of c^* from Figure 3.41 corresponding roughly to 7.5 mM for both 0.5 M and 0.8 M NaBr.

3.3.4 Comparison between TTAB and CTAB – Tail length influence on micellar size and flexibility

The structure of TTAB's surfactant ion differs from that of CTAB only by the tail length, 14 vs. 16 carbons, but this difference is significant for wormlike micellar structure. The cross-sectional radii, r_{cs} , for TTAB (with mean value of 1.95 nm from the results of fits) are smaller than for CTAB (with a mean value of 2.22 nm from the fits) by about 2.7 \AA ($\sim 2.5 \text{ \AA}$ for a two carbon chain length). This is expected for micelles growing

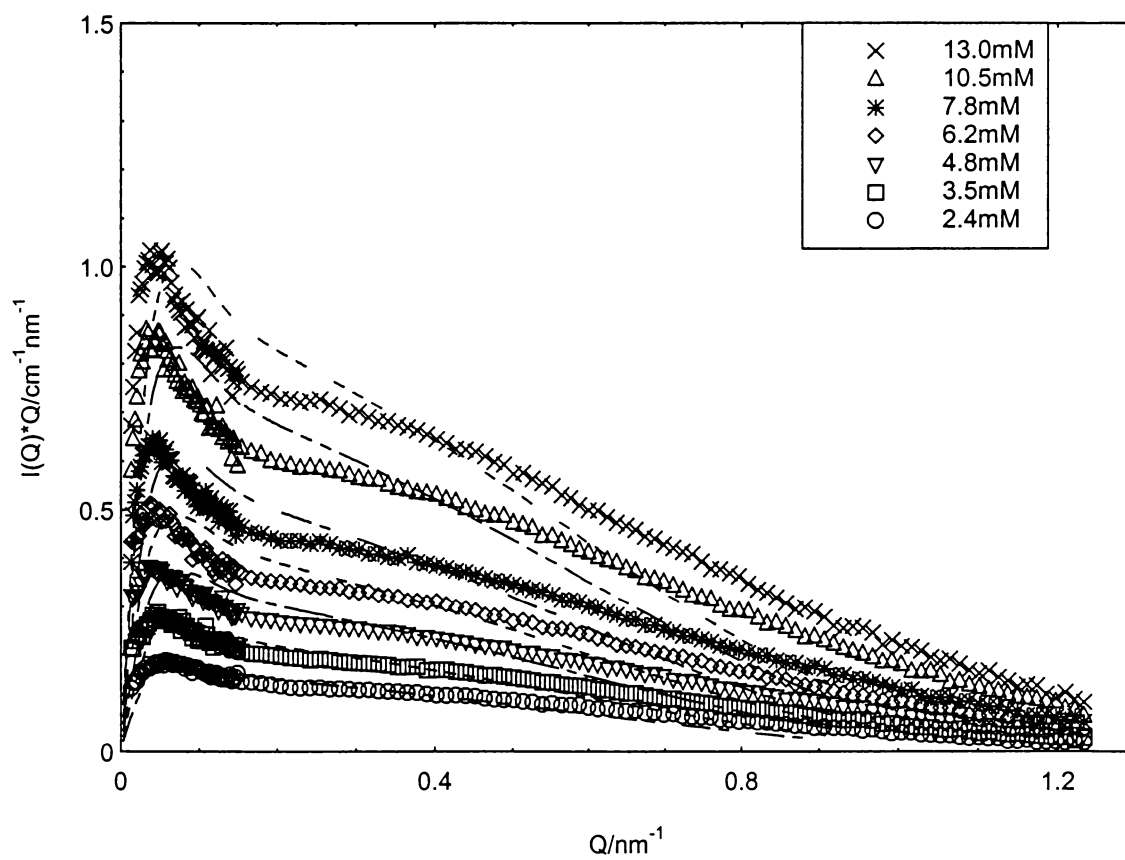


Figure 3.43 Bending rod plots of SANS data for CPyBr with fits in 0.25M NaBr, including the effects of intermicellar interaction

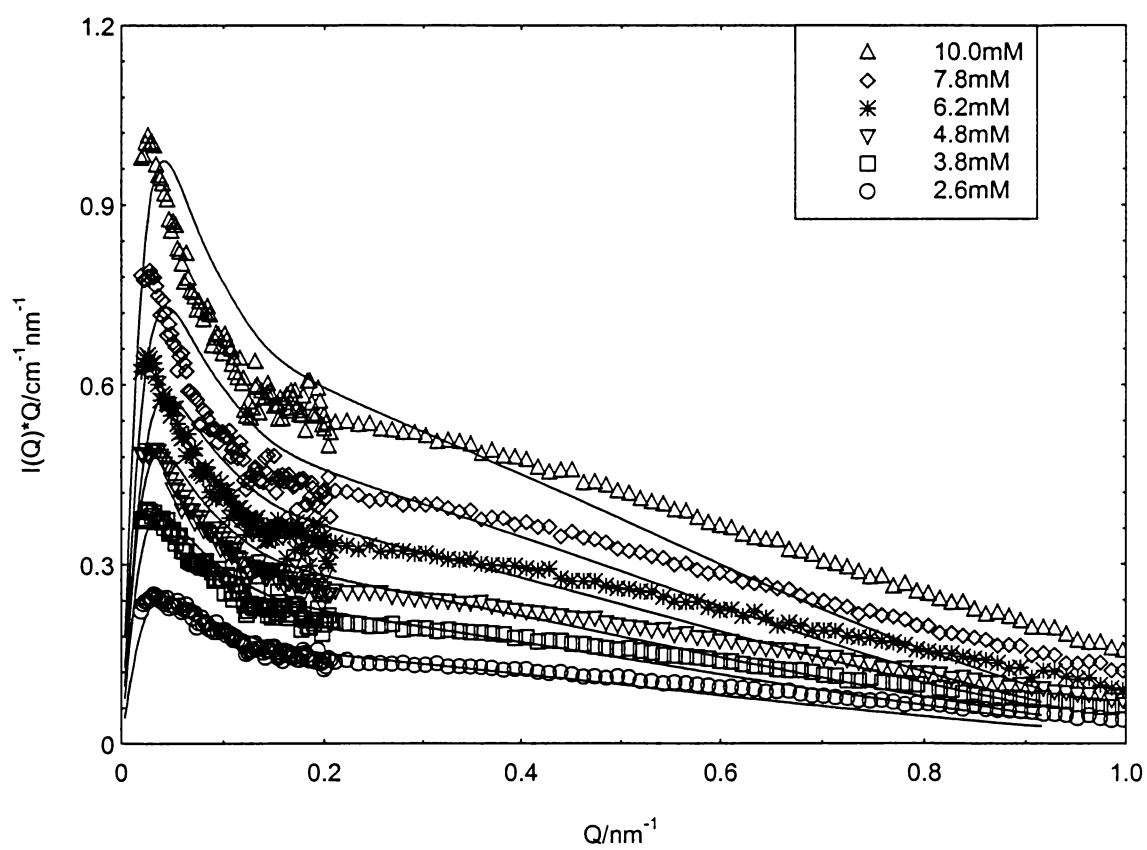


Figure 3.44 Bending rod plots of SANS data for CPyBr with fits in 0.50M NaBr, including the effects of intermicellar interaction

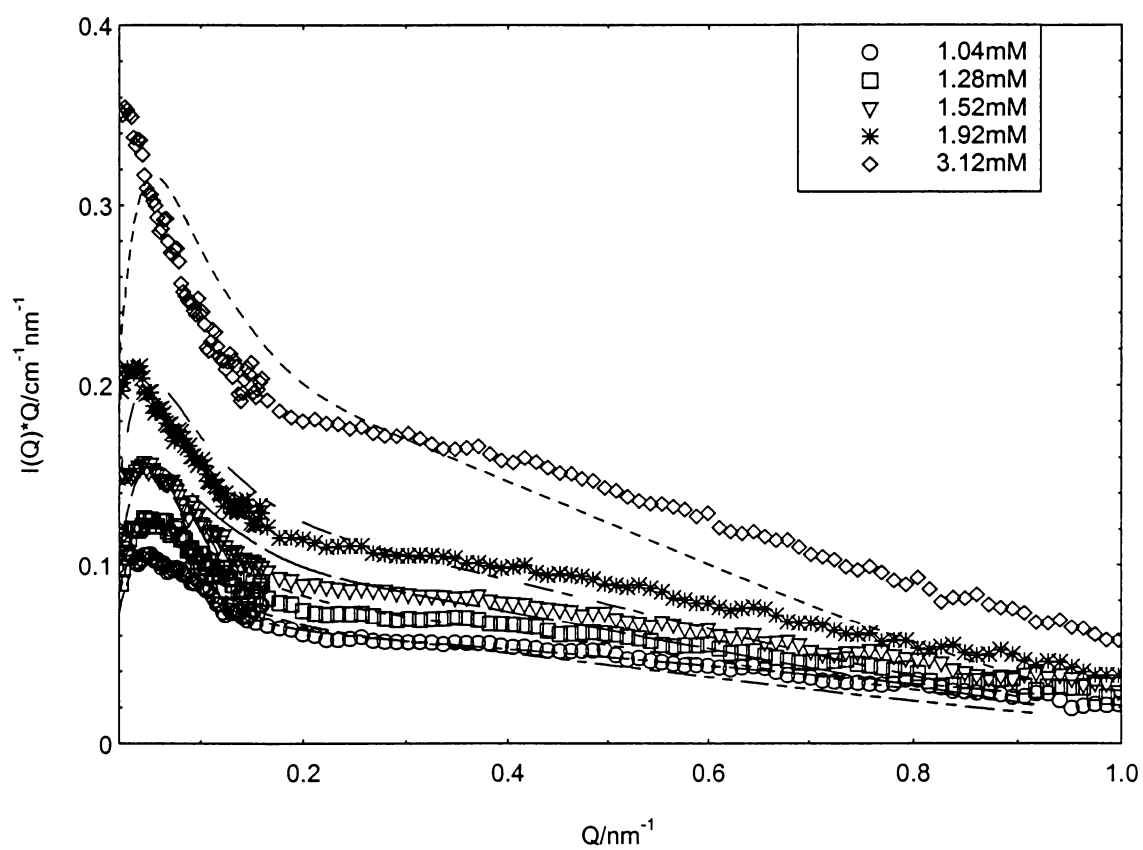


Figure 3.45 Bending rod plots of SANS data for CPyBr with fits in 0.80M NaBr, including the effects of intermicellar interaction

unidimensionally along the long axis rather than the cross-section as well. The number of monomers per unit length does not change in either TTAB or CTAB micellar structures, indicating that ionic strength, c_s , has no effect on the local micellar structure, but only the size and flexibility of the micelles. We recall from Chapter I that the micellar persistence length, l_p , is related to the bending modulus (w) of the local micellar structure. In the work of Ben Shaul,¹⁵ a relationship of $w \sim r_{cs}^3$ is predicted. With larger r_{cs} , the micelles are harder to bend and thus have a large w and persistence length. The experimental results for $l_{p,c=0}$ are present in Table 3.9. We did not observe the larger persistence length expected for CTAB micelles, indicating that the ionic strength also plays an important role, even at high c_s . The dependence of $l_{p,c=0}$ on ionic strength follows Eqn 1.6, in which $l_{p,0}$ (the intrinsic persistence length) and $l_{p,e}$ (electrostatic persistence length) are introduced.¹² From our experiments, we observed that the higher the ionic strength the smaller $l_{p,e}$, this agrees the theory that the ionic strength increase can screen the electrostatic interactions. Further discussion on the $l_{p,e}$ will be in the Section 3.5.

Our data disagree with the effect of salt observed by Imae and Ikeda³³ whose SLS experiments suggested that increasing the ionic strength can increase the persistence length of the TTAB and CTAB in NaBr solutions. SANS is more appropriate for determining persistence length because SANS provides the right length scale to get the l_p directly, while SLS cannot measure it directly.

For the contour length, the scaling exponent (α) for TTAB micellar growth in 3M NaBr solutions is smaller than for CTAB in 1.0M NaBr solutions below c^* . This is consistent with the generally-accepted idea that the energetic advantage for a surfactant

Table 3.9 Persistence length and α for CTAB, TTAB and CPyBr in aqueous NaBr

CTAB

C_s/M	α	$l_{p,c=0}$ (Å)
0.25	0.12 ± 0.01	174 ± 9
0.50	0.40 ± 0.01	144 ± 12
1.00	1.11 ± 0.02	138 ± 5

TTAB

C_s/M	α	$l_{p,c=0}$ (Å)
1.50	0.22 ± 0.01	141 ± 7
3.00	0.48 ± 0.01	124 ± 6

CPyBr

C_s/M	α	$l_{p,c=0}$ (Å)
0.25	0.33 ± 0.02	144 ± 8
0.50	0.34 ± 0.02	126 ± 6
0.80	0.45 ± 0.03	96 ± 5

ion to occupy a cylindrical rather than a spherical micellar environment increases with increasing surfactant chain length. Another way to say this is that end-cap energies are larger for CTAB.

3.3.5 Comparison between CPyBr and CTAB – Head group influence on micellar size and flexibility

CPyBr has a less bulky head group than CTAB. A similar r_{cs} from the fits, 2.12nm for CPyBr and 2.22nm for CTAB, indicates that the chain length determines the micellar cross sectional radii. The micelles grow unidimensionally along their long axis rather than along the cross section as well. As for CTAB, increases in ionic strength have no effect on the CPyBr local micellar structure: N/L remains approximately constant. For CPyBr micelles, the scaling exponent for the dependence of contour length on surfactant concentration is smaller than for CTAB micelles at each salt concentration investigated. At the same salt and surfactant concentrations, CTAB micelles are always larger than CPyBr micelles, indicating that CTAB micelles have a larger end-cap energy than CPyBr micelles. Table 3.9 tabulates $l_{p,c=0}$ values, which clearly indicate that the persistence length for CPyBr micelles is smaller than for CTAB. This can be explained by Ben-Shaul's theory¹⁵ of molecular contributions to the bending modulus, with the less bulky head group having the smaller bending modulus. Increases of the ionic strength can cause $l_{p,e}$ to decrease have also been observed in both cases, and details will be discussed in Section 3.5.

3.4 THE INFLUENCE OF MIXED COUNTERIONS ON MICELLAR STRUCTURE AND FLEXIBILITY: NaTos/Cl, NaSal/Cl, AND Na26ClBz/Cl

The earliest work on the role of counterion structure in promoting formation of wormlike micelles, includes pioneering work on CTASal,⁹¹ and on CTAB/KBr.¹² More recently, viscoelastic properties of CTAB/HSal systems were studied,⁹² and simulation and free energy models were used to study the effect of counterion orientation on the thermodynamics of micellar formation in mixed CTAB/NaSal systems.⁹³ In 1996, Magid and co-workers had used SANS to study CTA26ClBz, CTA35ClBz, CTA34ClBz, and CTA4ClBz, investigating the effect of different chloride substitution patterns in the counterions on the micellar size and properties.⁹⁴ A detailed study was made on the effect of mixed counterions of Na26ClBz/NaBr on the micellar structure.⁹⁵ In the mixed CTA26ClBz/Cl micellar systems in aqueous Na26ClBz/Cl at constant salt concentration, increasing the mole percent of Na26ClBz first causes micelle growth followed by a decrease in micellar size.⁶⁵ Figure 3.46 summarizes the experimental results, and this reversion of the micellar size have also been observed for CTA and TTA micelles by using Sal as counterion.^{25, 96} Cationic surfactants with halide counterions alone do not show this reversion of size.

CTATos micelles have also been studied by using fluorescence quenching to study the sphere to rod transition,⁹⁷ and by using fluorescence recovery after fringe pattern photobleaching (FRAPP) to study the growth and entanglement in micellar solutions with and without added salt.⁹⁸ More recently, L. Walker and co-workers have studied the rheology of CTATos solutions.⁹⁹ They found shear-induced micellar structures, as have other groups in the past few years. The formation of shear-induced near-surface liquid

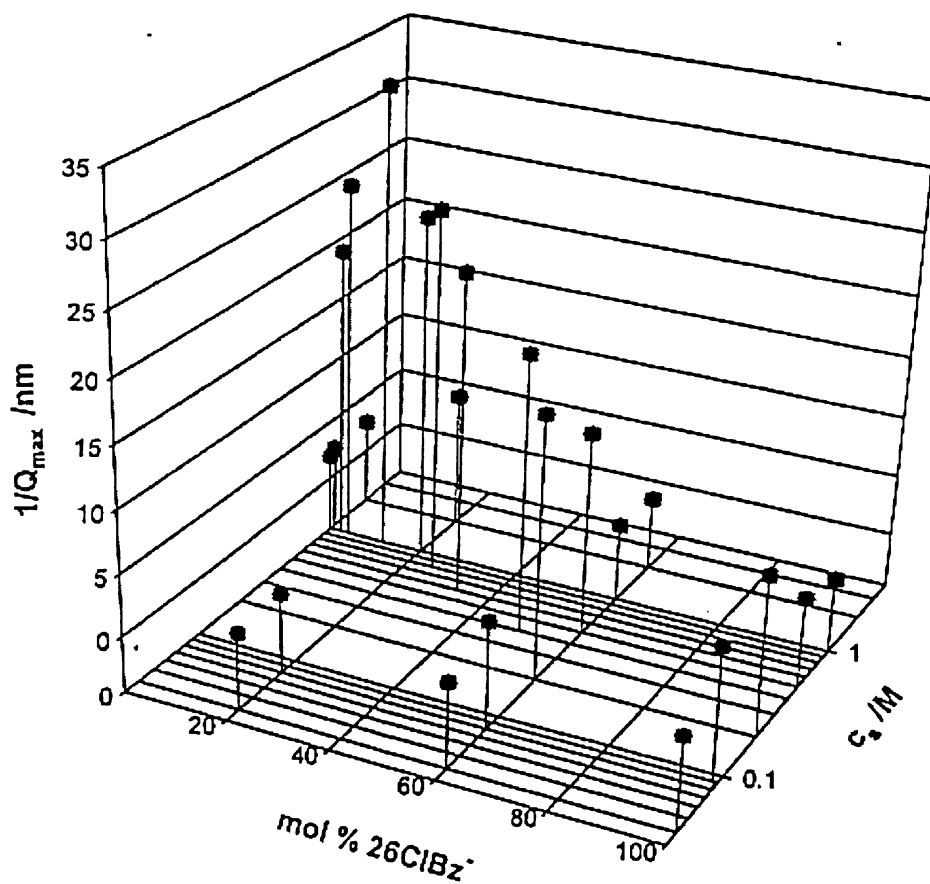


Figure 3.46 Evolution of micellar size as a function of c_s and mole fraction of 26ClBz, taking the $1/Q_{\max}$ value derived from bending rod plots as proportional to the micellar R_g values. From reference [65].

mesophases in a wormlike micellar solution have also been studied.¹⁰⁰ In the 1990s, substituted naphthalenes (carboxylates, sulfonates) as the counterion have also been studied for CTA.¹⁰¹ All of these aromatic counterions are penetrating and thus have been proposed to act as cosurfactants on the micellar surface.^{101, 102}

Several questions have been raised from these studies. Is the micellar size reversion a general phenomenon for all cationic surfactants with organic penetrating counterions? Do the Sal and Tos also act like cosurfactants on the cationic micellar surfaces? In this section we report on studies using mixed counterions, in order to understand the impact of penetrating vs. nonpenetrating counterions, with the latter being chloride or bromide. At constant total salt concentration, changing the mol % of penetrating counterion - such as salicylate (Sal), p-toluenesulfonate (Tos), 3,5-dichlorobenzoate (3,5ClBz) and 2,6-dichlorobenzoate (2,6ClBz) - causes the micellar size and flexibility to change. The same phenomenon can also be observed by keeping the mole percent of penetrating counterion constant and changing the total salt concentration or the surfactant concentration.

3.4.1 The CTATos/Cl micellar system in aqueous NaTos/Cl

SANS curves for CTATos/Cl micellar system were obtained at 40°C in D₂O at various salt concentrations. We looked at CTA micelles in 2 mole %, 5 mole % and 12 mole % NaTos in 0.15M, 0.25M and 1M total salt (NaTos + NaCl) concentrations. Curves for CTATos micelles at 7.5mM surfactant in different concentrations of pure NaTos were also obtained. SANS curves for the systems investigated are shown in Figures 3.47-55. For 7.5M CTATos in pure NaTos solutions, Figure 3.47 makes clear that micellar sizes increase from 0.02 to 0.05M NaTos, then decreases as more salt is

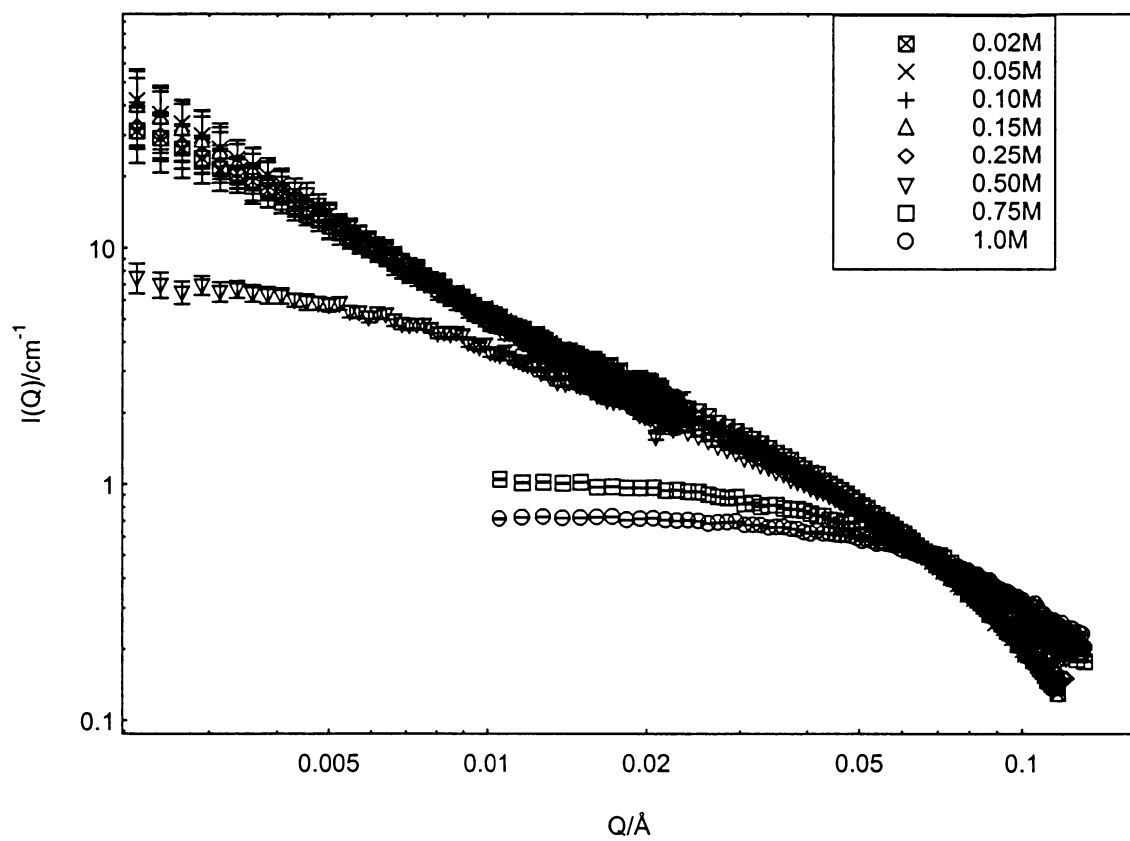


Figure 3.47 SANS curves for 7.5mM CTATos micelles in NaTos solutions at 40°C.

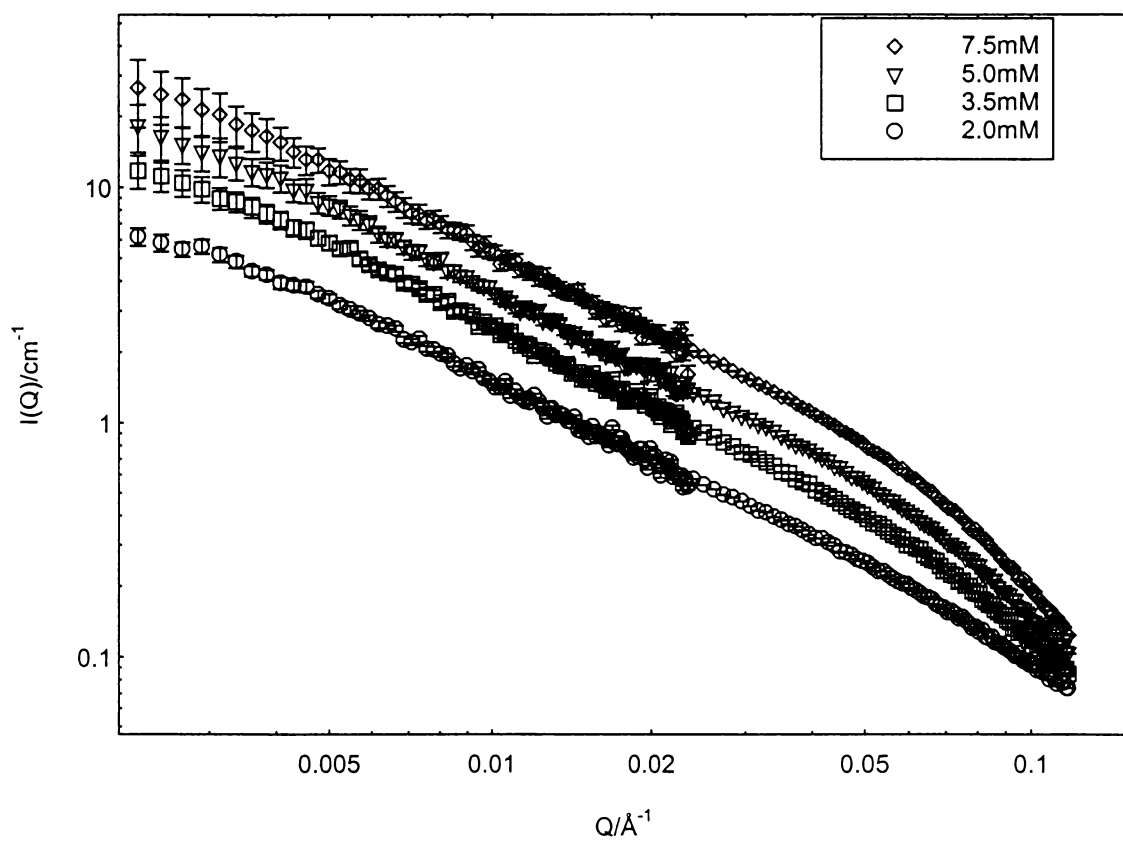


Figure 3.48 SANS curves for CTATos in 2 mole % NaTos/Cl in 0.15M total salt at 40°C.

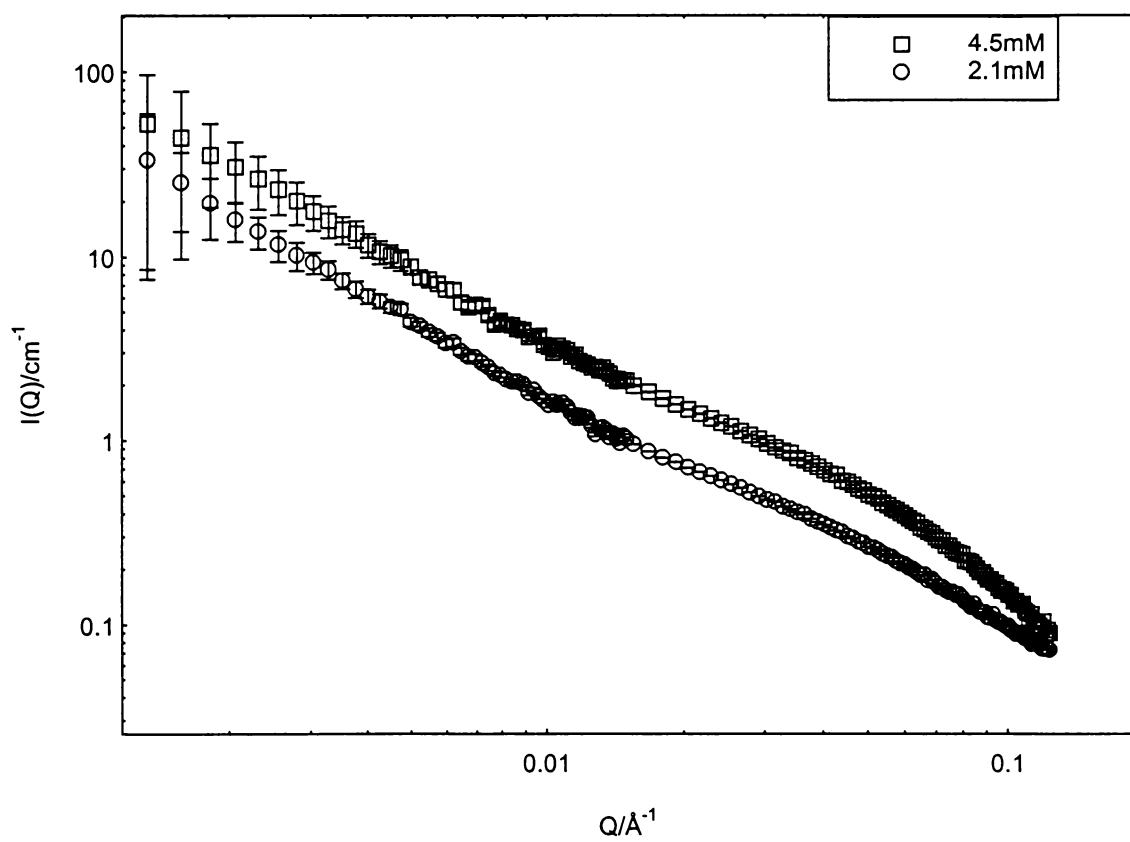


Figure 3.49 SANS curves for CTATos in 12 mole % NaTos/Cl in 0.15M salt at 40°C.

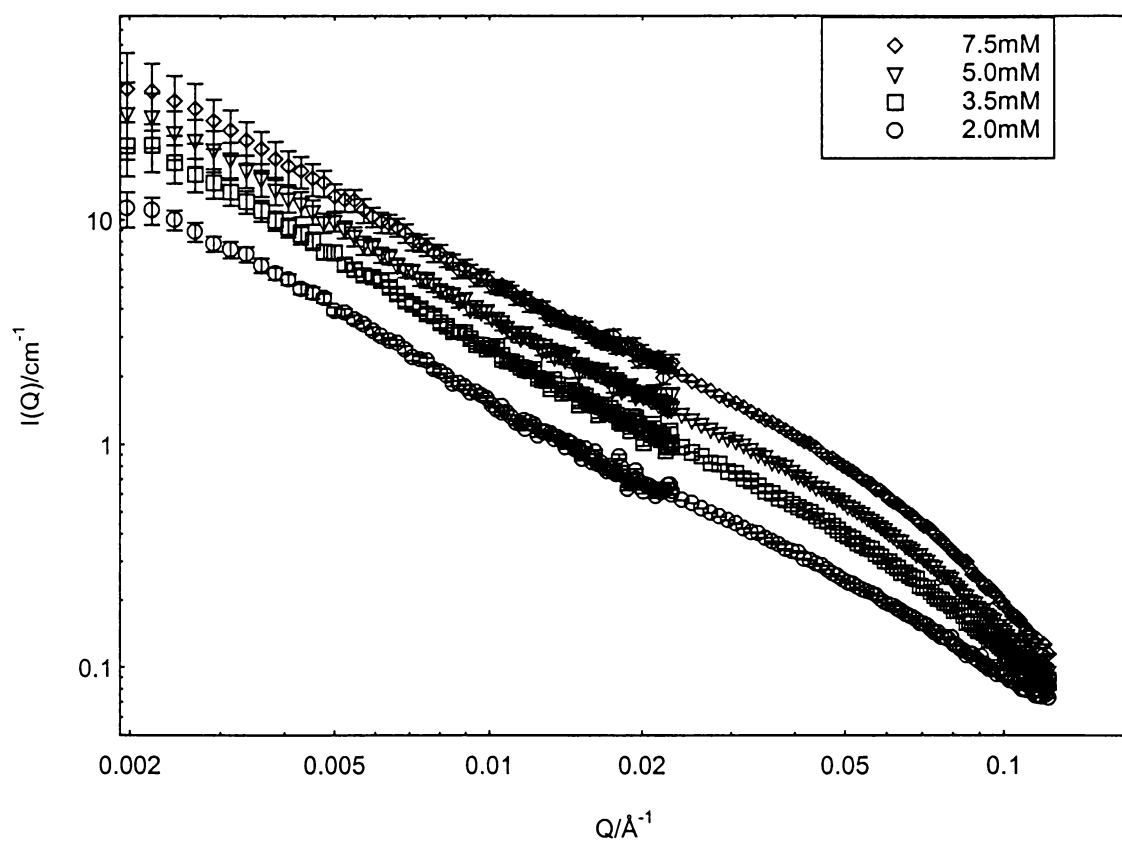


Figure 3.50 SANS curves for CTATos in 2 mole % NaTos/Cl in 0.25M salt

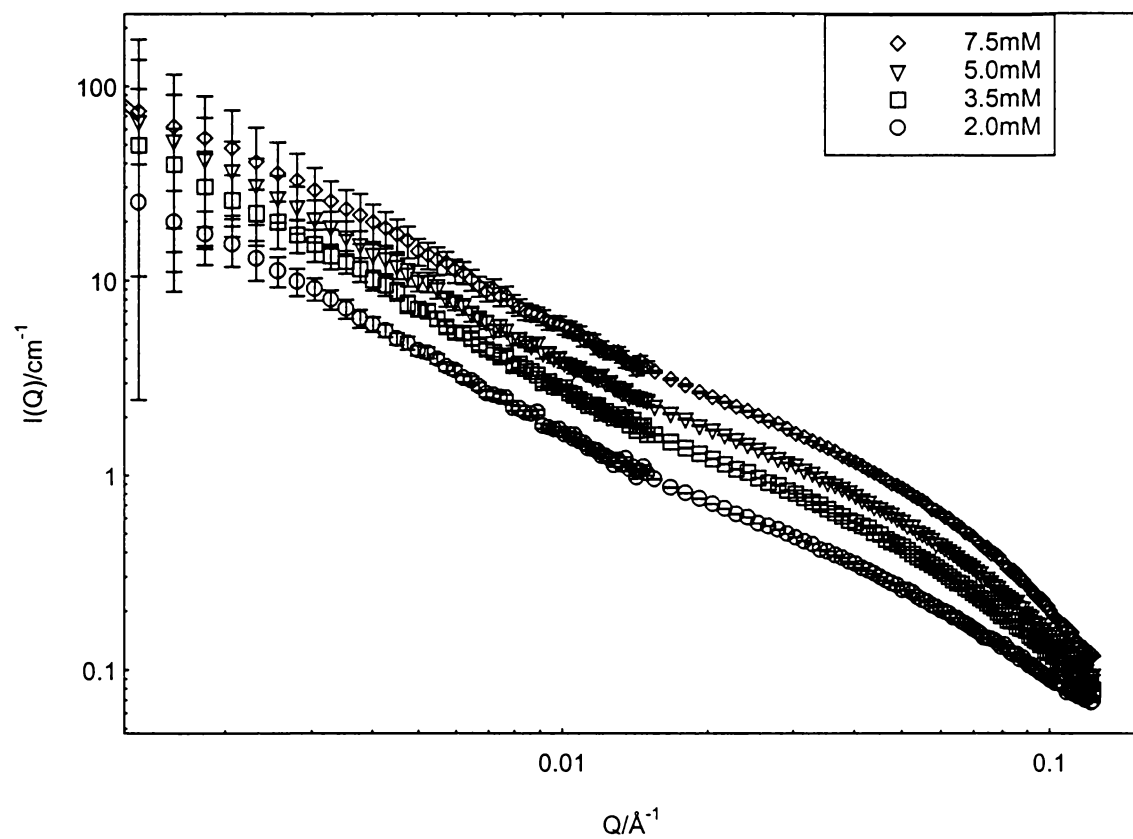


Figure 3.51 SANS curves for CTATos in 5% mole NaTos/Cl in 0.25M salt at 40°C.

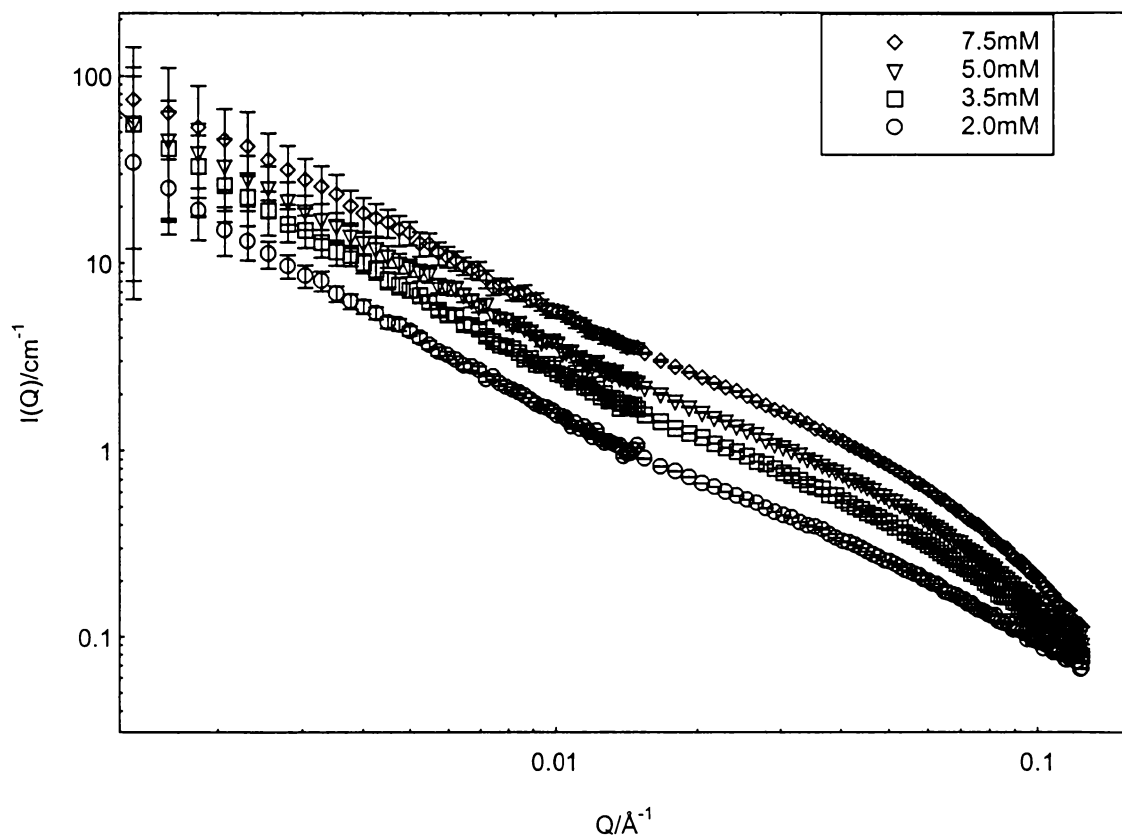


Figure 3.52 SNAS curves for CTATos in 12 mole % NaTos/Cl in 0.25M salt at 40°C.

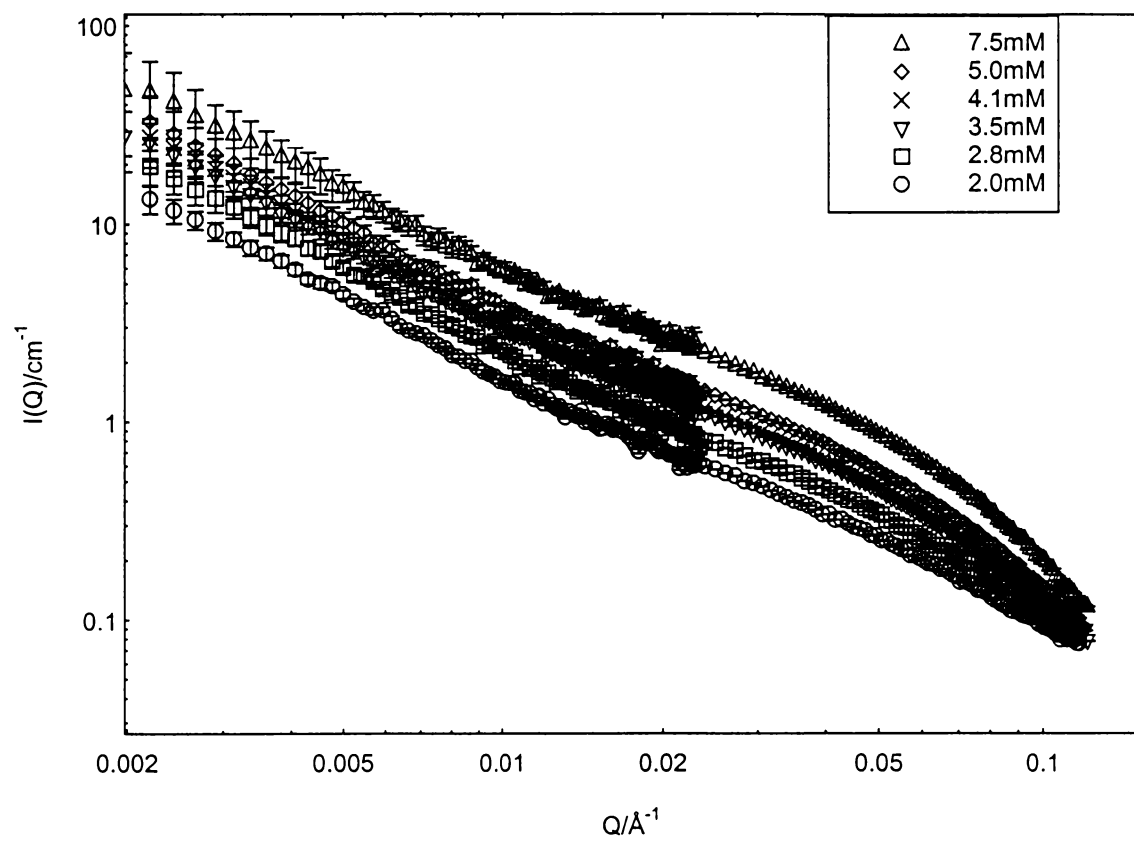


Figure 3.53 SANS curves for CTATos in 2 mole % NaTos/Cl in 1M salt at 40°C.

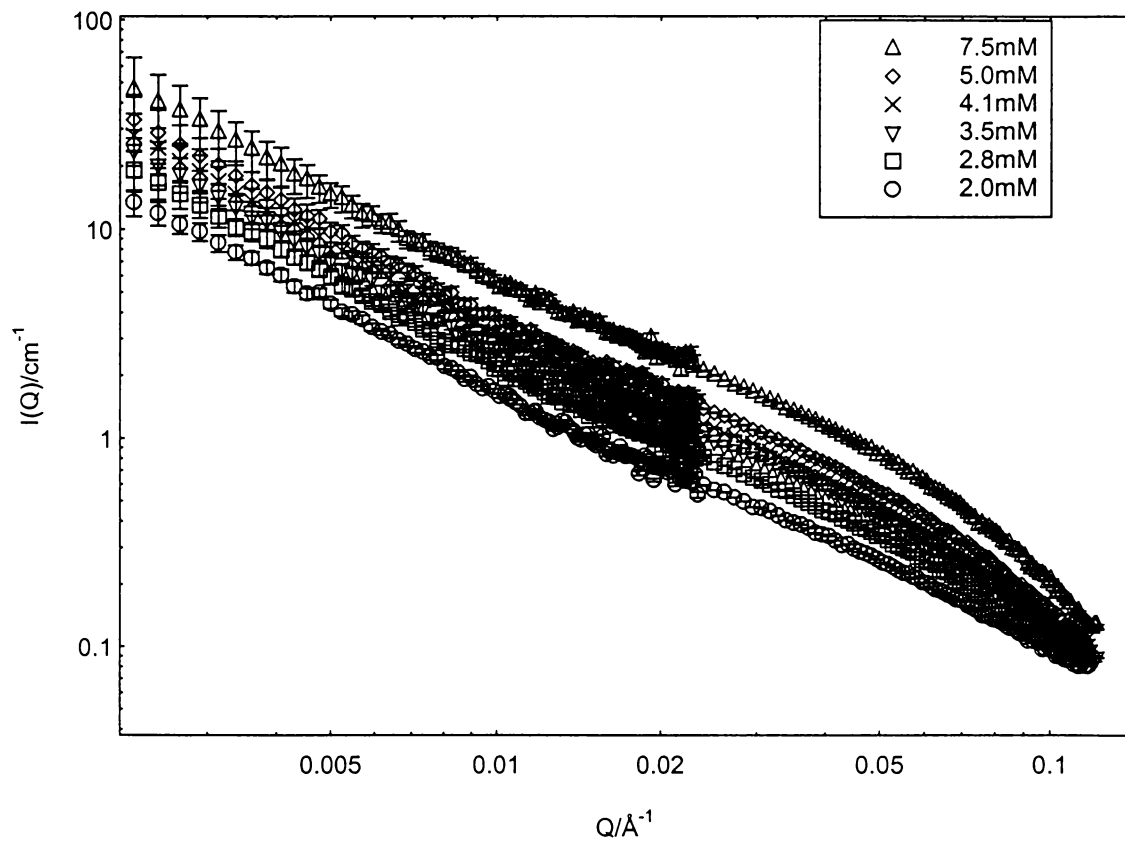


Figure 3.54 SANS curves for CTATos in 5 mole % NaTos/Cl in 1M salt at 40°C

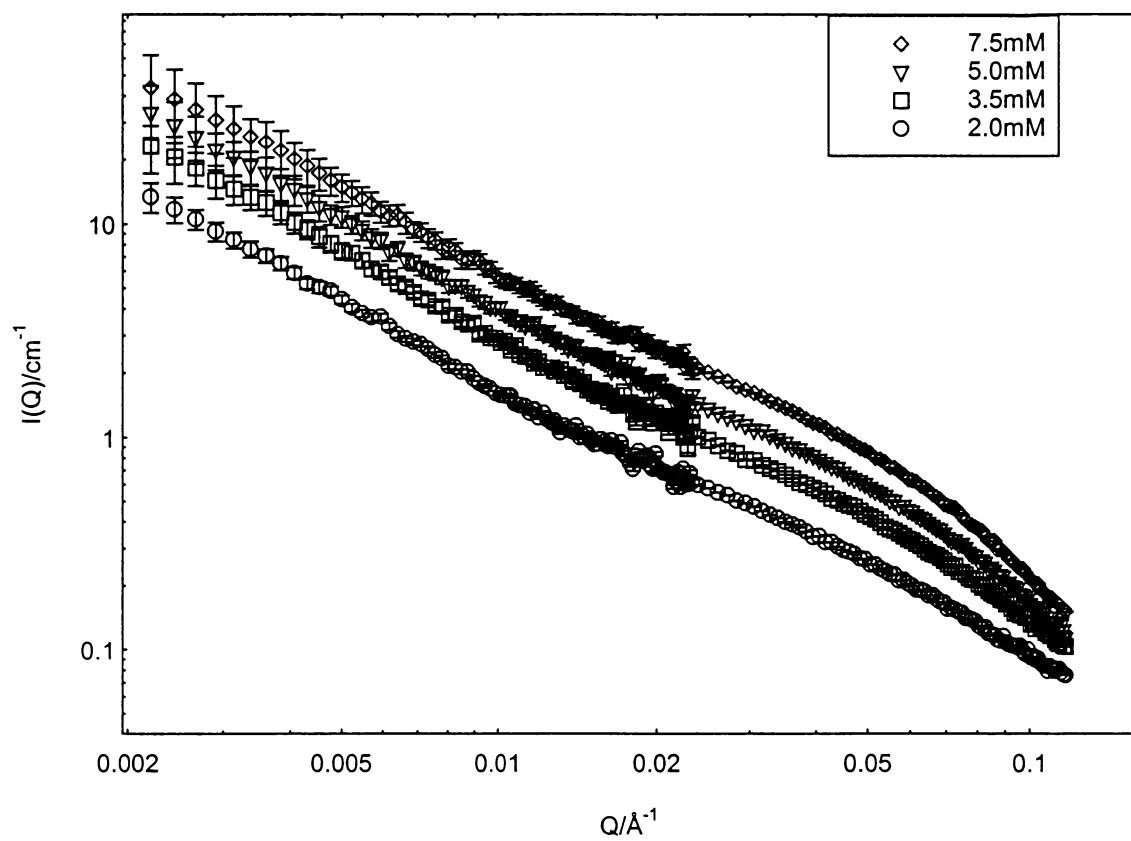


Figure 3.55 SANS curves for CTATos in 12 mole % NaTos/Cl in 1M salt 40°C

added. This effect has also been observed for Na₂₆ClBz, which penetrates into the micellar surface and drives the micelles back to smaller size at higher salt concentration. A more detailed study on why the micellar size reversion occurs at higher salt concentration in the case of Na₂₆ClBz will be discussed in detail in Chapter IV.

In Section 3.3, we already established that the micellar cross sectional radii are mainly based on the surfactants' tail lengths and that the micelles grow unidimensionally. Here we will concentrate on micellar size and flexibility. The fits presented for the full scattering curves were performed without taking intermicellar interactions into account, since attempts to include them previously led to poor fits. This means that the persistence lengths reported at finite c (surfactant concentration) are apparent values. We fit the scattering curves by using Eqn. 2.42-2.44 and the same fitting program described in Sections 3.2 and 3.3. The value of the scattering from solvent (the background) was fixed. The micellar polydispersity was also fixed ($z = 1$). A grid search method for weighted non-linear least-squares fitting was used. The fitting uses r_{cs} , $2l_p$ and $\langle L_n \rangle$ as variables, and the overall R_g can be calculated from l_p and $\langle L_n \rangle$ by using Eqn 2.44. The results are tabulated in Table 3.10 and the experimental and fitted curves are shown in bending rod plots in Figures 3.56-64.

The CTATos micelles grow rapidly even at very low surfactant concentrations. We checked whether the solutions have c 's above or below c^* by calculating them using Eqn. 1.7. The number N/L ($24 \text{ monomer-nm}^{-1}$) was used based on the results of CTAB micelles discussed in section 3.3. The contour lengths and radii of gyration from Table 3.10 were also used here. The results are tabulated in Table 3.11 with total salt (c_s), mole percent of Tos (mole %), the surfactant concentration (c) used for c^* prediction.

Table 3.10 Fitted parameters for CTATos micelles in aqueous NaTos/NaCl mixed salt solutions, without taking intermicellar interactions into account

5:95 CTATos/Cl in 0.25M salt						
[CTA] /mM	A	Background	r_{cs} /Å	R_g /Å	$\langle L_n \rangle$ /Å	$\langle 2L_p \rangle$ /Å
2.0	37.7±2.4	0.0552	21.9±0.1	1022	4344±268	421±8
3.5	97.5±16	0.0552	21.7±0.1	1356	6332±521	487±8
5.0	130±9	0.0552	21.7±0.1	1337	5910±429	520±8
7.5	116±5	0.0552	21.4±0.1	1008	3511±158	555±10
12:88 CTATos/Cl in 0.25M salt						
2.0	64.1±7.1	0.0552	21.2±0.1	1443	7853±859	418±8
3.5	134±16	0.0552	21.4±0.1	1670	9216±968	474±7
5.0	96.6±4.7	0.0552	21.3±0.1	1156	4730±230	502±8
7.5	125±5	0.0552	21.1±0.1	1082	3972±147	552±8
12:88 CTATos/Cl in 0.15M salt						
2.1	59.8±6.0	0.0552	21.2±0.1	1341	6898±690	420±8
4.5	101.2±6.5	0.0552	21.2±0.1	1262	5388±340	516±8
2:98 CTATos/Cl in 1M salt						
3.5	77.2±5.1	0.0597	22.3±0.1	1122	4648±304	479±7
7.5	116±7.0	0.0597	22.2±0.1	984	3362±191	558±10
5:95 CTATos/Cl in 1M salt						
3.5	67.9±4.9	0.0597	21.6±0.1	1094	4547±328	465±7
7.5	124±6.8	0.0597	21.5±0.1	1021	3868±210	497±7
12:88 CTATos/Cl in 1M salt						
3.5	55.4±3.0	0.0597	20.3±0.1	958	3937±203	414±6
7.5	93.6±4.0	0.0597	20.7±0.1	909	3118±133	511±7
2:98 CTATos/Cl in 0.25M salt						
2.0	19.5±0.6	0.0597	22.0±0.1	708	2458±77	392±6
3.5	44.0±1.8	0.0597	22.0±0.1	847	3086±126	437±7
5.0	62.8±2.4	0.0597	22.0±0.1	873	3068±115	475±7
7.5	78.2±2.9	0.0597	21.7±0.1	824	2551±94	545±9
CTATos in 0.25M NaTos						
7.5	59.1±1.6	0.0597	19.2±0.1	709	2176±58	475±7

Table 3.10 (continued)

2:98 CTATos/Cl in 1M salt						
[CTA] /mM	A	Background	r_{cs} /Å	R_g /Å	$\langle L_n \rangle$ /Å	$\langle 2L_p \rangle$ /Å
2.0	29.2±1.9	0.0599	22.1± 0.1	868	3471±217	390±7
2.8	51.2±3.9	0.0599	22.3±0.1	1003	4318±329	405±6
4.1	87.9±9.4	0.0599	22.2± 0.1	1149	5048±534	450±7
5.0	90.2±7.3	0.0599	22.2±0.1	1050	4227±340	467±7
5:95 CTATos/Cl in 1M salt						
2.0	29.8±1.8	0.0599	21.4± 0.1	869	3643±219	364±6
2.8	52.3±4.2	0.0599	21.6±0.1	1040	4492±361	418±6
4.1	84.1±8.6	0.0599	21.8± 0.1	1125	4865±494	452±7
5.0	102±11	0.0599	21.7±0.1	1145	4936±536	461±7
12:88 CTATos/Cl in 1M salt						
2.0	22.7±0.9	0.0599	19.5± 0.1	699	2659±219	338±5
3.5	50.5±3.0	0.0599	20.1±0.1	861	3459±202	385±6
5.0	77.7±4.8	0.0599	20.5± 0.1	927	3647±222	427±6
7.5	94.7±5.1	0.0599	20.6±0.1	852	2967±158	470±7
2:98 CTATos/Cl in 0.15M salt						
2.0	7.57±0.2	0.0563	20.8± 0.1	400	938±19	422±10
3.5	15.5±0.4	0.0563	21.1±0.1	461	1097±26	474±11
5.0	24.4±0.7	0.0563	21.1± 0.1	500	1190±35	515±14
7.5	39.1±1.5	0.0563	21.1±0.1	543	1255±47	591±20
7.5mM CTATos in NaTos						
[NaTos] /M	A	Background	r_{cs} /Å	R_g /Å	$\langle L_n \rangle$ /Å	$\langle 2L_p \rangle$ /Å
0.02	74.1±4.7	0.0563	21.3± 0.1	871	2278±146	759±18
0.05	112.5±7.8	0.0563	20.8±0.1	1010	3764±262	504±7
0.10	104.9±7.5	0.0563	20.5± 0.1	964	3630±256	473±7
0.15	88.1±5.3	0.0563	19.8±0.1	874	3145±186	459±7

Table 3.11 Results of c^* calculation for CTATos micelles in mixed salt

c_s (M)	mole % Tos	c (mM)	c^* (mM)
0.15	2	7.5	14.9
0.15	12	2.1	5.4
0.25	2	7.5	8.7
0.25	5	3.5	4.8
0.25	12	3.5	3.8
1.0	2	5.0	6.9
1.0	5	5.0	6.2
1.0	12	5.0	8.7

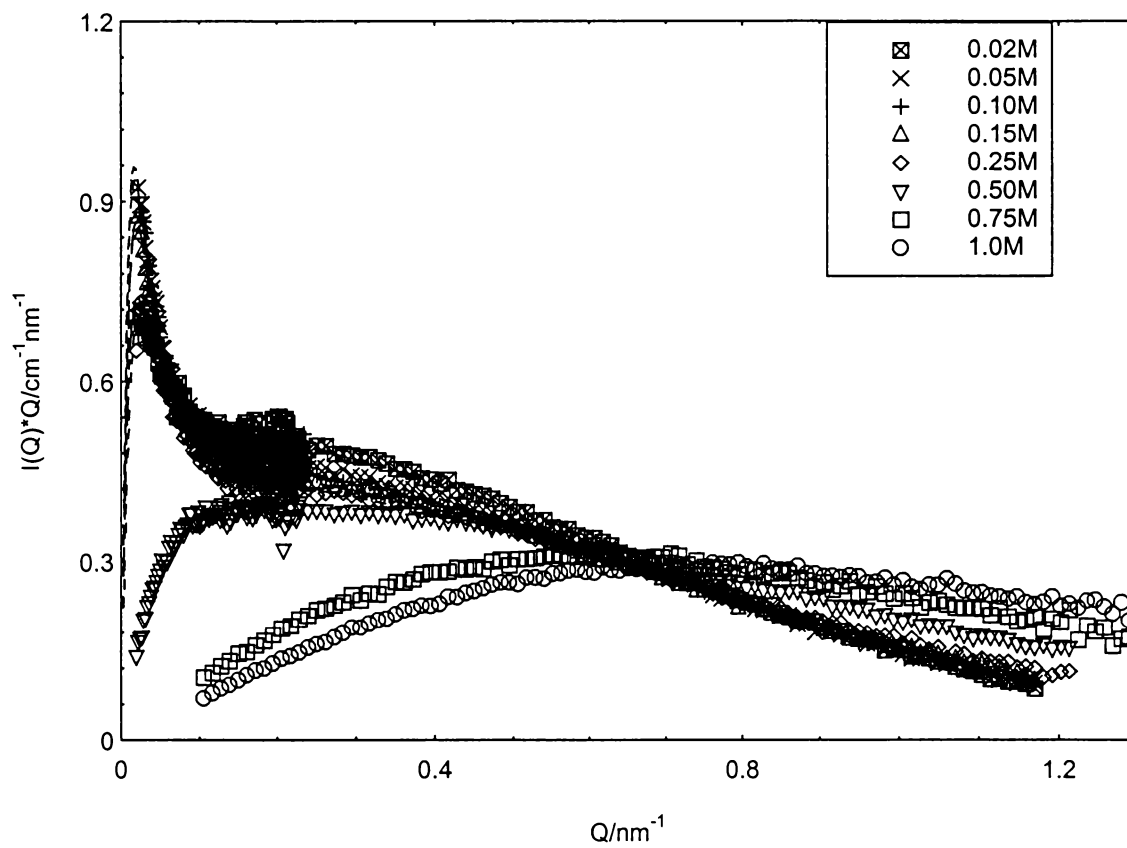


Figure 3.56 Bending rod plots of SANS data for CTATos in NaTos solutions (fits are shown for wormlike chain)

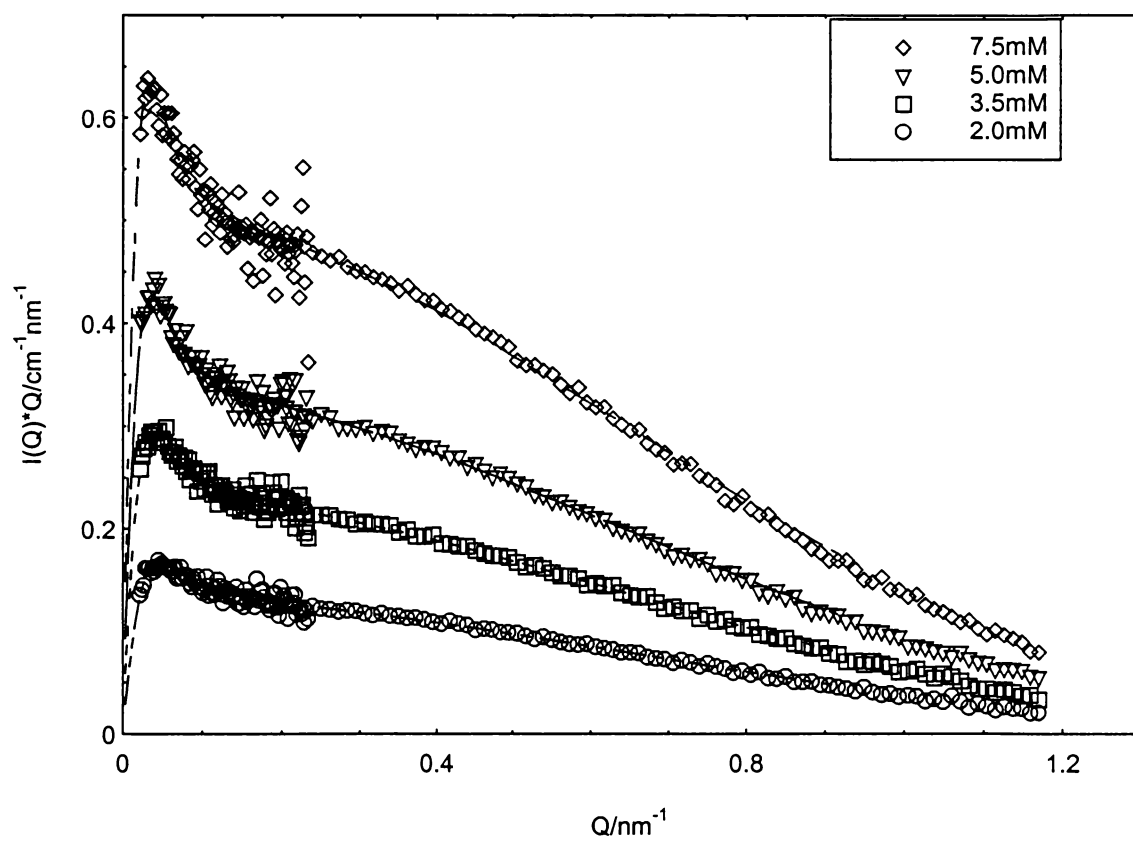


Figure 3.57 Bending rod plots of SANS data for CTATos in 2 mole % NaTos in 0.15M NaTos/NaCl. Fit without taking intermicellar interactions into account.

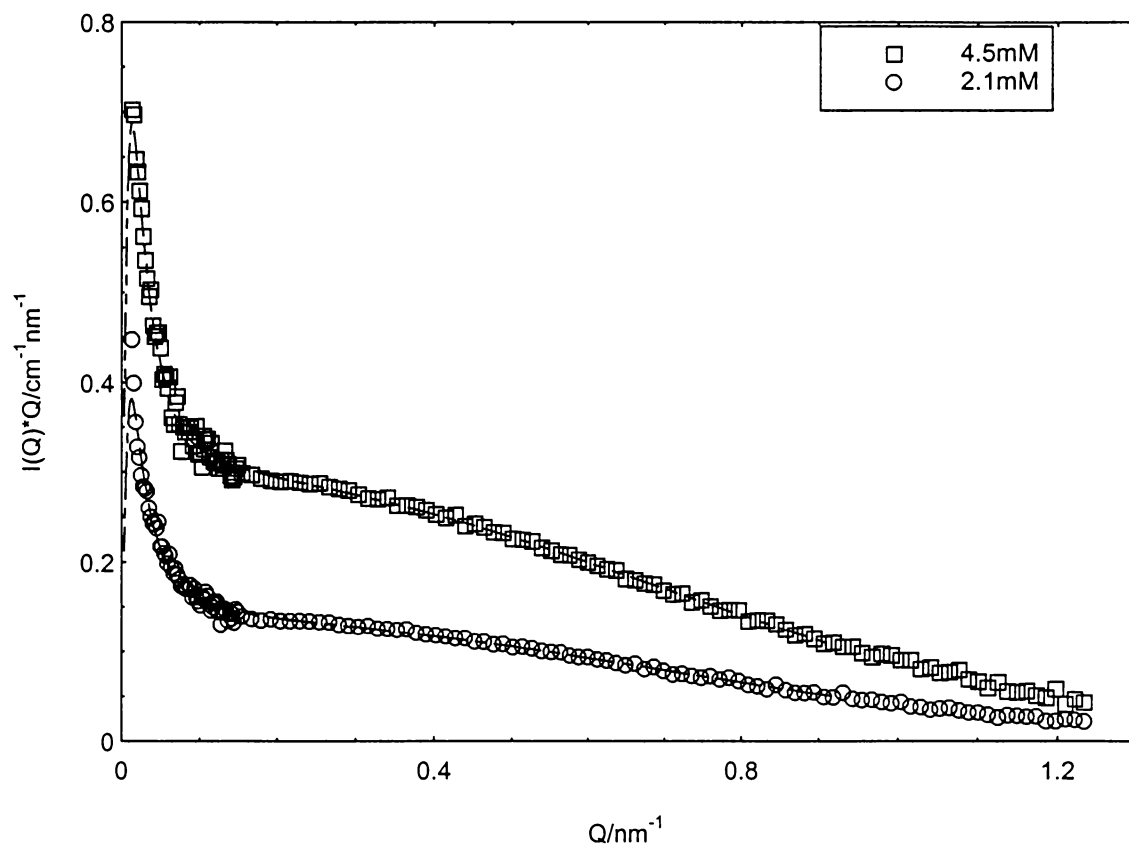


Figure 3.58 Bending rod plots of SANS data for CTATos in 12 mole % NaTos in 0.15M NaTos/NaCl. Fit without taking intermicellar interactions into account.

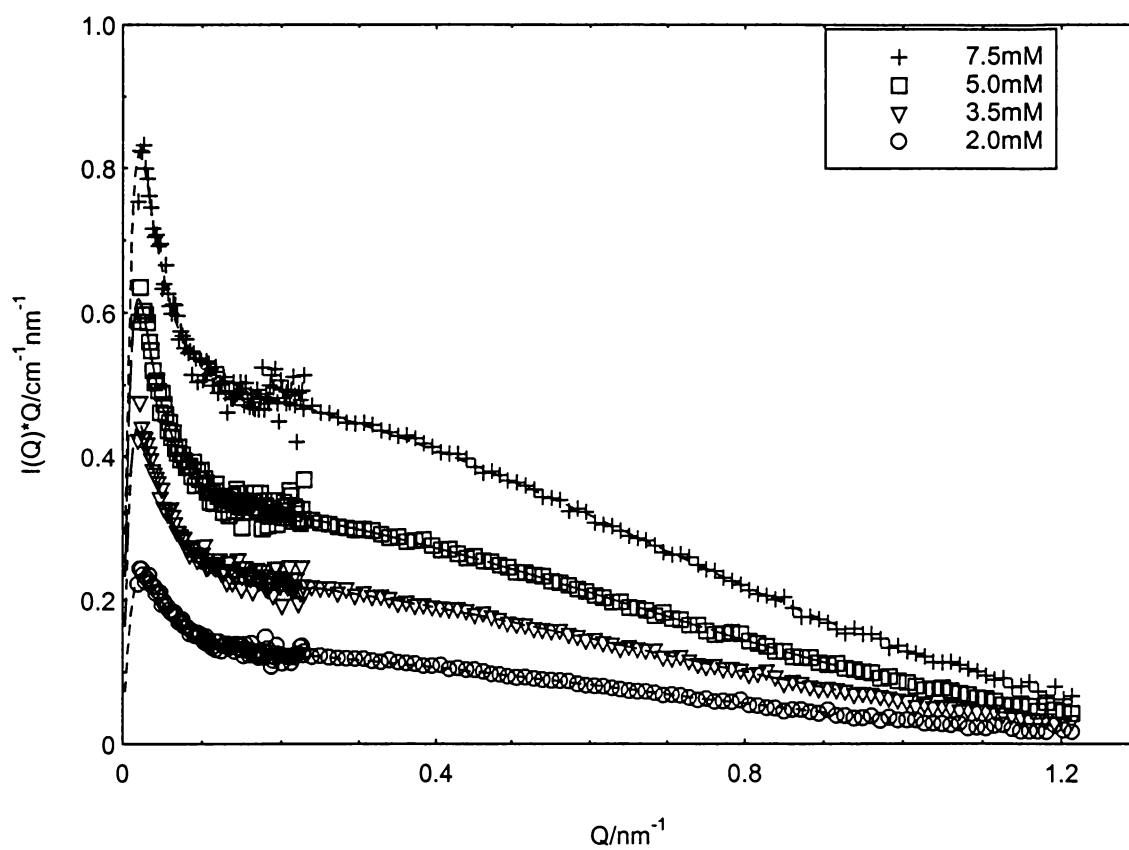


Figure 3.59 Bending rod plots of SANS data for CTATos in 2 mole % NaTos in 0.25M NaTos/NaCl. Fit without taking intermicellar interactions into account.

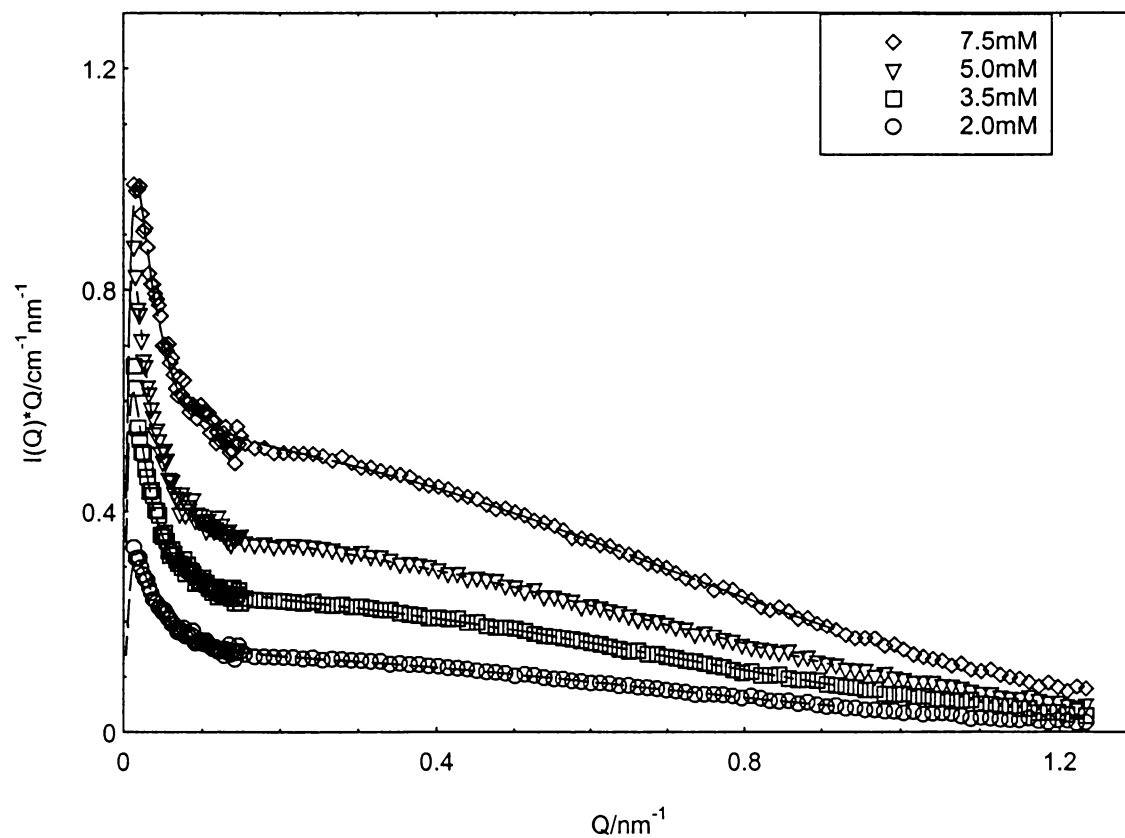


Figure 3.60 Bending rod plots of SANS data for CTATos in 5 mole % NaTos in 0.25M NaTos/NaCl. Fit without taking intermicellar interactions into account.

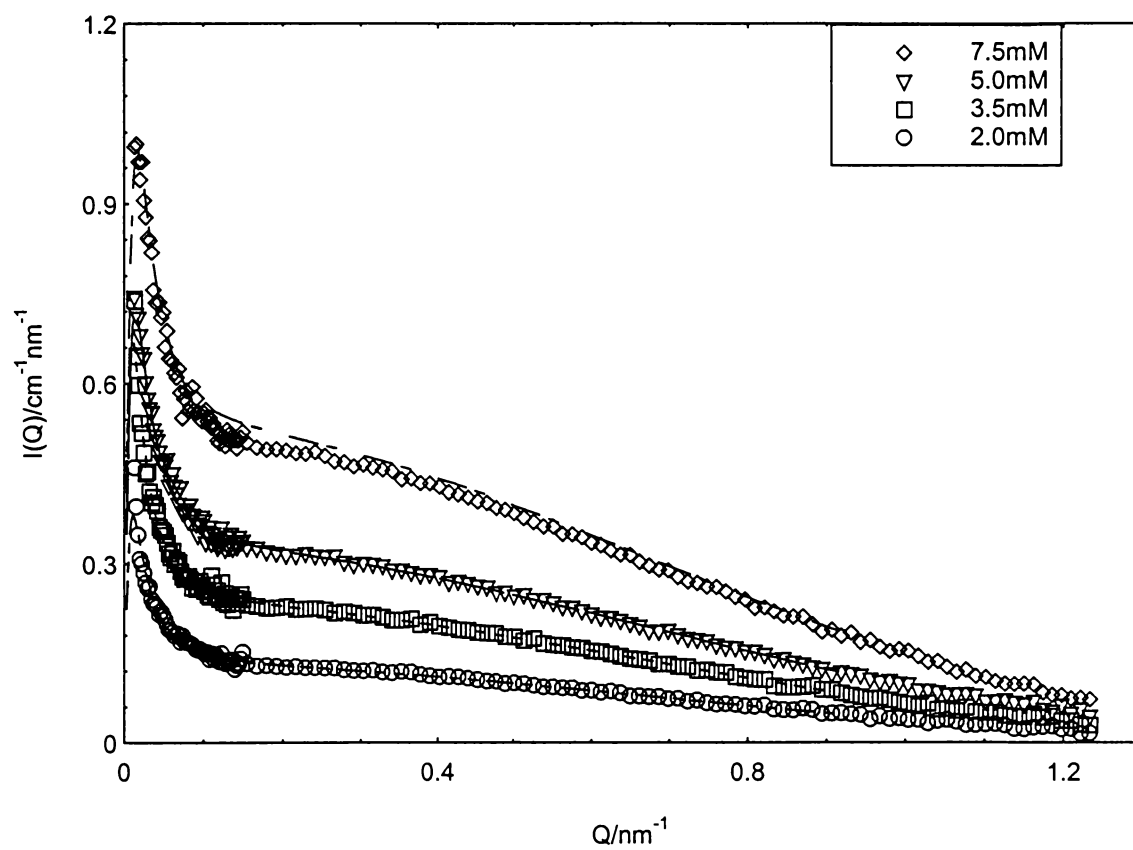


Figure 3.61 Bending rod plots of SANS data for CTATos in 12 mole % NaTos in 0.25M NaTos/NaCl. Fit without taking intermicellar interactions into account.

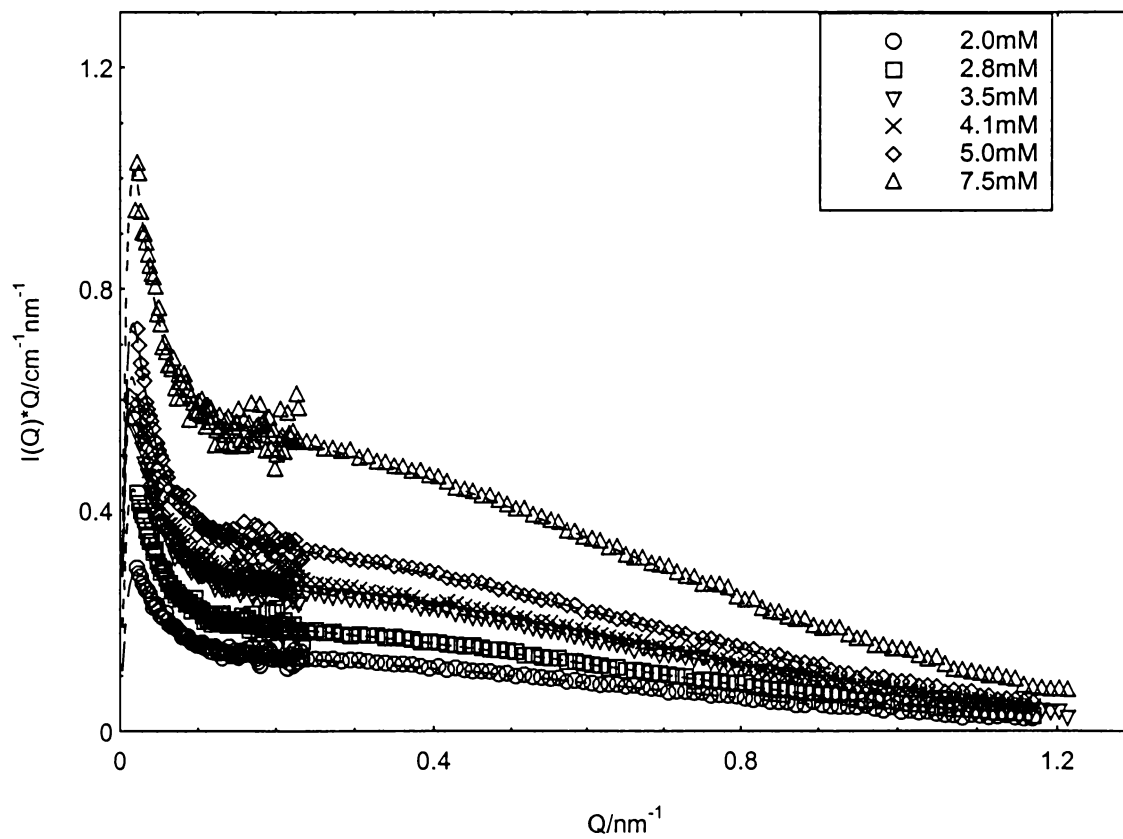


Figure 3.62 Bending rod plots of SANS data for CTATos in 2 mole % NaTos in 1.0M NaTos/NaCl. Fit without taking intermicellar interactions into account.

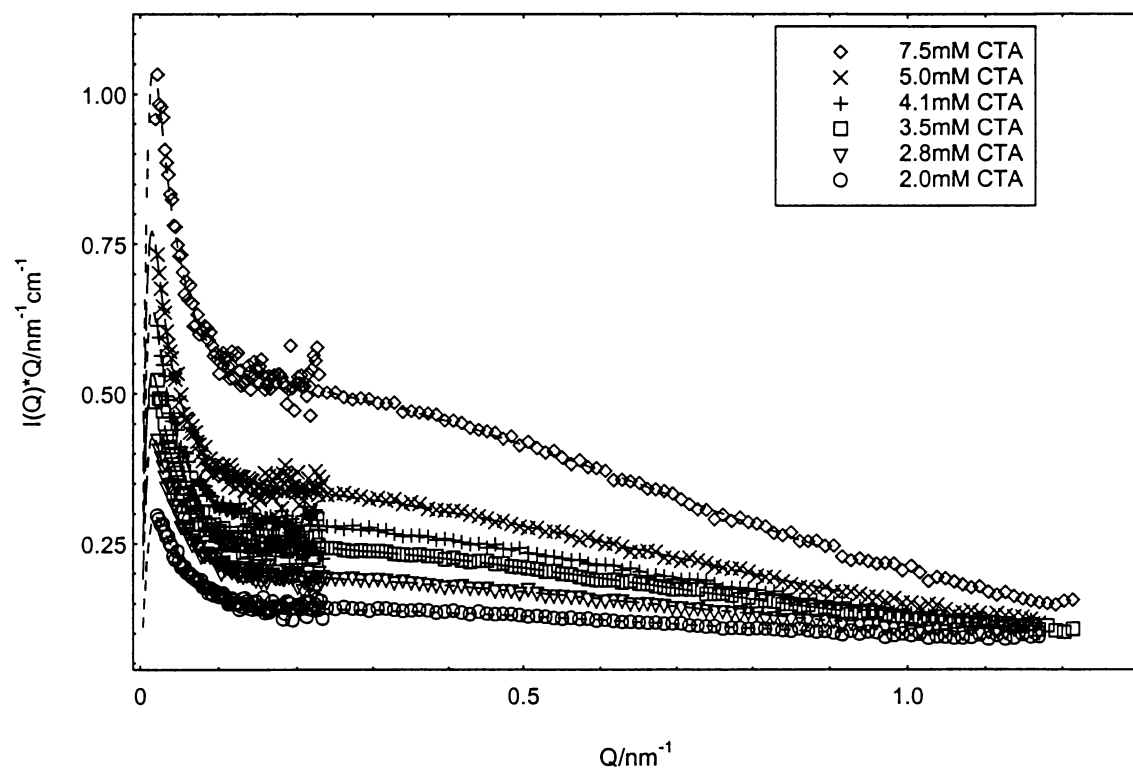


Figure 3.63 Bending rod plots of SANS data for CTATos in 5 mole % NaTos in 1.0M NaTos/NaCl. Fit without taking intermicellar interactions into account.

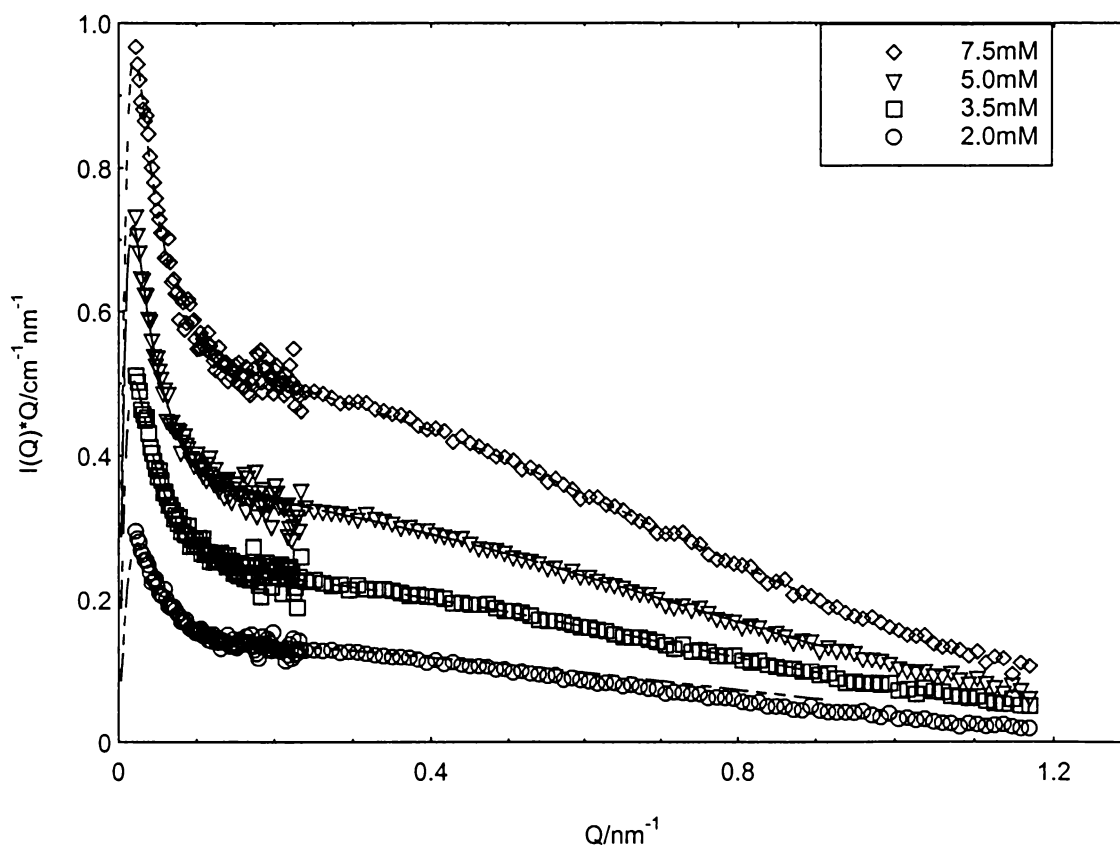


Figure 3.64 Bending rod plots of SANS data for CTATos in 12 mole % NaTos in 1.0M NaTos/NaCl. Fit without taking intermicellar interactions into account.

All the micellar contour lengths from the fits are plotted in Figure 3.65. For 2 mole % NaTos in 0.15M salt, the micellar contour length increases with c , and the sizes of the micelles are small compared to the results at other concentrations. For 12 mole % in 0.15M salt, only two surfactant concentration were studied. The micellar contour length decreases as c increases from 2.0mM to 4.1mM; this does not agree with the prediction that both of these solutions are dilute, $c < c^*$ (5.1mM). For 5 mole % NaTos in 0.25M salt, the micelles present at 3.5mM are large enough to predict a $c^* = 4.8\text{mM}$; and in fact the measured contour length is already decreasing at $c = 5.0\text{mM}$. In other words, above c^* a mesh size is being detected. The largest micellar size was achieved at 3.5mM CTA in 12 mole % NaTos in 0.25M salt, again consistent with the c^* prediction (3.8mM). In both 0.15 and 0.25M total salt, the micellar size increases at constant surfactant concentration as the mole % of NaTos increases below c^* , but this was not observed at 1M salt. In 1M salt, the micellar size shows smaller changes as the surfactant concentration increases. c^* is no longer obvious from contour length, and the contour lengths decrease from 5 mole % NaTos to 12 mole %. These results agree with Schurtenberger and coworkers'¹⁰³ work on nonionic surfactant $C_{16}E_6$, showing that above the c^* , the individual micelles no longer dominate the scattering. Instead, the scattering is typical of wormlike chains in semidilute solutions of neutral polymers, with a decrease in concentration dependent correlation length (ξ_s) of the mesh as the surfactant concentration increases.

The fitted apparent Kuhn lengths of the micelles increase as the surfactant concentration increases. At each salt series, the real Kuhn lengths can be derived by extrapolating to zero surfactant concentration. Kuhn lengths are shown in Figure 3.66.

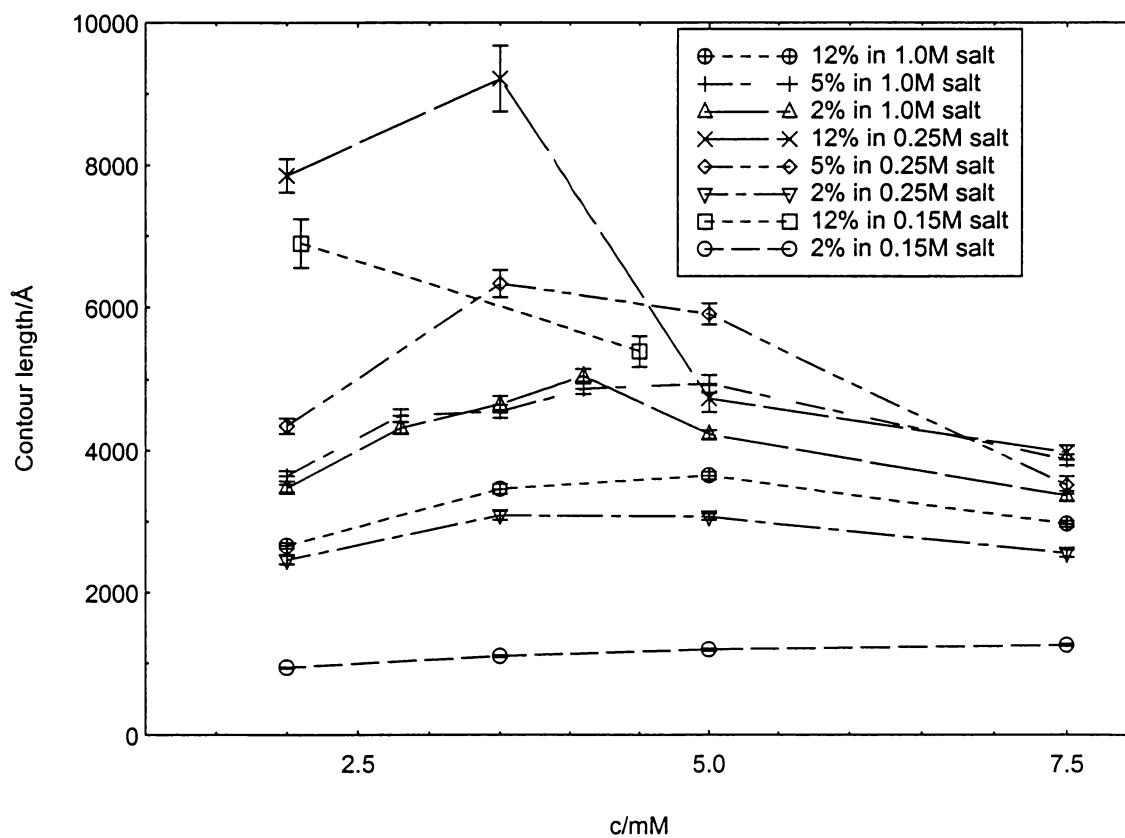


Figure 3.65 Dependence of micellar contour lengths on CTATos concentration in NaTos/Cl systems

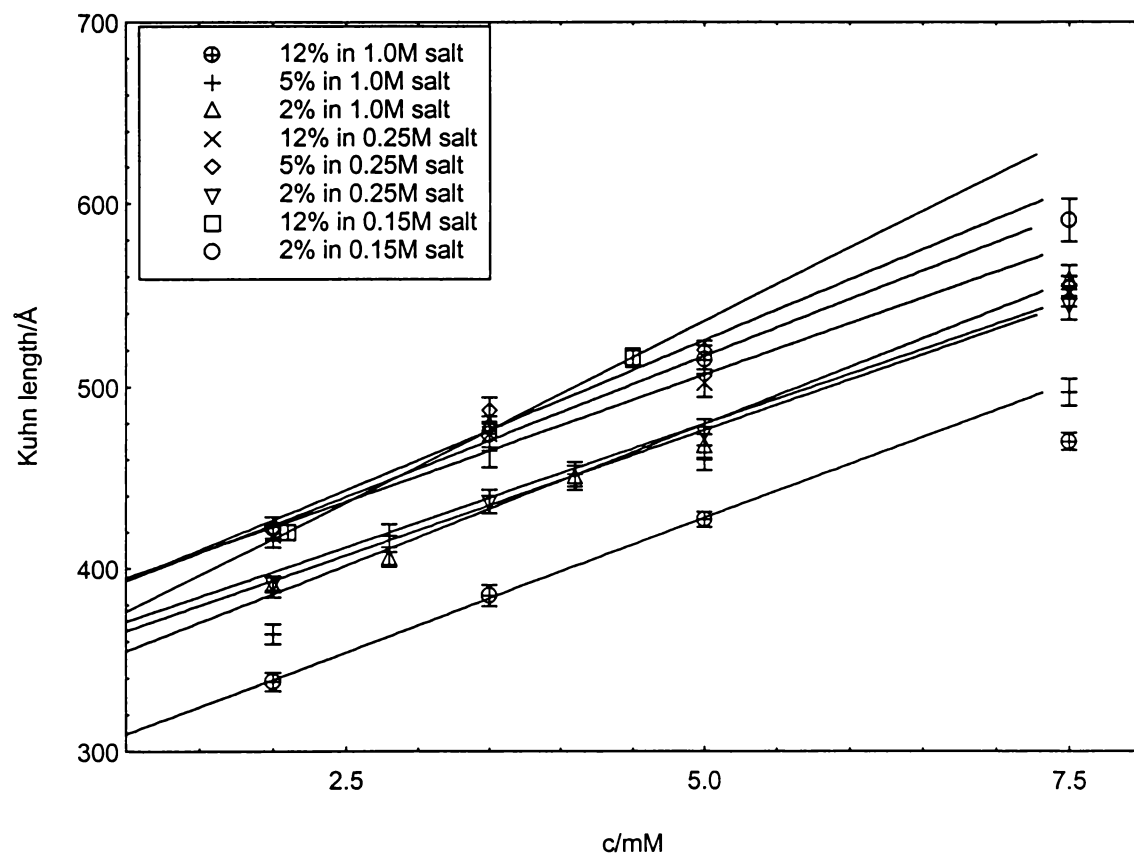


Figure 3.66 Dependence of micellar Kuhn lengths on CTATos concentration in NaTos/Cl systems

The persistence lengths, $l_p, c=0$, extrapolated to zero surfactant concentration, are shown as follows: $182 \pm 12 \text{ \AA}$ at 2 mole % NaTos in 0.15M; $168 \pm 9 \text{ \AA}$ at 12 mole % NaTos in 0.15M; $169 \pm 8 \text{ \AA}$ at 2 mole % NaTos in 0.25M; $183 \pm 9 \text{ \AA}$ at 5 mole % NaTos in 0.25M; $180 \pm 8 \text{ \AA}$ at 12 mole % NaTos in 0.25M; $140 \pm 7 \text{ \AA}$ at 2 mole % NaTos in 1.0M; $115 \pm 7 \text{ \AA}$ at 5 mole % NaTos in 1.0M; and $132 \pm 9 \text{ \AA}$ at 12 mole % NaTos in 1.0M. Unlike the contour length, we did not observe an effect from c^* , because SANS provides direct access to the micellar structure on the length scale of the Kuhn lengths. The length scale provided by the SANS for Kuhn length is in the intermediate Q region and only weakly dependent on intermicellar interactions and polydispersity effect. From the results on the persistence lengths, we observe in some cases the expected decrease with increasing ionic strength. This is the case for 2 and 5 mole percent NaTos salt, but not 12 mole percent NaTos systems, where the persistence length is largest at 0.25M total salt concentration instead of at 0.15M.

For CTATos in pure NaTos, the micellar contour lengths show an increase as the salt concentration increases from 0.02M to 0.05M. Above 0.05M NaTos, the micellar size starts to decrease. The c^* was also calculated for all the NaTos concentrations and only 7.5mM CTATos in 0.05M NaTos is above c^* (6.9mM in this case). Above 0.5M NaTos, the micelles are no longer large enough to be wormlike and fits are not included. Compared with the result⁶⁵ for CTA26ClBz in Na26ClBz solutions, where a maximum in contour length was reached at 0.2M salt, pure tosylate is more effective at causing a turnover in micellar size.

3.4.2 The CTASal/Cl micellar system in aqueous NaSal/Cl

SANS curves are discussed here for the CTASal/Cl micellar system in D₂O at 40°C. The effect of surfactant concentration effect was studied at 2 mole percent of NaSal in total salt (NaSal+NaCl) concentrations of 0.15, and 0.25M. CTASal of 10mM in different mole percents of NaSal in 0.25M total salt concentrations were also studied. Figures 3.67-69 present the SANS curves obtained for these systems. Some of the SANS experiments, namely 2, 10, 25, 50 and 80 mole % salicylate at 0.25M total salt, were performed at SINQ, in Switzerland. We encountered experimental difficulties there related to instability in detector electronics, so these data are less reliable than those from NIST. The surfactant concentration series at 2mole % salicylate were studied at NIST.

CTASal micelles also revert to globules in pure NaSal salt as the salt concentration reaches 1M. For 10.0mM CTASal/Cl in 0.25M total salt with different mole percents of NaSal in NaSal/Cl solutions, Figure 3.69 shows that the micellar size increases from sphere to long extended structures as the mole percent increases. The maximum in size occurs in the range of 5 to 25 mole percent Sal⁻. This phenomenon is similar to the effect of Na₂₆ClBz and NaTos, with increasing mole percents of penetrating counterion causing reversal in micellar size at higher salt concentration. Compared to NaTos and Na₂₆ClBz, the NaSal is the most effective at reducing the micellar size, while Na₂₆ClBz is least effective. On the other hand, nonpenetrating counterions like Cl⁻, Br⁻ never show the size reversal as counterion concentrations increase. The micellar size of 10mM CTASal at 0.25M NaSal is still larger than the size of 10mM CTAB in 0.25M NaBr

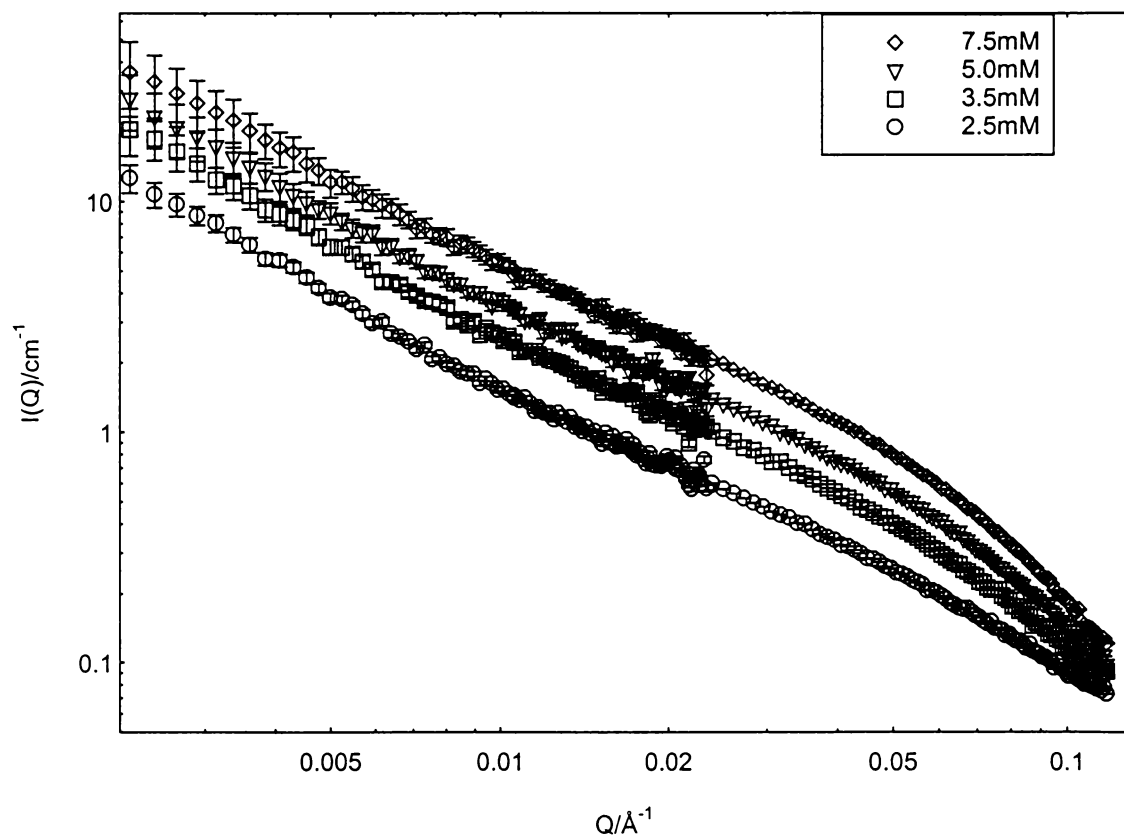


Figure 3.67 SANS curves for CTA micelles in 2 mole % NaSal/Cl in 0.15M salt at 40°C

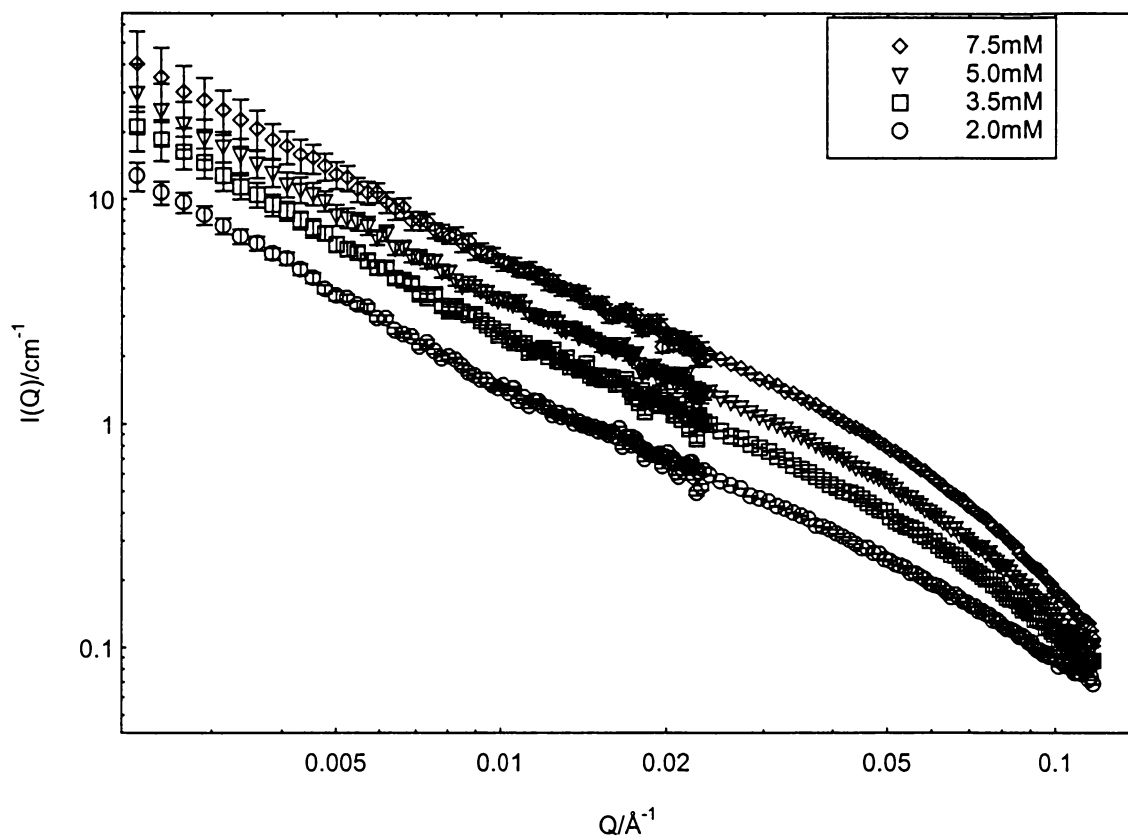


Figure 3.68 SANS curves for CTA micelles in 2 mole % NaSal/Cl in 0.25M salt at 40°C

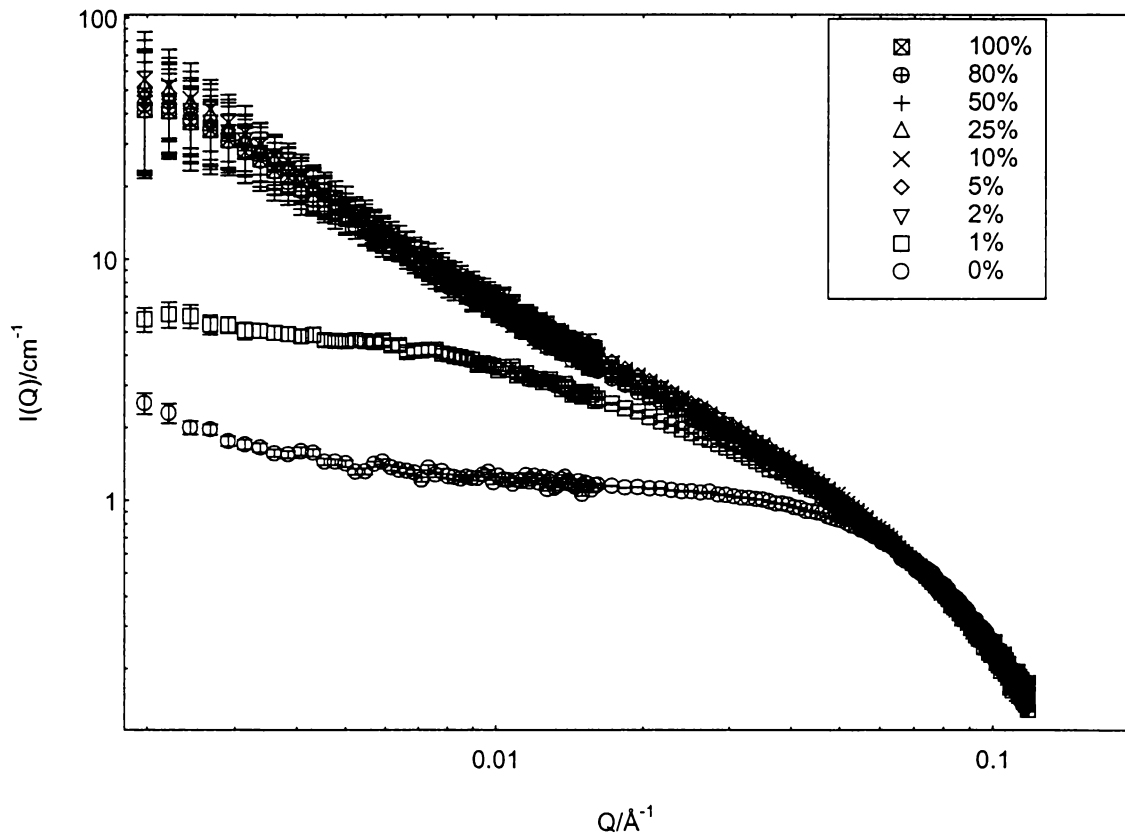


Figure 3.69 10mM CTACl in NaSal/Cl at 0.25M total salt, with the mole % of NaSal changing from 0% to 100%

solutions, but it will decrease as the NaSal concentration increases and increase as NaBr concentration increases.

The fits of the full scattering curve were performed without taking intermicellar interactions into account, using Eqn. 2.42-2.44. The polydispersity of the micellar system are fixed ($z=1$) and the value of scattering from solvent was also fixed. A grid search method for weighted non-linear least squares fitting was also used here and the detailed fitting results are tabulated in Table 3.11. The bending rod plots together with related fits are shown in figure 3.70-72.

Based on the fitting results, c^* was calculated by using Eqn. 1.7. The weight-average molecular weight was calculated from the fitted contour length, and R_g was directly from the fits. The solutions at 3.5mM CTA, which have the micelles with the largest fitted R_g 's, were tested. The c^* s obtained were: 4.8mM for 2 mole percent NaSal in 0.15M salt, and 4.5mM for 2 mole percent NaSal in 0.25M salt.

Figure 3.73 shows the fitted contour lengths, and their turnover with increasing c is consistent with a c^* between 3.5 and 5.0mM for both salt concentrations. The apparent Kuhn lengths increase as the surfactant concentration increases in both 2 mole percent Sal⁻ in 0.15M, and 0.25M NaSal/Cl. Figure 3.74 shows the Kuhn lengths, and as before, the real Kuhn lengths can be derived by extrapolating to zero surfactant concentration. The persistence lengths, $l_{p,c=0}$, are: $191 \pm 12\text{\AA}$ and $223 \pm 15\text{\AA}$ for 2 mole percent in 0.15M and 0.25M salt respectively. The system does not show Kuhn lengths decreasing as the total counterion concentration increases, the same phenomenon as was observed for 5 mole percent NaTos from 0.15M to 0.25M total salt.

Table 3.12 Fitted parameters for CTASal micelles in aqueous NaSal/NaCl mixed salt solutions without taking intermicellar interactions into account

2:98(mole percent) CTASal/Cl in 0.15M salt						
[CTA]/mM	A	Background	r_{cs} /Å	R_g /Å	$\langle L_n \rangle$ /Å	$\langle 2L_p \rangle$ /Å
2.0	37.3±3.7	0.0563	22.4± 0.1	1097	4449±440	483±8
3.5	75.9±11.8	0.0563	22.7±0.1	1265	5131±795	557±10
5.0	88.7±12.9	0.0563	22.4± 0.1	1184	4198±609	635±12
7.5	103.0±9.4	0.0563	22.4±0.1	1039	3252±298	675±13.2
2:98 CTASal/Cl in 0.25M salt						
2.0	42.1±5.5	0.0563	22.5± 0.1	1209	5098±659	503±8
3.5	82.0±13.3	0.0563	22.7±0.1	1328	5600±906	552±9
5.0	90.8±11.8	0.0563	22.7± 0.1	1170	4317±556	591±10
7.5	113±11	0.0563	22.5±0.1	1072	3592±341	628±11
10mM CTASal/Cl in 0.25M salt						
mole%. of NaSal	A	Background	r_{cs} /Å	R_g /Å	$\langle L_n \rangle$ /Å	$\langle 2L_p \rangle$ /Å
0	Too small to be fit by wormlike micellar model					
1						
2	101±6	0.0590	22.5± 0.1	841	2476±141	602±12
5	153±20	0.0590	22.3± 0.1	1182	3692±492	770±17
10	215±31	0.0590	22.1± 0.1	1362	5309±768	636±9
25	143±11	0.0590	21.4± 0.1	1067	3725±294	586±8
50	107±6	0.0590	20.7± 0.1	933	2945±182	598±10
80	99±6	0.0590	20.2± 0.1	900	2866±186	569±10
100	98±7	0.0590	20.1± 0.1	887	2709±185	599±12

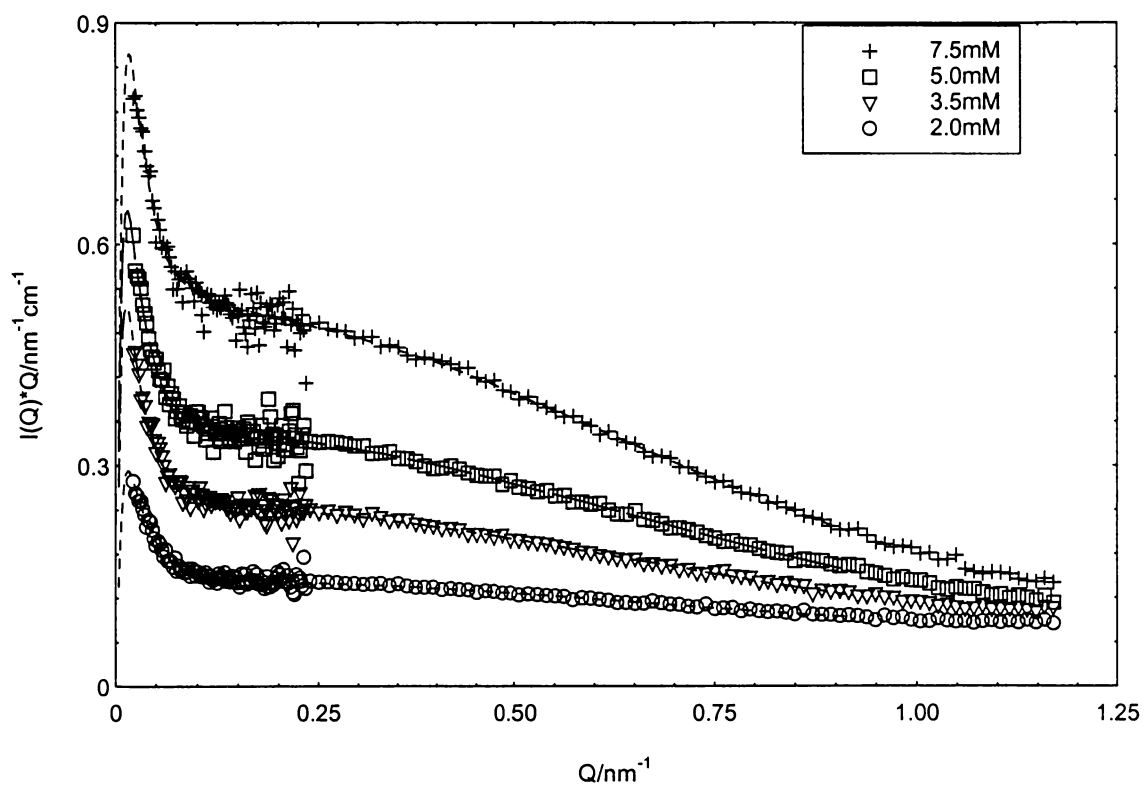


Figure 3.70 Bending rod plots of SANS data for CTASal with fits in 2 mole percent NaSal in 0.15M NaSal/NaCl. Fit without taking intermicellar interactions into account

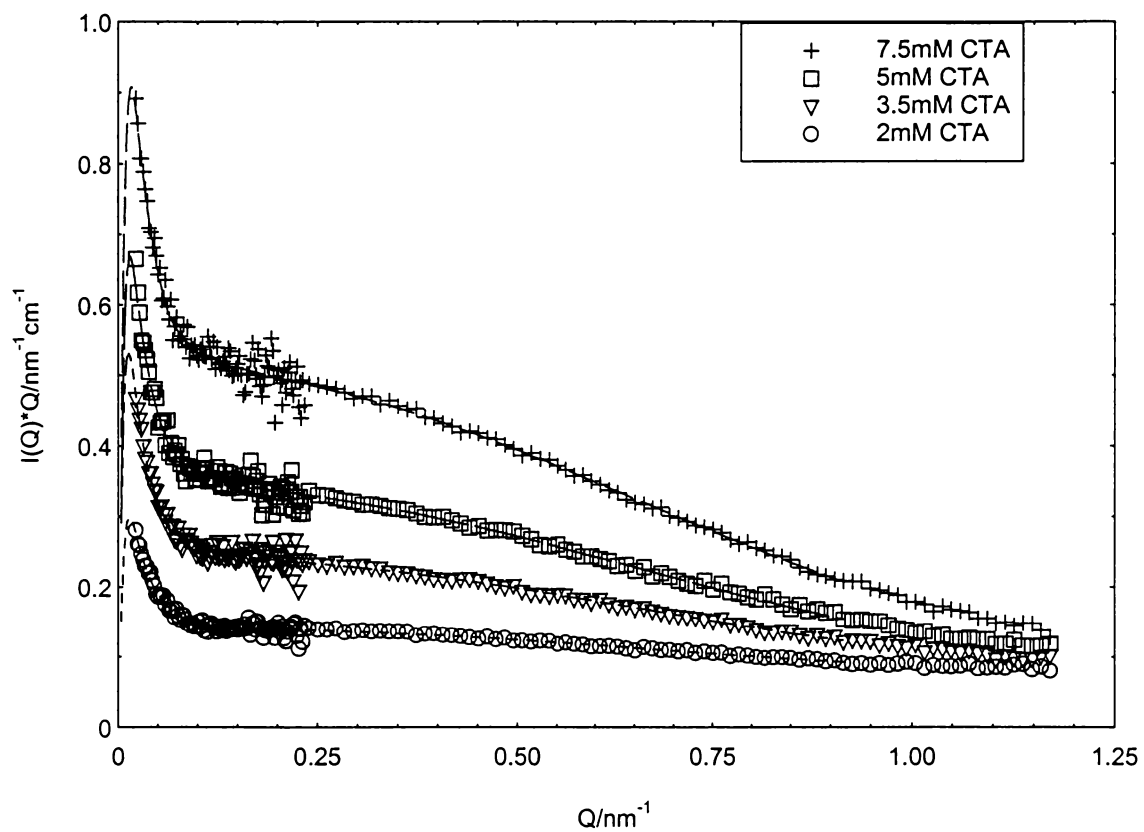


Figure 3.71 Bending rod plots of SANS data for CTASal with fits in 2 mole percent NaSal in 0.25M NaSal/NaCl. Fit without taking intermicellar interactions into account.

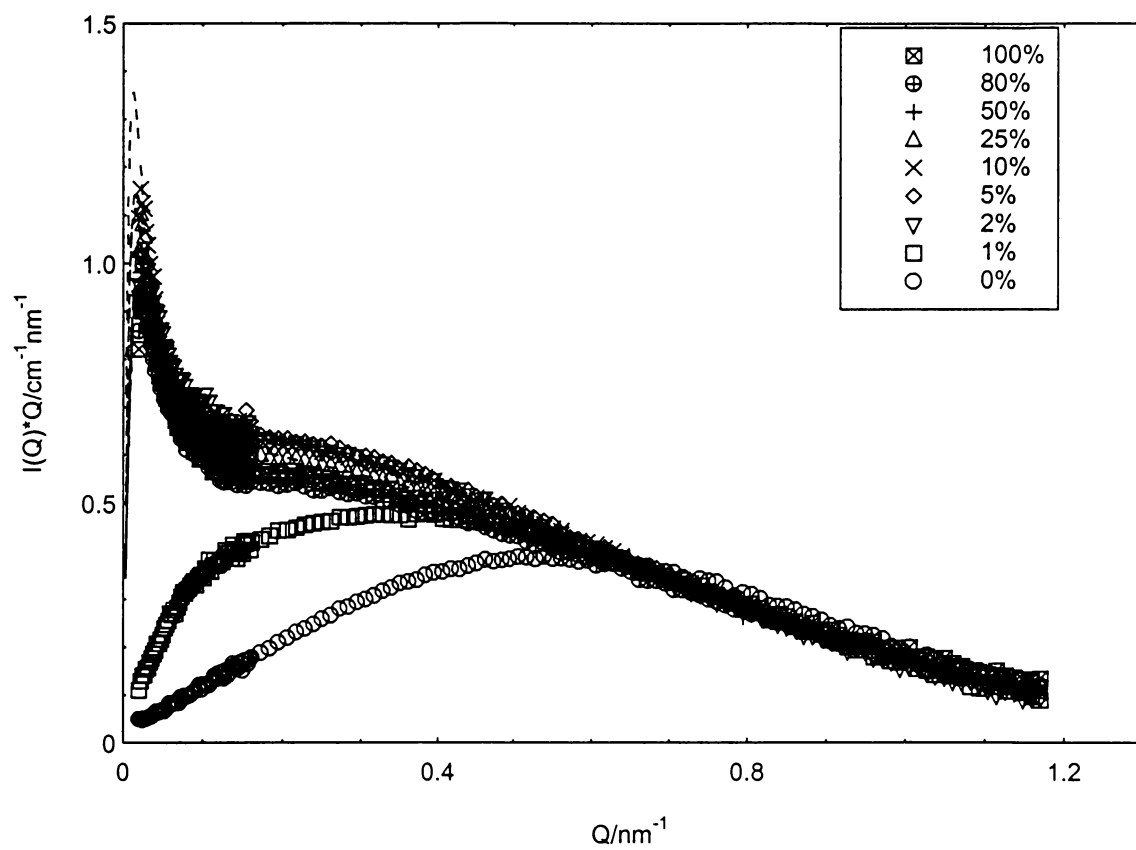


Figure 3.72 Bending rod plots of SANS data for CTASal with fits in 0.25M total salt with mole percent of NaSal changing from 0% to 100%. Fit without taking intermicellar interactions into account.

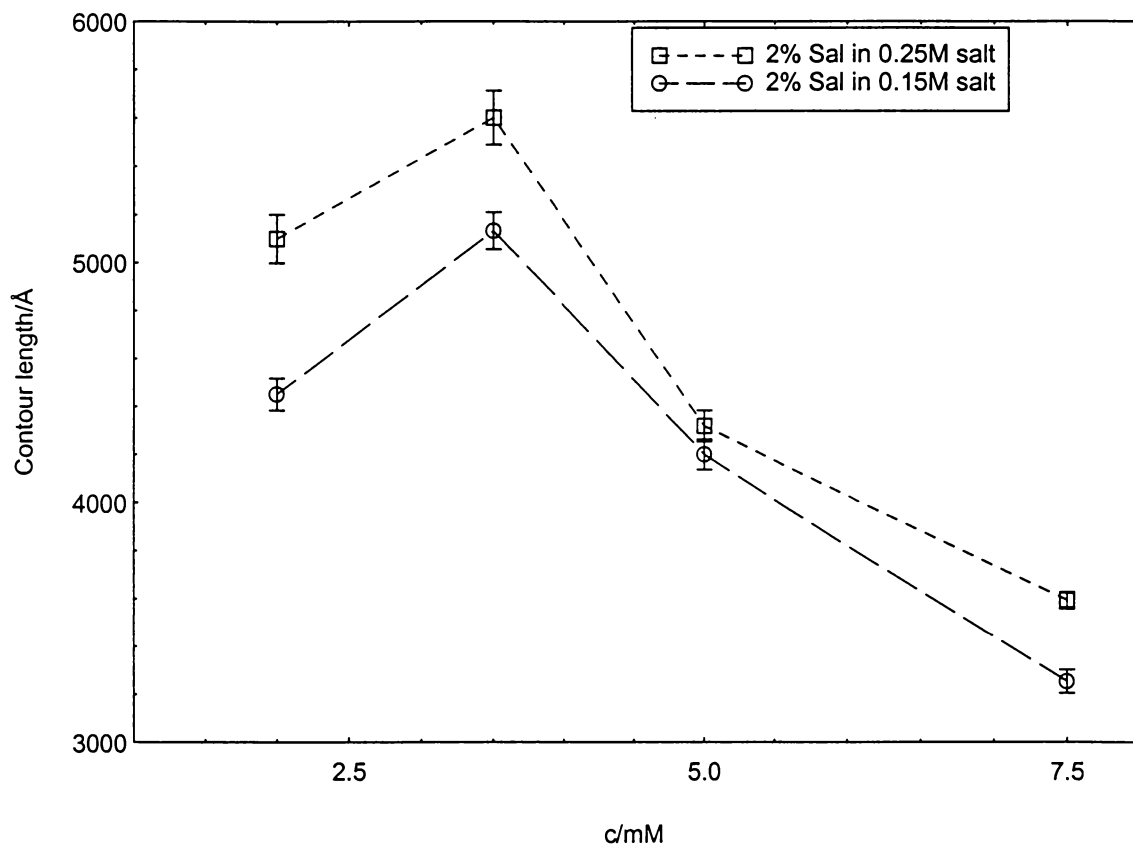


Figure 3.73 Contour lengths for CTASal micelles in 2mole% NaSal/Cl solutions

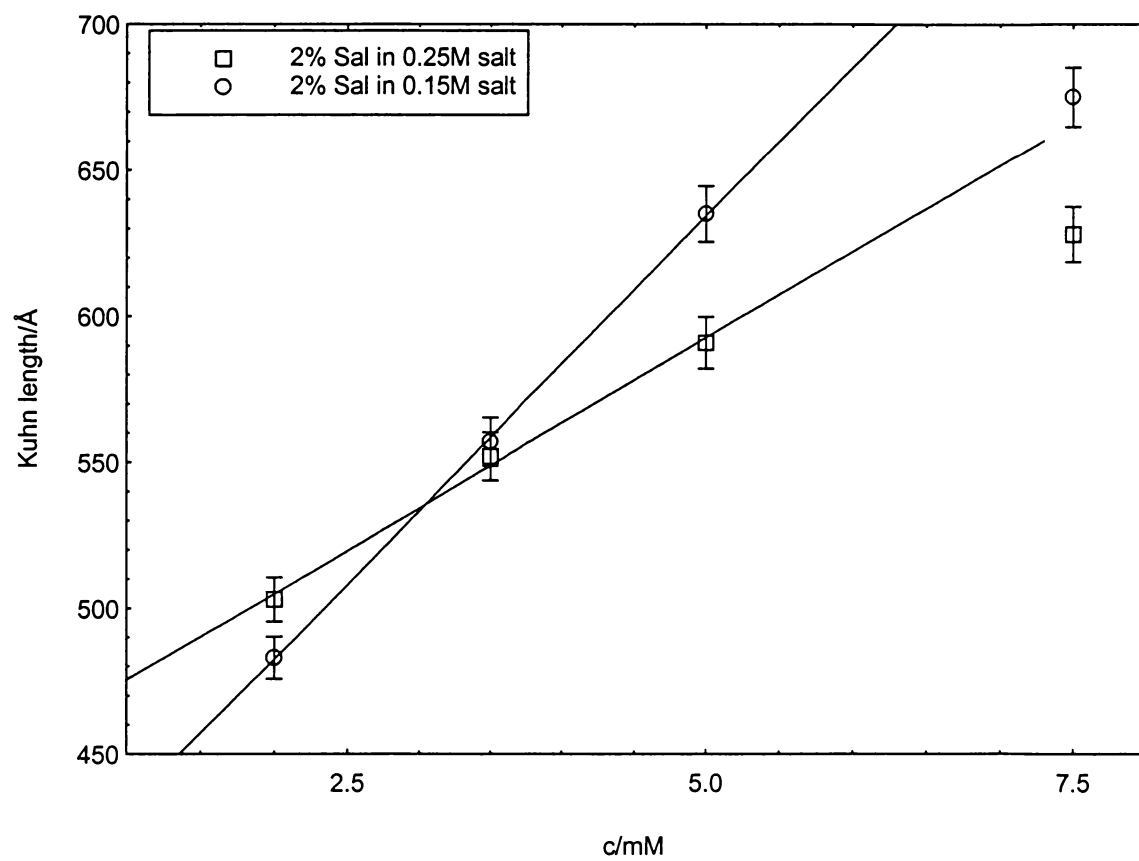


Figure 3.74 Dependence of micellar Kuhn lengths on CTASal concentration in 2 mole% NaSal/Cl in 0.15M salt

3.4.3 The CTA26ClBz/Cl micellar system in aqueous Na26ClBz/Cl

CTA26ClBz/Cl micellar systems were studied using SANS at 25°C: 10mM CTA26ClBz in 4M Na26ClBz/Cl with the mole percent of Na26ClBz increasing from 0% to 10%, Figure 3.75; 10mM CTA26ClBz in 2M Na26ClBz/Cl with the mole percent of Na26ClBz increasing from 0% to 15%, Figure 3.76. These experiments were performed following previous work in our group which concentrated on the dependence of micellar size on the ionic strength and mole percent of 26ClBz in mixed salt solutions of lower ionic strength. Figure 6c in reference 26 is analogous to figure 3.77 and 3.88, discussed below. In that work, a micellar size increase was reported in 1M mixed salt solution as the mole percent of Na26ClBz increased from 0% to 12%, followed by a decrease in micellar size as the % of Na26ClBz increases further. Here, we want to explore what will happen as the ionic strength increases for the mixed salt solutions. We realize that the single surfactant concentration studied, 10mM, is above c^* at some salt contents, below at others.

The full scattering curves were fit using Eqn. 2.42-2.44 and the same program described in previous sections. A flat background from solvent is subtracted and $M_w/M_n = 2$ is assumed ($z = 1$), as used for large micelles. The fitting results are tabulated in Table 3.13 and the experimental and fitted curves are shown as bending rod plots in Figure 3.77-78. As previously observed for mixed CTA26ClBz/Cl micellar systems,²⁶ the apparent Kuhn lengths decrease as the mole percent of Na26ClBz increases. In the results presented here, the decrease is from 684 to 520Å for 4M and 561 to 397Å for 2M total salt concentrations, Figure 3.79. Since only one surfactant concentration was studied, it is not possible to obtain values for $l_{p,c=0}$.

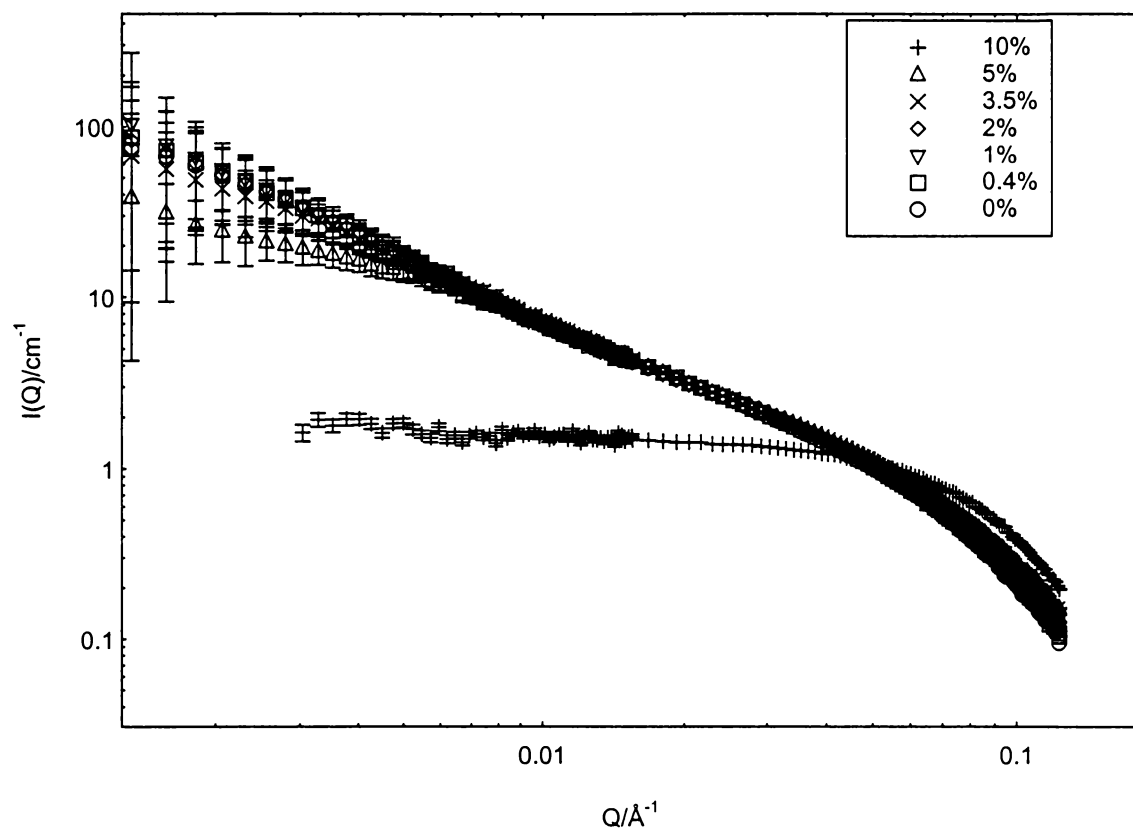


Figure 3.75 SANS curves for CTA26ClBz in 4M Na26ClBz/Cl at various mole percents of Na26ClBz at 25°C

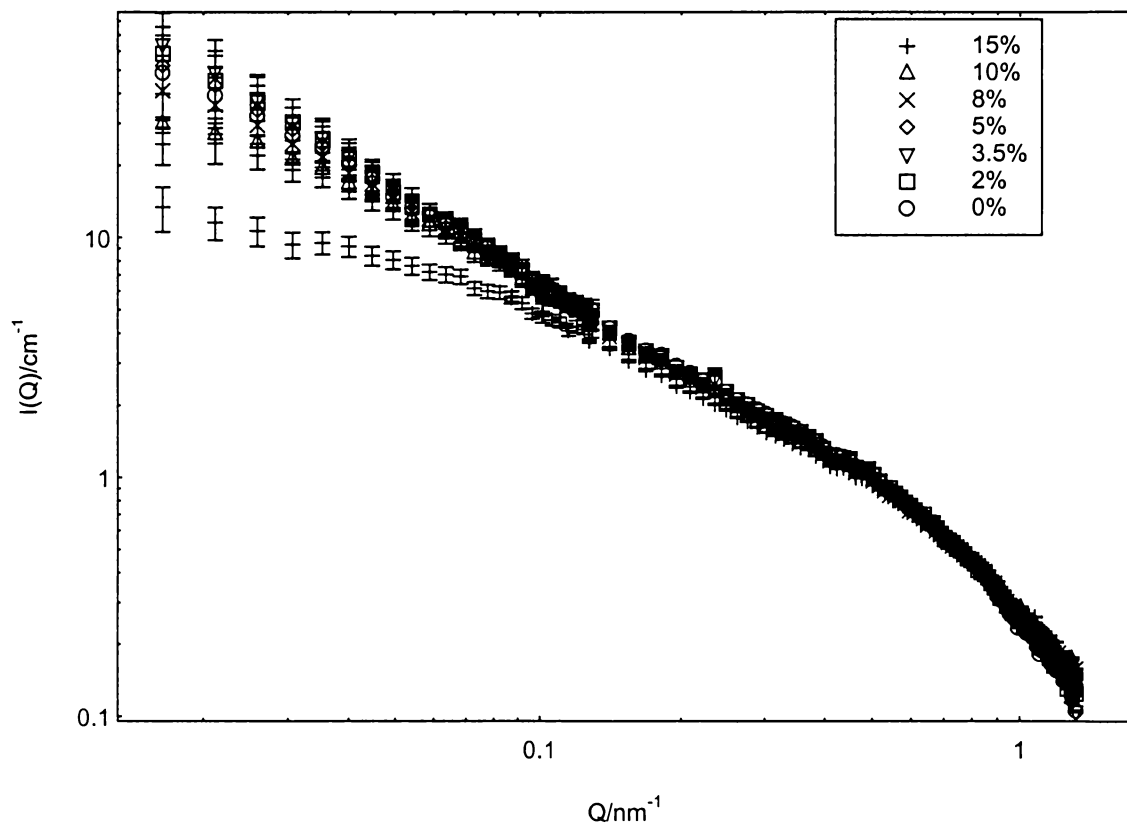


Figure 3.76 SANS curves for CTA26ClBz in 2M Na26ClBz/Cl at various mole percents of Na26ClBz at 25°C

Table 3.13 Fitted parameters for CTA26ClBz/Cl micelles in aqueous Na26ClBz/Cl mixed salt solutions, without taking intermicellar interactions into account

10 mM CTA2,6 in 4M salt						
Mole % Na _{2,6}	A	Background	r_{cs} /Å	R_g /Å	$\langle L_n \rangle$ /Å	$\langle 2L_p \rangle$ /Å
	110±3	0.0474	22.7±0.1	890	2677±78	616±10
0%	129±4	0.0474	22.5±0.1	1010	3079±98	684±10
0.4%	139±5	0.0474	22.2±0.1	1055	3357±115	668±10
1.0%	158±7	0.0474	21.6±0.1	1111	3825±177	624±9
2.0%	119±4	0.0474	20.8±0.1	925	2885±92	604±9
3.5%	71±2	0.0474	20.0±0.1	649	1715±49	555±13
5.0%	26.4±0.7	0.0474	17.1±0.2	331	640±16	520±30
10 mM CTA2,6 in 2M salt						
0.0%	66.8±4.3	0.0678	19.7±0.2	678	1826±116	561±30
2.0%	93.2±6.5	0.0678	19.3±0.2	824	2590±180	533±22
3.5%	103±7	0.0678	18.8±0.2	862	2922±205	495±19
5.0%	79.5±5.1	0.0678	18.8±0.3	758	2330±148	506±22
8.0%	50.6±2.5	0.0678	17.8±0.3	559	1535±74	449±21
10.0%	34.3±1.4	0.0678	17.2±0.2	436	1028±39	457±24
15.0%	10.9±0.4	0.0678	12.8±1.0	204	361±12	397±49

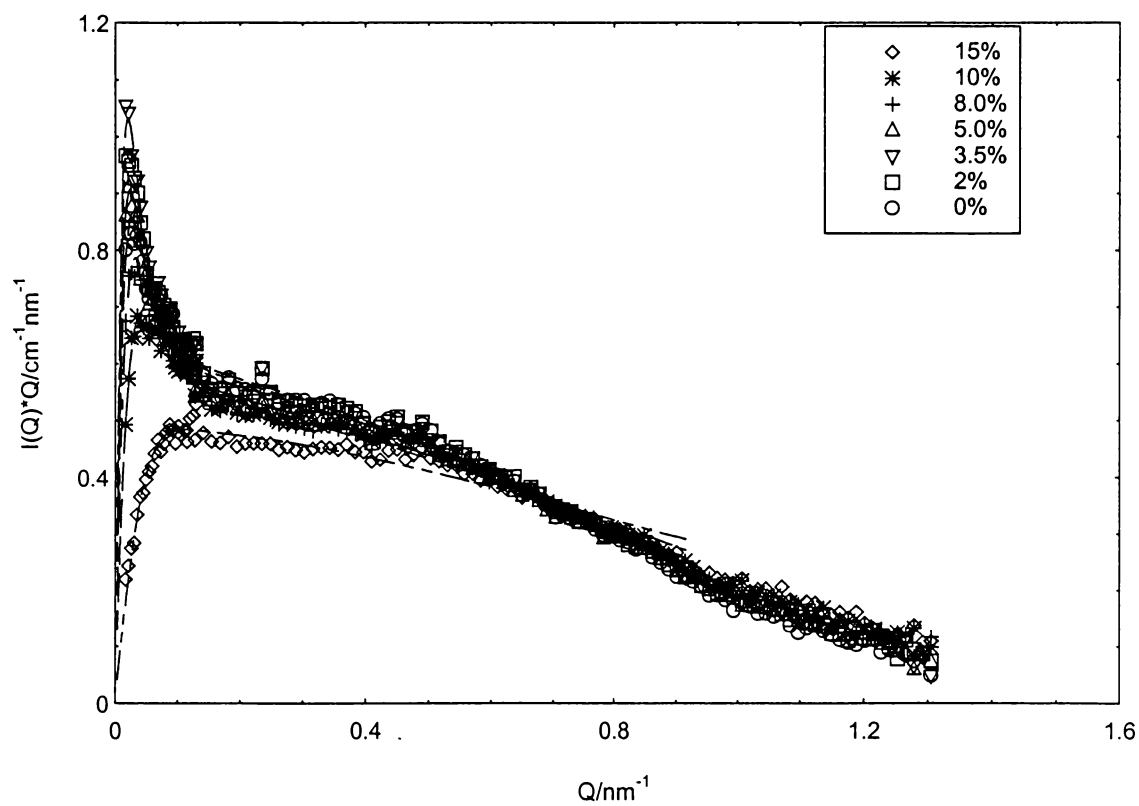


Figure 3.77 Bending rod plots of SANS data with fits for CTA26ClBz in 2M Na26ClBz/Cl at various mole percents of Na26ClBz at 25°C

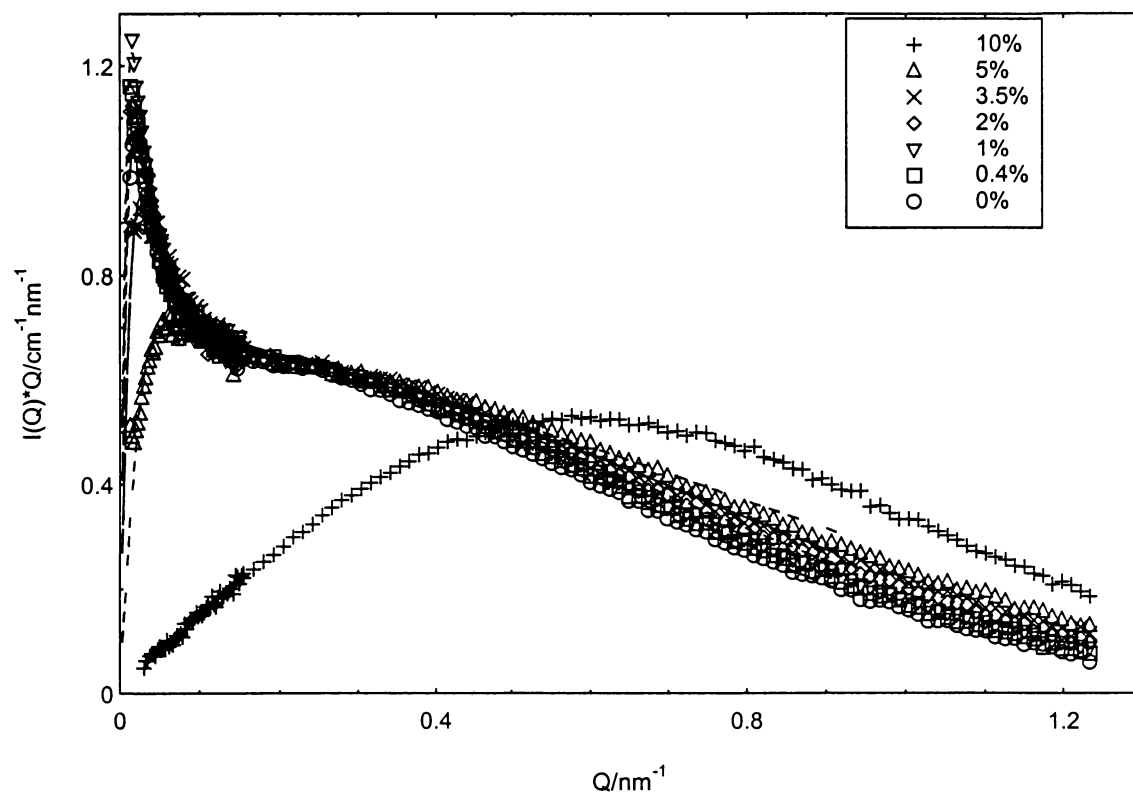


Figure 3.78 Bending rod plots of SANS data with fits for CTA26ClBz in 4M Na26ClBz/Cl at various mole percents of Na26ClBz at 25°C

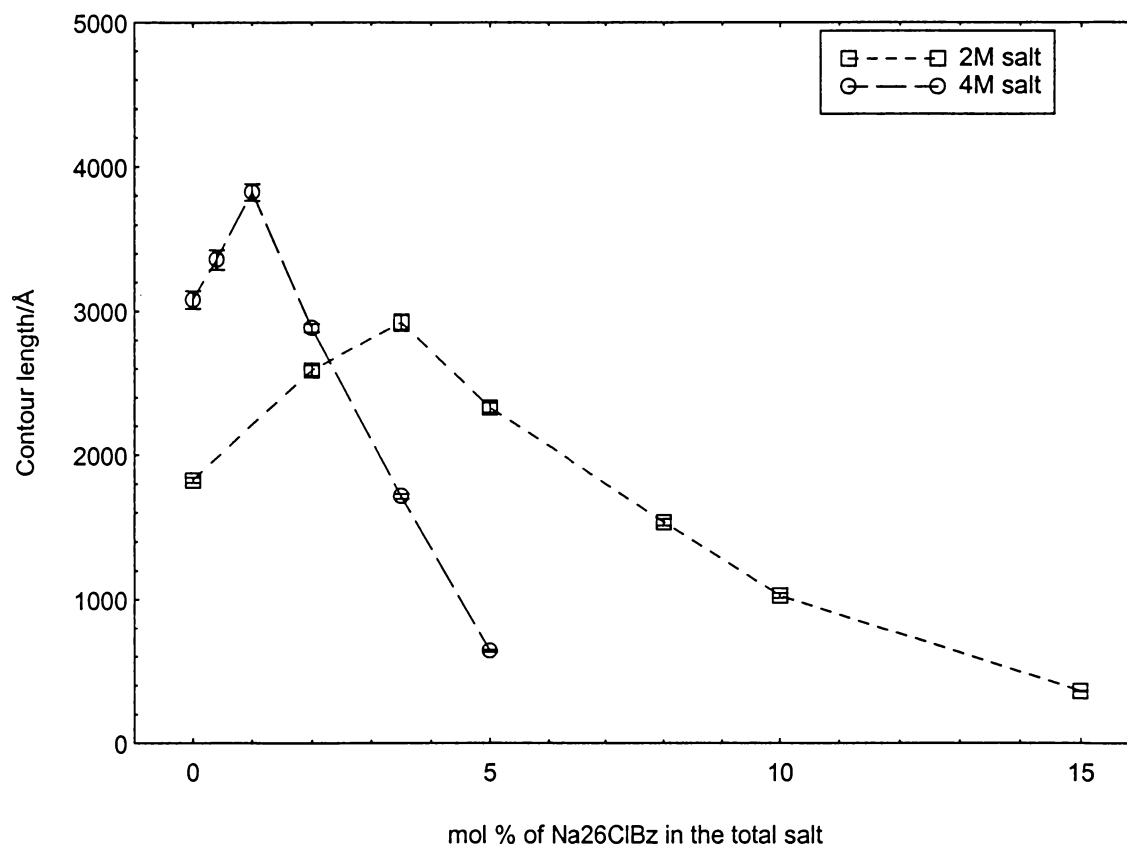


Figure 3.79 Contour lengths for CTA₂₆ClBz in 2M and 4M total salt, as a function of the mole % of Na₂₆ClBz

The contour lengths from the fits are shown in Figure 3.80. Compared with the case of 1M total salt,⁹⁵ where the micellar size reaches a maximum at 12 mole percent Na26ClBz, the micellar size reaches a maximum at 3.5 mole percent in 2M total salt and 1 mole percent in 4M total salt.

The changing of micellar size by changing the ratio of the counterions is consistent with the counterion effect on the micellar end-cap energies from G_1 and G_2 , and the electrostatic contribution G_3 from Eqn. 1.1. The micellar growth or shrinkage is mainly based on the energy competition between spherical (sph or end-cap) and cylindrical (cyl) surfactant environments. The cylindrical environment is characterized by smaller areas per head group, suggesting less hydrocarbon/water interface per surfactant ion, and a smaller cross-sectional radius.

Two parameters, γ (the counterion inventory) and κ^{-1} (the Debye screening length), are introduced as important for the changes in micellar size. γ , the fraction of bound counterions that are 26ClBz^- , is defined as $[26\text{ClBz}^-]_{\text{mic}}/0.9c$, which can be calculated from the selectivity coefficient, K as follows:⁹⁴

$$K_{26\text{ClBz}^-/\text{Cl}^-} = ([26\text{ClBz}^-]/[\text{Cl}^-])_{\text{mic}}([\text{Cl}^-]/[26\text{ClBz}^-])_{\text{free}} \quad (3.1)$$

Assuming 90% counterion binding on the micellar surface, $[26\text{ClBz}^-]_{\text{mic}} + [\text{Cl}^-]_{\text{mic}} = 0.9c$. In order to establish the value γ at the maximum in micellar size, use $K = 16.8$.⁹⁴ The following γ s are: for 1 mole % in 4M Na26ClBz, γ is 15%; 3.5 mole % in 2M, γ is 38%; and 12 mole % in 1M Na26ClBz, γ is 60%.

The dependence of the micellar size on γ comes from the following factor: 1) An increase in γ can decrease the cross-sectional radii, as the alkyl chains pack around the

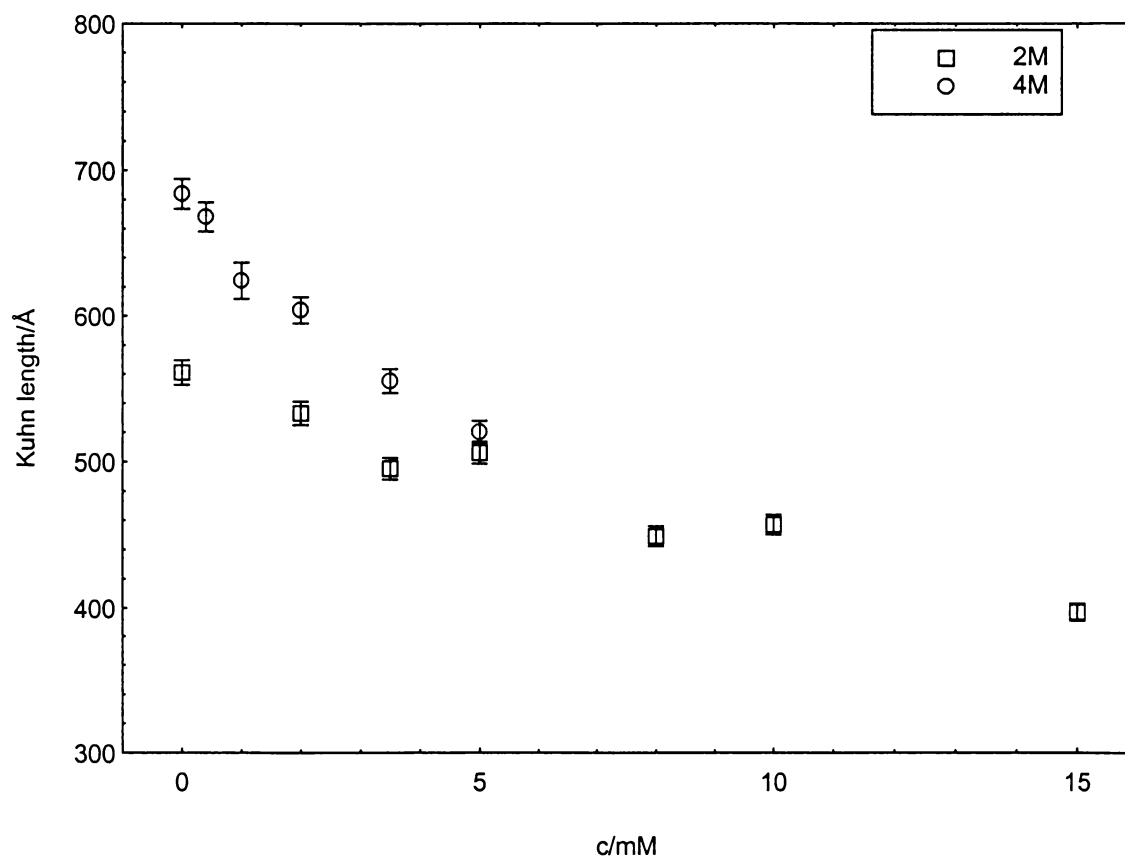


Figure 3.80 Dependence of micellar Kuhn lengths for CTA26ClBz, in 2M and 4M total salt, on the mole % of Na26ClBz

counterions' aromatic rings, thus increasing the number of gauche conformations in the cylinder portion. This makes $G_{1, \text{cyl}}$ less favorable relative to $G_{1, \text{sph}}$. 2) The increase in γ can decrease the surface energy (G_2), depending on whether the increase in A_{hg} or the decrease in hydrocarbon/water interface tension dominates. 3) The increase in γ can decrease the electrostatic energy between the head groups and have end-cap less favored. The increase in salt concentration affects G_3, cyl relative to G_3, sph up to 1M salt, put its importance at 2M and 4M salt, because $G_3 \propto \kappa^{-1}$, is doubtful.

Thus we assume that the usual case is that $G_{3, \text{sph}} - G_{3, \text{cyl}}$ is either always negative (electrostatics favor sphere) or can be neglected. Counterion penetration (increase γ) can diminish the difference, lower $G_{3, \text{cyl}}$ relative to $G_{3, \text{sph}}$. Further, we assume that increasing γ can change the sign of $G_{1, \text{sph}} - G_{1, \text{cyl}}$ from positive at low γ to negative to positive at high γ . And, we guess that the lowering of interfacial tension with increasing γ outweighs the increased exposure of interface, so that the term $G_{1, \text{sph}} - G_{1, \text{cyl}}$ becomes more negative (sph favored). Thus spheres are of lower free energy at high γ .

3.5 CONCLUSIONS

3.5.1 Micellar flexibility

Real total persistence lengths obtained by extrapolating to $c = 0$ from the apparent persistence lengths measured by SANS for the micellar systems studied in this chapter are in the range of 96Å to 240Å. In chapter I, we have discussed that determinations of persistence lengths by light scattering give anomalously large values that sometimes

show (apparent) increases, instead of the expected decreases, with increasing ionic strength. The results

from LS come from the comparison of R_g and the hydrodynamic radius R_h or the apparent molar mass M_{app} and R_g .^{96, 101, 102} In the analysis of LS data, polydispersity and intermicellar interactions have not been taken into account in some cases. Neglecting the polydispersity in model calculations for semi-flexible particles leads to an overestimation of l_p due to characteristic weighting of the experimental quantities determined in SLS and DLS experiments.¹⁰³ The results from the LS highly depend on the interactions between the particles. SANS measurements provide a length scale suitable for direct measurement of l_p 's. As Schurtenberger and Pedersen have shown,¹⁰³ by extrapolating to zero surfactant concentration, the influences of interparticle interactions are removed and real l_p are obtained.

Effect of ionic strength (c_s)

The effect of ionic strength has been studied in Section 3.2 and 3.3 for several different surfactant systems, both anionic and cationic. In all the systems, the total persistence length decreases as the ionic strength increases. This behavior has also been observed for highly flexible polyelectrolytes such as sodium polystyrenesulfonate (NaPSS).^{104, 105} From Eqn. 1.8, the persistence length can be presented as intrinsic persistence length, $l_{p,0}$, and electrostatic persistence length, $l_{p,e}$. The intrinsic persistence length depends on the cross-sectional radius.

For NaPSS, $l_{p,0}$ is generally accepted to be 14\AA .¹⁰⁶ Nordmeier and Dauwe¹⁰⁴ observed $l_p = 52\text{\AA}$ for 84% quaternized NaPSS at 2M NaCl. This suggests that the

majority of the polymer coils' rigidity is still of electrostatic origin, even when the Debye screening length is only 0.2nm (2M NaCl). Some more rigid polyelectrolytes, such as sodium hyaluronate³⁶ in 0.4M NaCl or DNA¹⁰⁵ in 0.5M LiCl do show scaling law behavior, $l_{p,e} \sim c_s^{-x}$. However the exponent obtained experimentally does not agree with Debye-Huckel-based models ($x=1$):^{36,37} x equals 0.5 for hyaluronate and NaPSS, and 0.3 for DNA. LeBret's numerical approach³⁸ to persistence lengths can give $x = 0.5$.

In order to test the scaling law for $l_{p,e}$, for our micellar systems, we choose the $l_{p,0}$ values as follows based on the approach of Appell and Porte¹⁴: SDS is 78 Å; CTAB and CPyBr are 90 Å (with same cross-sectional radius); and TTAB is 84 Å (cross-sectional radius between SDS and CTAB). These equation used in reference 14 is: $\langle \cos\phi \rangle = \exp(-2d/l_{p,0}) = 0.25$. In the model, the wormlike chain is considered equivalent to beads of diameter d on a string, and a hydrated cross-sectional diameter is used. A hydrated diameter 50 Å for SDS¹⁰⁷ was used instead of 34 Å derived from neutron scattering (neutron scattering provides the dimension). Similar to the SDS, a value of 60 Å for CTAB was used instead of 48 Å from neutron scattering.¹⁴ An estimate of 54 Å used for TTAB gave us an $l_{p,0}$ value of 84 Å. Figures 3.81-3.84 show $\ln(l_{p,e})$ vs. $\ln(c_s)$ for these systems. Although we did see $l_{p,e}$'s decreasing with increasing c_s , we did not observe scaling laws for our systems. This suggests that the partitioning between $l_{p,e}$ and $l_{p,0}$ is more difficult than expected, namely the excluded volume effect, and solvent quality changes can all be a reason to change $l_{p,0}$. For all the value of $l_{p,e}$ s, the only one that reaches zero is for CPyBr in 0.8M NaBr systems. Unfortunately, we do not have data in 1M salt to support this conclusion.

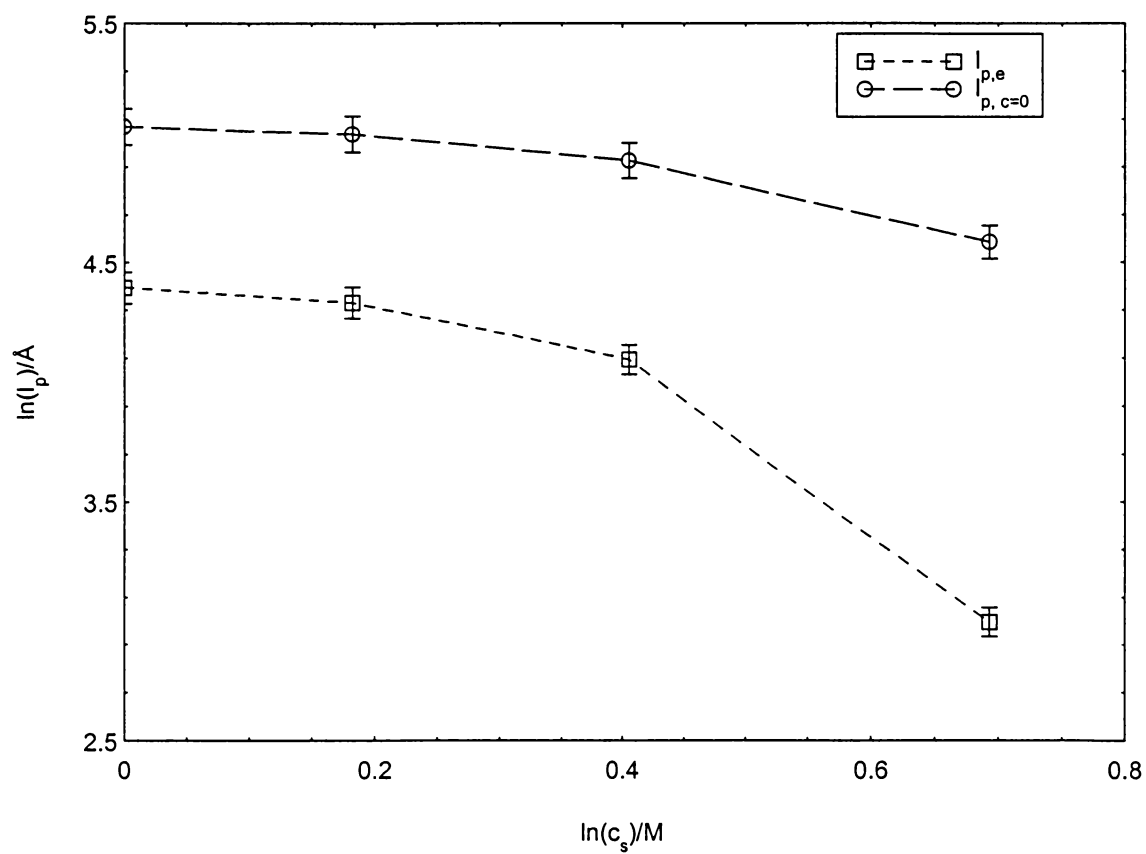


Figure 3.81 $\ln(l_p)$ vs. $\ln(c_s)$ for SDS micellar systems at 45°C

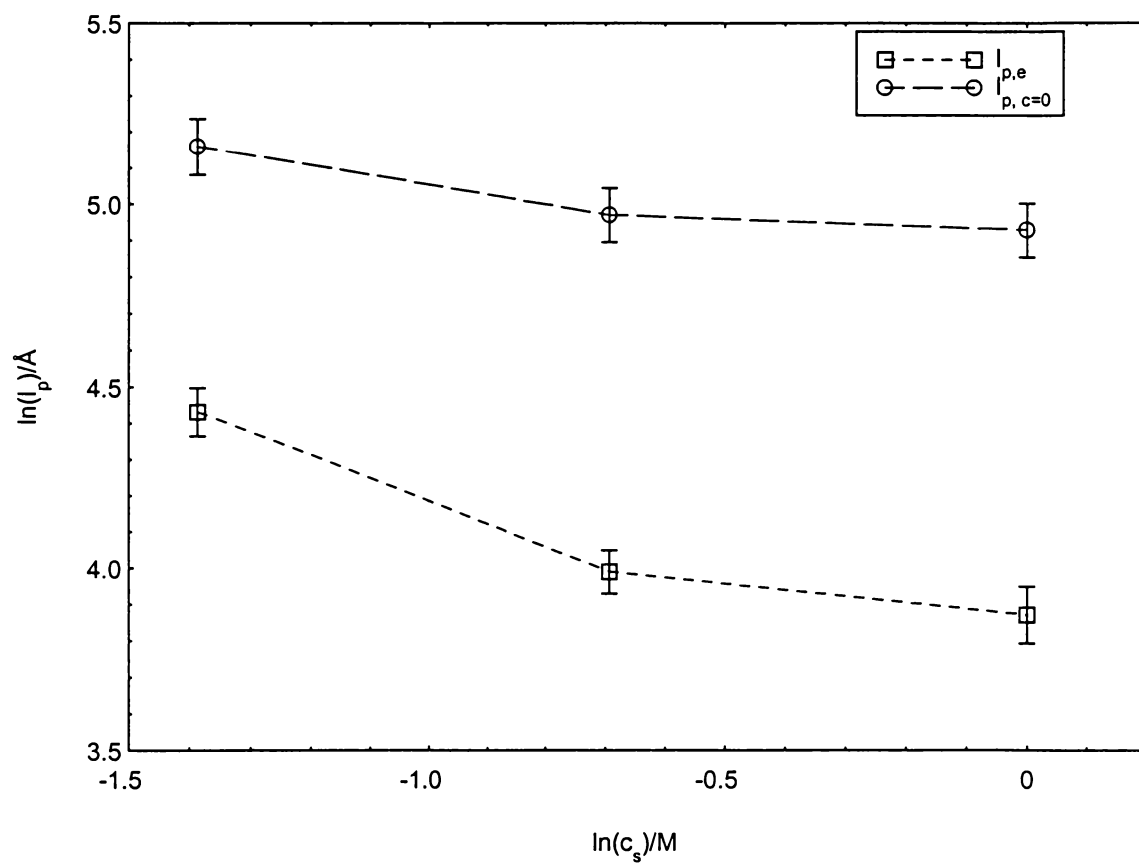


Figure 3.82 $\ln(l_p)$ vs. $\ln(c_s)$ for CTAB micellar systems at 40°C

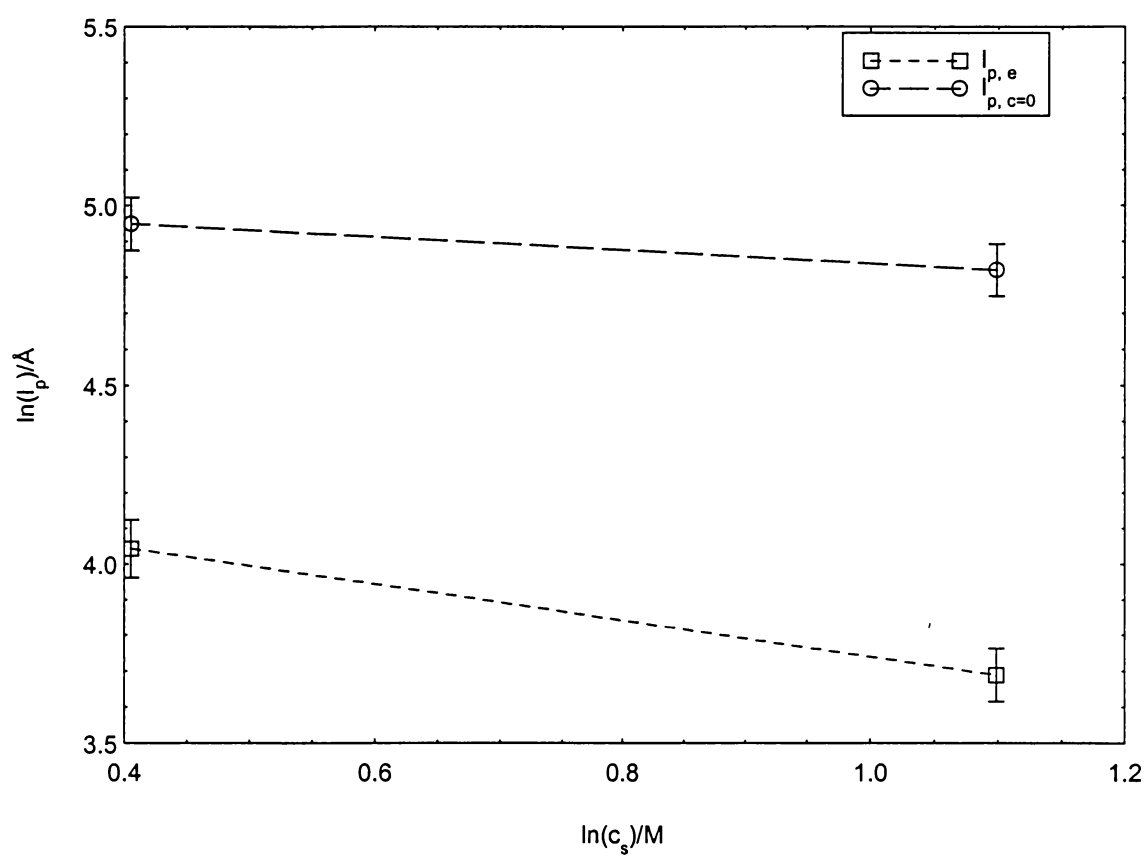


Figure 3.83 $\ln(l_p)$ vs. $\ln(c_s)$ for TTAB micellar systems at 40°C

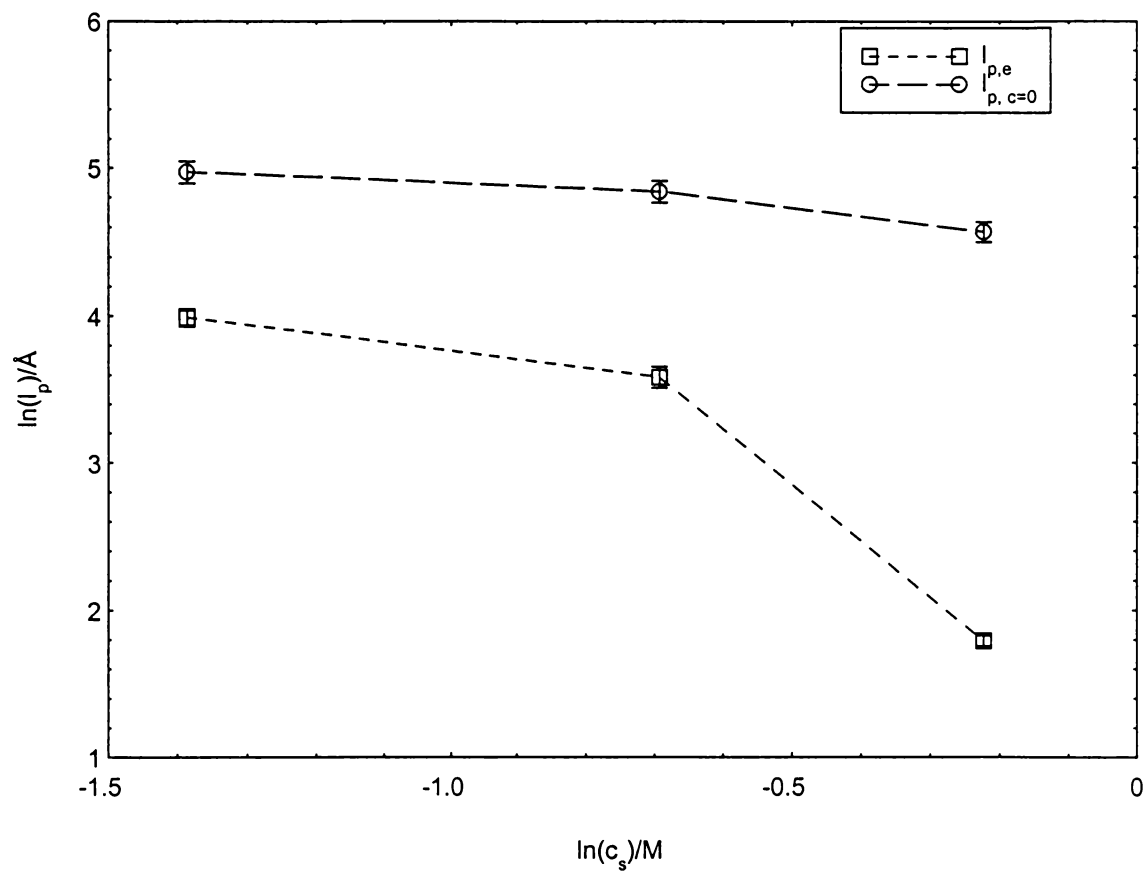


Figure 3.84 $\ln(l_p)$ vs. $\ln(c_s)$ for CPyBr micellar systems at 40°C

Effect of tail length and head group structure

We observed the unexpected result, Table 3.9, that the persistence length for TTAB at higher ionic strength is similar to CTAB micelles at lower ionic strength. Extrapolating the data in Figure 3.82 for the CTAB micelles to 1.5M NaBr, we obtain a $l_{p,t}$ value of 132 Å. For TTAB micelles, we expected a smaller $l_{p,0}$ as discussed above, thus giving a smaller $l_{p,t}$ for the TTAB micelles compared to the CTAB micelles at 1.5M NaBr. Instead, the value obtained for the TTAB micelles was 141 Å. The difference in the two is only 9 Å, not much larger than the error bars on the two numbers. This further supports that the partitioning between $l_{p,e}$ and $l_{p,0}$ may be more complicated than what we expected. SDS micelles have a larger total persistence length than CTAB micelles in 1M salt. This indicates that the persistence length depends on the structure of the surfactant. Persistence lengths of CPyBr, which has a less bulky head group, decreases more rapidly than CTAB as the ionic strength increases because a less bulky head group make the counterions easier to screen the electrostatic interactions and thus make the ionic strength changing more effective on the changing of the electrostatic persistence length.

Effect of counterion structure

We already know that 26ClBz^- makes CTA micelles more flexible than Br^- .^{65, 95} CTA micelles in 0.25M NaBr have an $l_{p,c=0}$ of 174Å. For CTA micelles in mixed NaTos/Br systems, at 2, 5, and 12 mole % NaTos in 0.25M total salt, assuming a selectivity coefficient, K , equal to 80, we have Tos^- 62%, 81% and 92% respectively of total counterions on the micellar surface. The mean persistence length equals 177Å, which is similar to CTAB micelles in 0.25M NaBr. This can be further verified from

NaBr, where $l_{p,app}$ is 241Å. For CTA in mixed NaSal/Br systems, at 2 mole % NaSal in 0.25M total salt a K of 80 predicts 62% Sal^- on the micellar surface, we have a persistence length 223Å, which is larger than in 0.25M NaBr. From these results, we find that the counterion increases the micellar flexibilities as follows: NaSal < NaTos ~ NaBr < Na26ClBz.

3.5.2 Micellar size

Effect of counterion structure on growth of wormlike micelles

With different counterions, the micellar size changes. For example, our published data shows that:²⁶ $\langle L_n \rangle$ is 66Å for 7.5mM CTACl in 1M NaCl; $\langle L_n \rangle$ is 507Å of 20mM CTA26ClBz for 0.2M Na26ClBz. The data in this chapter shows that: $\langle L_n \rangle$ is 1638Å for 7.5mM CTAB in 0.25M NaBr; $\langle L_n \rangle$ is 2176Å for 7.5mM CTATos in 0.25M NaTos; and $\langle L_n \rangle$ is 2709Å for 10mM CTASal in 0.25M NaSal. At low salt, we obtain the order of effectiveness in producing growth as follows: NaCl < Na26ClBz < NaBr < NaSal < NaTos. For penetrating counterions, a smaller contour length was observed for 26ClBz⁻ compared with Sal⁻ and Tos⁻ counterions because Sal⁻ and Tos⁻ bind more strongly than 26ClBz⁻, causing a more rapid screening of head group repulsions and hence micellar growth. The weaker binding for 26ClBz⁻ is probably due to the steric bulk of Cl's adjacent to the COO⁻ groups, which makes the counterion more difficult to insert between the head groups. By using mixed salts (penetrating plus nonpenetrating counterions), we can increase the micellar size dramatically in some systems. In previous research, mixed Na26ClBz/NaCl at various mole percent of Na26ClBz was been studied, and we observed that the micellar size for mixed salt of Na26ClBz/NaCl at some percentage

$\langle L_n \rangle$ is 1768Å for 5.0mM CTA26ClBz/Cl in 12 mole % of Na26ClBz in 1M Na26ClBz/Cl) is larger than in either NaCl or Na26ClBz alone. NaTos/NaCl and NaSal/NaCl have also been studied during the last few years, and we observed that the micellar sizes in both cases can increase dramatically (above 5000Å). For 3.5mM CTATos/Cl in 2 mole % of NaTos in 1M NaTos/Cl, $\langle L_n \rangle$ reaches 4648Å. For 3.5mM CTASal/Cl in 2 mole % of NaSal in 1M NaSal/Cl, $\langle L_n \rangle$ reaches 5600Å.

Effect of counterion structure on reversion of micelles from wormlike to globular

In Section 3.3, the scaling law for surfactant $\langle L_n \rangle$ vs. c has been discussed, and we observed that the micelles continue to grow for nonpenetrating counterions as the counterion concentration increases. For penetrating counterions, a reversion of the micelles from wormlike to globular has been observed as a general phenomenon as the salt concentration increases for NaSal, NaTos, and Na26ClBz systems. Further study on why the micelles get smaller when NaClBz is the salt will be discussed in Chapter IV.

CHAPTER IV

USING INTERNAL AND EXTERNAL CONTRAST VARIATION TO STUDY THE DETAILED STRUCTURE OF THE MICELLAR SURFACE

4.1 INTRODUCTION

Micellar structure in aqueous solutions of cationic surfactants such as cetyltrimethylammonium (CTAX) can be changed by changing the counterions, X^- .^{65, 95} With increasing counterion concentration, some nonpenetrating counterions (Cl^- , Br^-) can increase the micellar size in order from globular, to short rod, to elongated wormlike micelles. Other counterions (26ClBz etc.) penetrate into the micellar interface to change the micellar structure in order from globular micelles, to short rods, to elongated wormlike micelles, and finally back to globular micelles. There is still no clear explanation on why the penetrating counterions drive the micellar size smaller again at higher salt concentration. Do the counterions bind to the micellar surface at a counterion to surfactant ratio greater than one, causing the net micellar charge to reverse from positive to negative and increase the electrostatic energy (G_3 in eqn. 1.1) on the surface? Does the penetrating counterion penetrate into the micellar surface more deeply at higher salt concentration and increase the surface energy (G_2 in eqn. 1.1)? Or is there a combination of both? Studying the interaction between counterion and cationic surfactant - both the amount of counterion binding and the binding loci - can help us fully understand the formation of the micelles and why some penetrating counterions cause a reversal of the micellar size. SANS has been used to determine the internal structure of rod-like and spherical micellar structures by the methods of external and internal contrast

variation.^{71-74, 108, 109} For CTA2,6-dichlorobenzoate, we have used deuterated 2,6-dichlorobenzoate counterion, surfactant with deuterated C₁₆ tails, and changes in the D₂O/H₂O content of the solvent in our experiments, in order to get detailed information on counterion binding.

4.1.1 External and internal contrast variation

For external contrast variation, we change the scattering length density of the solvent, ρ_s , and keep the micellar scattering length density, $\bar{\rho}_m$, constant. The surfactant concentration is also held constant. Using different mixtures of H₂O and D₂O as the solvent, we can change the scattering length density very easily. Salt also affects ρ_s , and this is taken into account. Detailed calculations will appear in the following sections. From Guinier plots, we observed changes in R_g with changes in ρ_s . Using a plot of $I(0)^{1/2}$ vs. percentage of the D₂O, or ρ_s from equation 2.54, we can get a straight line. The match point, where $I(0)^{1/2} = 0$, is reached when $\rho_s = \bar{\rho}_m$. From $\bar{\rho}_m$, the micellar contents and in particular the percentage of counterion binding on the micellar surface can be derived. We used deuterated Na26ClBz or the deuterated surfactant to make the micelles have larger contrast between the shell and core of the micelle itself. Figure 4.1 gives some idea about the contrast between core, shell and the solvent. Our purposes in designing the experiments are not only to find the percentage of the counterion binding, but also to fit the full scattering curves to get details of the micellar internal structure. This includes finding a reasonable model for the structure on the micellar surface.

For internal contrast variation, we changed the percentage of the tail-deuterated surfactant CTA-d₃₃-2,6 in the micelles to change the overall micellar scattering length density, $\bar{\rho}_m$, while keeping ρ_s constant. In this case, protiated Na26ClBz was used in order to provide higher contrast between the micellar core and shell. In order to have less incoherent scattering, we use D₂O as our solvent. As for external contrast variation, internal contrast variation can also provide R_g and $\bar{\rho}_m$ for the overall micelles. We observed significant dependence of R_g on ρ_c (scattering length density of the core).

Our experiments used 20mM surfactant in 1M aqueous salt, because the high concentration of common-ion salt promotes a decline in micellar size back to globules.^{65,95} Lower salt concentrations were also studied to get information on counterion binding while the micelles are still large.

4.1.2 Effect of salt on ρ_s

Scattering length densities are calculated from atomic scattering lengths and the volumes using Eqn. 2.14. The individual atomic scattering lengths used can be found in Table 2.1, and the scattering lengths, the volumes and scattering length densities for molecules or molecular fragments in our experimental systems can be found in Table 4.1. The salt effect must be considered when calculating ρ_s . For example, 1M Na26ClBz will occupy nearly 12% of overall solution volume, based on reported molar volumes.¹¹⁰ Table 4.2 reports values of ρ_s , calculated using Eqn. 4.1 for the various solutions used:

$$\rho_s = \frac{\sum b}{\sum V} = \frac{\rho_{sol}(V - V_{salt}) + V_{salt}\rho_{salt}}{V} \quad (4.1)$$

Table 4.1 Volume, scattering length and densities used in contrast variation experiments

	$b \times 10^{12} \text{ cm}$	$V \times 10^{24} \text{ cm}^3 (\text{\AA}^3)$	$\rho \times 10^{-10} \text{ cm}^{-2} (\times 10^6 \text{\AA}^{-2})$
H ₂ O	-0.168	29.9	-0.562
D ₂ O	1.914	30.2	6.338
-CH ₂ -	-0.083	26.9	-0.308
-CH ₃	-0.457	54.3	-0.842
-N ⁺ (CH ₃) ₃	-0.431	102.3	-0.421
Na ₂₆ ClBz-h	6.968	196.8**	3.545
26ClBz ⁻ -h	6.613	183.2**	3.610
Na ₂₆ ClBz-h (87.6% d)	9.704	196.8*	4.931
26ClBz-d (87.6% d)	9.342	183.2*	5.099
C ₁₆ H ₃₃ (CTA tail)	-1.702	457.8	-0.371
C ₁₆ D ₃₃ (CTA tail, 99% d)	32.651	457.8*	7.132

* Assuming no effect of H/D substitution on volumes of 26ClBz and surfactant ion.

** Volume calculated from reference [110]

Table 4.2 ρ_s for external contrast variation and ρ_c for internal contrast variation

Deuterated Na26ClBz

1M Na26ClBz-d		0.4M Na26ClBz-d	
%* of D ₂ O*	$\rho_s \times 10^6 \text{ \AA}^{-2}$	% of D ₂ O	$\rho_s \times 10^6 \text{ \AA}^{-2}$
100	6.174	100	6.274
85	5.257	90	5.616
70	4.345	80	4.957
55	3.431	70	4.298
40	2.517	60	3.639
20	1.299	50	2.981
10	0.689	30	1.663
		20	1.005

* % is volume percent

Protiated Na26ClBz

1M Na26ClBz-h		0.2M Na26ClBz-h	
%* of D ₂ O	$\rho_s \times 10^6 \text{ \AA}^{-2}$	% of D ₂ O	$\rho_s \times 10^6 \text{ \AA}^{-2}$
100	6.012	100	6.278
93	5.586	70	4.253
72	4.306	60	3.578
60	3.574	40	2.227
40	2.356	20	0.877
20	1.137		

* % is volume percent

0.4M salt in D₂O: $6.211 \times 10^{-6} \text{ \AA}^{-2}$ ρ_c for internal contrast variation

CTA-d ₃₃ /CTA-d ₃₃	
%* of D-tail	$\rho_c \times 10^6 \text{ \AA}^{-2}$
100	7.132
93	6.607
85.61	6.052
70	4.881
50	3.381
30	1.880
0	-0.371

* % is mole percent

where ρ_s is the solvent, D₂O or D₂O/H₂O, scattering length density, ρ_{salt} is the scattering length density of the salt, protiated or 87.6% deuterated Na₂₆ClBz in this case. V is the overall solution volume, and V_{salt} is the volume of the salt in the solution. For example, for 20mM surfactant in 1M salt solutions, assuming 100% counterion binding on the micellar surface, the salt in the solution will be 0.98M. Then

$$V_{salt} = 0.98M \times 196.8A^3 \times N_A \quad (4.2)$$

where N_A is Avogadro's number.

4.1.3 Core plus shell model for the micelles

Core plus shell models were used to analyze the micellar structure. These models simply divide the micelle into a core region containing all or part of the hydrocarbon tails, and a shell containing the remainder of the hydrocarbon tails and the hydrophilic head groups plus the counterions with or without hydration. The hydration can change $I(Q)$ at finite Q but including it has no effect on $\bar{\rho}_m$. The overall scattering length density of the micelle, $\bar{\rho}_m$, depends on the scattering length density of core and shell, ρ_c and ρ_{sh} :

$$\bar{\rho}_m = \frac{\rho_c V_c + \rho_{sh} V_{sh}}{V_c + V_{sh}} \quad (4.3)$$

where V_c and V_{sh} are the volume of the core and shell, respectively. These values can be calculated from the aggregation number and the volume of the surfactant tail, head group and counterion.

$$V_c = \bar{N}_{agg} V_{tail} \alpha \quad (4.4)$$

$$V_{sh} = \bar{N}_{agg} \left[(1 - \alpha) V_{tail} + V_{head} + fV_{an} + \beta V_s \right] \quad (4.5)$$

where V_{tail} , V_{head} , V_{an} , V_s are the volume of surfactant tail, surfactant head group, anionic counterion, and solvent respectively. α is the fraction of hydrocarbon tail in the core, β is a hydration number that includes the waters of hydration for both head group and counterion, and f is the fraction of counterion bound per surfactant ion at the micellar surface. ρ_c and ρ_{sh} can also be calculated from the following equations:

$$\rho_c = \frac{b_c}{V_c} = \frac{\bar{N}_{agg} b_{tail} \alpha}{\bar{N}_{agg} V_{tail} \alpha} = \frac{b_{tail}}{V_{tail}} \quad (4.6)$$

$$\rho_{sh} = \frac{b_{sh}}{V_{sh}} = \frac{\bar{N}_{agg} [(1-\alpha)b_{tail} + b_{head} + fb_{an} + \beta b_s]}{\bar{N}_{agg} [(1-\alpha)V_{tail} + V_{head} + fV_{an} + \beta V_s]} = \frac{(1-\alpha)b_{tail} + b_{head} + fb_{an} + \beta b_s}{(1-\alpha)V_{tail} + V_{head} + fV_{an} + \beta V_s} \quad (4.7)$$

The ρ_{sh} can be changed by the percentage of the counterion binding and the hydration number of the head group and the counterions.

4.1.4 Radius of gyration

The radius of gyration changes when ρ_{sh} or ρ_c changes for this core plus shell model. Only for particles with homogenous ρ 's is R_g independent of contrast. For this model Eqn. 2.21 can be rewritten as:

$$R_g^2 = \frac{R_{g,c}^2 W_c + R_{g,sh}^2 W_{sh}}{W_c + W_{sh}} \quad (4.8)$$

where the subscripts c and sh represent the core and shell, respectively. And the weighting factors are given by

$$W_c = \int (\rho_c - \rho_s) d^3 r \quad (4.9)$$

$$= \bar{N}_{agg} \alpha (b_{tail} - \rho_s V_{tail}) \quad (4.10)$$

$$W_{sh} = \int (\rho_{sh} - \rho_s) d^3r \quad (4.11)$$

$$= \bar{N}_{agg} (b_{sh} - \rho_s V_{sh}) \quad (4.12)$$

The partial radii of gyration of core and shell, $R_{g,c}$ and $R_{g,sh}$, have been discussed in chapter II, eqn. (2.23-2.29). We can get the following simplified equations for the core plus shell model:

$$R_g^2 = \frac{1 \Delta \rho_1 r_c^4 + \Delta \rho_2 (r_{sh}^4 - r_c^4)}{2 \Delta \rho_1 r_c^2 + \Delta \rho_2 (r_{sh}^2 - r_c^2)} \quad (4.13)$$

for cross-section of cylinder or wormlike chain and

$$R_g^2 = \frac{3 \Delta \rho_1 r_c^5 + \Delta \rho_2 (r_{sh}^5 - r_c^5)}{5 \Delta \rho_1 r_c^3 + \Delta \rho_2 (r_{sh}^3 - r_c^3)} \quad (4.14)$$

for spherical radius of gyration. In both cases

$$\Delta \rho_1 = \rho_c - \rho_s \quad (4.15)$$

$$\Delta \rho_2 = \rho_{sh} - \rho_s \quad (4.16)$$

4.2 EXTERNAL CONTRAST VARIATION FOR PROTIATED CTA USING DEUTERATED Na26ClBz AS THE SALT

In order to increase the overall micellar contrast and increase the contrast between the core and shell of the micelles, deuterated Na26ClBz was used. The detailed synthetic approach and the determination of the percentage of deuteration of the Na26ClBz will be discussed in the experimental chapter. Based on previous research,^{65,95} here we concentrated on the surfactant concentration at 20mM with salt concentrations of 0.4M and 1M. The micelles at these concentrations are cylindrical (ellipsoidal) micelles and

spherical (globular) micelles, respectively. More detailed fitting of the full scattering curves will be done for the 1M salt solutions, where the micelles are back to minimum size. A series of samples are made by mixing two 20mM surfactant solutions, each containing 1M salt, in various ratios; one solution is in D₂O, the other in H₂O.

Figure 4.1 depicts ρ_c , ρ_{sh} and ρ_s for the samples studied at 1M Na26-d₃-ClBz. The shell scattering length density, ρ_{sh} , is estimated assuming that the shell is dry and the counterion binding is 100%. ρ_{core} is calculated only based on the hydrocarbon tails and the core radius is set to 21 Å based on the tail length of CTA. We also observed that the contributions of the core and shell to R_g and $I(0)$ changes as ρ_s changes. From 100% D₂O to 50% D₂O, the contribution of the core dominates the R_g .

Below the 40% D₂O in the solvent, the shell contribution starts to increase. At some point between 40% and 50% D₂O, the condition $\rho_s = \rho_{sh}$ is satisfied, and only the core contributes to the scattering.

4.2.1 Radius of gyration

The scattering curves of these systems are represented in Figure 4.2 and Figure 4.3. Figure 4.2 presents the data for 20mM CTA26-d₃-ClBz in 1M salt solutions with solvent D₂O percentages from 100% to 25%, and Figure 4.3 presents the data for 20mM CTA26ClBz in 0.4M salt solutions with solvent D₂O percentages from 100% to 30%. In both cases $I(0)$ decreases as ρ_s approaches $\bar{\rho}_m$. In 1M salt, the scattering curves have no upturn in $I(Q)$ in the small Q region, indicating that the micelle is smaller in 1M than in 0.4M salt.

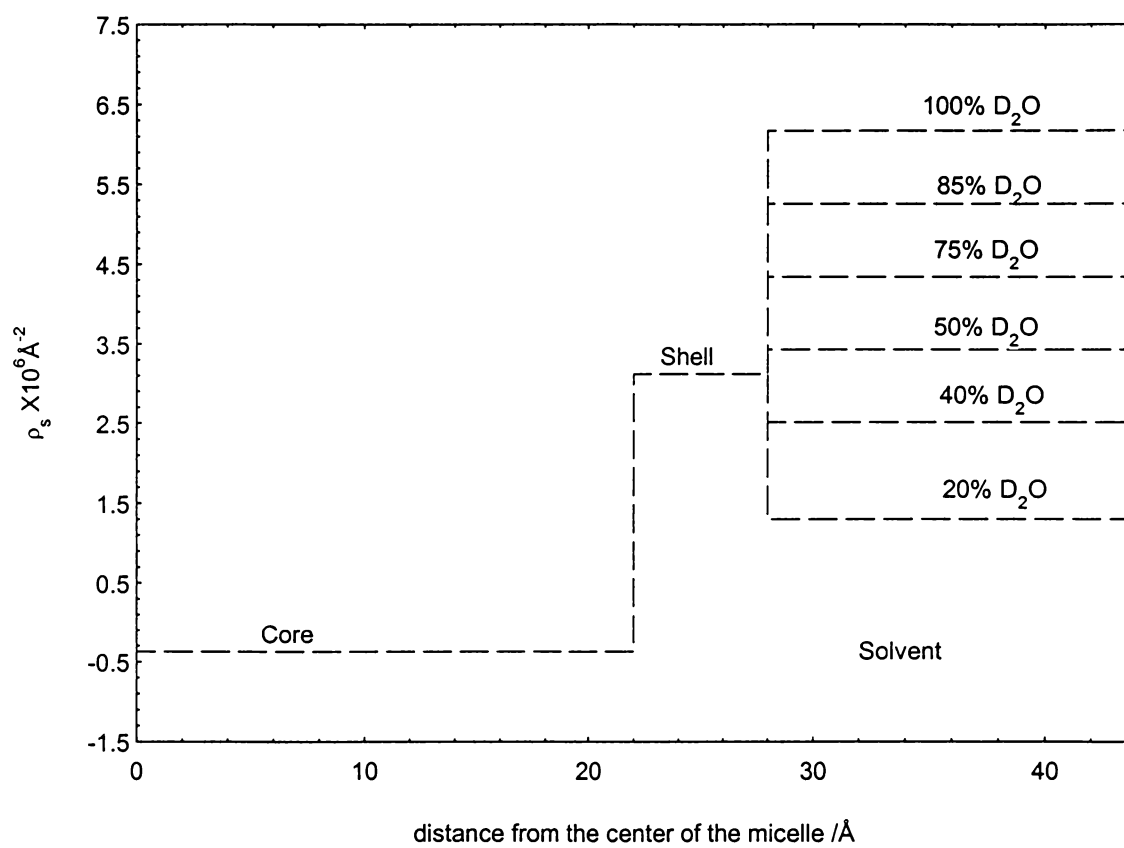


Figure 4.1 Scattering length density profiles for CTA/26-d₃-ClBz micelles in H₂O/D₂O mixture containing 1M Na26-d₃-ClBz. Percents of D₂O are by volume.

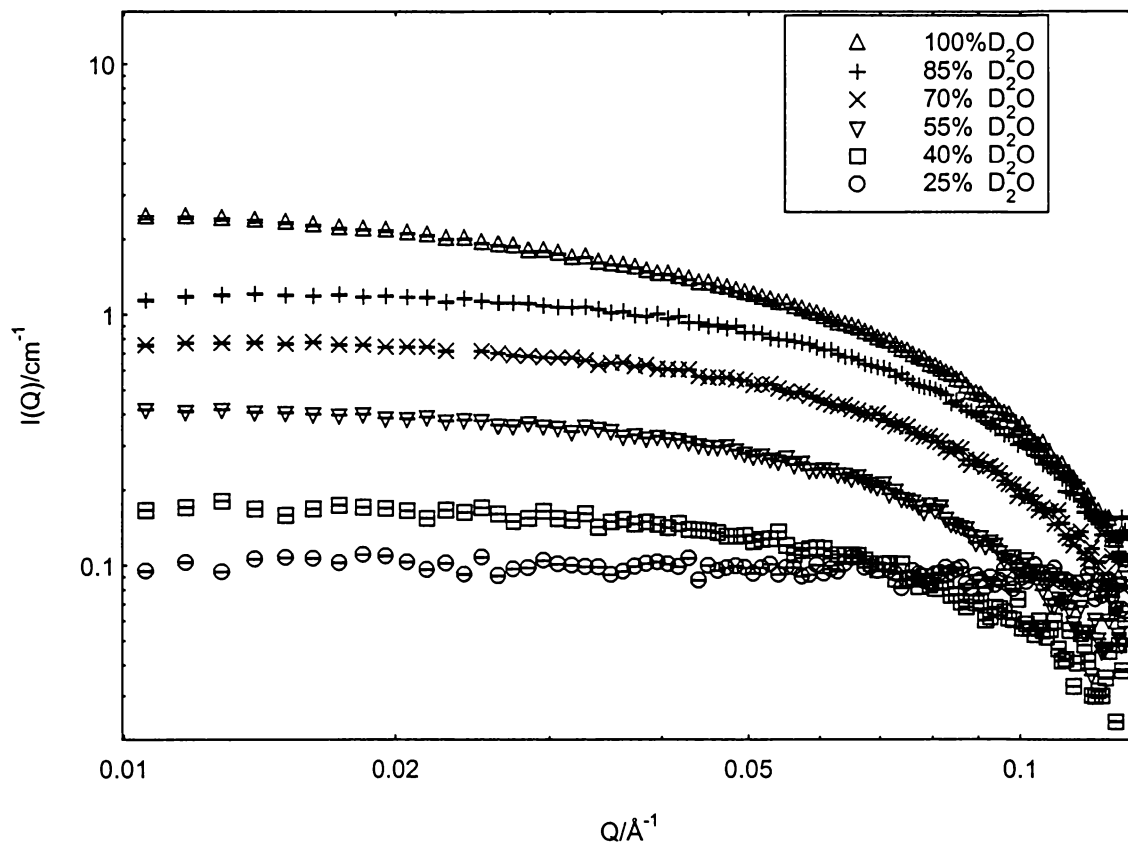


Figure 4.2 External contrast variation for CTA micelles in 1M salt, using deuterated Na26ClBz to increase the shell contrast with the core at different volume percents of D_2O in the solvent

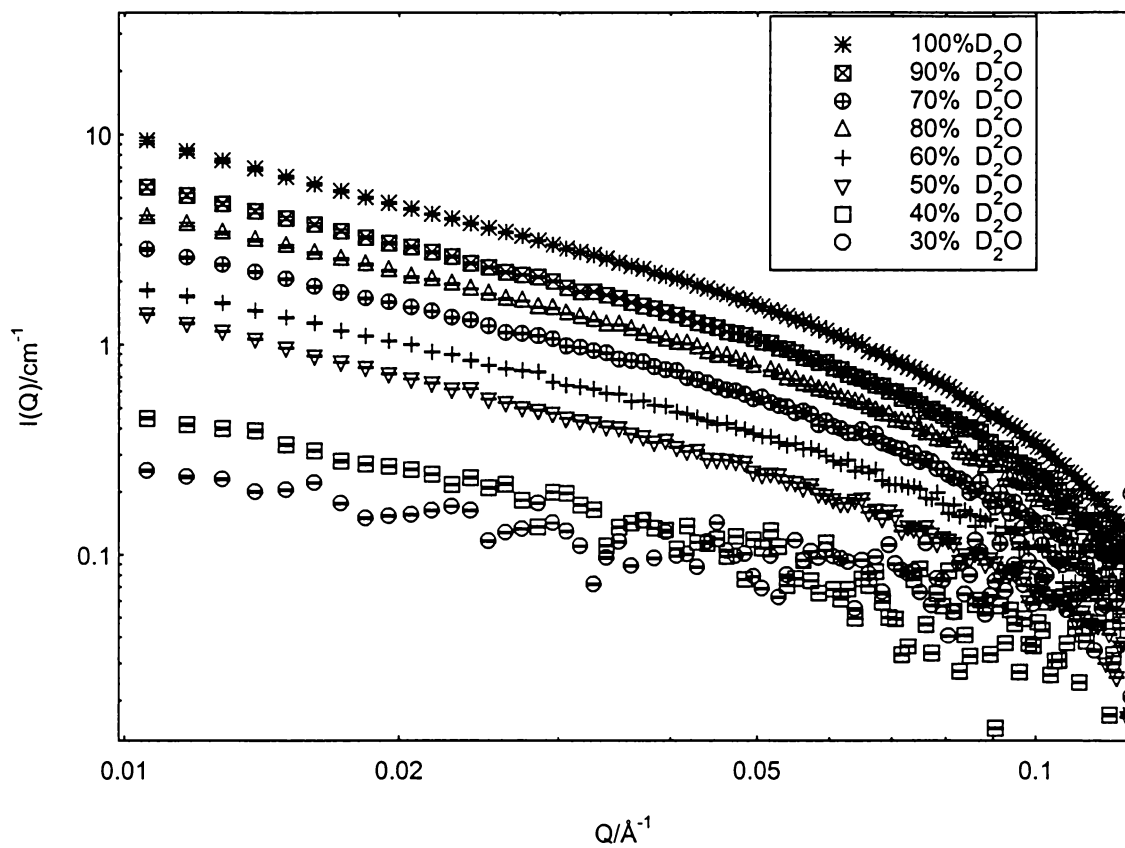


Figure 4.3 External contrast variation for CTA micelles in 0.4M salt, using deuterated Na26ClBz to increase the shell contrast with the core at different volume percents of D_2O in the solvent

The differences in micellar structure can be seen more clearly in the Guinier plots, $\ln(I(Q))$ vs. Q^2 . Figures 4.4 and 4.5 show the curves for the micelles in 70% D₂O. In 1M salt solution, we observed a straight line in the Guinier plot at both small and large Q , indicating that principal micellar axes are approximately the same – the micelles are globular or slightly ellipsoidal and their R_g 's can be obtained by fitting the Guinier plots in the region $0.08\text{nm}^{-1} < Q < 1\text{nm}^{-1}$. The results are shown in Table 4.3. We observed that R_g changes with ρ_s . In 0.4M salt, there are two regions in the plot. At smaller Q ($Q < 0.05 \text{ nm}^{-1}$ or $QR_g \ll 1$) the region with larger slope reflects the overall micellar R_g , and the larger Q region with smaller slope indicates the second length scale, the micellar cross-section. In both regions, the Guinier plot did not give a good straight line meaning that the Guinier plot cannot be used to obtain values for these two length scales. A Guinier-like plot, $\ln[I(Q)*Q]$ vs. Q^2 , as discussed in Chapter II, can be used here to derive the cross-sectional radius of gyration, $R_{g,cs}$. Figure 4.6 gives an example of this plot, and radii and the weight average number of monomers per unit length, N/L , can be obtained by fitting the plots in the region $0.15\text{nm}^{-1} < Q^2 < 1\text{nm}^{-1}$. Results are also given in Table 4.3. We can see the N/L is about same at all D₂O contents, except at low scattering contrast where the error bars are large. This means that the structure parameters of the systems are constant except the scattering contrast, and the R_g 's are changing only because of the changes in contrast.

4.2.2 Match point and percentage of counterion binding

Values for $I(0)$ can be derived from the Guinier plots for the 1M salt solutions and from the Guinier-like plots for the 0.4M salt solutions. Results are tabulated in Table 4.3.

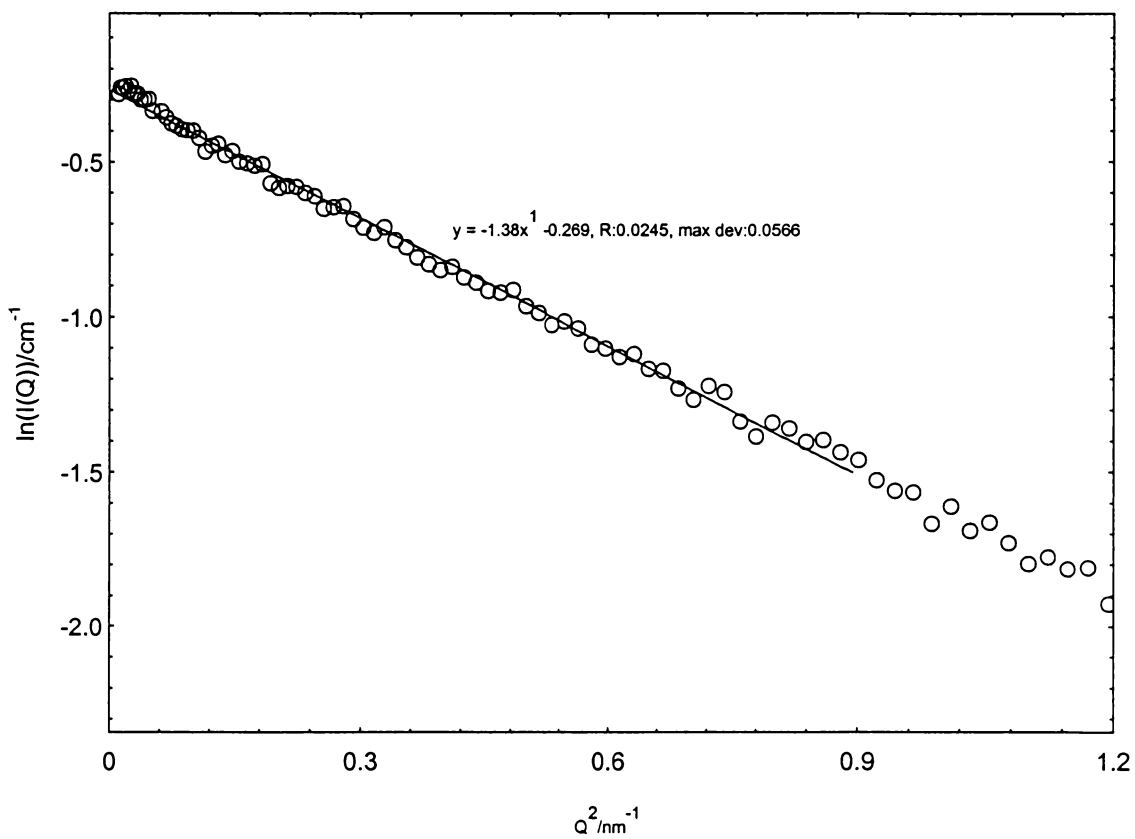


Figure 4.4 Guinier plot of 20mM CTA26CIBz in 1M Na26-d₃-CIBz solutions at 70% D₂O in the solvent

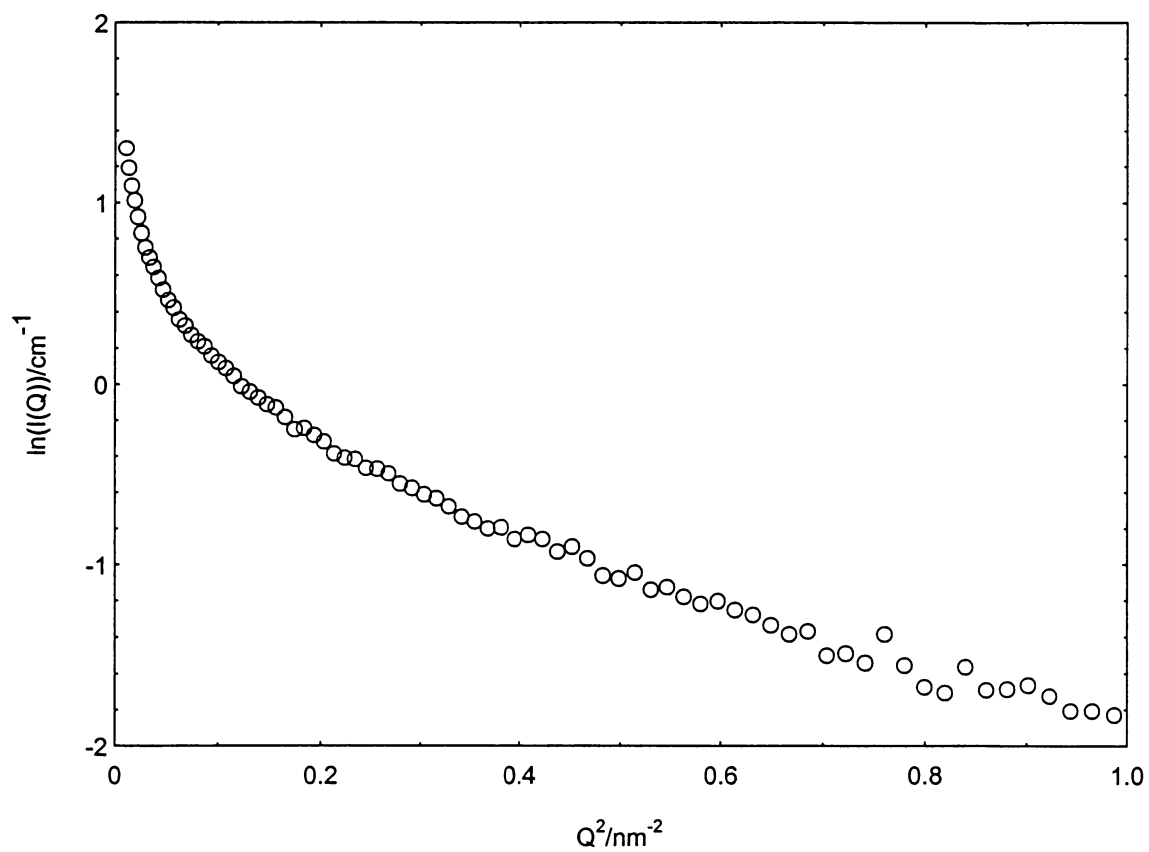


Figure 4.5 Guinier plot of 20mM CTA26ClBz in 0.4M Na26-d₃-ClBz solutions at 70% D₂O in the solvent

Table 4.3 R_g and $I(0)$ from Guinier plots for 1M salt and $R_{g,cs}$ and $I(0)$ together with N/L from Guinier-like plots for 0.4M salt

1M Na26-d₃-ClBz

%* of D ₂ O	$I(0)^{1/2}/\text{cm}^{-1/2}$	$I(0)/\text{cm}^{-1}$	$R_g/\text{Å}$
100	1.340 ± 0.003	1.796 ± 0.008	22.25 ± 0.04
85	1.107 ± 0.003	1.225 ± 0.008	20.57 ± 0.05
70	0.874 ± 0.003	0.764 ± 0.007	20.35 ± 0.04
55	0.639 ± 0.003	0.408 ± 0.008	20.64 ± 0.03
40	0.415 ± 0.002	0.172 ± 0.006	18.49 ± 0.04

* % is volume percent

0.4M Na26-d₃-ClBz

%* of D ₂ O	$I(0)^{1/2}/\text{cm}^{-1/2}$	$I(0)/\text{cm}^{-1}$	$R_g, \text{cs}/\text{Å}$	$N/L \times 10^8 \text{ cm}^{-1}$
100	0.941 ± 0.002	0.885 ± 0.005	14.10 ± 0.03	1.507 ± 0.006
90	0.824 ± 0.003	0.679 ± 0.008	14.14 ± 0.02	1.507 ± 0.003
80	0.703 ± 0.003	0.494 ± 0.007	13.57 ± 0.05	1.487 ± 0.008
70	0.592 ± 0.004	0.350 ± 0.012	13.41 ± 0.03	1.512 ± 0.005
60	0.477 ± 0.003	0.228 ± 0.009	12.33 ± 0.04	1.529 ± 0.006
50	0.393 ± 0.004	0.154 ± 0.014	12.75 ± 0.04	1.824 ± 0.005

* % is volume percent

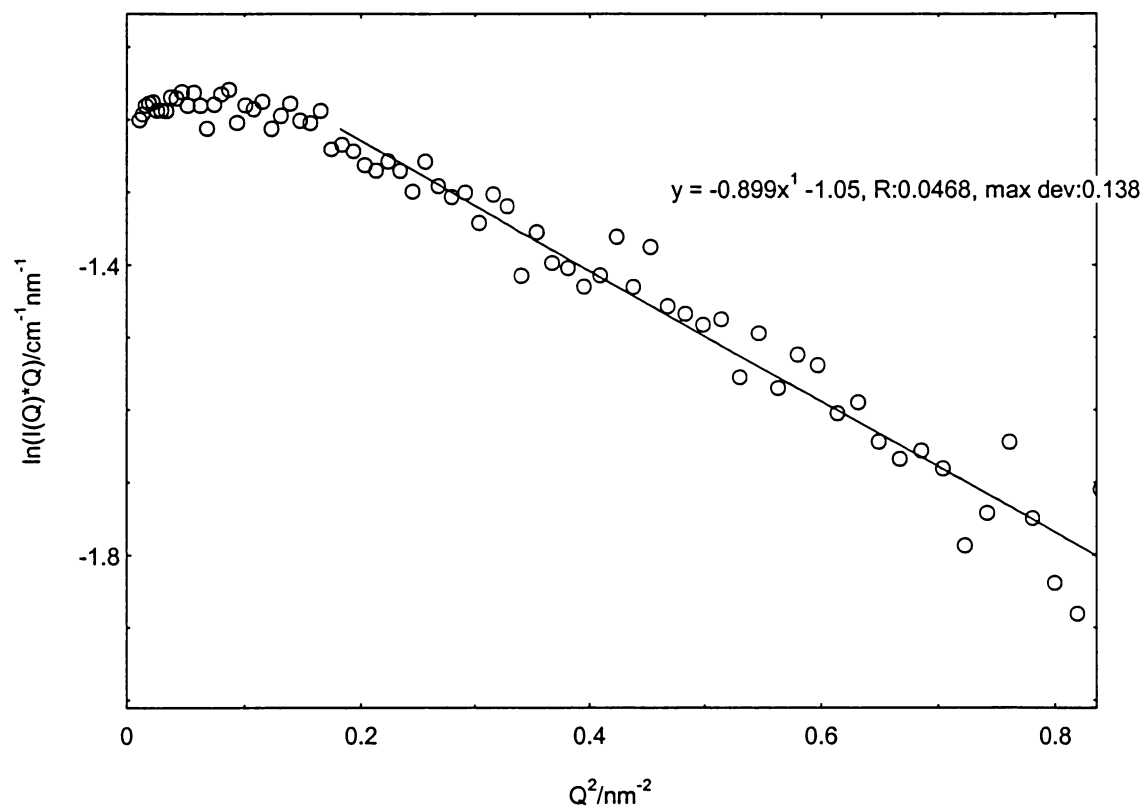


Figure 4.6 Guinier-like plot of 20mM CTA26CIBz in 0.4M Na26-d3-CIBz solutions at 70% D₂O in the solvent

Plots of $I(0)^{1/2}$ vs. the percentage of D_2O are given in Figure 4.7 and Figure 4.8. From the respective match points, $\bar{\rho}_m$ is obtained; from it, we get counterion binding fraction $f = 0.92 \pm 0.05$ for 1M salt and $f = 1.02 \pm 0.05$ for 0.4M salt by using Eqn. 4.3.

4.2.3 Details of the micellar structure

We first concentrate on fitting the full scattering curves for solutions in 1M salt. The fitting used Eqn. 2.19, and the Percus-Yevick hard sphere expression for the structure factor.^{63,64} After first trying to use the form factors of Eqn. 2.34-2.38, the spherical or ellipsoidal form factors, we determined that the overall micellar shape is more likely ellipsoidal. For a core plus shell ellipsoid, the structure of micelles can be described by several quantities: the semiminor axis of the micellar core (A2), the semiminor axis of the overall micelle (A1), the overall axial ratio (ECC1, the overall semimajor axis can then be calculated from $ECC1 \times A1$), and the micellar core axial ratio (ECC2, the core semimajor axis is equal to $ECC2 \times A2$). These numbers are correlated to the surfactant aggregation number (AGG), the hydration number and the counterion binding fraction (f). Because the solvent scattering runs with large H_2O volume fraction have strong incoherent scattering (which is not completely flat at the Q range for our experiments), point-by-point background subtractions were performed before fitting the data, rather than subtracting a flat background.

In order to achieve the best fits, different models for the micelles were tried. During the fits, we noticed that both the ECC and the shell thickness (thick) cannot be varied at the same time because they are directly correlated to each other. Different fixed shell thicknesses were first tested for micelles without or with hydration (in the case with

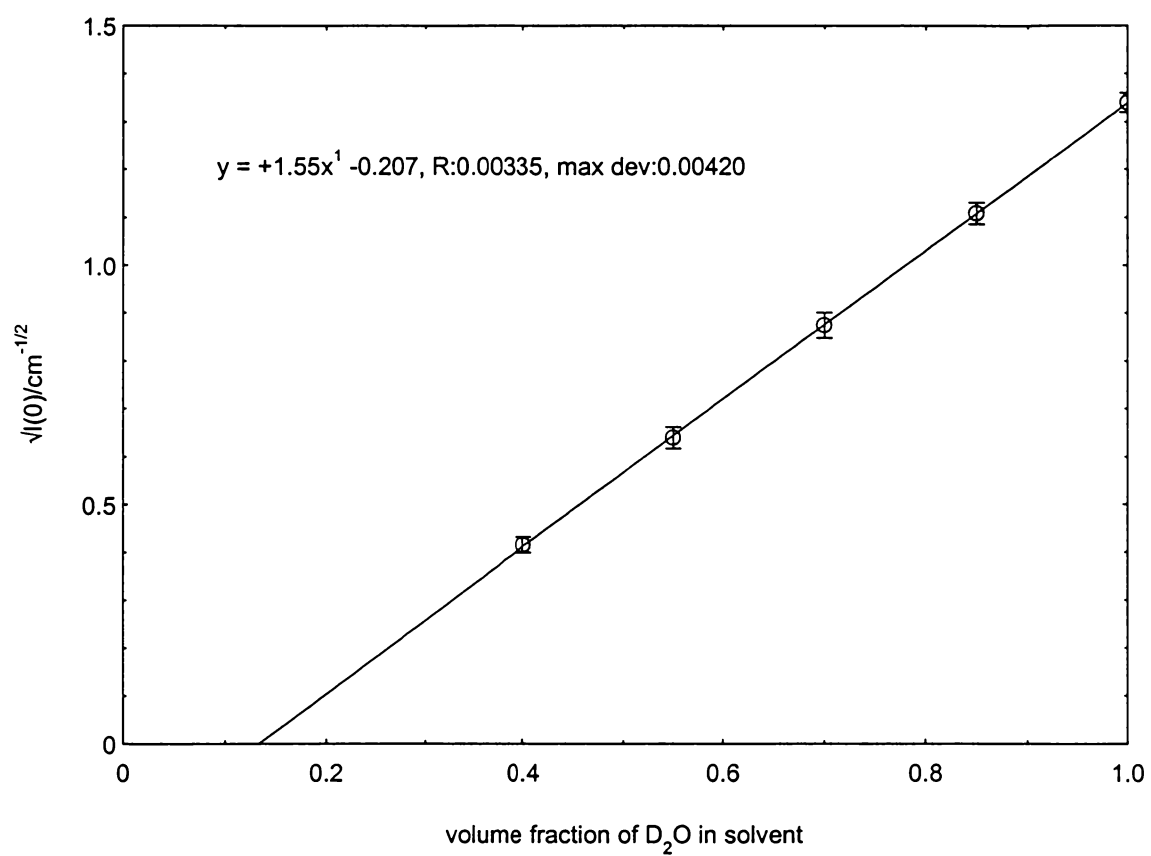


Figure 4.7 $I(0)^{1/2}$ vs. fraction of D₂O in the solvent for CTA micelles in 1M Na26-d3-ClBz. From external contrast variation.

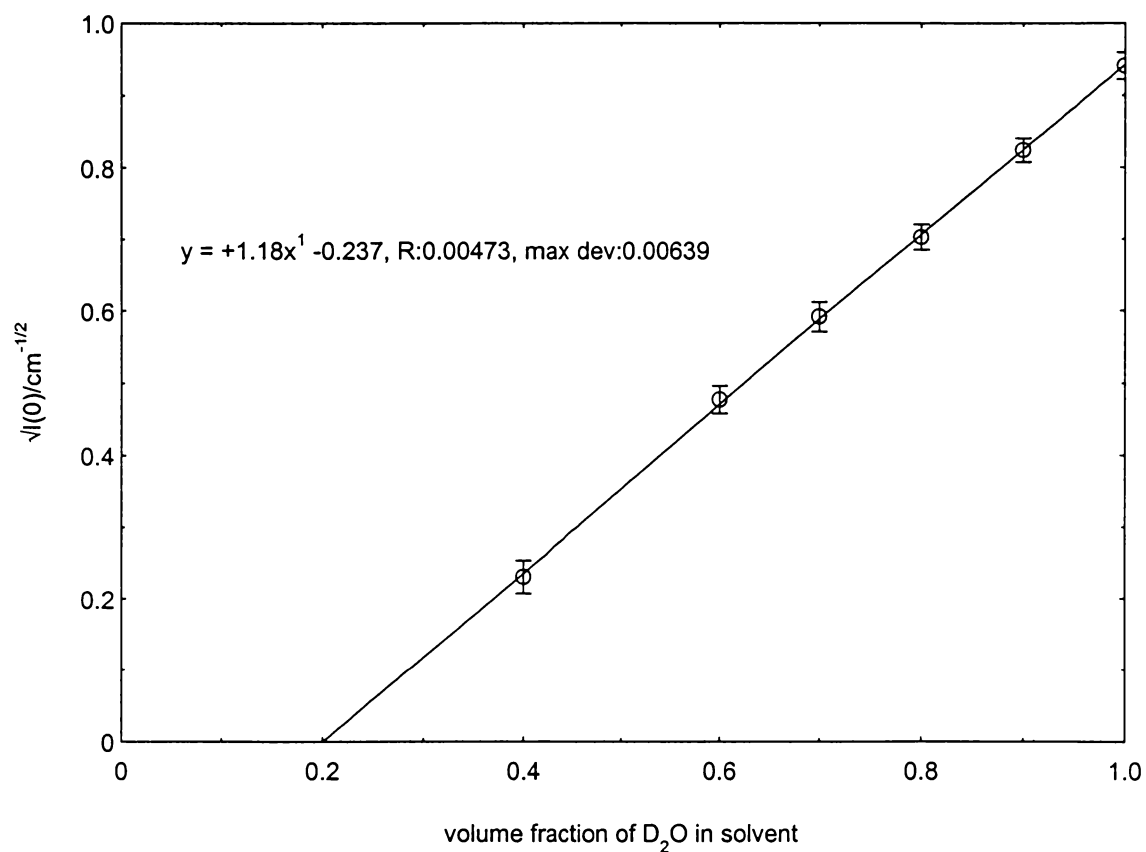


Figure 4.8 $I(0)^{1/2}$ vs. fraction of D₂O in the solvent for CTA micelles in 0.4M Na26-d3-CIBz. From external contrast variation.

hydration, a hydration number of 6 is chosen for the counterion and 3 for the head group), and shell thicknesses as of 4Å and 6Å were found best respectively for the cases without and with hydration included. During the fits, we tried varying AGG or ECC1 and ECC2, or both, with or without hydration in the micellar shell structure. Brief descriptions of each model are given above each block of results in Table 4.4.

An overall overview of the models is: in the first two blocks (models), AGG, ECC1, and ECC2 all vary, with the hydrocarbon tail fraction inside the micellar core (ALF). For the remaining models, ALF is fixed at 0.98 and AGG is fixed at 90, 100 or 110, and the fitting was performed without or with extra counterion bound on the micellar surface ($f > 1$) to test the hypothesis of charge reversal. Table 4.4 tabulates the results at different volume fractions of D2O (ϕ). Also tabulated are CHI, the quality of the least square fitting; R1 and R2, the equivalent spherical radii of the micellar core and overall micelle; B2, the scattering length density of the shell; and BBS, the solvent ρ with the effect of salt taken into account. Figure 4.9 shows an example of the fits to the scattering curves for 1M salt at 70% D2O with ECC varying, AGG = 100, ALF = 0.98, no hydration and with extra counterion ($f = 1.1$).

In this series of scattering curves, the micellar shell does not dominate the scattering. High H₂O content is needed to match or nearly match ρ_s to ρ_c . At high H₂O content, the incoherent scattering from solvent greatly affects the I(Q) values for the samples. In order to observe the shell structure, we instead tried using deuterated micellar core to increase contrast of the core. These experiments are discussed in the next section.

Table 4.4 Results of fitting the full scattering curves in the Q range $0.1-1.2\text{\AA}^{-1}$ for CTA micelles in 1M Na26-d₃-ClBz. External contrast variation studies.

Vary: AGG, ECC1, ECC2, ALF; fix: thick=6Å; with hydration; $f=1$.

$\phi(D_2O)$	AGG	CHI	ECC1	ECC2	A1(Å)	A2(Å)	ALF	R1(Å)	R2(Å)	B2	BBS
1.0	144	5.23	3.0456	3.7811	22.69	16.69	1.11	26.00	32.89	5.03	6.19
0.85	96	1.46	2.1135	2.5217	22.37	16.37	1.05	22.28	28.71	4.25	5.29
0.70	94	1.23	2.2849	2.7791	21.60	15.60	1.03	21.93	28.45	3.67	4.38
0.55	115	1.21	2.1359	2.5223	22.64	17.64	1.11	24.01	30.44	3.39	3.46
0.40	73	1.13	2.4768	3.1422	19.32	13.32	0.94	19.50	26.13	2.45	2.54

Vary: AGG, ECC1, ECC2, ALF; fix: thick=4Å, without hydration, $f=1$.

$\phi(D_2O)$	AGG	CHI	ECC1	ECC2	A1(Å)	A2(Å)	ALF	R1(Å)	R2(Å)	B2	BBS
1.0	144	6.71	3.1912	3.7335	20.16	16.16	1.00	25.08	29.69	2.94	6.19
0.85	98	1.52	2.1386	2.4184	20.28	16.28	0.97	21.85	26.12	2.81	5.29
0.70	96	1.38	2.3171	2.6544	19.62	15.62	0.96	21.62	25.96	2.76	4.38
0.55	117	1.18	2.1350	2.3948	21.47	17.47	1.00	23.38	27.65	2.96	3.46
0.40	81	1.07	2.4924	2.9180	18.03	14.03	0.92	20.05	24.44	2.58	2.54

Vary: ECC1, ECC2, Ecc1=Ecc2; fix: AGG=100, ALF=0.98, with hydration; $f=1$.

$\phi(D_2O)$	AGG	CHI	ECC1	ECC2	A1(Å)	A2(Å)	ALF	R1(Å)	R2(Å)	B2	BBS
1.0	100	7.31	4.5527	4.5527	17.55	13.30	0.98	22.04	29.09	4.46	6.19
0.85	100	1.38	2.1680	2.1680	22.48	17.03	0.98	22.04	29.09	3.99	5.29
0.70	100	1.36	2.3561	2.3561	21.86	16.57	0.98	22.04	29.09	3.51	4.38
0.55	100	1.21	2.7404	2.7404	20.79	15.75	0.98	22.04	29.09	3.03	3.46
0.40	100	1.10	2.2078	2.2078	22.34	16.92	0.98	22.04	29.09	2.55	2.54

Vary: ECC1, ECC2; fix: AGG=100, ALF=0.98, thick=6, with hydration; $f=1$.

$\phi(D_2O)$	AGG	CHI	ECC1	ECC2	A1(Å)	A2(Å)	ALF	R1(Å)	R2(Å)	B2	BBS
1.0	100	7.02	3.8384	5.3781	18.58	12.58	0.98	22.04	29.09	4.48	6.19
0.85	100	1.42	2.0620	2.2357	22.86	16.87	0.98	22.04	29.09	3.99	5.29
0.70	100	1.40	2.1940	2.4328	22.39	16.39	0.98	22.04	29.09	3.51	4.38
0.55	100	1.20	2.4500	2.8315	21.58	15.58	0.98	22.04	29.09	3.03	3.46
0.40	100	1.10	2.0426	2.2072	22.93	16.93	0.98	22.04	29.09	2.55	2.54

Vary: ECC1, ECC2; fix: AGG=100, ALF=0.98, thick=6, with hydration; $f=1.3$.

$\phi(D_2O)$	AGG	CHI	ECC1	ECC2	A1(Å)	A2(Å)	ALF	R1(Å)	R2(Å)	B2	BBS
1.0	100	6.67	4.0229	4.9370	18.95	12.95	0.98	22.04	30.13	4.64	6.19
0.85	100	1.55	2.1655	2.0723	23.29	17.29	0.98	22.04	30.13	4.15	5.29
0.70	100	1.39	2.3907	2.3696	22.53	16.53	0.98	22.04	30.13	3.67	4.38
0.55	100	1.29	2.8043	2.9516	21.37	15.37	0.98	22.04	30.13	3.19	3.46
0.40	100	1.02	2.7075	2.8112	21.62	15.62	0.98	22.04	30.13	2.70	2.54

* Unit for B2 and BBS: 10^{-6}\AA^{-2}

Table 4.4 (continued)

Vary: ECC1, ECC2; fix: AGG=100, ALF=0.98, thick=6, with hydration; $f = 1.1$.

$\phi(D_2O)$	AGG	CHI	ECC1	ECC2	A1(Å)	A2(Å)	ALF	R1(Å)	R2(Å)	B2	BBS
1.0	100	6.92	3.9025	5.2239	18.70	12.70	0.98	22.04	29.45	4.54	6.19
0.85	100	1.46	2.0990	2.1804	22.99	16.99	0.98	22.04	29.45	4.05	5.29
0.70	100	1.40	2.2570	2.4063	22.45	16.45	0.98	22.04	29.45	3.57	4.38
0.55	100	1.23	2.5606	2.8625	21.53	15.53	0.98	22.04	29.45	3.09	3.46
0.40	100	1.07	2.2490	2.3948	22.48	16.48	0.98	22.04	29.45	2.61	2.54

Vary: ECC1, ECC2; fix: AGG=110, ALF=0.98, thick=6, with hydration; $f = 1.0$.

$\phi(D_2O)$	AGG	CHI	ECC1	ECC2	A1(Å)	A2(Å)	ALF	R1(Å)	R2(Å)	B2	BBS
1.0	110	5.82	3.6422	4.7674	19.52	13.52	0.98	22.75	30.03	4.47	6.19
0.85	110	2.25	1.8229	1.8353	24.58	18.58	0.98	22.75	30.03	3.99	5.29
0.70	110	1.87	1.9811	2.0498	23.91	17.91	0.98	22.75	30.03	3.51	4.38
0.55	110	1.13	2.2860	2.4854	22.80	16.80	0.98	22.75	30.03	3.03	3.46
0.40	110	1.21	1.8638	1.8900	24.40	18.40	0.98	22.75	30.03	2.55	2.54

Vary: ECC1, ECC2; fix: AGG=100, ALF=0.98, thick=4, without hydration; $f = 1.1$.

$\phi(D_2O)$	AGG	CHI	ECC1	ECC2	A1(Å)	A2(Å)	ALF	R1(Å)	R2(Å)	B2	BBS
1.0	100	7.43	4.1105	5.4242	16.55	12.55	0.98	22.04	26.50	2.96	6.19
0.85	100	1.25	2.0982	2.2985	20.70	16.70	0.98	22.04	26.50	2.96	5.29
0.70	100	1.26	2.2488	2.5052	20.23	16.23	0.98	22.04	26.50	2.96	4.38
0.55	100	1.34	2.5536	2.9378	19.39	15.39	0.98	22.04	26.50	2.96	3.46
0.40	100	1.00	2.2496	2.5063	20.23	16.23	0.98	22.04	26.50	2.96	2.54

Vary: ECC1, ECC2; fix: AGG=100, ALF=0.98, thick=4, without hydration; $f = 1.3$.

$\phi(D_2O)$	AGG	CHI	ECC1	ECC2	A1(Å)	A2(Å)	ALF	R1(Å)	R2(Å)	B2	BBS
1.0	100	7.53	4.1060	5.6054	16.41	12.41	0.98	22.04	26.28	2.85	6.19
0.85	100	1.24	2.0871	2.3581	20.56	16.56	0.98	22.04	26.28	2.85	5.29
0.70	100	1.26	2.2101	2.5323	20.17	16.17	0.98	22.04	26.28	2.85	4.38
0.55	100	1.30	2.4691	2.9095	19.44	15.44	0.98	22.04	26.28	2.85	3.46
0.40	100	1.02	2.0642	2.3260	20.64	16.64	0.98	22.04	26.28	2.85	2.54

Vary: ECC1, ECC2; fix: AGG=90, ALF=0.98, thick=4, without hydration; $f = 1.0$.

$\phi(D_2O)$	AGG	CHI	ECC1	ECC2	A1(Å)	A2(Å)	ALF	R1(Å)	R2(Å)	B2	BBS
1.0	100	8.30	4.0798	6.2055	17.58	11.58	0.98	21.28	28.09	4.48	6.19
0.85	100	1.35	2.2852	2.6780	21.33	15.33	0.98	21.28	28.09	3.99	5.29
0.70	100	1.27	2.3902	2.8514	21.01	15.01	0.98	21.28	28.09	3.51	4.38
0.55	100	1.42	2.6069	3.2219	20.41	14.41	0.98	21.28	28.09	3.03	3.46
0.40	100	1.03	2.1962	2.5344	21.61	15.61	0.98	21.28	28.09	2.55	2.54

* Unit for B2 and BBS: 10^{-6}Å^{-2}

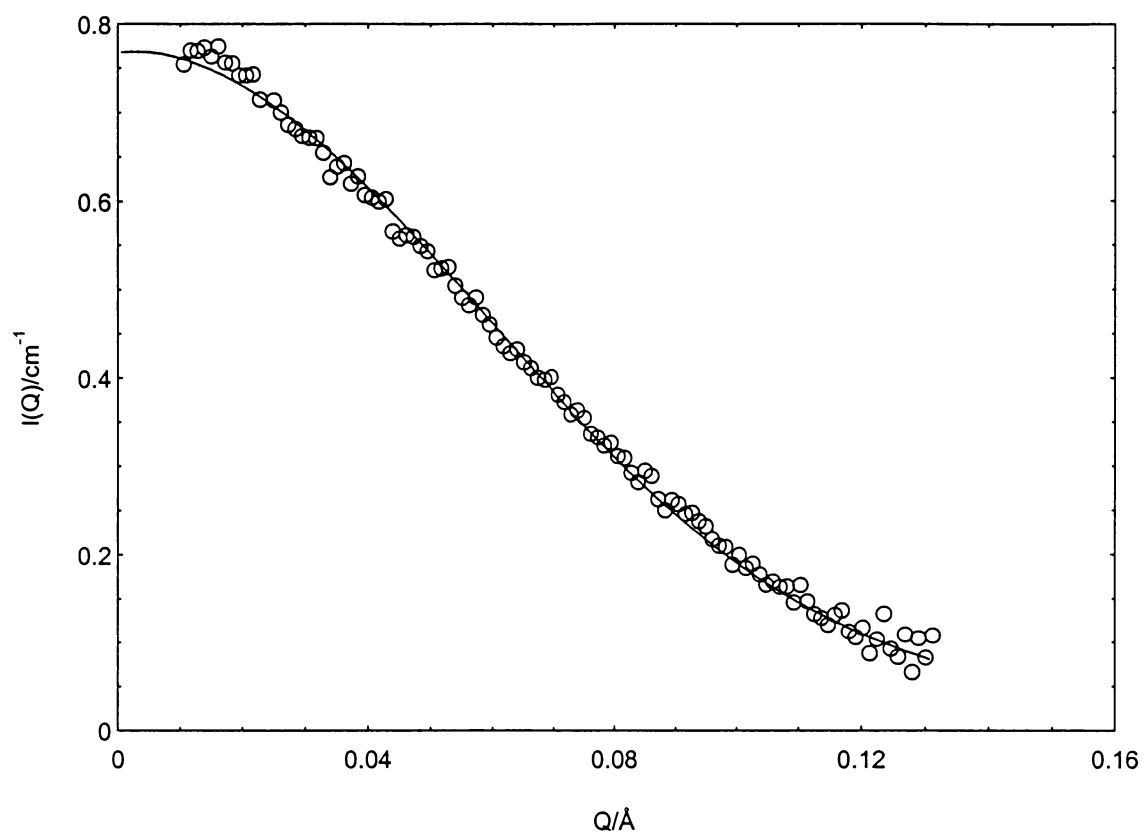


Figure 4.9 Scattering curve and related fits for 20mM CTA in 1M salt at 70% D₂O

4.3 EXTERNAL CONTRAST VARIATION FOR CTA-d₃₃

In the last section we explained that the shell structure cannot be easily observed because of the high H₂O content in the solvent needed to match the ρ_c . Using deuterated CTA-d₃₃-26ClBz increases the core scattering length density (to a value above that of D₂O), and increases the contrast between core and shell. Protiated counterions are used here also to increase the contrast between the core and shell. Synthesis of deuterated CTA-d₃₃-26ClBz is discussed in chapter V. The scattering length densities of this micellar system are represented in figure (4.10), and we can see that the shell structure is more visible as ρ_s increases. As before, we also include the effect of salt in the calculation of ρ_s . For D₂O percents by volume from 20% to 38%, both core and shell contrast with solvent decrease; above 38%, the core contrast continues to decrease and the shell contrast starts to increase.

We did a series of experiments at Argonne National Laboratory (ANL) with 20mM CTA-d₃₃ surfactant in 1M Na26ClBz aqueous solutions and repeated several samples having overall low scattering intensities at NIST to get more detailed information on the shell structure. External contrast variation was also used for 20mM CTA-d₃₃ in 0.2M salt. The SANS curves are presented in Figures 4.11 and 4.12, for 1M salt and 0.2M salt, respectively. As observed already, the micelles are smaller in 1M salt than in 0.2M salt.

4.3.1 Local structure and match point

The Guinier plot for 1M salt at 70% D₂O solvent and the Guinier-like plot for 0.2M salt are shown in Figures 4.13 and 4.14. We used the same Q range as before ($0.08\text{nm}^{-1} < Q < 1\text{nm}^{-1}$ for Guinier plots and $0.15\text{nm}^{-1} < Q^2 < 1\text{nm}^{-1}$ for Guinier-like plots) to fit the

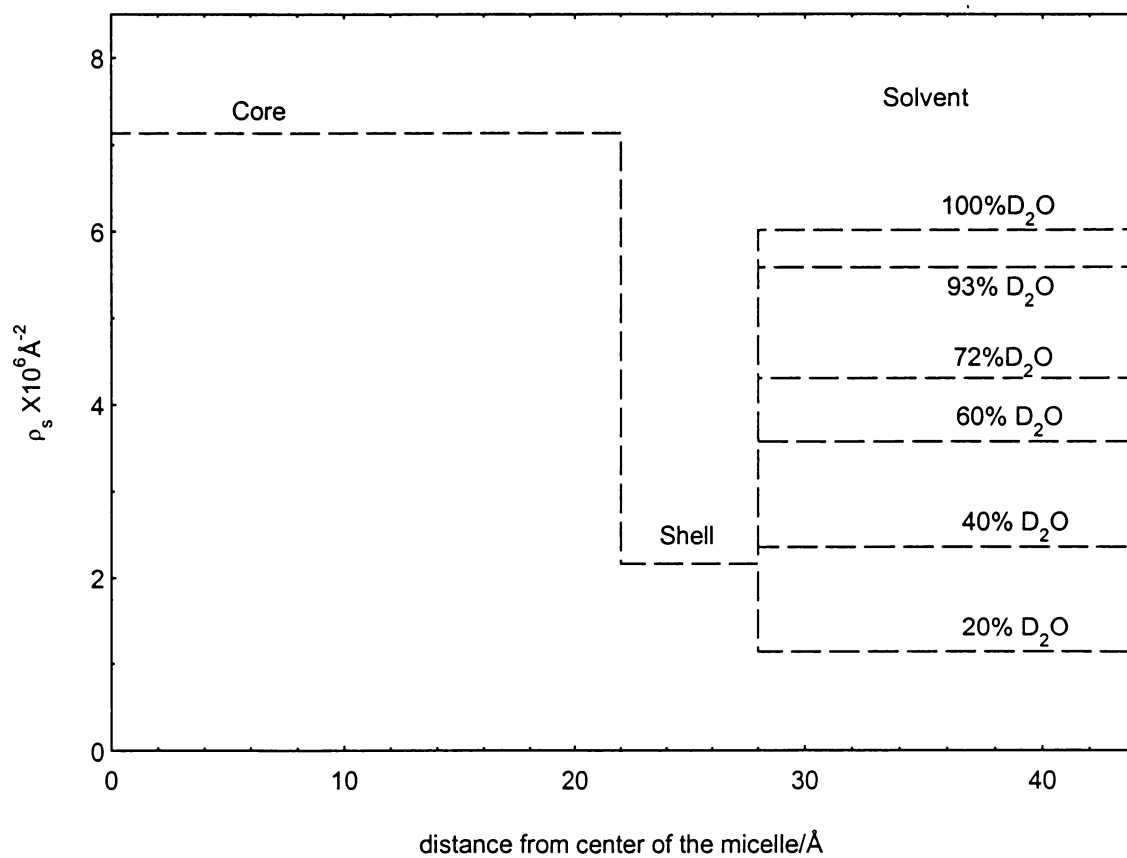


Figure 4.10 Scattering length density profiles for CTA-d₃₃ /26ClBz micelles in H₂O/D₂O mixture containing 1M Na26ClBz. Percents of D₂O are by volume.

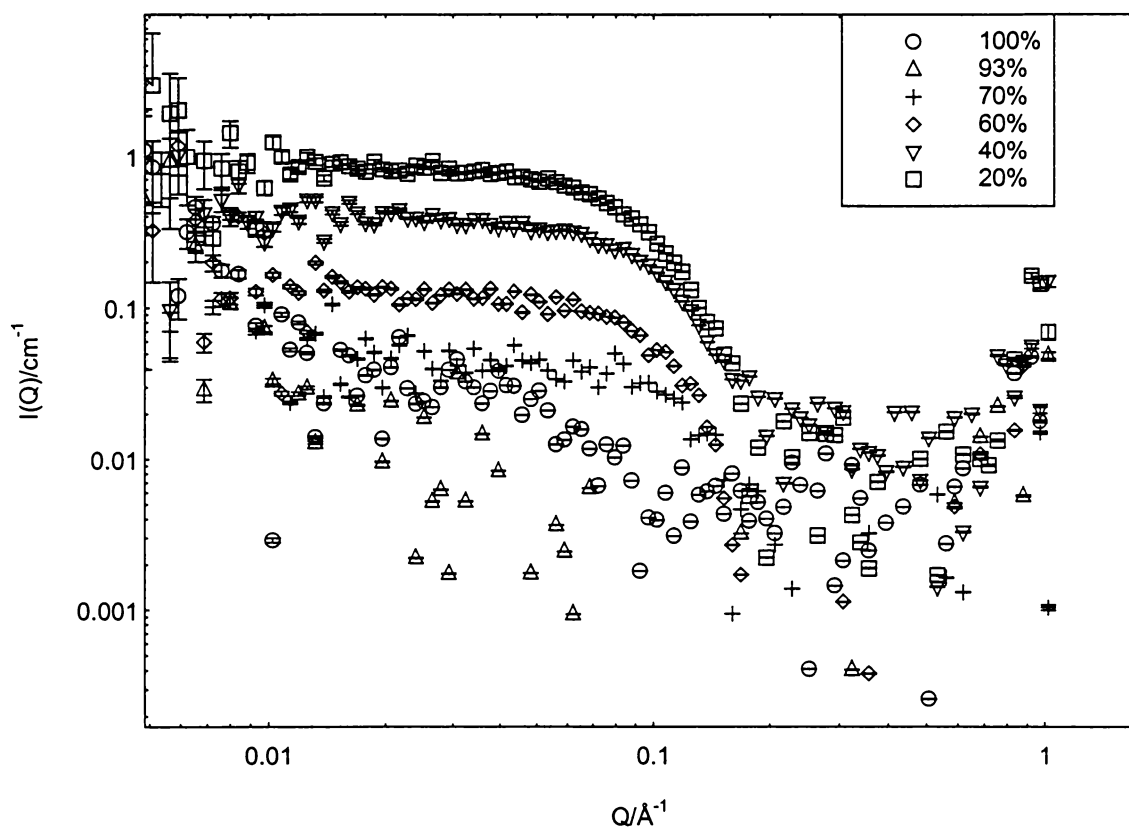


Figure 4.11 External contrast variation for CTA micelles in 1M salt, using CTA- d_{33} to increase the shell contrast with the micellar core at different volume % of D_2O in the solvent

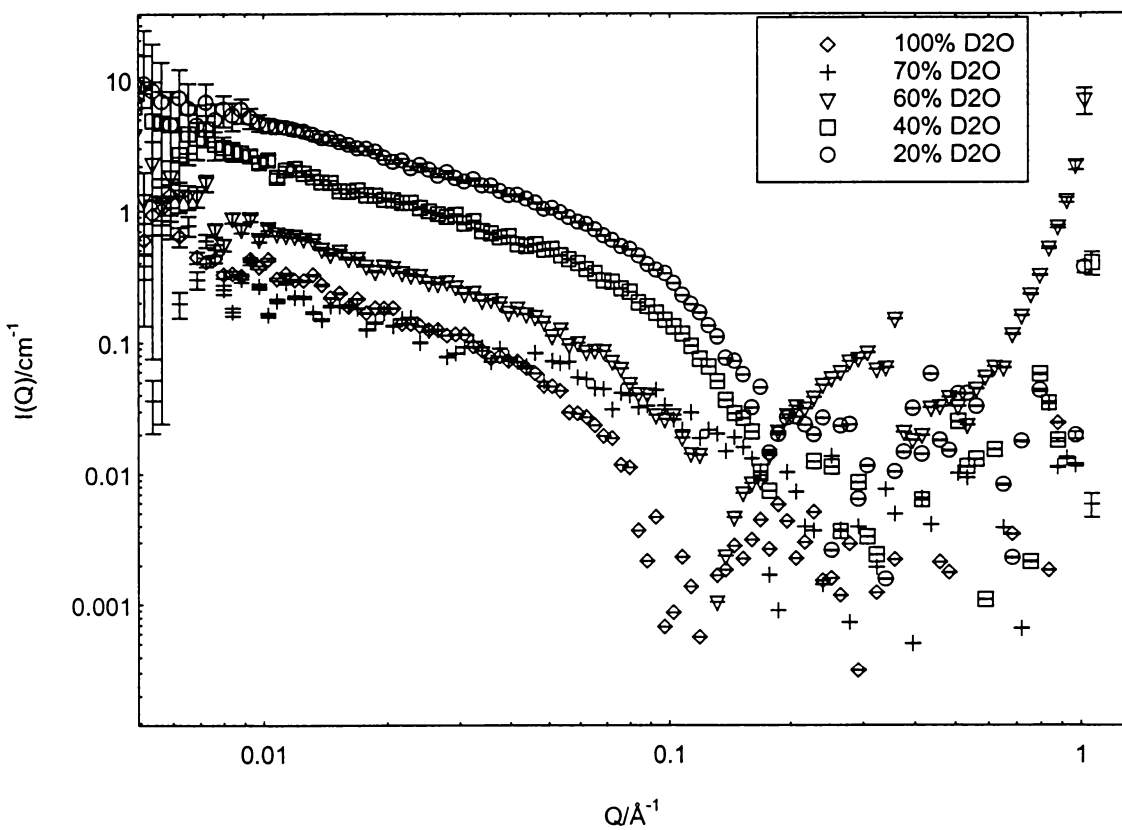


Figure 4.12 External contrast variation for CTA micelles in 0.2M salt, using CTA- d_{33} to increase the shell contrast with the micellar core at different volume % of D_2O in the solvent

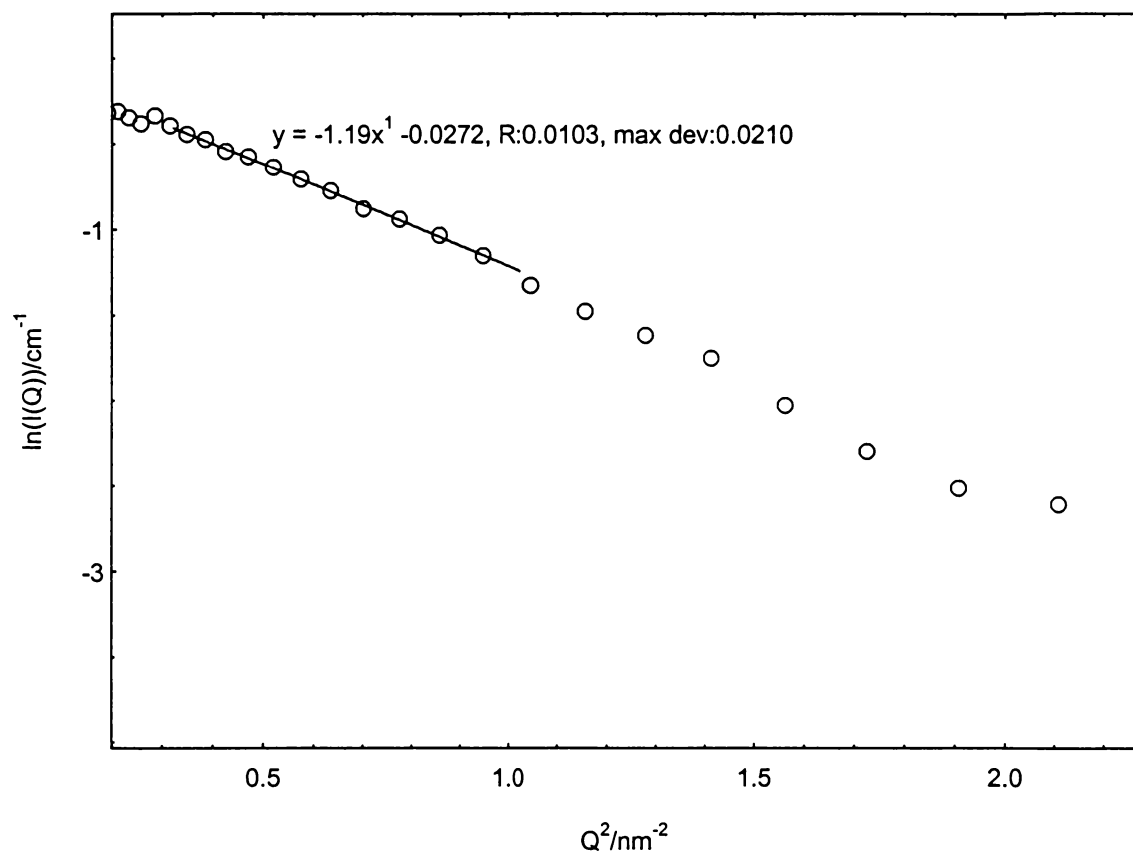


Figure 4.13 Guinier plot for external contrast variation in 1M salt by using CTA-d₃₃ at 20% of D₂O in the solvent

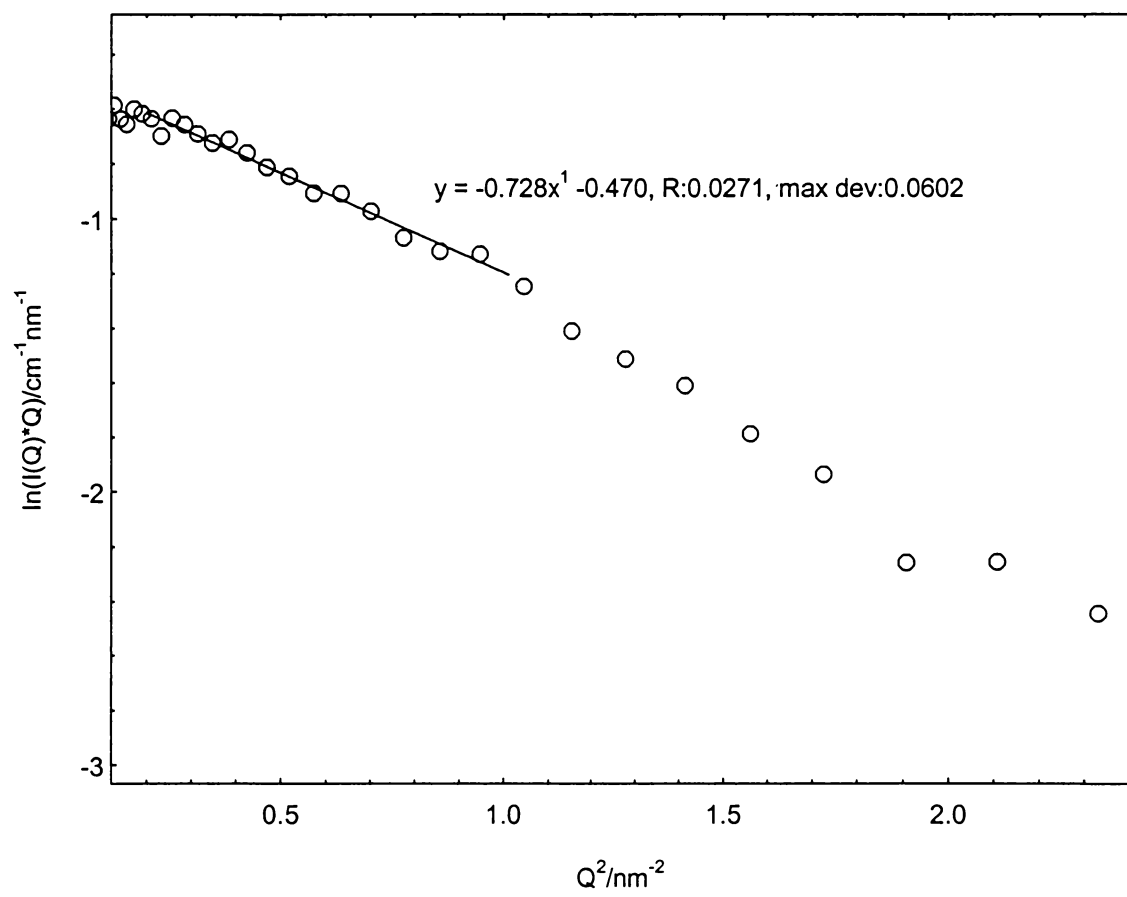


Figure 4.14 Guinier-like plot for external contrast variation in 0.2M salt by using CTA-d₃₃ at 20% of D₂O in the solvent

scattering curves, and the results are tabulated in Table 4.5. For 1M salt solutions, the overall R_g 's obtained varied dramatically from 10Å to 31Å. In the case of 0.2M salt, the $R_{g,cs}$ vary from 4Å to 27Å and show the same trend as for the spherical micelles. The values of N/L are again approximately around 1.5×10^8 monomer/cm as in the previous contrast variation series, except for the scattering curve in 100% D_2O .

Match points are obtained by plotting $I(0)^{1/2}$ vs. % D_2O , see Figures 4.15 and 4.16. Using the match points of 85.14% D_2O for 1M salt and 85.25% D_2O for 0.2 M salt, we obtain counterion binding fractions, f , for 1M salt of 1.20 ± 0.05 and 0.86 ± 0.05 for 0.2 M salt. The NIST data show very good overlap with that of the Argonne in 1M salt concentrations, as shown in Figure 4.15. In figure 4.16, we see that fitting only the first 4 points to get the $I(0)^{1/2}$ gives $f = 1.18 \pm 0.07$ for 0.2M salt, indicating that a small shift in the % D_2O at the match point produces a large change in f . This will be discussed further in Section 4.5.

4.3.2 Shell structure and overall micellar structure

The NIST NG7 SANS instrument, with its high flux and resolution, is well-suited for measuring weakly scattering samples, such as those whose SANS curves are presented in Figure 4.17. We can see clearly the consequence of shell contrast in the scattering curve, with a maximum in $I(Q)$ appearing between 1 and 2 nm^{-1} . As we assumed, the shell structure become more visible as ρ_s approaches ρ_c . Figure 4.17 shows that the most pronounced maximum occurs for 100% D_2O , and then decreases as the H_2O content increases. The full scattering curves in Figure 4.17 are fitted by using the form

Table 4.5 Results of external contrast variation for CTA-d₃₃ micelles: R_g and I(0) from Guinier plots for 1M salt and R_{g,cs} and I(0) together with N/L from Guinier-like plot for 0.2M salt

CTA-d₃₃ in 1M salt, external contrast¹

%* of D ₂ O	I(0) ^{1/2} (cm ⁻²)	I(0) (cm ⁻¹)	R _g (Å)
100	0.207 ± 0.012	0.0429 ± 0.006	28.19 ± 0.02
93	0.097 ± 0.031	0.0095 ± 0.007	31.08 ± 0.02
70	0.211 ± 0.014	0.0446 ± 0.008	9.81 ± 0.03
60	0.372 ± 0.018	0.138 ± 0.012	16.31 ± 0.01
40	0.642 ± 0.012	0.412 ± 0.016	17.83 ± 0.02
20	0.986 ± 0.008	0.973 ± 0.014	18.89 ± 0.02

* % is volume percent

CTA-d₃₃ in 1M salt, external contrast²

%* of D ₂ O	I(0) ^{1/2} (cm ⁻²)	I(0) (cm ⁻¹)	R _g (Å)
100	0.222 ± 0.010	0.0493 ± 0.004	27.77 ± 0.02
93	0.120 ± 0.021	0.0144 ± 0.006	33.76 ± 0.02
70	0.231 ± 0.011	0.0534 ± 0.005	10.16 ± 0.03
60	0.366 ± 0.009	0.134 ± 0.008	14.85 ± 0.02

* % is volume percent

CTA-d₃₃ in 0.2M salt, external contrast¹

%* of D ₂ O	I(0) ^{1/2} (cm ⁻²)	I(0) (cm ⁻¹)	R _{g,cs} (Å)	N/L (Å ⁻¹)
100	0.240 ± 0.014	0.0578 ± 0.007	27.31 ± 0.03	2.737
70	0.182 ± 0.018	0.0330 ± 0.008	4.005 ± 0.04	1.522
60	0.304 ± 0.014	0.0926 ± 0.012	16.25 ± 0.03	1.543
40	0.552 ± 0.012	0.304 ± 0.016	12.59 ± 0.03	1.569
20	0.791 ± 0.008	0.625 ± 0.014	12.07 ± 0.02	1.547

* % is volume percent

¹ Measured at IPNS, Argonne National Laboratory

² Measured at NIST's Center for Neutron Research

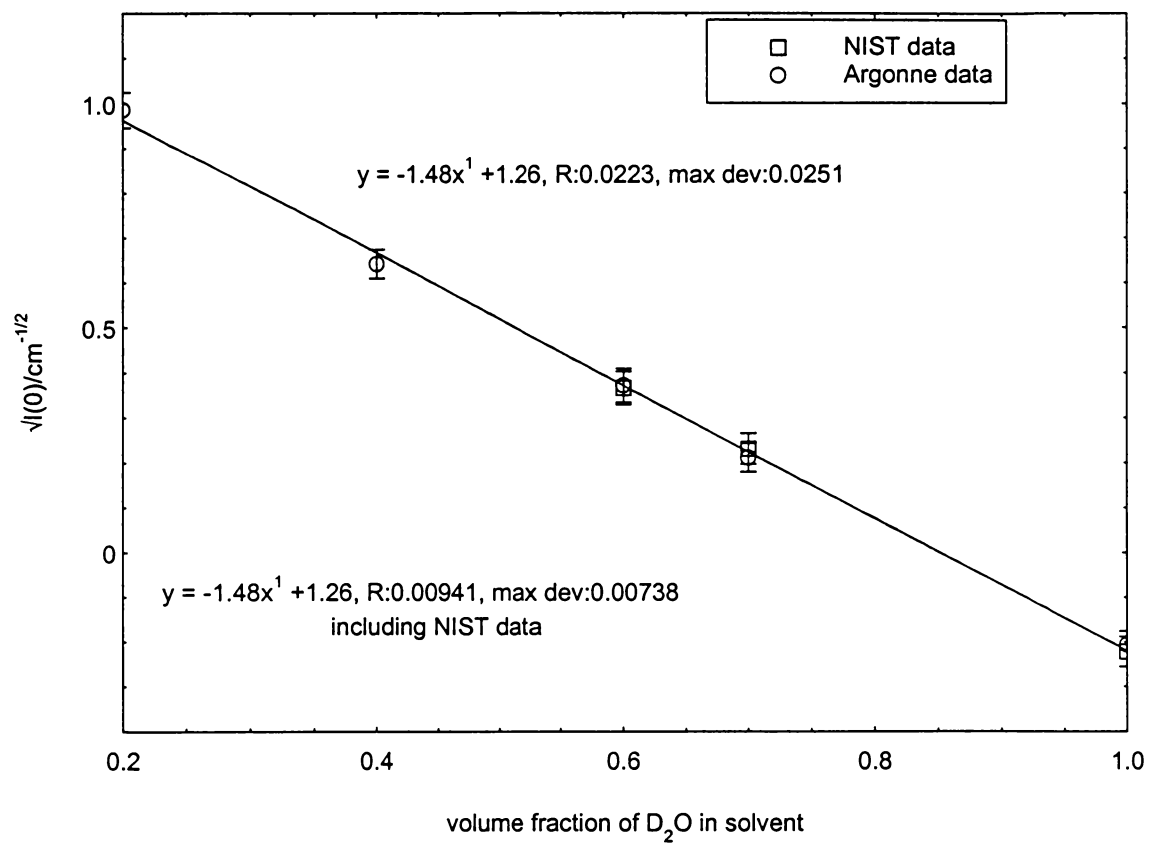


Figure 4.15 $I(0)^{1/2}$ vs. volume fraction of D₂O in the solvent for CTA-d₃₃ micelles in 1M Na₂₆ClBz, from external contrast variation

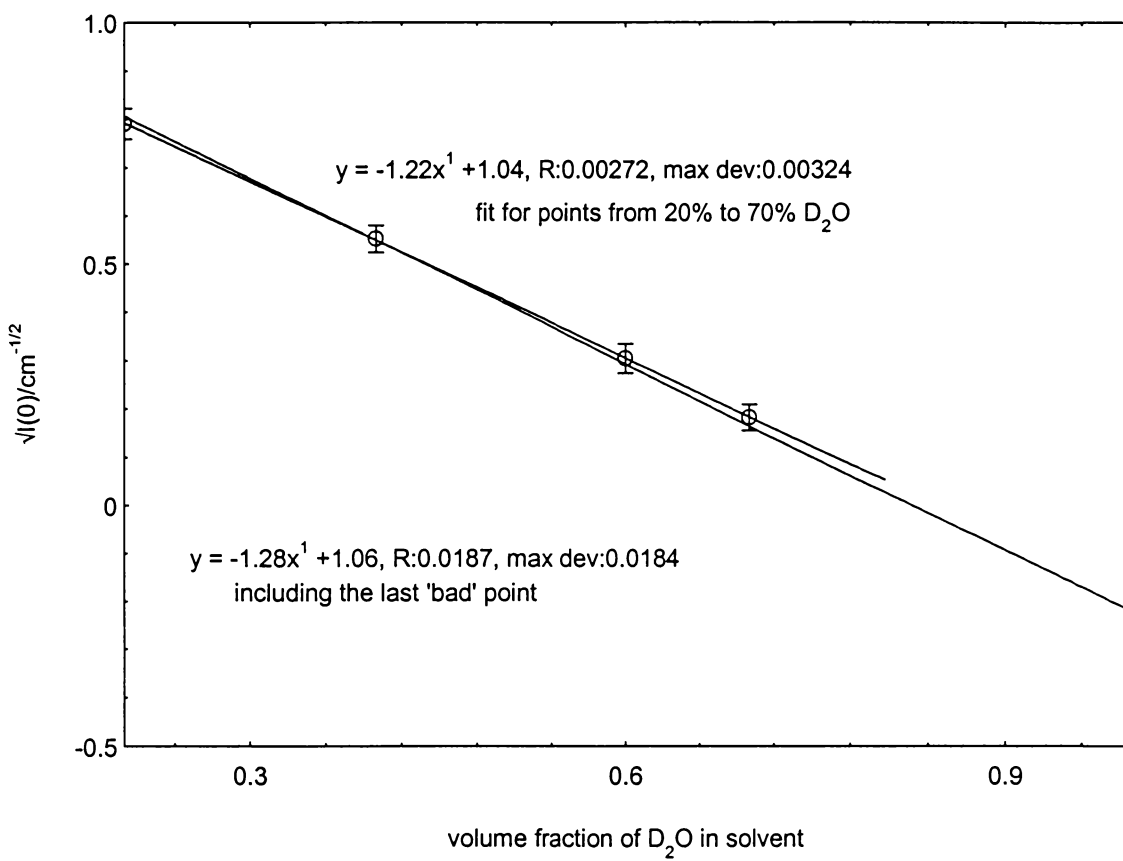


Figure 4.16 $I(0)^{1/2}$ vs. volume fraction of D_2O in the solvent for CTA- d_{33} micelles in 0.2M Na26ClBz, from external contrast variation

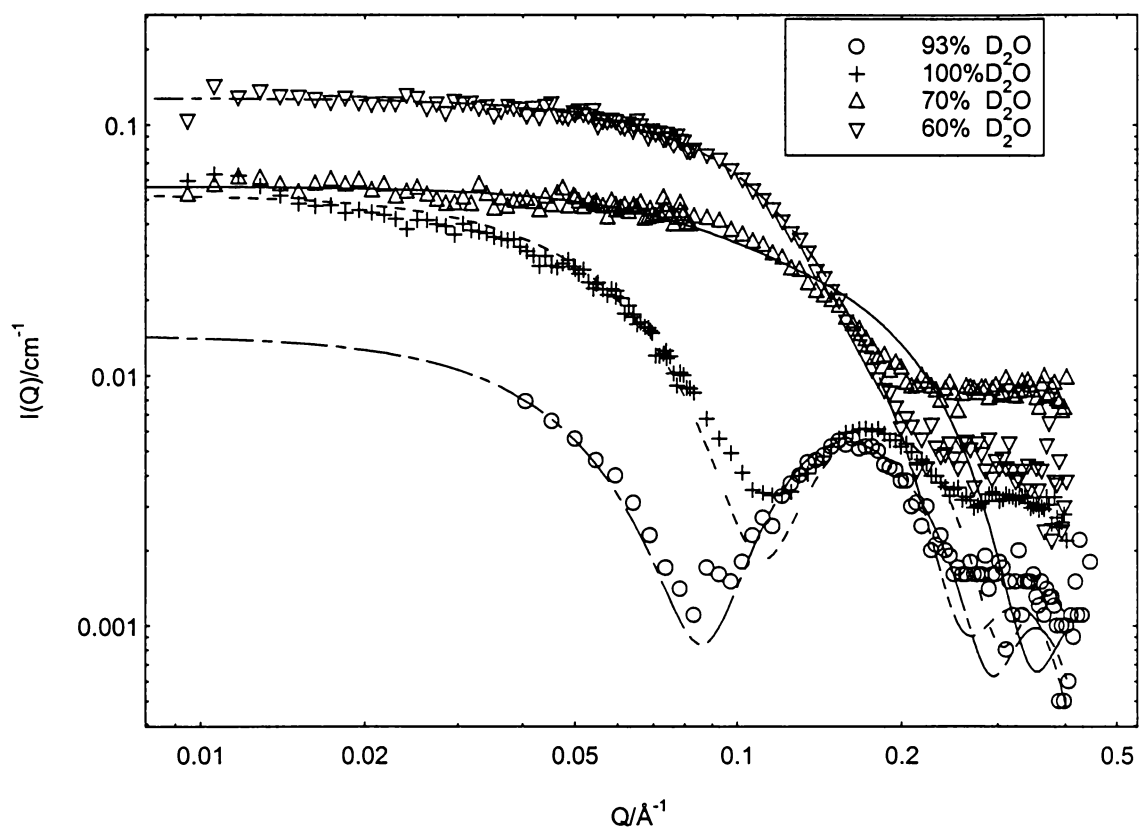


Figure 4.17 External contrast variation for CTA micelles in 1M Na_26ClBz using CTA- d_{33} to increase the shell contrast with the core at different volume % of D_2O in the solvent. Fits to the experimental data are also shown.

factor in chapter II (Eqn 2.37) and the same fitting program described previously. Only the data from NIST are fitted, since the data from Argonne are of poorer quality. Point-by-point background (solvent) subtractions were performed before fitting the data. The data at 100% D₂O was first fitted by using the many models described in Section 4.2. The best models based on those results were then used for the other samples at lower %'s of D₂O. The fitted results are presented in Table 4.6 under the heading "external contrast variation". The models used have ALF fixed at 0.98, no hydration, extra counterion binding on the micellar surface ($f = 1.3$), and thick = 4Å. The eccentricities ECC1 and ECC2 are varied, and AGG either varies or is fixed at AGG = 100 (a brief description of the model is also list on the top of each table block).

4.4 INTERNAL CONTRAST VARIATION USING CTA-d₃₃/CTA-d₀ MIXTURES

In the last two sections, we used external contrast variation, changing ρ_s in order to study the core plus shell structure of the micelles. Internal contrast variation can also be used to study our micellar system by adjusting the ρ_c and keeping the ρ_s constant. In this case, we used D₂O as our solvent for lower incoherent scattering. The internal contrast variation can be achieved by using a mixture of CTA-d₃₃ and CTA-d₀ surfactant. Figure 4.18 provides the calculated ρ_s , ρ_c and ρ_{sh} values for this experimental series. A match point is not achievable experimentally because the percentage of deuterated tail must exceed 100% in order to provide a high enough overall micellar scattering length density to match the solvent.

We performed the experiments at Argonne for Na26ClBz concentrations of 1M, 0.4M and 0.2M with a constant surfactant concentration of 20mM. The scattering curves

Table 4.6 Results of fitting the full scattering curves in the Q range 0.02~0.38 Å⁻¹ for CTA-d₃₃ micelles and CTA-d₀ micelles in 1M Na₂6CIBz. External and internal contrast variation respectively.

External contrast variation

Vary: AGG, ECC1, ECC2; fix: thick=4, ALF=0.98, without hydration, $f = 1.3$.

ϕ	AGG	CHI	ECC1	ECC2	A1(Å)	A2(Å)	ALF	R1(Å)	R2(Å)	B2	BBS
1.0	80	4.36	1.7412	1.8035	20.85	16.85	0.98	20.51	25.08	2.35	6.01
0.93	87	1.31	1.7331	1.7593	21.45	17.45	0.98	21.07	25.77	2.35	5.59
0.70	76	4.07	2.8902	3.4767	17.30	13.30	0.98	20.15	24.64	2.35	4.18
0.60	100	1.82	2.0509	2.0957	21.25	17.25	0.98	22.07	27.00	2.35	3.57

Vary: ECC1, ECC2; fix: AGG=100, ALF=0.98, thick=4, without hydration, $f = 1.3$.

ϕ	AGG	CHI	ECC1	ECC2	A1(Å)	A2(Å)	ALF	R1(Å)	R2(Å)	B2	BBS
1.0	100	4.84	2.2067	2.2261	20.71	16.71	0.98	22.04	26.96	2.35	6.01
0.93	100	1.48	2.0681	2.1195	21.16	17.16	0.98	22.04	26.96	2.35	5.59
0.70	100	4.29	3.2455	3.7334	18.21	14.21	0.98	22.04	26.96	2.35	4.18
0.60	100	1.82	2.0503	2.0970	21.22	17.22	0.98	22.04	26.96	2.35	3.57

Internal contrast variation (CTA-d₃₃/CTAd₀)

Vary: AGG, ECC1, ECC2; fix: thick=4, ALF=0.98, without hydration, $f = 1.3$.

ϕ	AGG	CHI	ECC1	ECC2	A1(Å)	A2(Å)	R1(Å)	R2(Å)	B1	B2	BBS
1.0	80	4.36	1.7412	1.8035	20.85	16.85	20.51	25.08	7.14	2.35	6.01
0.93	74	6.19	1.6001	1.6563	20.86	16.86	19.95	24.40	6.62	2.34	6.01
0.85	70	9.84	1.6392	1.7282	20.34	16.34	19.61	23.99	6.06	2.32	6.01
0.70	74	7.44	1.7834	1.8944	20.14	16.14	19.97	24.42	4.89	2.30	6.01

Vary: ECC1, ECC2; fix: AGG=100, ALF=0.98, thick=4, without hydration; $f = 1.3$.

ϕ	AGG	CHI	ECC1	ECC2	A1(Å)	A2(Å)	R1(Å)	R2(Å)	B1	B2	BBS
1.0	100	4.84	2.2067	2.2261	20.71	16.71	22.04	26.96	7.14	2.35	6.01
0.93	100	7.46	1.9090	1.9208	21.73	17.73	22.04	26.96	6.62	2.34	6.01
0.85	100	11.5	1.9917	2.0234	21.43	17.43	22.04	26.96	6.06	2.32	6.01
0.70	100	10.4	2.4286	2.5872	20.06	16.06	22.04	26.96	4.89	2.30	6.01

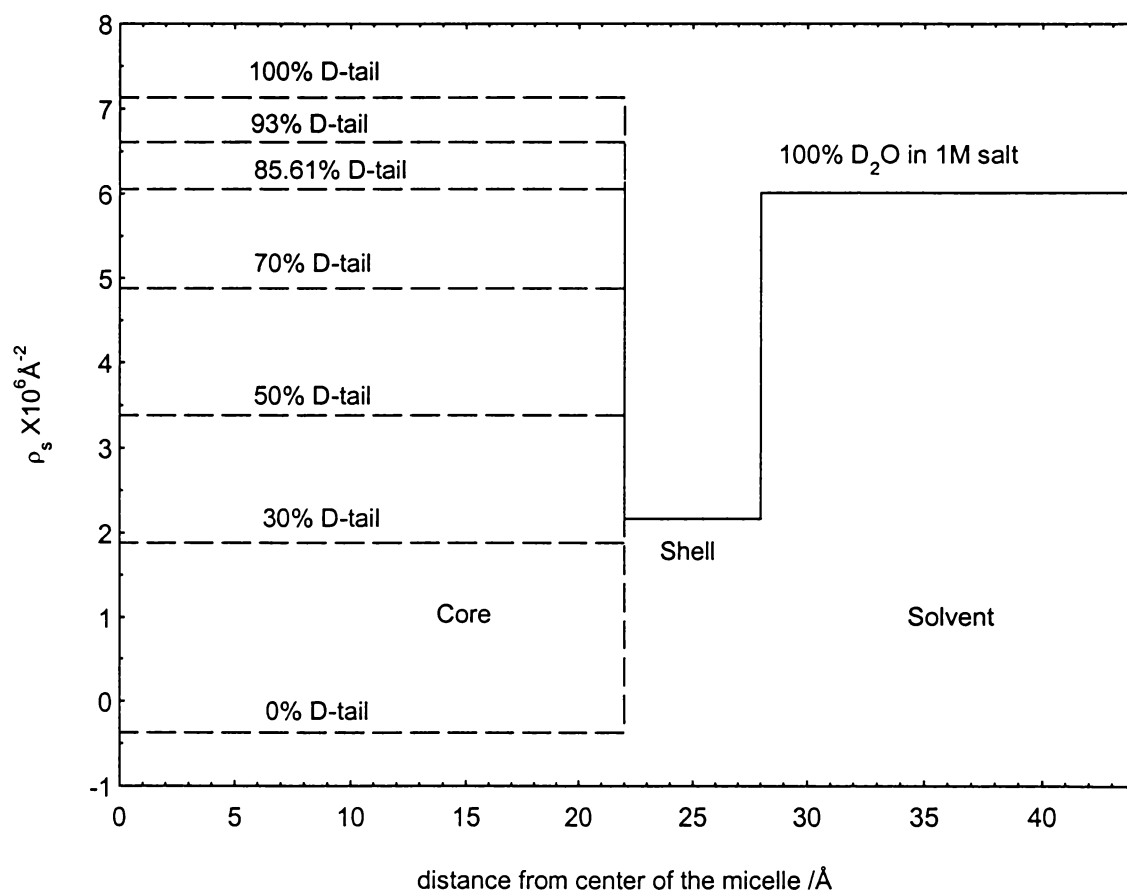


Figure 4.18 Scattering length density profiles for micelles of CTA-d₃₃/h₃₃-26ClBz mixture in D₂O containing 1M Na₂₆ClBz. Percents of D₂O are by volume.

are shown in Figures 4.19-4.21. In all cases, the scattered intensity decreases as the percentage of perdeuterated tails increase. Detailed experimental results are in Table 4.7. The counterion binding for these systems can be obtained from the match points calculated from the curves in Figure 4.22-4.24. The results are $f = 1.02 \pm 0.05$ for 1M salt from the match point of 118.4% d-tail; $f = 1.01 \pm 0.05$ for 0.4M salt from the match point of 122.8%; and $f = 0.83 \pm 0.07$ for 0.2M salt from the match point of 120.4%.

The NIST curves for internal contrast variation were fitted using eqn. 2.37 and the fitting program described in Section 4.2. The ρ_c 's used were based on Table 4.2. Point-by-point background subtractions of the solvent scattering were used for all the data. The solution containing 20mM CTA-d₃₃ and 1M Na₂6ClBz belongs both to the internal contrast series and the series in Section 4.3. As described in Section 4.3, the two best micellar models of many were chosen by evaluating the fitting results for this solution. The fitted results are presented Figure 4.25 and in Table 4.6 under the heading "internal contrast variation". The brief descriptions of the models used for each table are given at the top of each table block.

4.5 DISCUSSION AND CONCLUSIONS

Several groups^{25,109} have postulated charge reversal on the micellar surface as the driving force for decline in micellar size as the concentration of penetrating counterions increases. More recently, Warr and Cassidy¹⁹ measured zeta potentials and surface potentials on cationic micellar surfaces and concluded that even though the zeta potential becomes negative at the micellar surface as micellar size reversal occurs, the surface

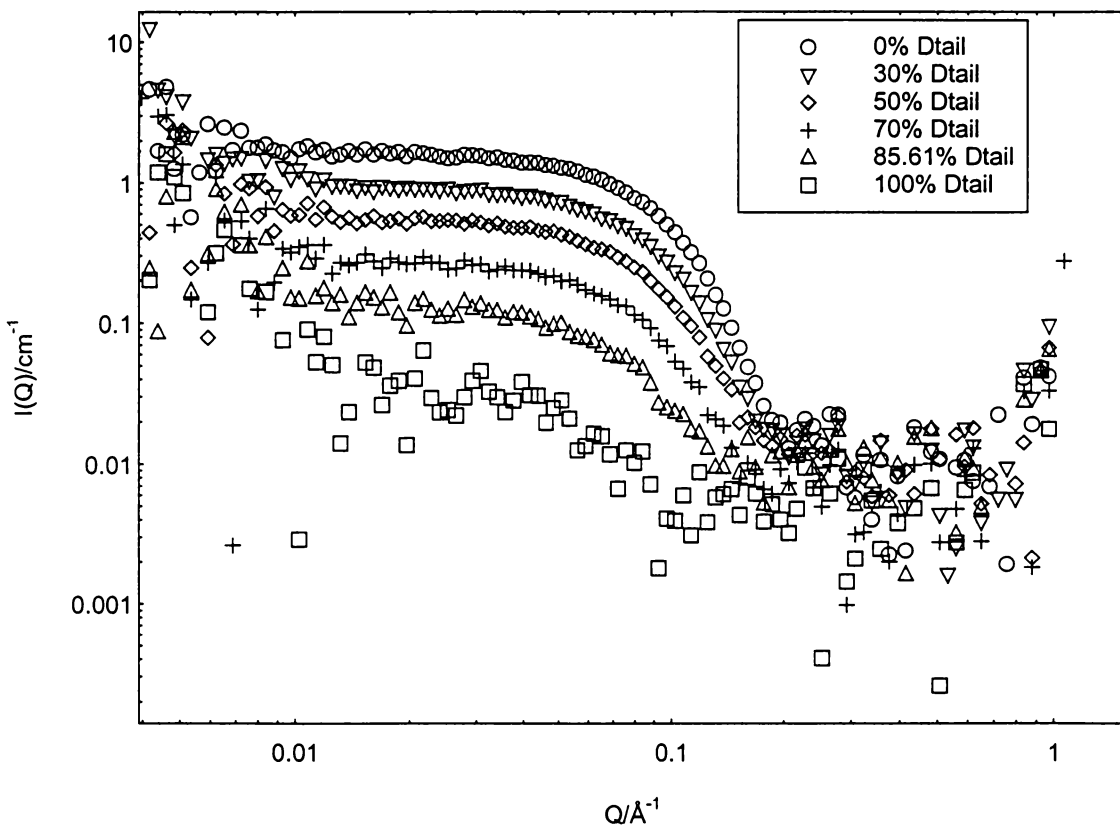


Figure 4.19 Internal contrast variation for CTA micelles in 1M Na₂6ClBz (D₂O) by varying CTA-d₃₃ mole percents

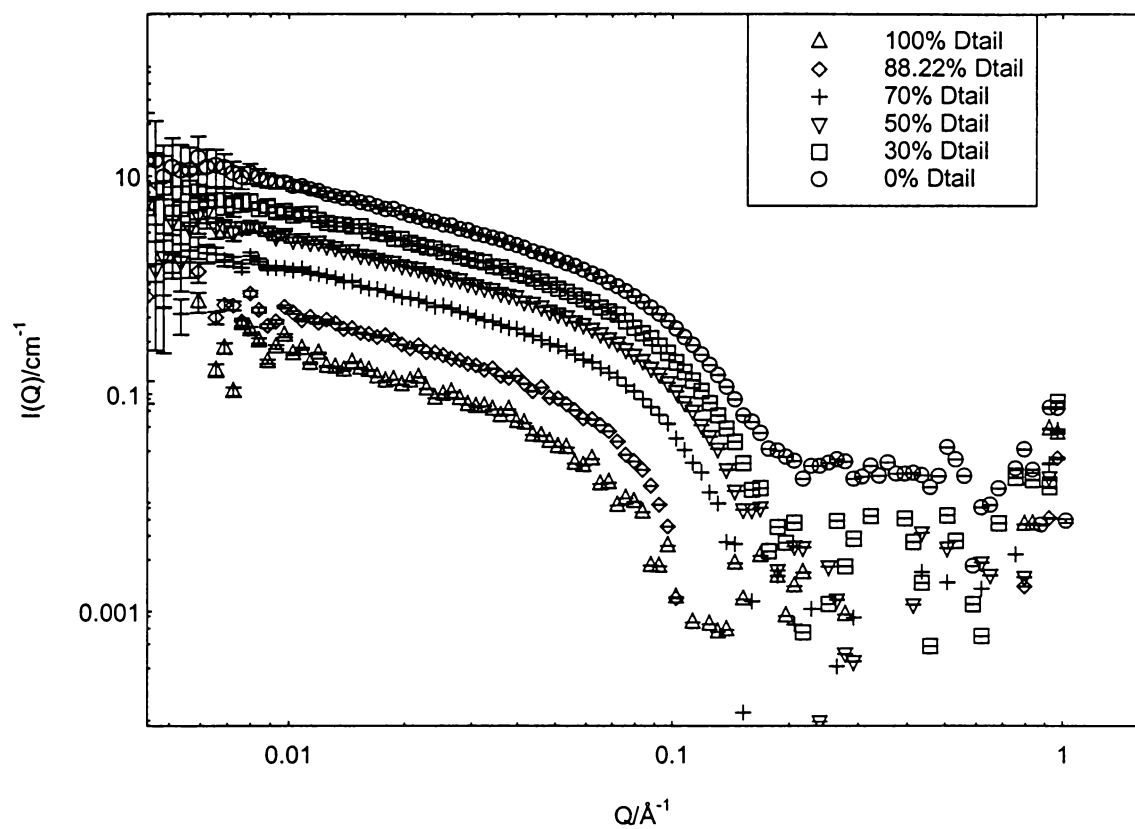


Figure 4.20 Internal contrast variation for CTA micelles in 0.4M Na₂₆ClBz (D₂O) by varying CTA- d_{33} mole percents.

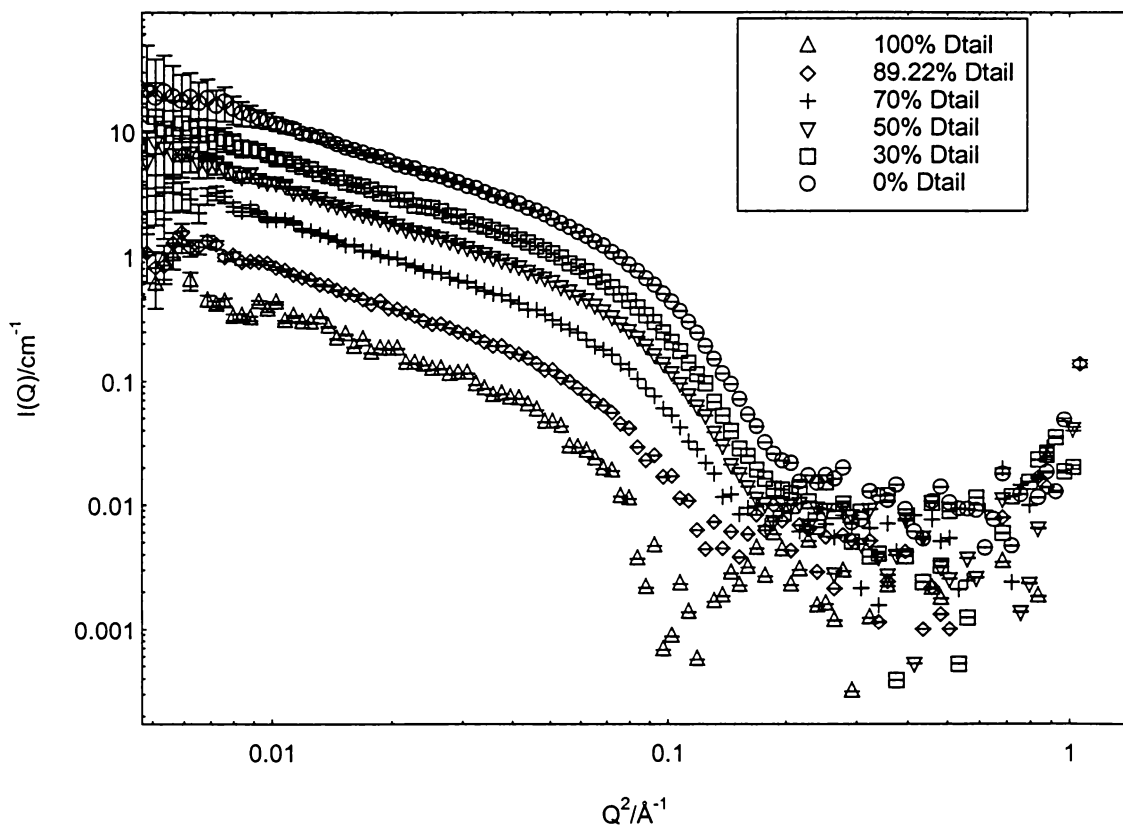


Figure 4.21 Internal contrast variation for CTA micelles in 0.4M Na₂₆ClBz (D₂O) by varying CTA-d₃₃ mole percents.

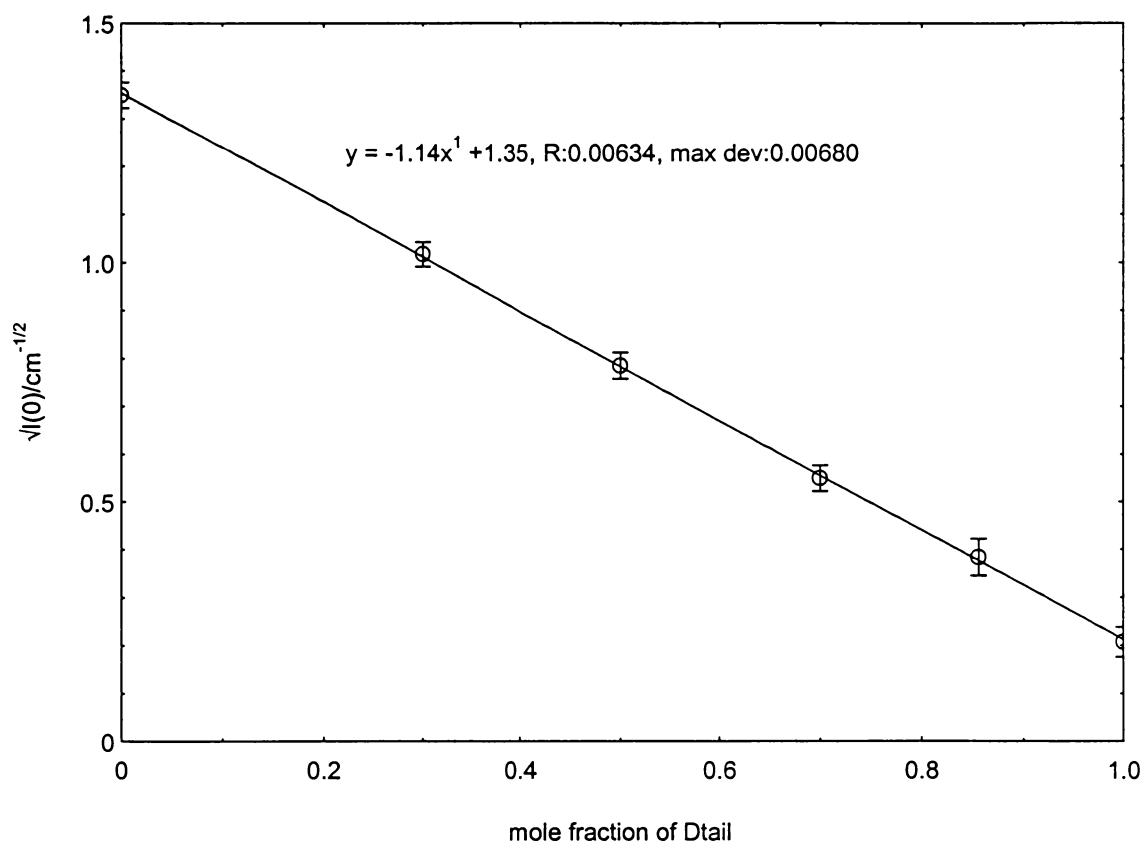


Figure 4.22 $I(0)^{1/2}$ vs. mole fraction of CTA-d₃₃ for CTA micelles in 1.0M Na₂₆ClBz, D₂O solvent

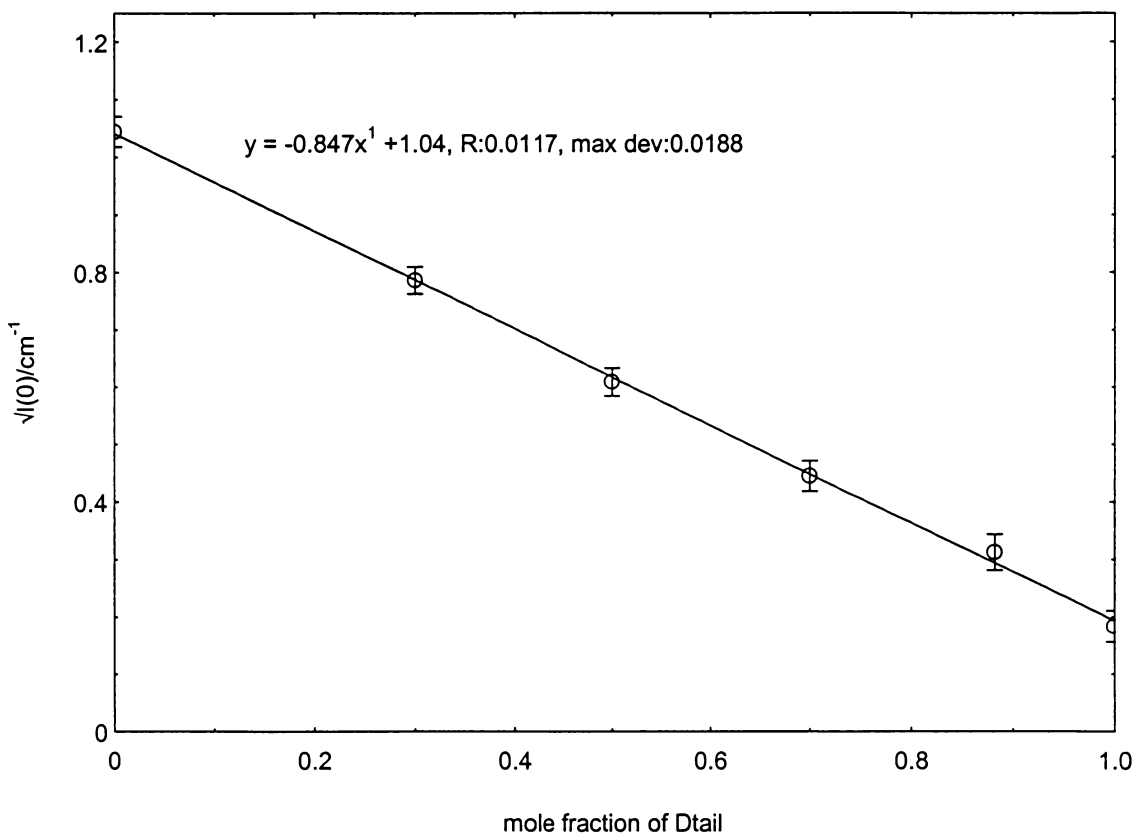


Figure 4.23 $I(0)^{1/2}$ vs. mole fraction of CTA-d₃₃ for CTA micelles in 0.4M Na₂₆ClBz, D₂O solvent

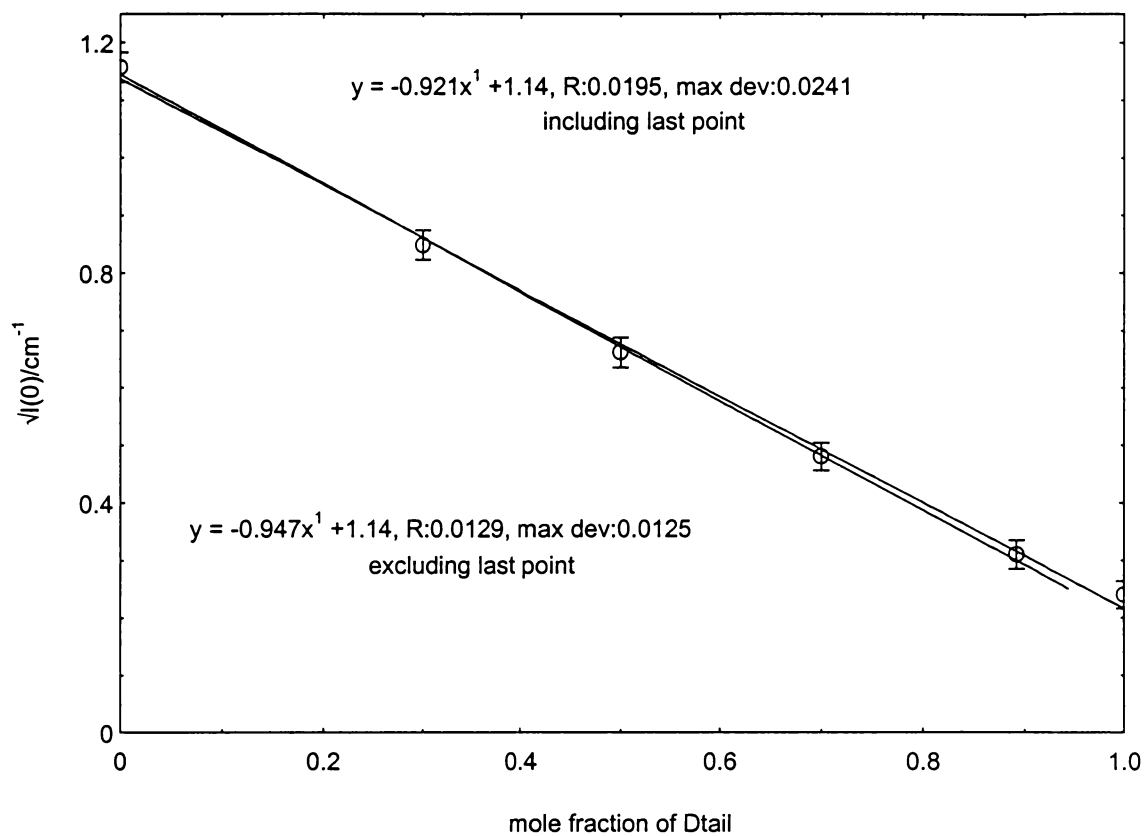


Figure 4.24 $I(0)^{1/2}$ vs. mole fraction of CTA- d_{33} for CTA micelles in 0.2M Na₂₆ClBz, D₂O solvent

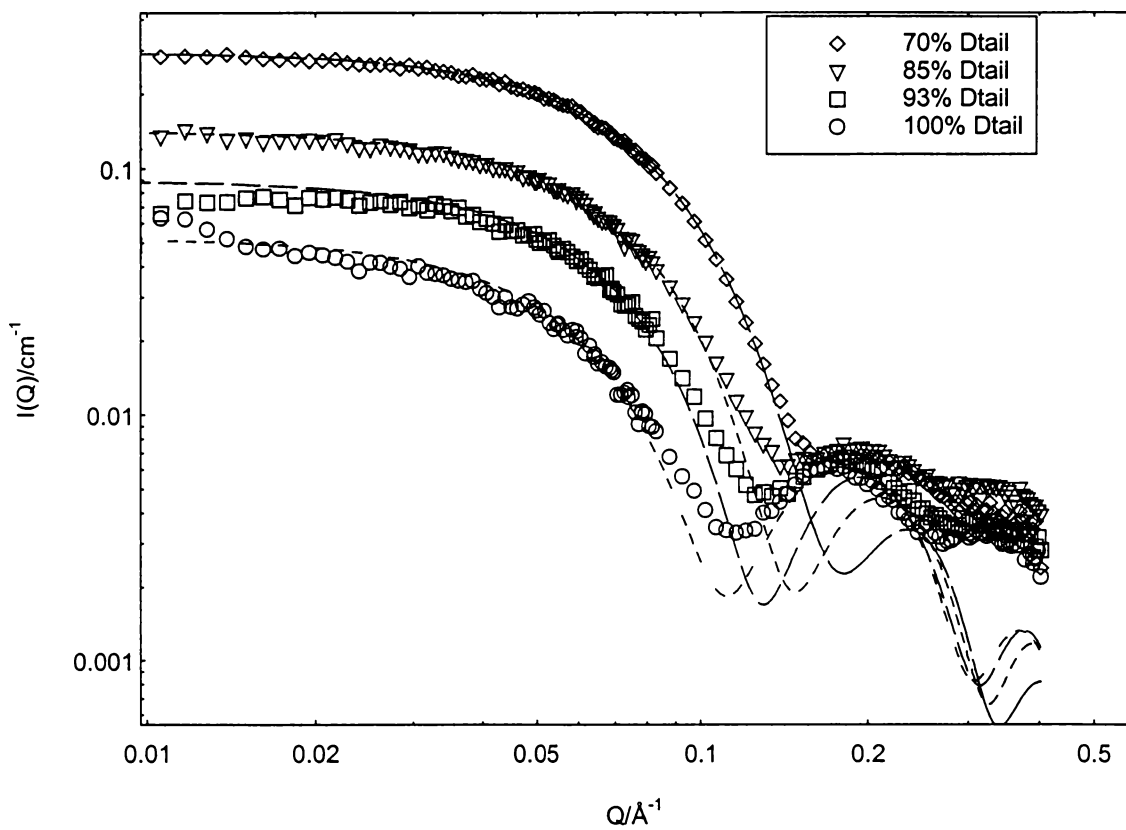


Figure 4.25 Internal contrast variation for CTA micelles in 1M Na₂6ClBz using CTA-d₃₃ to increase the shell contrast with the core at different mole % of CTA-d₃₃ in the core. Fits to the experimental data are also shown

Table 4.7 R_g and $I(0)$ from Guinier-plots for 1M Na26ClBz and $R_{g,cs}$ and $I(0)$ together with N/L from Guinier-like plots for 0.4M, 0.2M Na26ClBz by using CTA-d₃₃/CTA-d₀ in internal contrast variation experiments.

CTA-d₃₃/d₀ in 1M argonne internal

% of CTA- d ₃₃	$I(0)^{1/2}$ (cm ⁻²)	$I(0)$ (cm ⁻¹)	R_g (Å)
100	0.207 ± 0.013	0.0429 ± 0.006	28.19 ± 0.02
85.61	0.383 ± 0.010	0.147 ± 0.007	23.30 ± 0.02
70	0.549 ± 0.014	0.301 ± 0.008	21.56 ± 0.03
50	0.785 ± 0.008	0.616 ± 0.012	20.86 ± 0.02
30	1.017 ± 0.006	1.035 ± 0.014	20.42 ± 0.02
0	1.349 ± 0.005	1.820 ± 0.013	20.05 ± 0.02

CTA-d₃₃/d₀ 1M NIST internal

% of CTA- d ₃₃	$I(0)^{1/2}$ (cm ⁻²)	$I(0)$ (cm ⁻¹)	$R_{g,cs}$ (Å)
100	0.222 ± 0.012	0.0493 ± 0.007	27.77 ± 0.02
93	0.300 ± 0.012	0.0898 ± 0.008	25.28 ± 0.04
85.61	0.381 ± 0.008	0.145 ± 0.010	24.00 ± 0.03
70	0.554 ± 0.006	0.307 ± 0.008	22.58 ± 0.03

CTA-d₃₃/d₀ 0.4M argonne internal

% of CTA- d ₃₃	$I(0)^{1/2}$ (cm ⁻²)	$I(0)$ (cm ⁻¹)	$R_{g,cs}$ (Å)	N/L (Å ⁻¹)
100	0.183 ± 0.013	0.0334 ± 0.008	23.11 ± 0.03	1.811
88.22	0.312 ± 0.009	0.0973 ± 0.006	23.28 ± 0.04	2.198
70	0.445 ± 0.010	0.198 ± 0.009	16.61 ± 0.04	1.904
50	0.609 ± 0.008	0.371 ± 0.012	15.10 ± 0.02	1.859
30	0.786 ± 0.007	0.618 ± 0.010	14.21 ± 0.05	1.894
0	1.044 ± 0.005	1.090 ± 0.012	13.43 ± 0.05	1.898

CTA-d₃₃/d₀ 0.2M argonne internal

% of CTA- d ₃₃	$I(0)^{1/2}$ (cm ⁻²)	$I(0)$ (cm ⁻¹)	$R_{g,cs}$ (Å)	N/L (Å ⁻¹)
100	0.240 ±	0.0578 ±	27.31 ± 0.03	2.734
89.22	0.310 ±	0.0963 ±	19.13 ± 0.03	2.133
70	0.480 ±	0.230 ±	16.73 ± 0.02	2.085
50	0.662 ±	0.438 ±	15.62 ± 0.02	2.103
30	0.848 ±	0.719 ±	15.03 ± 0.03	2.130
0	1.157 ±	1.338 ±	14.49 ± 0.02	2.271

potential never becomes negative. They consider the surface potential to be reporting on the micellar charge at the level of head groups.

In the 1990s, Magid and coworkers⁹⁴ measured micellar surface potentials for CTACl/NaCl and CTA26ClBz/Na26ClBz solutions and found lower, although still positive, values of the potentials, even at high 26ClBz⁻ concentrations. At a given counterion concentration, the potentials were significantly smaller for 26ClBz than for Cl, indicating a higher concentration of counterions for the 26ClBz case in the inner part of the electrical double layer, near or at the micellar surface. Attempts to were also made to measure charge reversal coming from an excess of counterions in the outer part of the electrical double layer. That is, an attempt was made to determine the micellar zeta potentials in aqueous solutions containing up to 1M Na26ClBz. Unfortunately, the high electrical conductivity of the solution caused the measurement to fail.

SANS can provide an alternative measurement by using contrast variation to determine how much counterion has penetrated the micellar surface, inserting between the head groups. Detailed full curve fits can provide more information about the outer portion of the micelle, the shell. External and internal contrast variation experiments have been described in the last three sections, and counterion binding values have been derived from them. Do we have a definitive answer on why the micelles revert in size back to globules at high salt? The answers are YES and NO.

The NO answer comes from the challenging nature of these experiments. As already mentioned in section 4.3, the match point for the external contrast variation series (CTA-d₃₃) in 0.2M Na26ClBz changes from 82.82% to 85.24% depending on whether the $I(0)^{1/2}$ of the sample in 100% D₂O is included or not. The derived value of the

counterion binding parameter is very sensitive not only to the experimental match points, but also to some other numbers we used during our calculation, such as the percentage of D atoms in the CTA-d₃₃ surfactant that we bought from CDN Isotopes, Inc. The stated composition was 99.1%D, and let's assume a reasonable error bar on that value. If the actual composition is 100%D, not 99.1%D, the experimental value of f in 1M Na₂₆ClBz changes from 1.02 to 1.10; f in 0.4M Na₂₆ClBz changes from 1.01 to 1.09; f in 0.2M Na₂₆ClBz changes from 0.83 to 0.88. If the actual composition is smaller than 99.1%D, the experimental values will decrease by similar amounts.

There are other errors that can be minimized by careful preparation of the samples and fitting of the data, and using the average f 's from the three sequences. Table 4.8 lists all the results for f , R_g for 1M salt from Guinier analysis and the R_g derived from the full fits for the three contrast variation series. For the external contrast series with Na-d₃-₂₆ClBz, the R_g s from the full fits were calculated by using the ellipsoidal core plus shell (Eqn. 2.30) and also the equivalent spherical radii (Eqn. 2.29); for the other two series, only R_g based on the equivalent spherical radii were calculated. The R_g 's from the Guinier analyses and from the full fits show differences, but the qualitative trends in $R_g(\rho)$ indicate the micellar model used are physically reasonable.

The fits in Figure 2.17 are better than the fits in Figure 2.25 (this is obvious based on the CHI values from the fits), indicating we still have not found the best possible model(s) for all three systems or that there is no best model(s) fits for all three different series. From the result of the fits, we also observed some changes on ECC1 and ECC2 in the same series, which means the micellar structures have slightly changed as the D/H ratio changes. This agrees Berr's study¹¹¹ on solvent isotope effects on the structure of

CTAB micelles in aqueous solutions. He discovered that the aggregation number increases as the D₂O content increase for the protiated surfactant. This can be observed in all three experimental series. For protiated surfactant in external contrast variation experiments (Section 3.2), the aggregation number shows the trend increase as the D₂O content increase from 40% to 100%, except 55%. For the deuterated surfactant external contrast variation experiments, the aggregation number shows the trend decrease as the D₂O content increase from 60% to 100%, except 70%. And for the deuterated surfactant internal contrast variation experiments, the aggregation number shows slightly changes as the percentage of the deuterated surfactant change from 70% to 100%.

The micellar sizes decrease in order from wormlike, cylindrical to spherical as the Na₂6ClBz concentration increases from 0.2M, to 0.4M to 1M.^{65,95} The mean value of f listed in Table 4.8 increases (0.85 for 0.2M; 0.99 for 0.4M and 1.05 for 1M) as the micellar size decreases. A value of f greater than one was obtained from the experiments at 1M salt suggesting that a possible charge reversal appeared on the micellar surface at high salt concentration, which can charge up the micelles again and increase the electrostatic repulsions between the head groups. This is consistent with an increase in the area per head group which observed previously.⁶⁵ Since increasing the electrostatic repulsions between the head groups decreases the energy advantage for the locally cylindrical vs. spherical environments, $G_{3,cyl} - G_{3,sph}$ becomes more negative. This does contribute to the micelles becoming spheres or ellipsoids again. However, it is questionable whether the small change in f can be the only source of the large decline in the micellar size.

Table 4.8 Comparison of three different series of the counterion binding(f) on the micellar surface and the radius of gyration

Counterion binding fraction f

[salt]	Na26-d ₃ external	CTA-d ₃₃ external	CTA-d ₃₃ internal	Mean
1.0M	0.94 ± 0.05	1.20 ± 0.05	1.02 ± 0.05	1.05 ± 0.05
0.4M	0.96 ± 0.05		1.01 ± 0.05	0.99 ± 0.05
0.2M		0.86 ± 0.05	0.83 ± 0.05	0.85 ± 0.05

Na26-d₃ external contrast in 1M salt

Volume % of D ₂ O	R _g /Å Guinier plot	R _g /Å Ellipsoid (fits)	R _g (Å)/ spherical equivalent (fits)
100	22.25 ± 0.04	32.95	19.70
85	20.57 ± 0.05	21.96	19.48
70	20.35 ± 0.04	22.27	19.10
55	20.64 ± 0.03	23.10	18.44
40	18.49 ± 0.04	19.81	16.95

CTA-d₃₃ external contrast in 1M salt

Volume % of D ₂ O	R _g (Å) Guinier plot	R _g (Å)/ spherical equivalent (fits)
100	28.19 ± 0.02	28.29
93	31.08 ± 0.02	29.35
70	9.81 ± 0.03	6.73
60	16.31 ± 0.01	13.62
40	17.83 ± 0.02	16.79
20	18.89 ± 0.02	17.88

CTA-d₃₃ internal contrast in 1M salt

Volume % of D ₂ O	R _g (Å) Guinier plot	R _g (Å)/ spherical equivalent (fits)
100	28.19 ± 0.02	26.83
85.61	23.30 ± 0.02	23.14
70	21.56 ± 0.03	21.28
50	20.86 ± 0.02	20.00
30	20.42 ± 0.02	18.92
0	20.05 ± 0.02	18.55

The increase in the counterion binding affects other free energy terms as well. The increasing presence of counterions penetrating the plane of the surfactant head groups at the micellar surface can decrease the cross-sectional radius, thus increasing the number of gauche conformations of the surfactant tails inside the cylindrical core. This occurs to minimize packing voids caused by the surfactant tails being longer than the counterion's aromatic ring. The increase in gauche conformations and other chain constraints increase the $G_{1,cyl}$ relative to $G_{1,sph}$, and this makes $G_{1,sph}-G_{1,cyl}$ more negative, favoring spheres. As more penetrating counterions insert into the plane of the surfactant head group, the energy of the hydrocarbon/water interface will decrease, and this will decrease $G_{2,sph}$ more compared with $G_{2,cyl}$, and make $G_{2,cyl}-G_{2,sph}$ less positive. These contributions taken together make the spherical micelles more favorable.

CHAPTER V

EXPERIMENTAL SECTION

5.1 MATERIALS

Sodium dodecyl sulfate (SDS) was obtained from British Drug House (BDH) and was used as received. Cetyl(hexadecyl)trimethylammonium bromide (CTAB), and cetyltrimethylammonium chloride (CTACl) from Fluka chemicals were used as received. Tetradecyltrimethylammonium bromide (TTAB) and cetyltrimethylammonium *p*-toluenesulfonate (CTATos) were used as received from Aldrich. AR grade sodium chloride (NaCl), sodium bromide (NaBr), sodium *p*-toluenesulfonate (NaTos), sodium salicylate (NaSal) from Aldrich were used as received. Cetylpyridinium bromide monohydrate (CPyBr·H₂O) and cetylpyridinium chloride monohydrate (CPyCl·H₂O) were used as received from Fluka chemicals. The synthesis of sodium 2,6-dichlorobenzoate (Na26ClBz) from 2,6-dichlorobenzoic acid and the synthesis of cetyltrimethylammonium 2,6-dichlorobenzoate (CTA26ClBz) from CTAB will be described in the following sections. Deuterated nitrobenzene and CTAB, 99%D, were used as received from CDN isotopes. D₂O, 99.9%D, was obtained from CDN isotopes. Counterion exchange of CTA surfactant with deuterated C₁₆ tail, CTA-d₃₃-26ClBz follow the same method as used for the protiated surfactant. H₂O was obtained from a Milli-Q reagent water system.

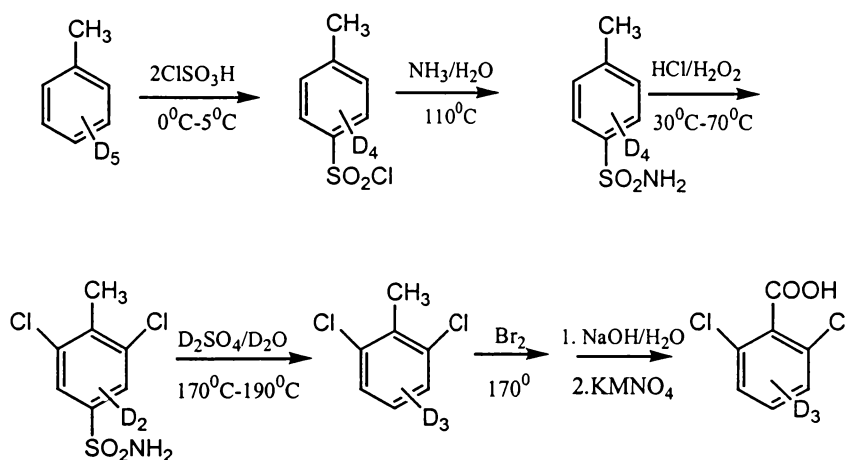
5.2 MAKING SOLUTIONS

Some of the surfactants are not easily dissolved in water at room temperature, and some surfactant solutions have large viscosities, making them difficult to transfer even

using digital pipets. In order to make solutions accurately or to double check the solution-making process, we used an analytical balance together with volumetric flasks and pipets to make the solutions. We make a surfactant stock solution which can be diluted to make a series of surfactant solutions of varying surfactant concentration. Alternatively, a stock solution in D₂O of fixed surfactant concentration can be mixed with one in H₂O to make samples for experiments using contrast variation.

5.3 SYNTHESIS OF DEUTERIATED 2,6-DICHLOROBENZOIC ACID

Because deuterated compounds are expensive and we needed relatively large amounts, we investigated two different synthetic schemes using protiated starting materials. However, in the schemes we show deuterated compounds. Scheme 1 starts with deuterated toluene.



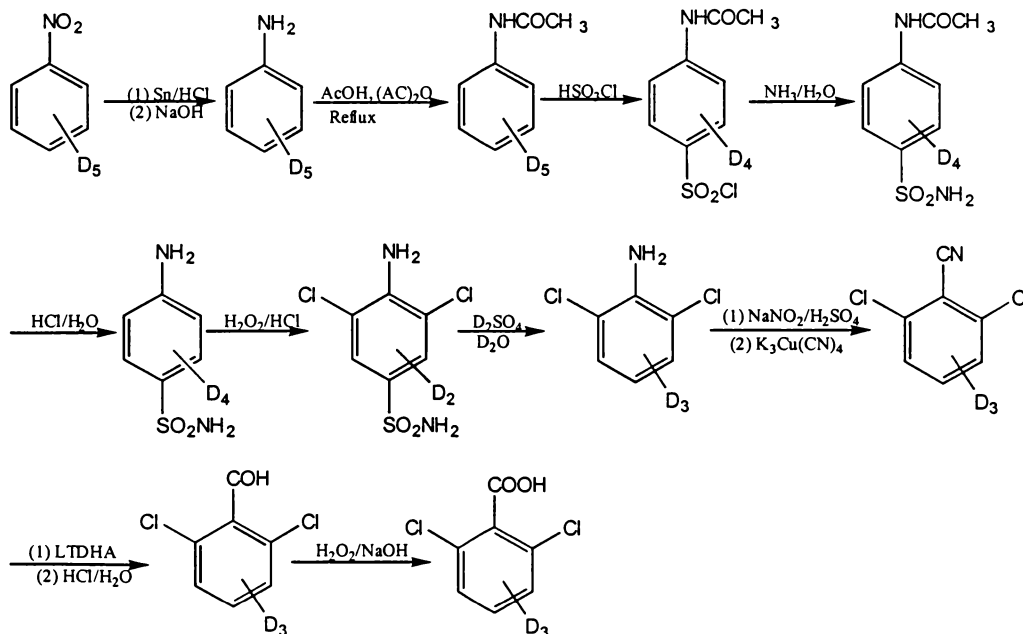
Scheme 1

Because the first step in scheme 1 has a yield of only 24%, this approach gives a final yield of 6.5-7.5% for the 2,6-dichlorobenzoic acid.

The other approach uses deuterated nitrobenzene as the starting material, scheme 2, with a final yield of 11.5-13%. We used this method to synthesize our deuterated compound with a price of approximately \$70/g. The experimental details are given below.

Aniline-d₅ (1)

Nitrobenzene-d₅ was purchased from CDN Isotopes. 50g of granulated tin and 25g of nitrobenzene were added to a round-bottom flask, cooled in the ice, with condenser, and 100mL concentrated hydrochloric acid was added in 10mL portions with vigorous stirring. After all the HCl was added, the reaction mixture was stirred at 100°C for one more



Scheme 2

hour to let the reaction proceed to completion. After the reaction mixture was cooled down, 75g of sodium hydroxide in 125 mL water solution was added, while the reaction flask was cooled in an ice-water bath to prevent volatilization of aniline. After steam distilling the reaction mixture until 400mL of solution was collected, 80g of sodium chloride was added to the distillate to reduce the solubility of aniline. The aniline was extracted by using ethyl ether. After the ether was distilled, the aniline was collected by distillation between 182-185°C (b.p. 184°C) with a yield of 93%.

Acetanilide-d₅ (2)

18 g aniline-d₅ (1), 20 mL acetic acid, 20 mL acetic anhydride and two pieces of zinc were placed in a round-bottom flask with condenser. After refluxing for one hour, the reaction mixture was poured into 300 mL cold water with stirring, the white product was collected and washed with cold water. The yield was 92%.

***p*-acetaminobenzenesulfonyl chloride-d₄ (3)**

22 g dry acetanilide-d₅ (2) was placed in a round-bottom flask with ice-water bath and 55 mL chlorosulfonic acid was added drop-wise. After the addition of acid was complete, the reaction mixture was kept in the water bath at 60-70°C for 2 hours, then the temperature was raised to 100°C for 30 minutes more to complete the reaction. The reaction mixture was added drop-wise to 300 mL of ice and water bath with stirring. The white solid was collected and washed on a Buchner funnel, and the compound was dried. The yield was 72%.

***p*-acetaminobenzenesulfonamide-d₄ (4)**

p-acetaminobenzenesulfonyl chloride-d₄ (3) was transferred into a 250 mL round-bottom flask and 60 mL concentrated aqueous ammonia solution and 60 mL water were added. The reaction mixture was stirred in an oil bath at 110°C for 10 min, during which time the solid changed to a more pasty suspension of the amide. After the suspension was cooled well in an ice bath, the product was collected by filtration. The yield of *p*-acetaminobenzenesulfonamide-d₄ yield was 93%.

***p*-aminobenzenesulfonamide-d₄ (5)**

After drying the *p*-acetaminobenzenesulfonamide-d₄ (4), which was a gray solid, it was transferred into a round-bottom flask with condenser, 18 mL concentrated HCl and 35 mL water were added to the flask, and the mixture was refluxed until all the solid dissolved. The reaction mixture was then heated at reflux for 10 min longer. No solid amide should appear when the reaction mixture was cooled down to room temperature. 3N sodium hydroxide solution was used to neutralize the acid solution. The reaction mixture was then cooled thoroughly in an ice bath and the *p*-aminobenzenesulfonamide was collected by filtration. The yield was 88%.

3,5-dichloro-4-aminobenzenesulfonamide-d₂ (6)

16 g *p*-aminobenzenesulfonamide-d₄ (5), 160 mL water and 16 mL hydrochloric acid were added to a round-bottom flask. The reaction mixture was stirred until all solid dissolved, and then 144 mL hydrochloric acid was added. After the reaction temperature was raised to 45°C in a water bath, 19.2 mL 30% hydrogen peroxide was added with vigorous

stirring to initiate the reaction. The reaction mixture was heated at 60°C for one hour, then cooled to 20°C. The pink solid was dried after filtration. The yield was 80%.

2,6-dichloroaniline-d₃ (7)

The crude 3,5-dichloro-4-aminobenzenesulfonamide-d₂ (6) and 64 mL 70% D₂SO₄ (40 mL deuterium sulfuric acid diluted with 24 mL deuterium oxide) were put into a 250mL round-bottom flask with condenser. The reaction mixture was stirred for 7 hours under oil bath heat at 170-190°C. The black mixture was steam distilled after the reaction. The white solid product that was collected had a m.p. at 39-40°C. The yield was 77%.

2,6-dichlorobenzonitrile-d₃ (8)

3.6 g of sodium nitrite was added to a 80mL beaker with 24 mL sulfuric acid slowly at 0°C, and the temperature was then raised to 55-60°C to dissolve all the solid. After the mixture cooled down to room temperature, 7.5 g 2,6-dichloroaniline-d₃ (7) and 18.5 mL acetic acid were added drop-wise into the acid solution at 20°C to form the 2,6-dichlorobenzediazonium sulfate solution. The reaction mixture was then poured slowly into an aqueous solution at 60°C containing 5.13 g copper cyanide, 15.39 g potassium cyanide and 45 g sodium carbonate. After the addition was complete, the reaction mixture was heated to 90°C for 10 min. After standing overnight, 5.1 g 2,6-dichlorobenzonitrile was collected by steam distillation from the reaction mixture. The yield was 64%.

2,6-dichlorobenzaldehyde-d₃ (9)

All glassware was dried in the oven, assembled hot and cooled under dry nitrogen. Tetrahydrofuran (THF) was distilled from benzophenone-sodium. Lithium aluminum hydride (LAH) and dihexylamine (DHA) were used directly as received from Aldrich. 2.67 g of LAH was dissolved in 30 mL THF, 48.9 mL of DHA was added drop-wise with vigorous stirring into the LAH solution at 0°C. The reaction mixture was stirred for 12 hours at 0°C until evolution of hydrogen was complete. Then the lithium tris-(dihexylamino)aluminum hydride (LTDHA) solution was added drop-wise with stirring into a solution containing 5.1 g 2,6-dichlorobenzonitrile (8) and 20 mL THF at 0°C. After one hour, the reaction mixture was treated with 60 mL 3N HCl to hydrolyze the 2,6-dichlorobenzhydrazine. The liquid was extracted by ether, the solid was filtered and washed several times. After removing the ether by rotary evaporation, 3.3 g of 2,6-dichlorobenzaldehyde-d₃ were obtained using a column chromatography. The yield was 74%.

2,6-dichlorobenzoic acid-d₃ (10)

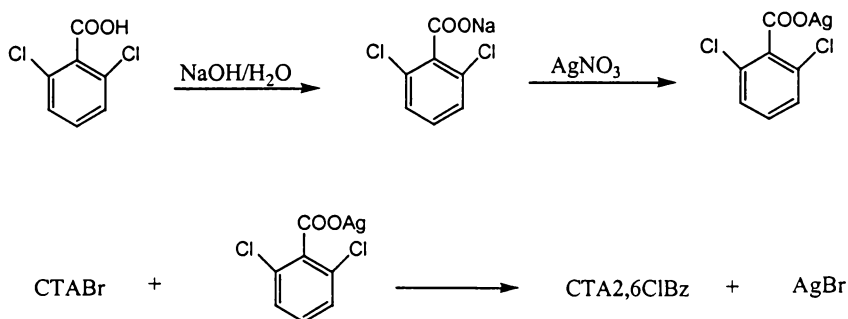
3.3 g of 2,6-dichlorobenzaldehyde-d₃ (9) was dissolved in 25 mL 10% sodium hydroxide solution, and 11.5 mL of hydrogen peroxide were added drop-wise at 75°C to oxidize the aldehyde. After the addition was complete the reaction mixture was held at 75°C for one more hour to complete the reaction. The reaction mixture was cooled down and filtered, and hydrochloric acid was used to precipitate the 2,6-dichlorobenzoic acid-d₃. The white solid was collected by filtration, and dried in a vacuum oven. The yield was 3.1g, 86%.

5.4 PREPARATION OF CETYLTRIMETHYLAMMONIUM 2,6-DICHLOROBENZOATE

Sodium 2,6-dichlorobenzoate was prepared by neutralizing 2,6-dichlorobenzoic acid with NaOH. CTA26ClBz surfactant was synthesized from CTAB by allowing it to react with Ag26ClBz. Deuterated Na-d-26ClBz and deuterated CTA-d₃₃-26ClBz were synthesized by using deuterated compounds as starting materials. The detailed synthetic approach is shown in scheme 3 and discussed below.

Sodium 2,6-dichlorobenzoate (Na26ClBz)

26g of sodium hydroxide was dissolved in 150mL water, heated to 90°C, and 100g of 2,6-dichlorobenzoic acid was added. The mixture was stirred until all the dichlorobenzoic acid was dissolved. The reaction mixture was then cooled to -20°C by



Scheme 3

using an ice/salt bath, and filtered. The collected white solid Na26ClBz was dried in the oven. The dried Na26ClBz was recrystallized from water. Elemental analysis was used to determine the purity of the product with the result: 39.54%C; 1.46%H; 33.16%Cl (Theoretical 39.50%C; 1.37%H; 33.32%Cl).

Silver 2,6-dichlorobenzoate (Ag26ClBz)

Ag26ClBz was synthesized by mixing a Na26ClBz solution with a AgNO₃ solution with 1:1 molar ratio. After stirring for several hours, the gray solid was filtered and dried in a vacuum oven for the next step.

Cetyltrimethylammonium 2,6-dichlorobenzoate (CTA26ClBz)

5g CTAB was dissolved in 40mL MeOH and 12g Ag26ClBz was added with stirring. The reaction mixture was stirred at 50°C overnight. The reaction mixture was cooled to 0°C and filtered, and the MeOH removed by rotary evaporation to get solid CTA26ClBz. The surfactant was recrystallized from CH₃CN. Elemental analysis of the CTA26ClBz gave: 65.96%C; 9.68%H; 2.97%N; and 14.98%Cl (Theoretical 65.79%C; 9.61%H; 2.95%N; 14.94%Cl).

5.5 USING NMR TO DETERMINE THE DEUTERATION OF Na-d₃-6ClBz

The percent deuteration of the Na-d₃-26ClBz is very important in the contrast variation experiments because it affects both ρ_{mic} and ρ_s . To determine it, a series of NMR spectra were acquired. In all cases, the same amount of protiated MeOH is added into the D₂O solvent to use as an integration standard. The integrations for a series of

concentrations of Na²⁶CIBz and Na²⁶-d₃-CIBz were measured. The result is coming from a series integral of the NMR measurement by using the concentration vs. integration slopes of protiated and deuterated Na²⁶CIBz. The percent deuteration is 87.6%.

5.6 NEUTRON PRODUCTION AND DETECTION

Neutron scattering experiments were mainly performed at the reactor source at the National Institute of Standards and Technology (NIST) Center for Neutron Research (NCNR) in Gaithersburg, Maryland. We also used SINQ, a pulsed neutron source at Paul Scherrer Institute (PSI) in Villigen, Switzerland and the Intense Pulsed Neutron Source (IPNS) at Argonne National Laboratory in Chicago, Illinois. In a reactor, neutrons are produced by a fission chain reaction. The reactor core is surrounded by moderators, often D₂O or H₂O, whose molecules undergo repeated collisions with the neutrons, which lose energy until they have an average thermal energy. The maximum flux of neutrons is designed to be just outside the core near the entrance to the beam tubes. Reactors usually operate as continuous sources of neutrons. Unlike the processes in the reactor core, production of neutrons by spallation involves highly energetic particles such as protons produced by a linear proton accelerator chipping (spalling) neutrons from heavy nuclei such as mercury. The neutrons produced have extremely high energies that also have to be reduced by moderation. Neutron guides are then used to transport the neutrons to the spectrometers. The interior of the guides is coated with suitable materials so that the neutron beam can be totally reflected.

In the neutron scattering experiment Q, the change in momentum transfer has to be measured with good precision. The process of defining the neutron beam is called

collimation. Collimators limit the size and angle of divergence of the incident beams. Monochromation refers to the selection of a particular wavelength or narrow band of wavelengths from the spread of wavelengths. There are basically only two ways of choosing a given wavelength. One is using the wave nature of the neutron via Bragg diffraction from a suitable crystal; the other is using the particle nature and a mechanical velocity selector to select a narrow velocity range. The scattered neutrons then can be measured by a two-dimensional area detector, divided into pixels (64×64 for the NIST detector). Varying the sample to detector distance and the wavelength of the incident beam can then span the Q range.

5.7 DATA COLLECTION, CORRECTION AND NORMALIZATION

In some cases, data must be acquired at more than one sample to detector distance (SDD) in order to cover the full Q range of interest. Also a reasonable overlap in Q range from one SDD to another is required to combine the different Q ranges into one single scattering curve. Data reduction is done for each run before combining the corrected data into a single scattering curve. Even though the fundamentals of the reduction are same, each facility uses its own program to do the data reduction. In this section, we use NIST as an example.

For liquids, the sample cells used in the experiment are usually quartz cells with 5mm, 2mm or 1mm path length depending on the sample. A thermostatted sample stage is always used to hold the cells exactly perpendicular to the neutron beam. Before running the experiments, we align the sample stage, beam center and beamstop. The beamstop can be positioned by placing a strong forward scattering sample in the sample holder and

starting data acquisition; adjusting the beamstop until the scattering image is symmetric around the beamstop. The beam center can then be measured with the beamstop moved out of the way.

After the instrument is ready, several standards are always measured in order to get the absolute scale. There are several standards used at NIST: silica is used for intermediate Q detector distances on the 30m SANS instrument; water is generally used for shorter wavelength or shorter detector distances on 30m SANS instrument where the silica sample scatters too strongly; and polystyrene is used for intermediate to long configurations of the 30m SANS instruments.

After these preliminaries are done (about three hours), the samples are ready to be run. Any SANS measurement from a sample solution requires also the measurement of the scattered intensity contributions from the empty cell (I_E) in the beam and from the ambient background (I_B) when a sheet of cadmium is used to block the beam. The transmission T , the ratio of neutrons not being scattered to the incident neutrons, for each sample should also be determined to correct for the attenuation of neutron intensity by the sample. The measurement of the transmission involves attenuating the neutron beam, moving the beamstop out and using the area detector to collect the data.

The measured intensity I_S of neutrons scattered by the sample is corrected for these various contributions:¹¹²

$$I_S^\circ = (I_S - I_E) - T_S / T_E (I_E - I_B) \quad (5.1)$$

Where, T_S , T_E are transmissions for sample and empty cell, respectively. I_S° is called the corrected intensity or $I(Q)$. The factor T_S / T_E is to correct for difference of attenuation of the incident beam in traversing the sample and the windows of the cell.

Data are placed on an absolute scale using measurements of a standard sample under the same spectrometer conditions as those used to acquire the data. The scattered intensity for the sample and standard $I(Q)$ are related to the absolute cross section $d\Sigma(Q)/d\Omega$ by the expression:

$$I(Q) = \Phi A d T (\Sigma(Q)/d\Omega) \Delta\Omega \varepsilon t \quad (5.2)$$

where Φ = flux on the sample,

A = sample areas,

d = sample thickness,

T = measured sample transmission,

$\Delta\Omega$ = solid angle subtended by the pixel i ,

ε = detection efficiency of pixel i ,

t = effective counting time, which was renormalized to give 10^8 monitor counts at

NIST

By dividing this expression for the sample by a similar expression for the standard, the absolute cross-section can be calculated from:

$$\frac{d\Sigma(Q)}{d\Omega} = \frac{I(Q)}{I_s(0)} \frac{MON_s}{MON} \frac{d_s}{d} \frac{T_s}{T} \frac{d\Sigma(0)}{d\Omega} \quad (5.3)$$

Where $I_s(0)$ = measured intensity of the standard sample at $Q = 0$,

d_s = thickness of the standard sample,

T_s = transmission of standard sample,

MON = monitor counts,

MON_S = standard monitor counts, note that $\text{MON}_S = \text{MON}$ if $I(Q)$ and $I_S(Q)$ are from radially averaged work files. Radial averaging means assigning the detector pixels in successive narrow annuli around the beam stop to their appropriate Q value and summing the counts in the pixels.

5.8 LEAST SQUARES FITTING FOR DATA REDUCTION

The weighted least-square methods use the chi-squared (χ^2) function as a measure for the deviation between the experimental data and the model fits. In neutron scattering experiments the measured intensity $I^{\text{exp}}(Q_i)$ is the dependent variable, depending on Q_i , the scattering vector and independent variable. Counting statistics will give rise to the statistical uncertainties σ_i on the data points $I^{\text{exp}}(Q_i)$. Chi-squared is defined as:

$$\chi^2 = \sum_{i=1}^N \left(\frac{I^{\text{exp}}(Q_i) - I^{\text{mod}}(Q_i)}{\sigma_i} \right)^2 \quad (5.4)$$

$I^{\text{mod}}(Q_i)$ are the model intensities which come from the fits. The goal of our fitting is try to minimize the chi-squared value. When $|I^{\text{exp}}(Q_i) - I^{\text{mod}}(Q_i)| \leq \sigma_i$, which means that the deviations are on average equal to or less than the statistical uncertainties. If this is true for every data point, $\chi^2 \leq 1$. More rigorous discussions of the chi-squared function are found elsewhere.^{113, 114} Since $I(Q)$ is not a linear function of Q , the method we used is called non-linear least squares fitting. In some cases, the fluctuations in the data come from the instrumental errors, and the uncertainties vary point by point. It is then necessary to weight the fits (by the reciprocal of the square of the statistical error of the

individual points), which can make the points with larger error bars have less contribution on the overall scattering curve fits. The fitting procedure utilized the standard non-linear least squares algorithm developed by Marquardt and Levenberg.¹¹⁴

The fitting programs were written in Fortran, and the programs were compiled by combining several different modules into a main executable program. The main program was used to read in data, call different subroutines, input initial guesses for parameters being varied and write out the fitted results. Before fitting, the data was always trimmed by deleting points with particularly large error bars (always first 10 points from the detector shadow, and last few points at high Q). The fitting parameters can be fixed or varied, and reasonable initial parameters were input to initiate the fitting process. We always fixed the background to a zero or nonzero number (flat background from solvent) based on the data reduction process corrected solvent runs. Details on the micellar models are discussed in chapters III and IV.

LIST OF REFERENCES

1. Lequeux, F.; Candau, S. J. *Structure and Flow in Surfactant Solutions*, ACS: Washington, DC 1994.
2. Lindman, B.; Wennerstrom, H. *Micelles: Amphiphile Aggregation in Aqueous Solution*, Topic in Current Chemistry, Springer-Verlag, New York, 1980.
3. Israelachvili, J. N. *Intermolecular and Surface Forces*, AP: New York, 1985.
4. Tanford, C. *The Hydrophobic Effect: Formation of Micelles and Biological Membranes*, John Wiley & Sons: New York, 1973.
5. Blankschtein, D.; Thurston, G. M.; Benedek, G. B. *J. Chem. Phys.* 1986, 85, 7268.
6. Heindl, A.; Kohler, H.-H. *Langmuir*, 1996, 12, 2464
7. Wennerstrom, H.; Lindman, B. *Physics Reports*, 1979, 52, 1.
8. Kruyt, H. R. ed., *Colloid Science, Voll*, Elsevier, New York, 1952.
9. Israelachvili, J. N.; Mitchell, D. J.; Ninham, B. W. *Biochem. Phys. Acta.* 1977, 470, 185.
10. Mittal, K. L. *Micellization, Solubilization, and Microemulsions* Plenum, New York, 1977.
11. Mukerjee, P. *J. Phys. Chem.* 1962, 66, 943.
12. Candau, S. J.; Hirsch, E.; Zana, R. *J. Phys. (paris)* 1984, 45, 1263.
13. Candau, S. J.; Hirsch, E.; Zana, R. *J. Coll. Inter. Sci.* 1985, 105, 521.
14. Appell, J.; Porte, G. *J. Coll. Inter. Sci.* 1982, 87, 492.
15. May, S.; Bohbot, Y.; Ben-Shaul, A. *J. Phys. Chem. B* 1997, 101, 8648.
16. Cates, M. E.; Candau, S. J. *J. Phys.: Condens. Matter* 1990, 2, 6869.
17. Kern, F.; Lequeux, F.; Zana, R.; Candau, S. J. *Langmuir* 1994, 10, 1714.

18. Magid, L. J. *J. Phys. Chem. B*, **1998**, *102*, 4064.
19. Cassidy, M. A.; Warr, G. G. *J. Phys. Chem.* **1996**, *100*, 3237.
20. Hayter, J. B.; Penfold, J. *Coll. Poly. Sci.* **1983**, *261*, 1022.
21. Quirin, F.; Magid, L. J. *J. Phys. Chem.* **1986**, *90*, 5435.
22. Carver, M.; Smith, T. L.; Gee, J. C.; Delichere, A.; Caponetti, E.; Magid, L. J. *Langmuir*, **1996**, *12*, 691.
23. Hayter, J. B. *Langmuir*, **1992**, *8*, 2873.
24. Imae, T.; Ikeda, S. *Coll. Polym. Sci.* **1987**, *265*, 1090.
25. Olsson, U.; Soderman, O.; Guering, P. *J. Phys. Chem.* **1986**, *90*, 5223.
26. Imae, T.; Kakitani, M.; Kato, M., Furusaka, M. *J. Phys. Chem.* **1996**, *100*, 20051.
27. Elworthy, P. H.; Macfalane, C. B. *J. Chem. Soc.* **1963**, 907.
28. Odijk, T.; Houwaart, A. C. *J. Polym. Sci., Poly. Phys.* **1978**, *16*, 627.
29. Tricot, M. *Macromolecules*, **1984**, *17*, 1698.
30. Odijk, T. *Biopolymers*, **1979**, *18*, 3111.
31. Porte, G. J.; Appell, J.; Poggi, Y. *J. Phys. Chem.* **1980**, *84*, 3150.
32. Appell, J.; Porte, G. J. *Coll. Inter. Sci.* **1981**, *81*, 85.
33. Imae, T.; Ikeda, S. *J. Phys. Chem.* **1986**, *90*, 5216.
34. Flamberg, A.; Pecora, R. *J. Phys. Chem.* **1984**, *88*, 3026.
35. Imae, T. *J. Phys. Chem.* **1990**, *94*, 5953.
36. Odijk, T. *J. Polym. Sci. B: Polym. Phys.* **1977**, *15*, 477.
37. Skolnick, J.; Fixman, M. *Macromolecules* **1977**, *10*, 944.
38. Le Bert, M. *J. Chem. Phys.* **1982**, *76*, 6243.

39. Fixman, M. *J. Chem. Phys.* **1982**, *76*, 6346.
40. Thies, M.; Hinze, U.; Paradies, H. H.; *Coll. Surf. A.* **1995**, *101*, 261.
41. Magid, L. J.; Triolo, R.; Gulari, E.; Bedwell, B. *Surfactants Solution*, [Proc. Int. Symp.], 4th, Plenum: New York, **1984**.
42. Schurtenberger, P.; Magid, L. J.; King, S. M.; Lindner, P. *J. Phys. Chem.* **1991**, *95*, 4173.
43. Long, M. A.; Kaler, E. W.; Lee, S. P.; Wignall, G. D. *J. Phys. Chem.* **1994**, *98*, 4402.
44. Liu, Y.C.; Ku, C. Y.; Lonostro, P.; Chen, S. H.; *Phys. Rev. E* **1995**, *51* 4598.
45. Aswal, V.K.; Goyal, P.S.; De, S.; Bhattacharya, S.; Amenitsch, H.; Bernstorff, *S. Chem. Phys. Lett.* **2000**, *329*, 336.
46. Bate, F. S. *Macromolecules*, **1985**, *18*, 525.
47. Higgins, J. S.; Benoit, H. C. *Polymers and Neutron Scattering*, Oxford, New York, **1994**.
48. Squires, G. L. *Introduction to the Theory of Thermal Neutron Scattering*, University Press: Cambridge, **1978**.
49. Hayter, J.B. *Physics of Amphiphilics: Micelles, Vesicles and Microemulsions*, NHPP: Amsterdam, **1985**.
50. Stuhrmann, H.B.; Miller, A. *J. Appl. Crystallogr.* **1978**, *11*,325.
51. Guinier, A.; Fournet, G. *Small Angle Scattering of X-rays*, Wiley-Interscience: New York, **1955**.
52. Flory, P.J. *Statistical Mechanics of Chain Molecules*, Wiley-Interscience: New York, **1969**.

53. Yoshizaki, T.; Yamakawa, H. *Macromolecules* **1980**, *13*, 1518.
54. Yamakawa, H. *Modern Theory of Polymer Solutions*, Harper&Row: New York, **1971**.
55. Teraoka, I. *Polymer Solutions*, Wiley-Interscience: New York, **2001**.
56. Kamide, K. Dobashi, T. *Physical Chemistry of Polymer Solutions*, Elsevier, New York, **2000**.
57. Pedersen, J. S.; Schurtengerber, P. *Macromolecules* **1996**, *29*, 7602.
58. Pedersen, J. S.; Laso, M.; Schurtengerber, P. *Phys. Rev. E* **1996**, *54*, R5917.
59. Mukerjee, P. *J. Phys. Chem.* **1972**, *76*, 565.
60. Lin, T. L.; Chen, S. H.; Gabriel, N. E.; Roberts, M. F. *J. Phys. Chem.* **1987**, *91*, 406.
61. Pedersen, J. S.; Schurtenberger, P. *J. Appl. Cryst.* **1996**, *29*, 646.
62. Papali, P. ed. *Physics of Amphiphiles – Micelles, Vesicals, and Microemulsions*, International School of Physics “Enrico Feimi”, Elsevier: New York, **1983**.
63. Percus, J. K.; Yevick, G. J. *Phys. Rev.* **1958**, *1*, 110.
64. Hayter, J. B.; Penfold, J. *Molecular Physics*, **1981**, *1*, 109.
65. Magid, L. J.; Li, Z.; Butler, P. D. *Langmuir*, **2000**, *16*, 10028.
66. Huber, K.; Stockmayer, W. H. *Macromolecules* **1987**, *20*, 1400.
67. Casassa, E. F. *J. Chem. Phys.* **1955**, *28*, 105.
68. Holtzer, A. *J. Polym. Sci.* **1955**, *17*, 433.
69. Schmidt, M.; Paradossi, G.; Burchard, W. *Makromol. Chem. Rapid Commun.* **1985**, *6*, 767.

70. Bragg, W. L.; Perutz, M. F. *Proc. Royal. Soc.* **1952**, *A213*, 425.
71. Worcester, D. L. *J. Appl. Cryst.* **1988**, *21*, 669.
72. Herbst, L.; Kalus, J.; Schmelzer, U. *J. Phys. Chem.* **1993**, *97*, 7774.
73. Schurtenberger, P.; Jerke, G.; Cavaco, C. *Langmuir*, **1996**, *12*, 2433.
74. Lin, T. L. *Physica B*, **1995**, *213-214*, 594.
75. Ohta, T; Oono, Y, *Phys. Lett*, **1982**, *89A*, 460.
76. Huisman, H. F. *Proc. Kon. Ned. Akad. Wet. Ser. B* **1964**, *67*, 367, 376, 388, 407.
77. Almgren, M.; Lofroth, J.-E.. *J. Colloid Interface Sci.* **1981**, *81*, 486.
78. Chen S.-H. *Annu. Rev. Phys. Chem.* **1986**, *37*, 351.
79. Cabane, B.; Duplessix, R.; Zemb, T. *J. Phys. Fr.* **1985**, *46*, 2161.
80. Zemb, T.; Charpin, P. *J. Phys. Fr.* **1985**, *46*, 249.
81. Corti, M.; Degiorgio, V. *J. Phys. Chem.* **1981**, *85*, 711.
82. Schurtenberger, P.; Cavaco, C.; Tiberg, F.; Regev, O. *Langmuir*, **1996**, *12*, 2894.
83. Pedersen, J. S. *Adv. Coll. Inter. Sci.* **1997**, *70*, 171.
84. De Gennes, P. G. *Scaling Concepts in Polymer Physics*, Cornell Univ. Press, New York, **1979**.
85. Anacker, E. W.; Ghose, H. M. *J. Am. Chem. Soc.* **1968**, *90*, 3161.
86. Arleth, L.; Bergstrom, M.; Pedersen, J. S. *Langmuir*, **2002**, *18*, 5343.
87. Maeda, H.; Kanakubo, Y.; Miyahara, M.; Kakehashi, R.; Garamus, V.; Pedersen, J. S. *J. Phys. Chem.* **2000**, *104*, 6174.
88. Porte. G.; Appell, J. *Surfactant Solutions*, **1984**, *2*, 805.

89. Alargova, R. G.; Kochijashky, I. I.; Sierra, M. L.; Zana, R. *Langmuir*, **1998**, *14*, 5412.
90. Hansson, P.; Jansson, B.; Strom, C.; Soderman, O. *Langmuir*, **2000**, *104*, 3496.
91. Kalus, J.; Hoffmann, H.; Reizlein, K.; Ulbricht, W.; Ibel, K. *Ber. Bunsen-Ges. Phys. Chem.* **1982**, *86*, 37.
92. Shikata, T.; Hirata, H. *Langmuir*, **1989**, *5*, 398.
93. Mohanty, S.; Davis, H. T.; McCormick, A. V. *Langmuir*, **2001**, *17*, 7160.
94. Magid, L. J.; Han, Z.; Warr, G. G.; Cassidy, M. A.; Butler, P. D.; Hamilton, W. *A. J. Phys. Chem. B* **1997**, *101*, 7919.
95. Magid, L. J.; Han, Z.; Li, Z.; Butler, P. D. *J. Phys. Chem. B*, **2000**, *104*, 6717.
96. Imae, T. *Colloid Polym. Sci.* **1989**, *267*, 707.
97. Gamboa, C.; Olea, A.; Rios, H.; Vargas, V. *Bol. Soc. Chil. Quim.* **1990**, *35*, 61.
98. Narayanan, J.; Manohar, C.; Langevin, D.; Urbach, W. *Langmuir*, **1997**, *13*, 398.
99. Walker, L. M. *Curr. Opin. in Coll. & Inter. Sci.* **2001**, *6*, 451.
100. Hamilton, W. A.; Butler, P. D.; Magid, L. J.; Han, Z.; Slawecki, T. M. *Phys. Rev. E* **1999**, *60*, R1146.
101. Hassan, P. A.; Candau, S. J.; Manohar, C. *Langmuir*, **1998**, *14*, 6025.
102. Brown, W.; Lohansson, K.; Almgren, M. *J. Phys. Chem.* **1989**, *93*, 5888.
103. Jerke, G.; Pedersen, J. S.; Egelhaaf, S. U.; Schurtenberger, P. *Langmuir*, **1998**, *14*, 6013.
104. Nordmeier, E.; Dauwe, W. *Polym. J.* **1992**, *24*, 229.
105. Eisenberg, H. *Acta. Polym.* **1998**, *49*, 543.

106. Foster, S.; Schmidt, M. *Adv. Polym. Sci.* **1995**, *120*, 51.
107. Mishic, J. R.; Fisch, M. R. *J. Chem. Phys.* **1990**, *92*, 3222.
108. Dingenouts, N.; Seelenmeyer, S.; Deike, I.; Roenfeldt, S.; Ballauff, M.; Lindner, P.; Narayanan, T. *Phys. Chem. Chem. Phys.* **2001**, *3*, 1169.
109. Brasher, L. L.; Kaler, E. W. *Langmuir*, **1996**, *12*, 6270.
110. Perron, G.; Desnoyers, J. E. *Fluid Phase Equilibria*, **1979**, *2*, 239.
111. Berr, S. S. *J. Phys. Chem.* **1987**, *91*, 4760.
112. *NIST Center for Neutron Research NG3 and NG7 30m SANS Instruments Manual*, January, **1999**.
113. Press, W.H.; Flannery, B. P.; Teukolsky, S.A.; Vetterling, W. T. *Numerical Recipes*, University press, Cambridge, **1989**.
114. Bevington, P. R. *Data Reduction and Error Analysis for the Physical science* McGraw-Hill, NewYork, **1969**.

VITA

Zhibin Li was born in Lanzhou, Gansu, P. R. China, on November 9, 1972. He stayed in his hometown until finished his high school work in June 1991, and then entered the University of Science and Technology of China, Hefei, Anhui, P. R. China. He graduated in 1996 with a B. S. degree in Applied Chemistry.

In August 1998 the author entered the graduate program in chemistry at the University of Tennessee, Knoxville. During his time as a graduate student, he went to NIST Center for Neutron Research, IPNS at Argonne National Laboratory, and SINQ in Switzerland to conduct small-angle neutron scattering experiments.